Understanding the mechanics of tissue growth in engineered scaffolds: Case of cartilage tissue

by

Umut Akalp

B.S., Bogazici University, 2008

M.S., Bogazici University, 2010

A thesis submitted to the

Faculty of the Graduate School of the

University of Colorado in partial fulfillment

of the requirements for the degree of

Doctor of Philosophy

Department of Civil Engineering

2017

This thesis entitled:
Understanding the mechanics of tissue growth in engineered scaffolds: Case of cartilage tissue
written by Umut Akalp
has been approved for the Department of Civil Engineering

_____

Prof. Franck J. Vernerey

_____

Prof. Stephanie J. Bryant

Date _____

The final copy of this thesis has been examined by the signatories, and we find that both the content and the form meet acceptable presentation standards of scholarly work in the above mentioned discipline.

Akalp, Umut (Ph.D., Civil Engineering)

Understanding the mechanics of tissue growth in engineered scaffolds: Case of cartilage tissue

Thesis directed by Prof. Franck J. Vernerey

Tissue failure due to aging or diseases reduces the quality of life for individuals. In the case of cartilage tissue, the current solution is to use implants to fulfill the functional duties of native tissue. However, this approach has limitations, such as periodic replacement and number of the required operations. Tissue engineering provides an alternative approach in which the aim is to regenerate the native tissue by a population of cells encapsulated in a scaffold (i.e. hydrogels). Although this approach is promising, there are several limitations regarding the design of these scaffolds which can be overcome only by the deep understanding of the coupling between mechanics and biological remodeling. For that reason, computational models are essential component of the ongoing research due to the cost and time limitations of the experimental studies.

The aim of this study is to present a 3D computational tool based on the existing theories of remodeling in biological materials. The tool is composed of two parts; (i) an optimization tool which allows to assess the property-structure-property relationship of the scaffolds, (ii) a 3D finite element model that captures the coupling between the mechanics and cell mediated remodeling. The optimization tool, so called *self learning algorithm* aims two objectives. First objective is to generate input data for the mechanistic model and simulate real cases, which will allow us to know where we are in our search for optimum scaffold properties. Second, a map between design parameters and physical properties has been built in order to direct our search in an efficient way. Second part of the computational tool is a 3D multi-scale, finite element (FE) model for remodeling in biological materials at finite growth. Both models are based on the mixture theory at finite strain and utilizes various existing theories including well known Flory-Rehner theory of swollen networks.

Dedication

To my beloved parents...

Acknowledgements

I owe a profound debt to many people who have contributed greatly to completing this dissertation.

I would like to express my deep gratitude to my supervisor Professor Franck J. Vernerey for his guidance, support, understanding and unfailing kindness throughout my education at the University of Colorado at Boulder. His trust in me and the freedom he provided in my research have greatly contributed to my personal and professional growth. I will always be inspired by the wonderful and rewarding experience of having worked with him and learned from him.

I am grateful to Professor Stephanie J. Bryant for her expert advice and her availability to me throughout the research process. Many thanks to Professor Alireza Doostan, Professor Ronald Pak and Professor Richard Regueiro for being a member of my committee and for their sincere interest in my work.

Sincere thanks to my dear friends Sina, Inom, Volkan, Yucel, Jenya, Reza, Louis, Eduard, Hyeon and Valentin for their support and all we shared for so many years. Many flowers to Martli family, for their unconditional help and friendship. Special thanks to Dave, David, Bob, Bruce, Robert and Tom for their support.

And for being so close to me from so faraway, for the loving support that made this all possible my thanks and my love to my parents Gulseren Akalp and Nizameddin Akalp.

Contents

Chapter

1 On the role of hydrogel structure and degradation in controlling the transport of cell-secreted matrix molecules for engineered cartilage 4

1.1 Introduction 4

1.2 Hydrogel structure: processing and mathematical description 7

1.2.1 Processing of cell-laden hydrogels and control of initial hydrogel structure . . 7

1.2.2 Overall modeling strategy of the macroscopic tissue evolution 8

1.3 The evolving structure and properties of degrading hydrogels 11

1.3.1 Physical Model of the Hydrogel 11

1.3.2 Hydrolytic degradation 13

1.3.3 Hydrogel processing and measurement of overall properties 14

1.4 Production and transport of ECM molecules within an evolving hydrogel structure . 17

1.4.1 Classification of ECM molecules and experimental observation 18

1.4.2 Modeling molecular transport in deforming hydrogels 20

1.5 Results and discussion 26

1.5.1 Role of initial hydrogel mesh size on ECM distribution 27

1.5.2 Role of hydrolytic degradation on ECM transport 28

1.5.3 Role of osmotic pressure in diffusion of molecules and creation of tissue . . . 30

1.5.4 Concluding remarks 31

2 Determination of the Polymer-Solvent Interaction Parameter for PEG Hydrogels in Water: Application of a Self Learning Algorithm 33

2.1 Introduction . . . 33

2.2 Mapping PEG hydrogel processing to properties . . . 35

2.2.1 General approach . . . 35

2.2.2 Application to PEG hydrogels . . . 37

2.2.3 Integration of experimental data and modeling . . . 41

2.3 Mechanistic model calibration . . . 44

2.3.1 Inverse problem for mechanistic model calibration . . . 46

2.3.2 **Acceleration via surrogate modeling** . . . 47

2.4 Predictive modeling of PEG hydrogel to determine χ . . . 48

2.4.1 Elucidating trends between control parameters and microstructure for PEG hydrogels . . . 49

2.4.2 Model Validation . . . 53

2.4.3 Quantifying the polymer-solvent interaction parameter during hydrolytic degradation of PEG hydrogels . . . 54

2.5 Summary and concluding remarks . . . 57

3 Tuning Reaction and Diffusion Mediated Degradation of Enzyme-Sensitive Hydrogels 61

3.1 Introduction . . . 61

3.2 Assessment degradation-diffusion parameters in 1D experiments . . . 63

3.3 Experimental section . . . 74

4 A computational model for hydrogels in tissue engineering part I: cell mediated degradation 76

4.1 Introduction . . . 76

4.2 Kinematics and Balance Laws for the scaffold . . . 78

4.2.1 Kinematics . . . 79
4.2.2 Mass Balance . . . 81
4.2.3 Balance of momentum . . . 82
4.2.4 Balance of Energy and Entropy Inequality . . . 83
4.3 Constitutive relations and complete mathematical model . . . 87
4.3.1 Constitutive Relations . . . 87
4.3.2 Complete mathematical model and non-dimensional forms . . . 91
4.3.3 Non-dimensional form of the mathematical model . . . 92
4.4 Finite element formulation and numerical aspects . . . 94
4.4.1 Weak form, linearization and discretization . . . 95
4.4.2 Concept of representative volume element and homogenization . . . 98
4.5 Results and Discussion . . . 101
4.5.1 Revisiting the Clausius-Duhem Inequality . . . 101
4.5.2 Model comparison with Mori-Tanaka analytic solution . . . 102
4.5.3 Mandel's Problem . . . 105
4.5.4 Degradation-transport characteristics and its impact on the construct elasticity 106
4.5.5 Impact of fluid flow on the gel degradation and its elasticity . . . 108
4.6 Concluding remarks . . . 112

5 Tuning Tissue Growth with Scaffold Degradation in Enzyme-Sensitive Hydrogels: a Mathematical Model 113

5.1 Introduction . . . 113
5.2 Growth in enzyme degradable hydrogel scaffold . . . 116
5.3 Model formulation . . . 121
5.3.1 Mass transfer . . . 121
5.3.2 Evolution of construct mechanics . . . 123
5.4 Model analysis and solution . . . 125

5.5 Results . . . 128
5.5.1 Degradation around a single cell . . . 129
5.5.2 The role of hydrogel degradation on the nature of ECM deposition . . . 132
5.5.3 Evolution of the construct's mechanical integrity during combined hydrogel degradation and ECM growth . . . 134
5.6 Discussion and Concluding remarks . . . 137

Bibliography 142

Appendix

A Derivation of Diffusion-Reaction Models 154
A.1 1D diffusion of enzyme in non-degrading hydrogel and estimation of enzyme characteristics . . . 156
A.2 Calibration and validation of the mathematical model with experimental data . . . 159
A.3 Non-dimensionalizing the governing equations . . . 161

B Finite Element Formulation for 3D Growth Model at Finite Strain 162

C Finite Element Formulation for 3D Growth Model at Small Strain 167

Tables

Table

1.1 Composition of native cartilage. 18

1.2 Inputs used in the model. 24

2.1 Control variables, internal state variables, and properties of interest in the hydrogel model. 38

2.2 Summary of model structure and parameters for degradable PEG hydrogels 40

3.1 Three hydrogels with differing enzyme concentrations were investigated with their properties of: enzyme concentration (C_e^o), which was maintained throughout the experiment, network connectivity (β), initial volumetric swelling ratio (Q^0), initial compressive modulus (E^0), polymer-solvent interaction param- eter (χ), and initial crosslink density in the swelling solvent (i.e., phosphate buffered saline ($\rho_x^{s,0}$). 64

3.2 Two hydrogels with the same microparticles were investigated with their properties of: initial volumetric swelling ratio (Q^0), initial compressive modulus (E^0), polymer-solvent interaction parameter (χ), network connectivity (β) as determined by the model, and initial crosslink density in the swelling solvent (i.e., phosphate buffered saline) ($\rho_x^{s,0}$). 69

4.1 Inputs used in the model. 103

5.1 Inputs used in the model. 128

A.1 Hydrogel formulations 156

A.2 Hydrogel formulations 156

Figures

Figure

1.1 *Mutiscale approach to modeling tissue production by cells encapsulated in hydrogels. Refer to the next sections for the parameters. Left: chondrocytes encapsulated within a PEG hydrogel, shown at day 3 after encapsulation. Cytosol of live cells fluoresce green showing the chondrocytic round morphology. Nuclei of dead cells fluoresce red. Scale bar indicates 100 microns. Right: chondroitin sulfate elaboration (red) by chondrocytes encapsulated within a degradable PEG hydrogel after 28 days in vitro. Cell nuclei are stained blue. Scale bar indicates 50 microns.* 7

1.2 *From real engineered tissues to an idealized mathematical model. Left picture shows cell nuclei (blue) and collagen (green). Scale bar represents 50 μm.* 9

1.3 *Schematics representing an idealized network structure formed from PEGDM or PEGLA-DM macromers by radical chain polymerization. Left, non-degrading (based on experimental timescale) PEGDM hydrogels form a stable network structure. Right, hydrolytically degradable hydrogels made of PEGLA-DM exhibit degradation and swelling with time.* 12

1.4 *(a) The nonlinear compressive/elastic modulus through the stress - strain curves for different crosslink densities. Experimental results and the model are compared. (b) The equilibrium swelling ratio as a function of crosslinking density for stable PEG hydrogels formed from PEGDM macromers obtained both experimentally and determined by the model. Error bars indicate standard deviation (n=3).* 15

1.5 *Swelling ratio Q over time in a bimodally degradable hydrogel consisting of a 95:5 weight ratio of PEGLA-DM and PEGDM.* 18

1.6 *Gauss error function used in the model to describe the constitutive relations.* Δ *is taken as* $4r_s$ *in the above figure.* 19

1.7 *Diffusivity of proteins through the hydrogel. How the size of a protein impacts the boundary conditions.* 20

1.8 *(ac) An experimental result and the model results for different crosslink densities of a stable hydrogel. Regarding the experimental pictures, chondroitin sulfate elaboration (red) by chondrocytes encapsulated within PEGDM hydrogels and cultured for 25 days in vitro with varied crosslinking density. Cell nuclei are stained blue. Scale bars indicate 50 microns. In the three-dimensional plots, the stress* P_{rr} *(kPa), strain* E_{rr}*, mesh size* ξ *(nm) and concentration* c^p *(mmol/mL) can be observed.* 21

1.9 *(a) The results for a non-degradable stable hydrogel, and (b) degradable hydrogel. First image is the experiment showing chondroitin sulfate elaboration (red) by chondrocytes at day 28 encapsulated within 10% w/w non-degradable PEGDM and degradable PEGLA-DM hydrogels. Cell nuclei are stained blue. Scale bars indicate 50* μ*m. In the three-dimensional plots, the stress* P_{rr} *(kPa), strain* E_{rr}*, mesh size* ξ *(nm) and concentration* c^p *(mmol/mL) can be observed. Note that due to differences in image processing between experiments, chondroitin sulfate staining is of lower intensity than shown in Fig. 1.8.* 22

1.10 *(a) The effect of swelling on the mesh size, and (b) the effect of the degradation rate k on the distribution of matrix molecules in the scaffold at day 25.* 29

1.11 *The different osmotic pressures (20, 200, 300, and 400 kPa) applied on the model to see the evolution of the diffusivity.* 29

2.1 Processing-microstructure and microstructure-properties maps. 37

2.2 Experimental tests provide sample points of the map between the control space **C** and the property space **g**. Uncertainties in control variables propagate to the property space; this aspect can be quantified by measuring the probability density function (PDF) in both domains through the realization of several experiments under similar design conditions. 42

2.3 Confidence intervals for (a) the swelling ratio and (b) the compressive modulus of three hydrogel designs. For each design, the properties of interest were measured three times, independently. The data set for each independent experiment can be represented as an interval by using the mean and standard deviation values. 43

2.4 Framework for model calibration from experiments. We consider the model as an active entity, represented by a robot that can observe the relationship between input and output obtained from experiments and adjust its free parameters to best fit the data. If it fails at doing so, the model may request a modification of its own structure, represented by differential equations. 45

2.5 Flowchart of the utilized model calibration algorithm. 46

2.6 (a) A surrogate model is an approximation which is constructed by using a set of realizations of model parameters (defined over an appropriate range) and the corresponding solutions of interest. (b) Surrogate model for swelling ratio of the initial PEG hydrogel properties based on equation (2.6). 47

2.7 Graphical representation of experimental results. A total of five PEG hydrogel designs was processed, for which both the equilibrium swelling ratio and Young's modulus (compression) were determined. For each design, the tests were repeated three times in order to quantify uncertainties in measured quantities of interest (depicted by error bars). Apart from these another PEG hydrogel design is processed to validate the calibration. 50

2.8 Minimization of the cost function (2.18) for an independent polymer-solvent interaction parameters: (a) Distance between experimental and model predictions in the ($Q^0 - E_c$) space, (b) Value of the polymer-solvent interaction parameters as a function of control parameters, and (c) Initial cross-link density in terms of control parameters. 51

2.9 Minimization of the cost function (2.18) for a dependent polymer-solvent interaction parameter: (a) Distance between experimental and model predictions in the ($Q^0 - E_c$) space, (b) Values of the polymer-solvent interaction parameter as a function of control parameters and (c) Initial cross-link density in terms of control parameters. . 53

2.10 Model validation. For a given hydrogel formulation (validation point in Fig.2.7), the map shown in Fig 2.9 was used to determine the cross-link density and polymer-solvent interaction parameters that lead to the compressive modulus and swelling ratio shown here for the validation point. Experiments for this gel formulation were also performed and compared with the prediction. We show here both calibration and validation points in the E_c-Q^0 space. 54

2.11 Experimental measurements and optimized model fitting assuming a constant value of the polymer-solvent interaction parameter during degradation. Evolution of (a) the compressive modulus and (b) the swelling ratio of a hydrogel immersed in aqueous solutions at pH of 9 and 11. (c) Predicted polymer-solvent interaction parameter and (d) change in kinetic coefficient with respect to the crosslinking density during degradation. 56

2.12 Experimental measurements and optimized model fitting for a variable Flory-Huggins parameter during degradation. Evolution of (a) the compressive modulus and (b) the swelling ratio of a hydrogel immersed in aqueous solutions at pH of 9 and 11. (c) predicted change in polymer-solvent interaction parameter and (d) kinetic constant with respect to the crosslinking density during degradation. 57

3.1 *(A) Schematic (left) represents diffusion-dominated hydrogel degradation where enzymes readily diffuse away from the encapsulated cell while simultaneously cleaving the crosslinks. Schematic (right) represents reaction-dominated hydrogel degradation where enzyme diffusion is restricted and/or enzymes are highly reactive to their substrate leading to hydrogel degradation immediately surrounding the encapsulated cell, leaving the bulk hydrogel in its original state. (B) Schematic of the enzyme-sensitive poly(ethylene glycol) (PEG) hydrogel used in the study, which is fabricated by photopolymerization of an 8 arm PEG functionalized with norbornene and a bis-cysteine peptide that is sensitive to collagenases. The hydrogel was fluorescently labeled by introducing a maleimide fluorophore, which reacts with pendant thiols. (C) Schematic of the 1D experimental system for studying enzyme-mediated hydrogel degradation. (D) Schematic of the 3D experimental system for studying enzyme-mediated hydrogel degradation whereby enzyme-loaded microparticles serve as cell-mimetics, which release enzymes with time but are not complicated by deposition of extracellular matrix.* 63

3.2 *Characterization of hydrogel degradation in 1D. Using the experimental set-up described in Figure 1C, fluorescent images are shown for each hydrogel case as a function of time whereby position 0 mm indicates the initial edge of the hydrogel prior to degradation (i, ii, iii). The enzyme source is located to the left of the hydrogel. The front, corresponding to reverse gelation, can be observed advancing away from the initial position (i.e., 0 mm) of the hydrogel over time. The velocity of the front was determined by plotting distance of the front as a function of time and using a linear fit (n = 3, data are mean with standard deviation as error bars) (iv, v).* . . 65

3.3 *Characterization of hydrogel degradation in 1D. The mathematical model was fit to the experimental data by varying network connectivity (β), radius of active enzyme (r_e), and the MichaelisMenten kinetic constants (k_{cat} and K_m), which are unknowns (i, ii, iii). The propagating front (distance versus time) and the corresponding velocity are shown for each hydrogel case (iv, v). In addition, spatiotemporal pattern of crosslink den- sity as a function of distance away from the enzyme source are shown for each crosslink hydrogel case for the initial time prior to degradation and after 74 and 148 h (vi, vii, viii). The initial variation in cross- link density was determined from the experimental system (at time 0), which arises from unconfined swelling at the edges of the hydrogel.)* 67

3.4 *Characterization of hydrogel degradation in 3D. In experiments, the set-up described in Figure 1D was used with a fluorescently labeled (red) hydrogel. In simulations, the enzyme radius and MichaelisMenten kinetic constants determined in the 1D experiments were used and the hydrogel was labeled red. Degradation of the low crosslink hydrogel is shown by representative confocal microscopy images of the hydrogel with void spaces (i), which at 0 h correspond to the microparticles. Over time, the overall fluorescence (ii) decreased as well as the compressive modulus (iii) for the hydrogel containing the collagenase-loaded microparticles. Hydrogels with BSA-loaded microparticles showed no change in overall fluorescence (ii) and a slow decrease in the compressive modulus (iii), corresponding to degradation of the microparticles. Simulation results matched experiments showing a diffuse front surrounding the microparticles (iv) and a rapid loss in the compressive modulus (v).* 69

3.5 *Characterization of hydrogel degradation in 3D. In experiments, the set-up described in Figure 1D was used with a fluorescently labeled (red) hydrogel. In simulations, the enzyme radius and MichaelisMenten kinetic constants determined in the 1D experiments were used and the hydrogel was labeled red. Degradation of the high crosslink hydrogel is shown by representative confocal microscopy images of the hydrogel with void spaces (i), which at 0 h correspond to the microparticles. Over time, the overall fluorescence was maintained, but the void spaces became significantly larger in the hydrogel containing the collagenase-loaded microparticles, as shown in the histogram plot (ii). Hydrogels with BSA-loaded microparticles showed no change in the size of the voids, as shown in the histogram plot (iii). Statistical analysis was performed using a nonparametric KolmogorovSmirnov test ($\alpha = 0.05$, $n = 8001300$). The compressive modulus (iv) decreased slowly over time in the hydrogels with the collagenase-loaded microparticles, but no change was observed in the BSA-loaded microparticles. Simulation results matched experiments showing a relatively sharp front surrounding the microparticles with a slight loss in hydrogel crosslinking (v) and correspondingly a slow loss in the compressive modulus (vi) over time.* 70

3.6 *(A) Dimensionless quantities identified by nondimensionalizing the governing equations for diffusion (Ficks second law) and reaction kinetics (MichaelisMenten kinetics) for enzyme-sensitive hydrogels. These four quantities are based on initial hydrogel properties, enzyme characteristics, and enzyme-substrate kinetics. The parameters and their description are listed in the table. (B) An example of contour plots for front velocity (in mm h^1) and front width (mm) as a function of κ and α_e for the case with a $\beta = 0.6$, $K_m = 1010^6$ M, and characteristic length of 2 mm.* . . 73

4.1 The objective of tissue engineering is to design scaffolds to encapsulate the cell, whose mission is to regenerate the damaged tissue in-vivo. 77

4.2 Configuration of the domain of interest at the initial and current frames 80

4.3 The constitutive relations of the model. (a) Boyce-Arruda (B-A) material model is a generalization of Flory's elastic potential for swollen networks. B-A captures the stiffening effect observed at high strain levels through the parameter N, which describes the level of flexibility of a polymer chain. (b) The diffusivity of cell-released particles follows the scaling law derived by Peppas et al. [89]. The diffusivity of the macromolecules decreases with the mesh size, reaching to a zero value when the mesh size is equal to the hydrodynamic radius r_e. To increase diffusivity, crosslinking density should decrease, which can be achieved by degradation. 91

4.4 (a) For the scaffold remodeling simulations we use two RVE's; (I) far from the boundaries of macro-scale domain and (II) in the vicinity of the macro-scale boundaries. (b) RVEs contain two cells as shown in the figure. The mesh is built using level set method. Since the periodicity is assumed, the cell distribution in $RVE-I$ and $RVE-II$ are the same. 100

4.5 (a) The degradation of the hydrogel at constant enzyme concentration following the rule (4.48) where $\kappa_e^I = 20$, $\kappa_e^{II} = 2$, $\rho = 1.5$ and $C_e = 1$. The corresponding swelling ratios are calculated using the Flory's steady state solution, where $\rho_c = 0.08$ Mole/Liter. As the degradation progresses, the mass of fluid, and therefore the swelling ratio, increases. The swelling is due to the incoming fluid flux $\nabla_{\mathbf{X}}\tilde{\mathbf{V}}_w > 0$. . 102

4.6 Comparison of the model results to the solution of Mori-Tanaka method. At the two extremes the elastic modulus of the composite converges to either the modulus of matrix or inclusions. Model also predicted the stress distribution around the soft inclusion is relatively low. 104

4.7 (a) Comparison of the model results to the analytical solution of Mandel's problem. (b) The model well captures the transient behavior described by the analytical solution. The pressure gradient generated a fluid flow through the end of the block. (c) Mesh convergence study show a second order convergence for the pressure field, which is in agreement with the theory. (d) Convergence of Newton-Raphson method is quadratic, as it is in the theory, which supports the accuracy of the linearization procedure. 106

4.8 (a) Parametric study using $\kappa_e I$ and r_e shows that the degradation characteristics ranges from a wide diffusion-like profile to a sharp wave-like profile. Speed of the degradation is also directly affected by the same parameters, which is observed via front speed. (b) Model Prediction for two extreme cases of degradation-diffusion model; degradation dominated case shows a sharp variation in crosslinking density similar to a wave front, while in the diffusion dominated case variation is similar to a diffusion profile. (c) In the diffusion dominated load carrying capacity is lost faster than in the case of degradation dominated since degradation evolves faster. $E_0 = 0.74RT$ where R is gas constant and T is the absolute temperature. For simplicity of the plots, crosslink density normalized as ρ/ρ_0 where $\rho_0 = 0.038$ Mole/Liter. . . . 109

4.9 (a) Effect of cyclic loading can be simulated considering half cycle. The macroscopic pressure gradient causes a fluid flow while the pressure variation along a RVE is negligible. (b) Two RVE's selected from different macroscopic regions in order to model the effect of fluid flow on diffusion dominated and reaction dominated degradation. $E_0 = 0.74RT$ where R is gas constant and T is the absolute temperature. For simplicity of the plots, crosslink density normalized as ρ/ρ_0 where $\rho_0 = 0.038$ Mole/Liter. 111

5.1 *Schematic of a enzymatically-degradable hydrogel made by photo-polymerization of monomers with enzyme sensitive peptide crosslinkers.* 116

5.2 *Cell mediated tissue growth in a porous scaffold. (a) The construct is composed of cells and the mixture of solid and fluid phases which are either secreted by cell or key elements of a hydrogel. (b) Tissue growth in a hydrogel at the microscale is shown. For convenience we classify cell-secreted molecules under two groups: enzymes and ECM, which are essential to model tissue growth and hydrogel degradation. (c) Cartilage cells secreted extracellular matrix, shown by histological images stained for aggrecan (red), which increased as a function of time. By week 12, there was evidence of matrix connectivity in the hydrogel. The compressive modulus of the construct decreased with culture time indicating that the hydrogel was undergoing bulk degradation.* 118

5.3 *(a) Relationship between particle diffusivity and cross-link density for two different particle sizes (enzyme and ECM molecules), characterized by the ratio r/ξ. (b) Restricted diffusion of two ECM building blocks (aggrecan and collagen) around chondrocytes encapsulated in 10% and 20% aggrecanase sensitive PEGDM hydrogels.* . . . 120

5.4 *Model domain and boundary conditions.* 126

5.5 *Characteristics of degradation dynamics as a function of the normalized enzyme size r_e^* and degradation rate κ_e^*. Plots (a,b,c) show the distribution of cross-link density in terms of the distance x from the cell surface for three specific times; one observes a transition from a diffusion-like profile to a narrow moving degradation front as r_e^* and κ_e^* increase. The relationship between the width and velocity of this traveling front and the parameters (r_e^*, κ_e^*) can be visualized on two-dimensional maps represented in (d) and (e), respectively.* 130

5.6 *Profile of polymer cross-link density, free ECM concentration and linked ECM concentration as a function of distance from the cell surface. Results are shown for three characteristic times during growth t=3.5, 7 and 10.5 day. (a) Slow ECM deposition in a hydrogel scaffold with a wide and slow degradation front; (b) Slow ECM deposition in a hydrogel scaffold with a sharp and and fast degradation front; (c) Fast ECM deposition in a hydrogel scaffold with a wide and slow degradation front and finally (d) Fast ECM deposition in a hydrogel scaffold with a sharp and and fast degradation front.* 134

5.7 *Evolution of construct modulus over time. The mechanical integrity is preserved in the case of sharp degradation front and fast deposition relative to the front speed.* . . . 137

A.1 *The experimental set-up, the initial hydrogel properties for the non- degradable hydrogel, and enzyme concentration used in this study.* 158

A.2 *Images were acquired of the fluorescently labeled collagenase as it diffused into the hydrogel over time. Fluorescence intensity, correlating to enzyme concentration, was determined as a function of position and time and normalized to the intensity in the reservoir. The reservoir was replenished daily to maintain a constant enzyme concentration.* 158

A.3 *The mathematical model was fit to experimental data and the average radius of the enzyme was estimated to be 6.5 nm.* 159

A.4 *Comparisons between experimental and model results for the 1D experiments for the 148 hour time point. The fluorescence intensity at each location in a given hydrogel and time point was normalized to the maximum fluorescence intensity. In the simulations, crosslink density is calculated as a function of time and distance away from the enzyme source. The model matches well to the experiments with respect to the propagating front and front width for all hydrogel cases. However due to the inherent experimental system limitations, the fluorescence intensity for the low crosslink density case did not match the predicted normalized crosslink density.* . . 160

B.1 Configuration of the domain of interest at the initial and current frames 163

C.1 *Convergence study. (a) Convergence of the error measure (C.31) in as a function of mesh size h. (b) Convergence of the error measure (C.31) in as a function of time step. (c) Comparison of the model prediction with the one presented in [135] for the evolution of crosslinking density using the mesh size and time step that are marked with red circles in (a) and (b).* 171

Introduction

Tissue failure due to aging or diseases reduces the quality of life for individuals. In the case of cartilage tissue, for instance, the current solution is to use implants to fulfill the functional duties of native tissue. However, this approach has limitations, such as periodic replacement and number of the required operations. Tissue engineering provides an alternative approach in which the aim is to regenerate the native tissue by a population of cells encapsulated in a scaffold (i.e. hydrogels). Although this approach is promising, there are several limitations regarding the design of these scaffolds. First, the scaffolds should maintain the mechanical support until the neo-tissue is well developed. Second, the scaffolds have to enable the tissue growth by providing space for the new extra-cellular matrix (ECM). For instance, non-degradable hydrogels allow only the generation of peri-cellular matrix while degradable hydrogels can promote the tissue growth far from the cells. However, degradation causes the loss of mechanical integrity before the successful tissue growth is achieved. Experimental studies have shown that the cell-mediated remodeling is affected and therefore can be tuned via mechanical properties and applying various types of stimuli to the construct (i.e., a population of cells encapsulated within a hydrogel). For instance, Bryant et al. showed that the cyclic loading and the mechanical properties of the hydrogels are coupled with the cell-mediated remodeling which may be originated from enhanced degradation process or improved transport of building blocks of ECM. These results suggest that the mechanics has significant effect on tissue growth; however, the thorough understanding of this effect demands computational models due to the cost and time limitations of the experimental studies.

One advantage of computational models is the ability to capture the coupling between re-

modeling and mechanics. In this context, consider the evolution in one of two ways: (a) removal of existing material (i.e. degradation), or (b) deposition of new material (i.e. tissue growth). Previous studies shows that we can govern the material removal or deposition using the similar mathematical models that has opposite effect. In order to track the material deposition/removal, the transport and chemical reactions of the building/demolishing blocks should be captured, and both of these mechanisms are coupled with the mechanics of scaffold (or encapsulating medium). A number of frameworks based on continuum mechanics has been developed for finite growth to capture this coupling between remodeling and mechanics. These frameworks also enable us to quantify the evolution of the overall mechanical properties, and this has been shown in. Although the computational tools that that are currently available have potential, the application of those models to tissue engineering is still in progress. In order to have a deep understanding of the evolution of hydrogel constructs, a 3D computational model at the cellular scale that captures the effects of finite strain is preferable.

The aim of this study is to present a 3D computational tool based on the existing theories of remodeling in biological materials. The tool is composed of two parts; (i) an optimization tool which allows to assess the property-structure-property relationship of the scaffolds, (ii) a 3D finite element model that captures the coupling between the mechanics and cell mediated remodeling. In the first chapter a 1D model is built to understand the effect of degradation on the mechanics of tissue growth. The model is based on the mixture theory at finite strain and Flory-Rehner theory of swollen networks. The study considers only the bulk degradation of hydrogels. In the chapter 2 a so called *self learning algorithm* is presented which allows us to build a mapping between hydrogel design parameters and hydrogel model's micro-structure parameters. This algorithm has been built for two reasons. First objective is to generate input data for the mechanistic model and simulate real cases, which will allow us to know where we are in our search for optimum scaffold properties. Second, a map between design parameters and physical properties has been built in order to direct our search in an efficient way. In the 3^{rd} chapter, the experimental and numerical studies of degradation in enzyme-sensitive hydrogels are presented. The numerical model consists

of the Finite Element Method (FEM) implementation of coupled diffusion-reaction equations in 1D. Further 3D FE model results are also presented in this chapter, for the details of this model we refer to the next chapter. In chapter 4, 3D multi-scale FE model for remodeling in biological materials at finite growth is presented. The thermodynamical and numerical aspects of the model is discussed in this chapter. Finally, chapter 5 discusses the coupling between mechanics and biological remodeling (i.e degradation and tissue growth) at micro scale via examples and shows its impact on the macroscopic properties. For the sake of clarity of the chapter, the model is reduced to the case of small strain.

Chapter 1

On the role of hydrogel structure and degradation in controlling the transport of cell-secreted matrix molecules for engineered cartilage

1.1 Introduction

It is well known that damage to articular cartilage of joints due to injury, disease or genetic disorders can lead to joint pain and reduced joint function, drastically affecting ones quality of life. With the prevalence of joint problems and related surgical procedures on the rise [66], new treatment options are clearly warranted. Tissue engineering is an attractive alternative having the potential to yield living functional cartilage. In this context, synthetic scaffolds have been developed to encapsulate chondrocytes (cartilage cells) and support new tissue production while recapitulating the native cartilage environment [139].

Encapsulation of cells in photopolymerizable and biodegradable hydrogels is one promising strategy being investigated for cartilage tissue engineering. This hydrogel platform can be injected and polymerized in situ for site-specific cell delivery and tailored to degrade over time, providing necessary space for new tissue growth. Poly(ethylene glycol) (PEG)-based hydrogels formed by photopolymerization hold promise because they recapitulate important aspects of the native tissue (e.g., maintaining the rounded chondrocyte morphology which is key to preserving the phenotype) [23, 40] and are easily functionalized with degradable linkers [130] and bioactive molecules [81]. For in situ cartilage tissue engineering, the scaffold must also withstand the in vivo physiological forces, a requirement that becomes even more important in large defects and joint resurfacing. In addition,

hydrogel degradation must be incorporated to permit macroscopic tissue growth, but its rate should match tissue growth in order to maintain mechanical integrity and thus function throughout tissue development. While PEG hydrogels can be designed with mechanical properties similar to that of native cartilage [24, 25, 156], engineering mechanically competent cartilage remains a major challenge.

In optimizing the design of biodegradable hydrogels for cartilage tissue engineering, it is critical to understand how hydrogel structure, across multiple length scales, and its temporal changes with degradation support the production, transport and deposition of extracellular matrix (ECM). Hydrogels are crosslinked polymer networks with an average crosslink density that influences the mechanical properties, degree of swelling, mesh size, and subsequently transport properties. Because ECM molecules typically have high molecular weights, a large mesh size is often desirable to promote transport of these molecules through the gel for homogeneous tissue development. But, this leads to a mechanically inferior hydrogel. In contrast, a high crosslink density, which can conserve mechanical integrity similar to that of cartilage, is usually prohibitory to ECM transport [110, 23]. As a result, ECM transport is restricted to regions near chondrocytes (the pericellular region). This increased local matrix deposition may in turn further inhibit long-range ECM transport. While the introduction of degradation into the hydrogels can overcome many of these shortcomings, this strategy is only beneficial if degradation kinetics properly match matrix transport and deposition. The latter has not yet been achieved.

Designing the structure of hydrogel scaffolds for optimal tissue development is therefore a very challenging task due to the high nonlinearity of the processes involved and the multiscale aspect of the problem. In that respect, mathematical models can provide a critical tool to guide the design of scaffolds but also to better understand the micro-mechanisms of tissue production, transport and deposition. The theories of mixture and poro-elasticity have proved to be an excellent framework onto which the deformation of tissues, such as cartilage can be studied [8, 62, 80]. The problem of matrix diffusion, transport and deposition was addressed by number of authors who

concentrated on the ECM synthesis, diffusion and deposition, both at the cellular [131, 142] and tissue scales [35]. The problem of cell mediated gel degradation was also assessed with a triphasic mixture model [154] to better understand how degradation may affect both transport properties and gel mechanics. Finally, on a more global scale, a similar multiphase model (made of linked ECM, scaffold and cells) was useful in deriving a steady-state solution representing healthy cartilage [58]. While the above studies have enabled a more quantitative understanding of the processes of synthesis, diffusion and deposition, few have considered the coupled physics of gel deformation, degradation and ECM transport. These processes have, however, proven to be key in designing hydrogel scaffolds for optimal tissue development.

For the work presented in this chapter, we take an integrated experimental/modeling approach to further understand the role of initial scaffold structure on the development of new tissue around ECM-producing chondrocytes (Fig. 1.1). The problem is described in term of an ECM-producing chondrocyte surrounded by a triphasic mixture consisting of a degrading gel, aqueous solvent and diffusing ECM molecules. The model shows, in agreement with experimental observation, how microstructural details such as crosslink density and degradation kinetics, can be tuned to achieve variation in matrix deposition and diffusion. In particular, we aim to illustrate that a quantitative understanding of the relationship between scaffold structure and tissue development will be essential in designing successful engineered tissues.

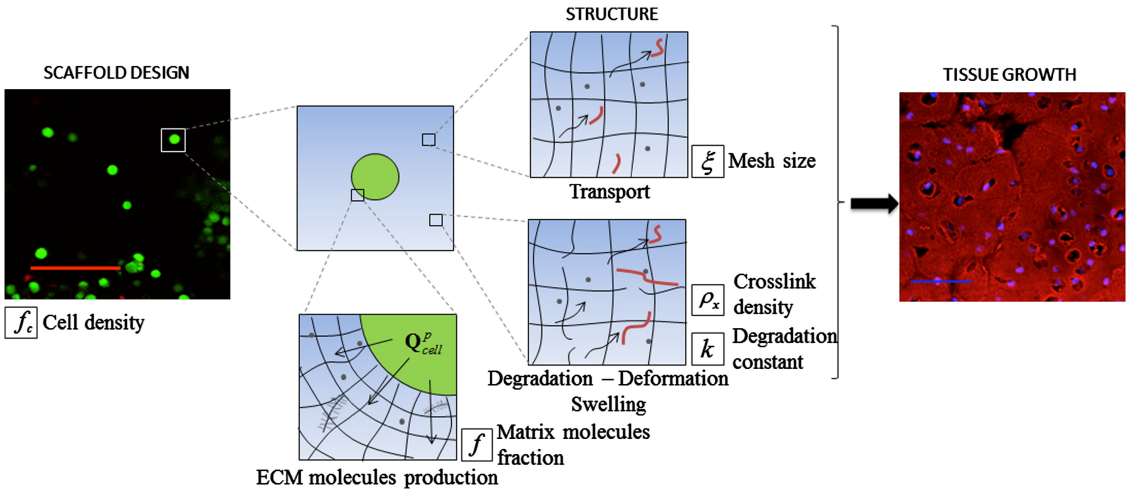

Figure 1.1: *Mutiscale approach to modeling tissue production by cells encapsulated in hydrogels. Refer to the next sections for the parameters. Left: chondrocytes encapsulated within a PEG hydrogel, shown at day 3 after encapsulation. Cytosol of live cells fluoresce green showing the chondrocytic round morphology. Nuclei of dead cells fluoresce red. Scale bar indicates 100 microns. Right: chondroitin sulfate elaboration (red) by chondrocytes encapsulated within a degradable PEG hydrogel after 28 days in vitro. Cell nuclei are stained blue. Scale bar indicates 50 microns.*

1.2 Hydrogel structure: processing and mathematical description

1.2.1 Processing of cell-laden hydrogels and control of initial hydrogel structure

The methods used to form biodegradable PEG hydrogels and encapsulate cells are described. Poly(ethylene glycol) (PEG) can be functionalized in numerous ways to add moieties for degradation and polymerization. Hydrolytically degradable lactides were reacted with PEG, MW 4600, to produce oligo(lactic acid)PEGoligo(lactic acid) (LAPEGLA) with an average of 23 lactic acid repeat units per side [130]. PEG (MW 4600) and LAPEGLA were endcapped with polymerizable methacrylates by microwave methacrylation [85] to produce PEG dimethacrylate (PEGDM) macromolecular monomers, which are essentially non-degrading on the time scale of the experiments, and degradable LAPEGLA dimethacrylate (PEGLA-DM) macromolecular monomers or macromers. Primary bovine chondrocytes isolated from the femoralpatellar groove of a 13 week

old calf (Research 87, Marlborough, MA) [110] were used as the model cell type. Hydrogels with different initial crosslink densities were formed through photopolymerization (365 nm, 10 min) of PEGDM and/or PEGLA-DM macromers at varying macromer concentrations (10, 15, or 20% w/w) with a photoinitiator (Irgacure 2959, 0.05% w/w) in chondrocyte culture medium. For cell encapsulations, chondrocytes were suspended in macromer solution at 50 million cells per mL macromer and photopolymerized. Cylindrical hydrogels (5 mm height and 5 mm diameter) were cultured up to 4 weeks in a humid environment at 37 ^{o}C in 5% CO2. The LIVE/DEAD membrane integrity assay was used to qualitatively assess cell viability within hydrogel constructs. Images were acquired using a confocal laser scanning microscope (CLSM, Zeiss LSM 510, Thornwood, NY).

1.2.2 Overall modeling strategy of the macroscopic tissue evolution

Multiscale computational modeling was employed to understand key microscopic processes driving tissue growth in terms of hydrogel structure, degradation and cell density. At the tissue level, these processes may be entirely described by continuous field equations in terms of hydrogel displacement u, solvent pressure p and concentration c_p of ECM particles (e.g., glycoproteins or proteins), all functions of location X and time t. To reduce the complexity of the problem, a homogeneous cell distribution was considered such that the analysis of the entire tissue could be summarized by a model volume consisting of a single spherical chondrocyte of radius R_c embedded in a spherical hydrogel domain with radius R_g. Overall cell volume fraction, f_c, (Fig. 1.2) can then be described through the relation:

$$R_c/R_g = f_c^{1/3} \tag{1.1}$$

In spherical coordinates, the fields are functions of R,θ and φ. However, in this simplified system, under centro-symmetric assumption, the continuous fields only depend on the distance R from the center of the chondrocyte (in the initial, dry state). The macroscopic problem therefore consists of evaluating the evolution of the following three fields:

$$u(r,t), p(r,t), c^p(r,t) \tag{1.2}$$

These fields evolve as a result of the constant release of ECM molecules by chondrocytes from the cell membrane and changes in the osmotic swelling of the hydrogel resulting from bulk degradation. As we will see, the combination of degradation and ECM production that results in the growth and organization of the new tissue is highly dependent on the initial hydrogel structure and the design of its degradation through the number of degradable linkages.

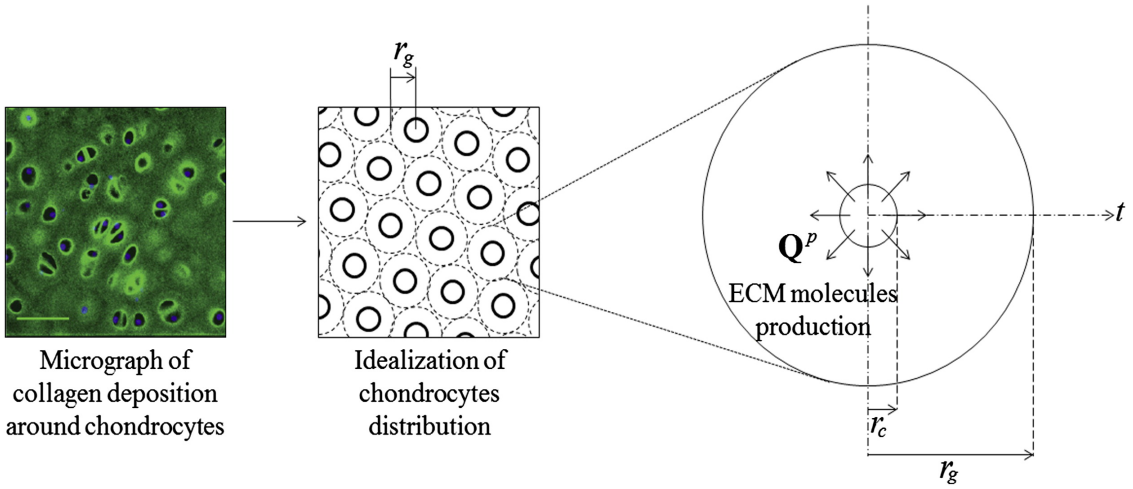

Figure 1.2: *From real engineered tissues to an idealized mathematical model. Left picture shows cell nuclei (blue) and collagen (green). Scale bar represents 50 μm.*

The crosslinked polymer network of the hydrogel can be considered as a hydrated elastic solid whose mechanics highly depend on the underlying molecular structure [69]. To represent hydrogel degradation and tissue growth, the hydrogel was considered as a mixture [147, 153, 151] of three different phases that consist of the solid (or polymer) phase, the fluid (or solvent) phase, and the unbound ECM molecules (proteoglycans, collagens) phase. Consistent with mixture theory, each phase (denoted by α=s,f,p, respectively) is described with its volume fraction ϕ^α such that

$$\phi^s + \phi^f + \phi^p = 1 \text{ , and } \phi^p \ll 1 \tag{1.3}$$

This equation implies that each phase is saturated within the mixture. It is also reasonable to assume that each phase is incompresssible at the microscopic level due to the relatively low physi-

ological pressure encountered in vivo. In other words, the true mass density $\rho^{\alpha R}$ of various phases remains constant during the growth process. Growth can however be measured by the change in effective mass density representing the mass of each phase per unit volume of mixture through the relation:

$$\rho^{\alpha}(R) = \phi^{\alpha}(R)\rho^{\alpha R}(R) \tag{1.4}$$

1.2.2.1 Deformation ad Swelling

A particular feature of hydrogels, and soft tissue in general, is that they commonly undergo very large deformations (changes in volume can reach more than 1000% during swelling). Such deformable materials are usually described within finite deformation elasticity. In this context, the location $\mathbf{x}$ of a material point on the crosslinked polymer is related to its original position $\mathbf{X}$ before deformation through the deformation gradient tensor $\mathbf{F}$:

$$\mathbf{F} = \frac{d\mathbf{x}}{d\mathbf{X}} = \begin{bmatrix} \frac{\partial r}{\partial R} & 0 & 0 \\ 0 & \frac{r}{R} & 0 \\ 0 & 0 & \frac{r}{R} \end{bmatrix} \tag{1.5}$$

where the current radius r is mapped to the initial radius R (before swelling). The determinant of $\mathbf{F}$ measures the change of volume between initial (dry polymer before swelling) and final configuration as follows:

$$dV = JdV_0 \text{ where } J = \det \mathbf{F} = \left(\frac{\partial r}{\partial R}\right)\left(\frac{r}{R}\right)^2 \tag{1.6}$$

The value of J at equilibrium is denoted as the volumetric equilibrium swelling ratio Q , which can be determined from experiments. The volume fraction ϕ^s_{eq} of the polymer at swelling equilibrium is related to Q:

$$\phi^s_{eq} = \frac{1}{Q} \tag{1.7}$$

where the volume fraction for the dry polymer is one.

1.2.2.2 Mechanical Equilibrium

The hydrogel is subjected to a variety of mechanical forces which through hydrogel deformation, have strong effects on gel permeability and degradation as well as transport and deposition of unbound ECM molecules. These forces are accounted for through the balance of momentum of the hydrogel in the form [84]:

$$\nabla_{\mathbf{X}} \cdot (\mathbf{P}^{eff} - J\pi\mathbf{F}^{-T}) = 0 \tag{1.8}$$

where $\mathbf{P}^{eff}$ is the nominal effective stress tensor i.e. the stress acting on the crosslinked polymer only, and π is the interstitial fluid pressure. The notation $\nabla_{\mathbf{X}}$ refers to the spatial differential operator with respect to the initial coordinates $\mathbf{X}$. This equation clearly shows the effect of fluid pressure on the stress experienced by the polymer network.

1.3 The evolving structure and properties of degrading hydrogels

The solid phase of the gel (described as a crosslinked polymer) is mechanically represented as a rubber-like material, where polymethacrylate chains are linked together by PEG or PEGLA crosslinks and swollen in an aqueous solvent (Fig. 1.3). The mathematical model to describe its deformation and swelling is introduced below.

1.3.1 Physical Model of the Hydrogel

1.3.1.1 Free Energy

The physical properties of a crosslinked polymer swollen with solvent (neglecting contributions from ECM molecules) are described by FloryRehner and rubber elasticity theories [47, 141]. These theories are based on the description of the free energy of a swollen gel [31] as the sum of contributions from elasticity/distortion ΔG^{el} and solvent mixing ΔG^{mix}.

$$\Delta G = \Delta G^{el} + \Delta G^{mix} \tag{1.9}$$

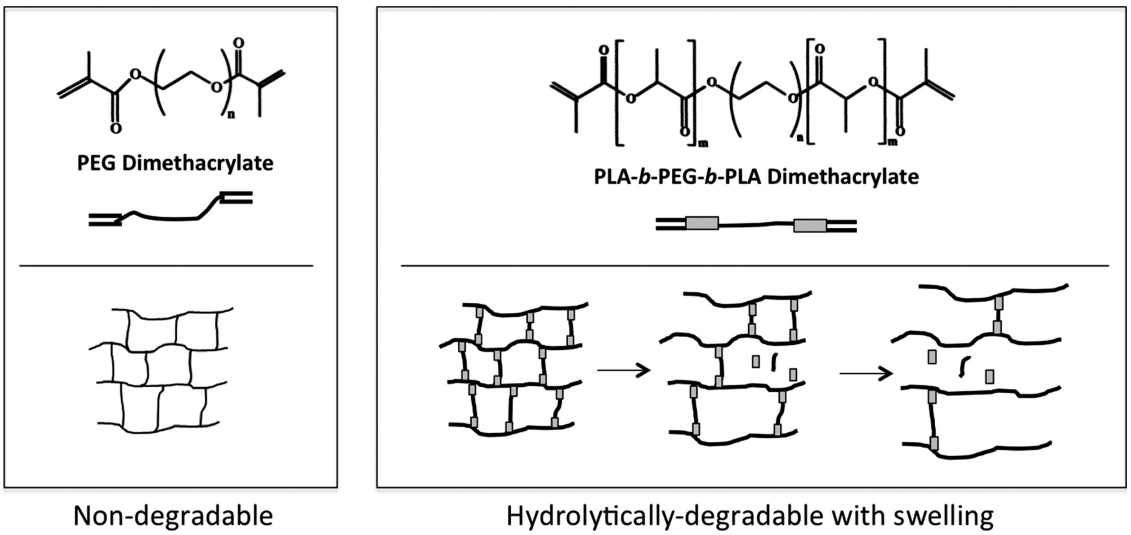

Figure 1.3: *Schematics representing an idealized network structure formed from PEGDM or PEGLA-DM macromers by radical chain polymerization. Left, non-degrading (based on experimental timescale) PEGDM hydrogels form a stable network structure. Right, hydrolytically degradable hydrogels made of PEGLA-DM exhibit degradation and swelling with time.*

where ΔG^{mix} is described by FloryHuggins theory [31] for two phases:

$$\Delta G^{mix} = k_B T(N_f \ln(\phi^f) + N_s \ln(\phi^s) + N_f \ln(\phi^s)\chi) \tag{1.10}$$

where N_α is the number of molecules, k_B is the Boltzman constant, T is the absolute temperature and χ is the FloryHuggins parameter (polymersolvent interaction). The latter describes the thermodynamic interactions between solvent and polymer molecules where a higher positive value of χ denotes a repulsive interaction between the solvent and polymer molecules. Because the polymer network is one molecule, we assume a negligible contribution from term 2 ($N_s \ln(\phi^s)$) in Eq. (10). The elastic contribution to the free energy ΔG is derived from [141], neglecting the phantom network theory [15] for simplicity. Denoting the quantities λ_1, λ_2 and λ_3 as the principal stretches in the principal directions of the right stretch tensor, the elastic free energy reads:

$$\Delta G^{el} = \frac{1}{2}\left(\lambda_1^2 + \lambda_2^2 + \lambda_3^2 - 3 - \ln(\lambda_1\lambda_2\lambda_3)\right) \quad \text{where} \quad G = \rho_x RT \tag{1.11}$$

where G is denoted as the shear modulus [15, 141] and is a function of the crosslinking density ρ_x. We also note that that for isochoric deformation $\lambda_1\lambda_2\lambda_3 = 1$, ΔG^{el} becomes the strain density

energy of a NeoHookean material. When the polymer interacts with water, however, significant volume change can be generated by osmotic pressure and the product $\lambda_1\lambda_2\lambda_3$ may become large enough to dominate the gel response.

1.3.1.2 Effective stressa and osmotic pressure

The effective stress $\mathbf{P}^{eff}$ is thermodynamically defined as the energy conjugate of the deformation gradient $\mathbf{F}$. It can therefore be defined in terms of the elastic free energy as:

$$\mathbf{P}^{eff} = \frac{\partial \Delta G^{el}}{\partial F} \tag{1.12}$$

The osmotic pressure, based on the same idea as a Cauchy and PiolaKirchhoff stress can be defined as:

$$\Pi = \frac{\partial G^{mix}}{\partial \mathbf{F}} \quad \text{where} \quad \Pi = J\pi\mathbf{F}^{-T} \tag{1.13}$$

where π is defined as a Cauchy osmotic pressure and Π is its associated Piola - Kirchhoff osmotic pressure. This equation, together with the mechanic equilibrium is defined as:

$$\mathbf{P}^{eff} - J\pi\mathbf{F}^{-T} = \frac{\partial \Delta G^{el}}{\partial F} - \frac{\partial G^{mix}}{\partial \mathbf{F}} \tag{1.14}$$

The only unknown that the mechanic equilibrium equation contains is the FloryHuggins parameter χ, which can be solved for by taking the derivatives of the elastic and mixing free energies with respect to the deformation gradient. Thus, Eqs. (11) and (14) gives a FloryHuggins parameter $\chi = 0.464$.

This relation enables the determination of osmotic pressure from free swelling experiments (described next). In particular, Eq. (14) can be used to relate the swelling ratio $Q = 1/\phi^s_{eq}$ to crosslink density ρ_x at constant osmotic pressure as depicted in Fig. 1.4

1.3.2 Hydrolytic degradation

During degradation, the macroscopic properties of the hydrogel evolve dynamically. As a first approach, hydrolytic degradation is described by pseudo first-order kinetics [97, 97], where

crosslink density decreases with degradation time:

$$\frac{d\rho_x}{dt} = -k\rho_x \tag{1.15}$$

where k is the pseudo first order rate constant for hydrolytic degradation. Thus as time evolves, crosslinks degrade randomly within the gel, which leads to decrease in the shear elastic modulus G (Eq. (11)) but increase in swelling and mesh size, where the latter improves transport of ECM molecules through the gel. Solving Eq. (15) yields the evolution of crosslink density in time as:

$$\rho_x(t) = \rho_{x0} \exp(-kt) \tag{1.16}$$

where ρ_{x0} is the initial crosslink density of the swollen hydrogel. It is important to note that this model represents a simplified model for degradation kinetics. As such, it does not capture more subtle elements of degradation such as the phenomenon of reverse gelation. Reverse gelation refers to the point when there are fewer than two crosslinks per kinetic chain resulting in highly branched soluble polymer chains [47]. The crosslink density at which reverse gelation occurs will depend largely on the length of the kinetic chain [97, 97]. Consequently for very short kinetic chains, reverse gelation can occur after only a few crosslinks have been broken. While not explicitly incorporated into this equation, the importance of this physical point should not be underestimated as it has the potential to dramatically influence how well macroscopic tissue can form prior to reverse gelation. It was shown that reverse gelation typically occurs when there is a 6080% mass loss for similar PEGLA hydrogels [97, 97].

1.3.3 Hydrogel processing and measurement of overall properties

In the above model, it can be seen that gel behavior is mainly described in terms of the structural quantity crosslink density ρ_x, which dictates shear modulus G, and the degradation behavior. Initial crosslinking density can be controlled experimentally by varying macromer length or the weight percent of PEG macromer in solution. While the rate of hydrolysis of the ester bond will not depend on hydrogel structure, the overall effective degradation rate can be altered by initial

crosslink density and the number of ester bonds within the crosslink. Two macroscopic experiments were performed to indirectly measure these quantities. For stable hydrogels formed from PEGDM macromers, the equilibrium mass swelling ratio was measured and converted to volumetric swelling ratio Q, and direct unconfined compressive tests were performed. In addition bimodal degrading hydrogels were formed such that a fraction of the crosslinks would degrade (PEGLA crosslinks), while the remaining crosslinks remain stable (PEG crosslinks) preventing the gel from undergoing rapid degradation and dissolution and loss of mechanical integrity [24, 25, 137]. For the bimodal degrading hydrogels, equilibrium volumetric swelling ratio Q was determined as a function of time. For the first experiment, hydrogels with varying crosslink density were made with 10%, 15%, and 20% PEGDM by weight, yielding 0.11, 0.22, and 0.38 M crosslinking densities, respectively, from Eq. (18). Swelling ratio and modulus were determined as a function of crosslink density and compared to theoretical prediction as shown in Fig. 1.4.

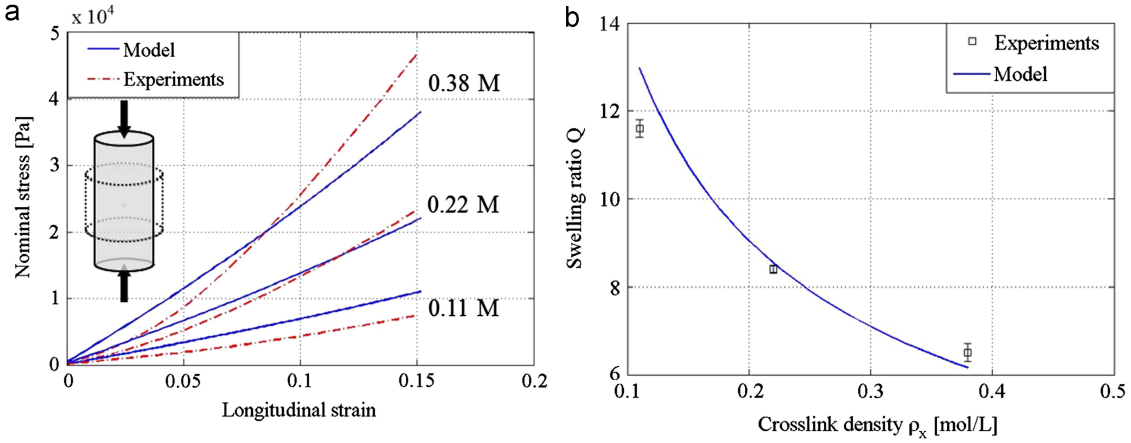

Figure 1.4: *(a) The nonlinear compressive/elastic modulus through the stress - strain curves for different crosslink densities. Experimental results and the model are compared. (b) The equilibrium swelling ratio as a function of crosslinking density for stable PEG hydrogels formed from PEGDM macromers obtained both experimentally and determined by the model. Error bars indicate standard deviation (n=3).*

1.3.3.1 Crosslinking density

The equilibrium volumetric swelling ratio Q can be determined experimentally by measuring the equilibrium swollen mass M_s of hydrogels, and then lyophilizing to obtain the dry polymer mass, M_s [69].

$$Q = J_{eq} = \frac{V}{V_0} = 1 + \frac{\rho_{pegdm}}{\rho_{solv}} \left(\frac{M_s}{M_d} - 1 \right) \tag{1.17}$$

In this relationship, ρ_{pegdm} and ρ_{solv} are the density of the PEGDM macromer and the solvent, and J_{eq} is the equilibrium jacobian, equivalent to Q . Therefore ϕ^s_{eq} is equal to the inverse of the swelling ratio Q.

At swelling equilibrium, considering the chemical equilibrium, we can assume that the change in chemical potential is zero, and we apply the definition that the partial derivative of ΔG (Eq. (9)) with respect to N_s is equal to the change in chemical potential. Applying this definition, simplifying and rearranging leads to the following definition for crosslinking density ρ_x (number of crosslinks per volume) of a polymer scaffold (see [47] chapter XIII 3 for more details). Neglecting the phantom network theory (no distinction between chain and chain-ends), one can show that:

$$\rho_x = \frac{-1}{V_1} \left(\frac{\ln(1 - \phi^s_{eq}) + \phi^s_{eq} + \chi(\phi^s_{eq})^2}{(\phi^s_{eq})^{1/3} - (\phi^s_{eq}/2)} \right) \tag{1.18}$$

where V_1 is the molar volume of the solvent. From this equation, experimental measurements of the swelling ratio Q are used to estimate hydrogel crosslinking density.

1.3.3.2 Gel elastic modulus

To ensure consistency between model and experiments regarding the change of gel stiffness with crosslink density, the stressstrain response of the hydrogel in uniaxial, unconfined compression was assessed through two different routes. On the experimental side, unconfined cylindrical hydrogels were compressed to 15% strain at a constant rate of 0.5 mm per minute (MTS Synergie 100, 10 N) and the resulting stress was assessed by dividing the compressive force by the initial specimen cross-sectional area (nominal stress). On the theoretical side, these conditions were reproduced by evaluating the longitudinal stress and strains (subjected to zero transversal stress) of

a hydrogel cylinder with varying crosslink densities using Eqs. (8) and (11). Comparing numerical and experimental results provided in Fig. 1.4 (a) that the present model captures the key trends in gel behavior with a minimal number of material parameters. A more sophisticated model of the hydrogel mechanics may be able to provide a closer estimation of the results.

1.3.3.3 Rate of degradation

The measurement of degradation rate can be inferred by measuring the evolution of swelling ratio exhibited by a gel over time. Indeed, referring to the right side of Eq. (11), it can be seen that crosslink degradation is directly associated with a weakening of,the gel's elastic modulus, which under the action of osmotic pressure, translates into swelling (or a decrease of the polymer volume fraction ϕ^s_{eq}). This informs us about the evolution of the equilibrium volumetric swelling ratio $Q = 1/\phi^s_{eq}$ over time. Using this method, it was possible to obtain a good match between the theoretical model and experimental measurements for a pseudo first-order degradation rate constant k equal to 0.11/day (Fig. 1.5). Swelling shows a general trend of an exponential increase with time [92], which was verified in a bimodally degradable system where 15 weight % macromer was used, where 95% of the macromer consisted of degradable PEGLA-DM and 5% was non-degradable PEGDM.

1.4 Production and transport of ECM molecules within an evolving hydrogel structure

In vivo, chondrocytes produce all of the components of cartilage, which include the collagens and proteoglycans described in Table 1.1. Tissue deposition is typified initially by the formation of a protective pericellular matrix found immediately surrounding the cell, characterized by a meshwork of collagen VI as well as collagen II and aggrecan [107]. Macroscopic tissue deposition can only occur when matrix is secreted and retained throughout the surrounding extracellular matrix. When encapsulated in a hydrogel network, chondrocytes similarly secrete extracellular matrix molecules, which, in time, begin to recapitulate the structure and organization of native cartilage. However, in

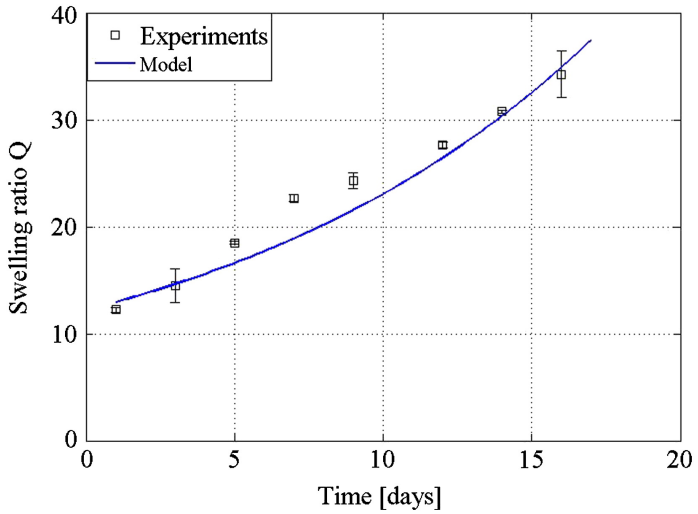

Figure 1.5: *Swelling ratio Q over time in a bimodally degradable hydrogel consisting of a 95:5 weight ratio of PEGLA-DM and PEGDM.*

this case, the evolving nature of the scaffold structure strongly influences the way matrix molecules are transported and deposited to form a new tissue.

Table 1.1: Composition of native cartilage.

	% by wet weight	Component	Size Scale	Structure
Collagens	20	Collagen II	400 nm	Linear Fibers
		Collagen VI	100 nm	Fibrilliar
Aggrecan, proteoglycans and their building blocks	5-7	Aggrecan aggregates	100 MDa	Highly branched
		Aggrecan	1-4 MDa	Branched
		Hyaluronan	1 MDa	Linear
		Link Protein	45 kDa	Globular
		Glycosaminoglycans	5-30 kDa	Linear
		Decorin	40 kDa	Globular
		Biglycan	40 kDa	Globular
Other	70-75	Water	$\ll \xi$	
		Salts	$\ll \xi$	

1.4.1 Classification of ECM molecules and experimental observation

At the molecular scale, the hydrogel is composed of a crosslinked network structure with a characteristic mesh size (varying with crosslinking density and degradation) that can permit or restrict diffusion of soluble molecules depending on their size relative to the average mesh size. As

a first step, the proposed model treats matrix molecules as either large or small to demonstrate restricted vs. free diffusion through the hydrogel mesh. Future versions of the model will attempt to account for the wide variety of matrix molecules secreted by chondrocytes. For reference, a summary of the main ECM molecules that make up articular cartilage is presented in Table 1.1. Relative composition of components is expressed as a percentage of wet weight [60], and the size scale and structure of collagens [91] and proteoglycans [60] are presented.

For cell-laden photopolymerized hydrogels cultured for several weeks, deposition of matrix molecules can be characterized experimentally in a variety of ways. For this study, we present qualitative methods which demonstrate spatial deposition of specific matrix molecules via immunohistochemical techniques. Immunohistochemical staining for chondroitin sulfate was applied to dehydrated, paraffin-embedded 10 μm-thick sections of hydrogels as previously described [110, 126]. Briefly, sections were mounted onto slides and rehydrated, treated with chondroitinase ABC, and probed with a primary antibody against chondroitin-6-sulfate (Chemicon, Billerica, MA) followed by an AlexaFluor 546-conjugated secondary antibody and counterstained with DAPI. Images were acquired with a confocal laser scanning microscope at 40 magnification (Fig. 1.8 and Fig. 1.9).

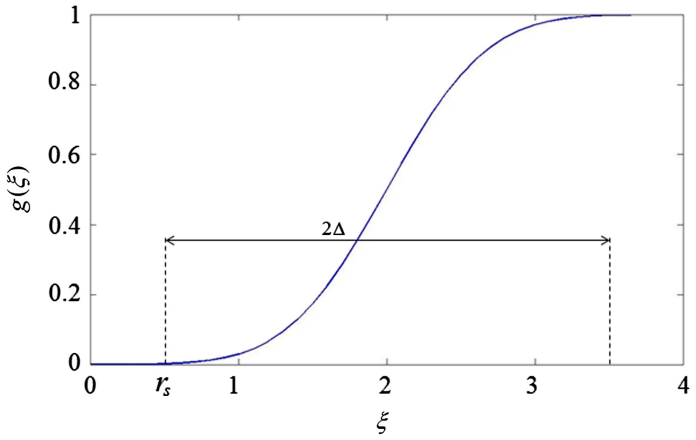

Figure 1.6: *Gauss error function used in the model to describe the constitutive relations.* Δ *is taken as* $4r_s$ *in the above figure.*

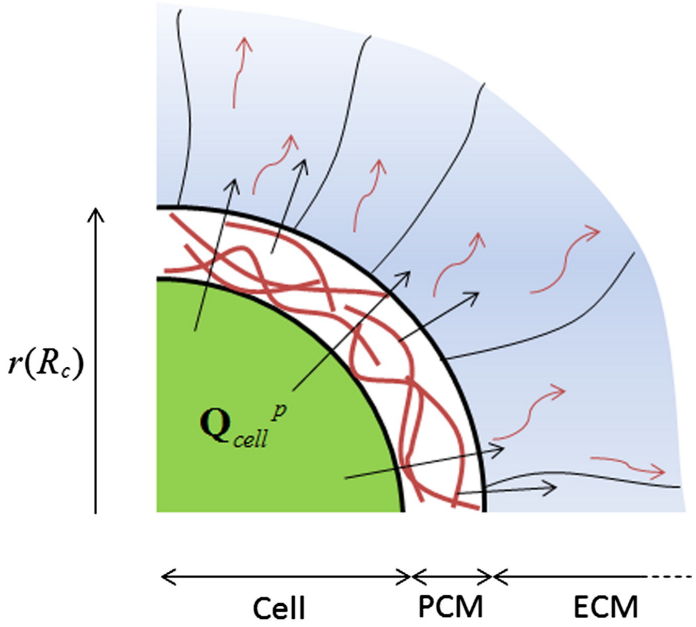

Figure 1.7: *Diffusivity of proteins through the hydrogel. How the size of a protein impacts the boundary conditions.*

1.4.2 Modeling molecular transport in deforming hydrogels

The transport of cell-secreted extracellular matrix molecules is a critical component of tissue growth, and tissue engineering strategies should aim to facilitate such processes. In the case of cells encapsulated in gels, controlled degradation of the gel crosslinks is required to achieve homogeneous distribution of cell-secreted matrix. Particularly, the rate and timing of this degradation are important factors. If degradation occurs too quickly, then major defects may develop that can have negative consequences on the macroscopic geometry and mechanical properties. If degradation occurs too slowly, the gel will prevent timely distribution of ECM molecules and tissue regeneration, entrapping the matrix molecules between cells and the gel, yielding only pericellular matrix tissue deposition. The ability to predict appropriate hydrogel degradation profiles coupled with cell-secreted matrix transport and tissue deposition requires a mathematical model that is able to capture the coupled physics between molecular transport, gel deformation and degradation. The theory of mixture provides an excellent framework in this context.

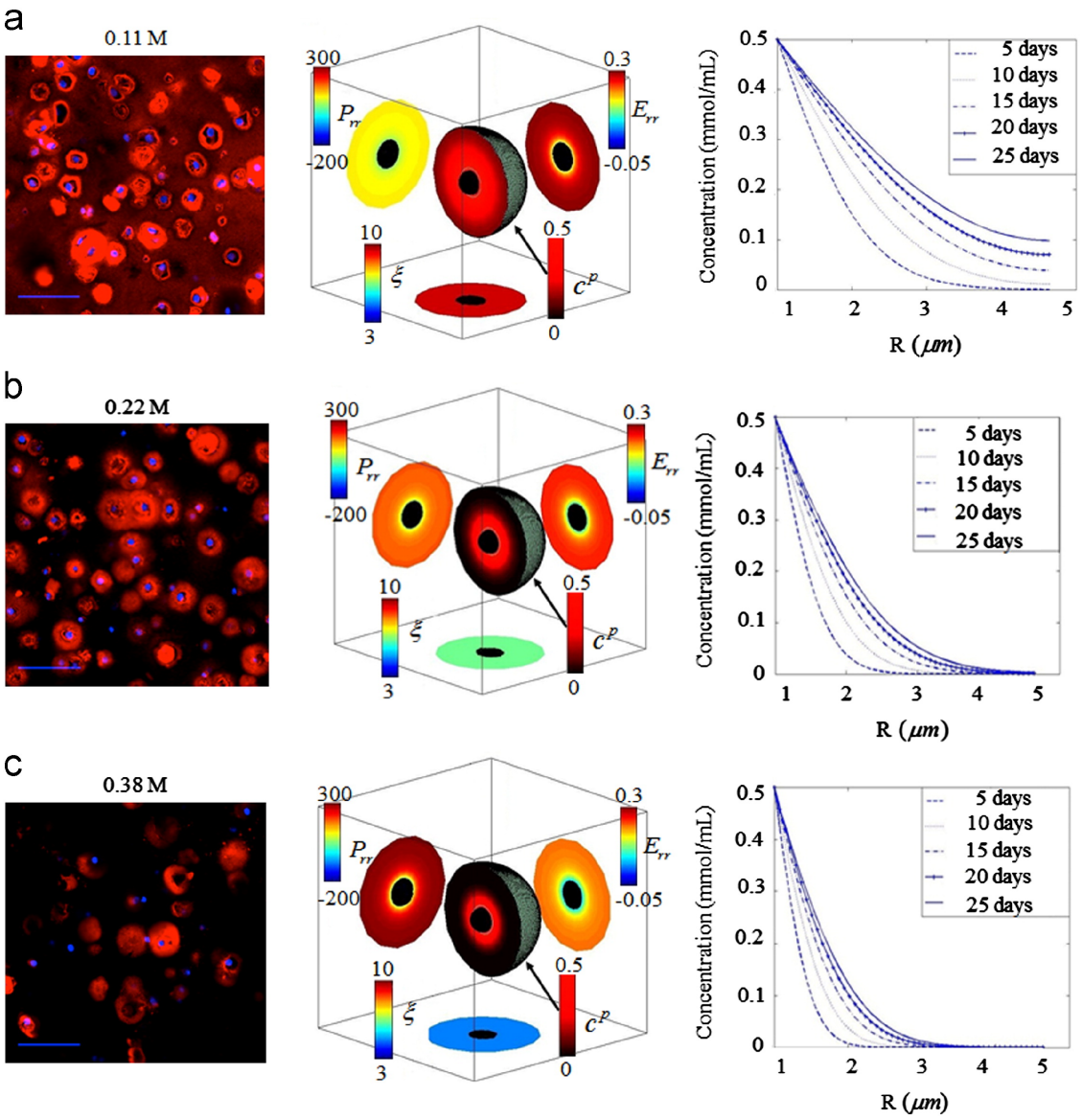

Figure 1.8: *(ac) An experimental result and the model results for different crosslink densities of a stable hydrogel. Regarding the experimental pictures, chondroitin sulfate elaboration (red) by chondrocytes encapsulated within PEGDM hydrogels and cultured for 25 days in vitro with varied crosslinking density. Cell nuclei are stained blue. Scale bars indicate 50 microns. In the three-dimensional plots, the stress P_{rr} (kPa), strain E_{rr}, mesh size ξ (nm) and concentration c^p (mmol/mL) can be observed.*

1.4.2.1 Mass Transport

From a modeling point of view, transport of water (f) and unbound extracellular matrix molecules (p) can be described by their volumetric flux, taken with respect to polymer motion:

$$\mathbf{q}^{\alpha} = \phi^{\alpha}(\mathbf{v}^{\alpha} - \mathbf{v}^{s}) \tag{1.19}$$

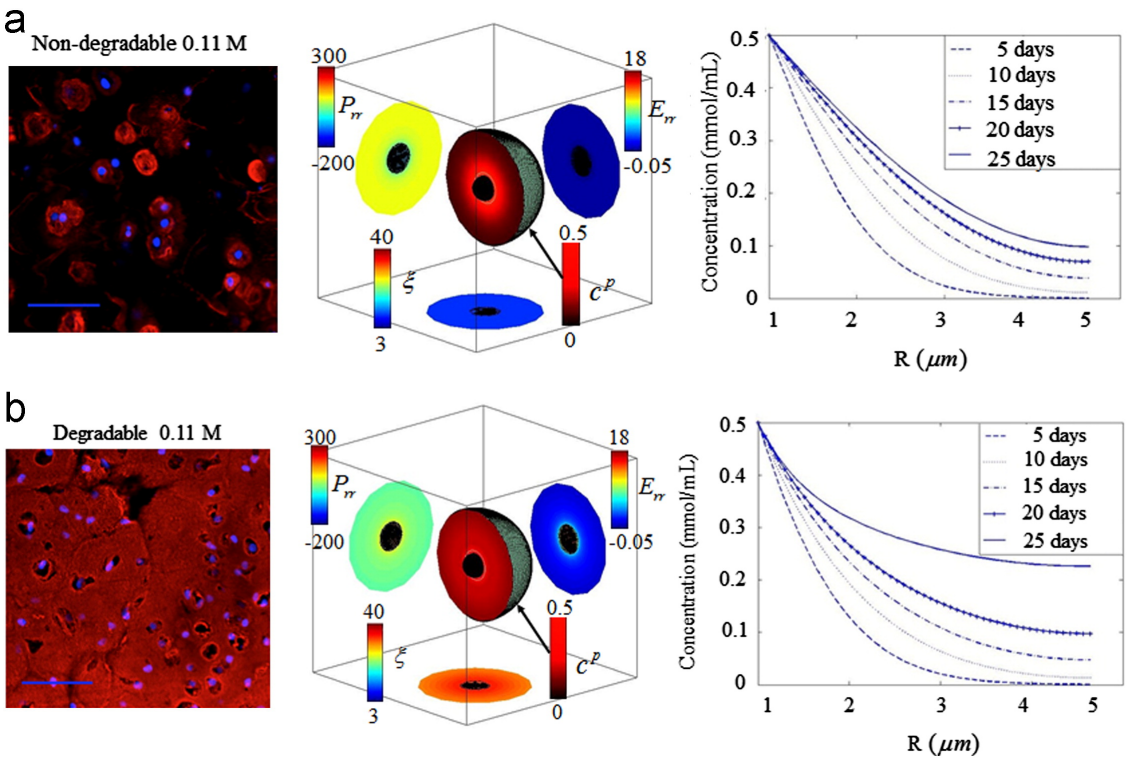

Figure 1.9: *(a) The results for a non-degradable stable hydrogel, and (b) degradable hydrogel. First image is the experiment showing chondroitin sulfate elaboration (red) by chondrocytes at day 28 encapsulated within 10% w/w non-degradable PEGDM and degradable PEGLA-DM hydrogels. Cell nuclei are stained blue. Scale bars indicate 50 μm. In the three-dimensional plots, the stress P_{rr} (kPa), strain E_{rr}, mesh size ξ (nm) and concentration c^p (mmol/mL) can be observed. Note that due to differences in image processing between experiments, chondroitin sulfate staining is of lower intensity than shown in Fig. 1.8.*

where $\alpha = f, p$. Note that this definition of flux is consistent with an Eulerian approach, i.e., the flux is defined as the volume of constituent α per unit of time, passing through a unit surface S in the deformed configuration. When large deformations are considered, however, it is convenient to define the Lagrangian flux.

$$\mathbf{Q}^\alpha = J\mathbf{F}^{-1}\mathbf{q}^\alpha \tag{1.20}$$

as the amount of constituent passing through a unit area in the reference gel configuration (defined in the dry state, i.e. initial configuration). Eq. (20) therefore shows the mapping of the flux from the current configuration to the dry polymer configuration. Using the assumption of incompressibility

for all constituents, it is possible to derive the equation of mass balance in the form:

$$J\frac{D\phi^{\alpha}}{Dt} + \nabla_X \mathbf{Q}^{\alpha} = -\phi^{\alpha}\frac{DJ}{Dt} \text{ where } \alpha = f, p \tag{1.21}$$

Here, the first equation quantifies the balance of mass of the fluid phase, while the second equation describes the balance of mass of the ECM molecules. Eq. (21) implies that the volumetric flux of the fluid phase (mapped back to the dry configuration) is directly linked to the swelling (or deswelling) J of the tissue.

1.4.2.2 Constitutive equation

An important aspect of the present study is the introduction of realistic constitutive relations governing the transport of ECM molecules and water through the gel and their relation to gel deformation and degradation. Assuming the effect of ECM molecules to be negligible on water flux, fluid flow can be expressed in terms of the pressure gradient $\nabla_X p$ as stated by Darcy's law:

$$\mathbf{Q}^{f} = -\kappa J\mathbf{F}^{-1}(\nabla_X p) \text{ where } \kappa = \frac{\xi^2(1-\phi^s)}{8\bar{\mu}_f \delta} \tag{1.22}$$

where κ is the isotropic gel permeability, δ is the tortuosity of the gel structure and $\bar{m}_f$ is the fluid viscosity (see Table 1.2). We note that the gel permeability to water is a function of polymer mesh size ξ [62], which is itself a function of gel crosslinking and can be related to swelling. This dependency was introduced by [15] as follows:

$$\xi = \xi_0(\phi^s)^{-1/3} \text{ where } \xi_0 = C_n^{1/2} n^{1/2} l \tag{1.23}$$

where ξ_0 is the mesh size of the dry polymer, l is the average bond length, C_n is the polymer characteristic ratio, and n is the number of bonds between crosslinks, which is determined from the molecular weight between crosslinks and molecular weight of the polymer repeat unit (see Table 1.2). It is clear from Eqs. (22) and (23) that gel swelling (through hydrolytic degradation for instance), by decreasing the value of ϕ^s, ultimately increases gel permeability and facilitates transport of water through the hydrogel. But also, the number of bonds between crosslinks n changes with changes in crosslink density [47], which means that the mesh size evolves with degradation.

Table 1.2: Inputs used in the model.

Inputs	Value	Unit	Reference
V_1	0.018	L/mol	Commonly known
ρ_{pegdm}	1.07	g/mL	Estimate
ρ_{solv}	1	g/mL	Commonly known
C_n	4		Merrill et al 1993
l	1.47	$\mathring{A}$	Commonly known
T	310	K	Physiological temperature
δ	2		Kestin et al 1981
$\bar{\mu}_f$	0.65×10^{-3}	$N.s/m^2$	Thorne et al 1995
M_p	20	kDa	Hardingham 2006

Because of their relatively small volume fraction, driving forces affecting the motion of unbound ECM molecules are of three types: an advection term (molecules tend to follow the solvent in its flow), a diffusion term within the solvent and thirdly, a term that describes resisting frictional forces from the hydrogel. To separate each contribution, we take the following approach. First, it is convenient to eliminate the friction force from the gel by considering the motion of ECM molecules in a pure solvent. In this case, the flux $\mathbf{q}^p_\infty$ can be readily decomposed into a component that follows the solvent flux given by Eq. (21) and a component representing the relative diffusion of the molecules in the solvent using Fick's law. This leads to [146]:

$$\mathbf{q}^p_\infty = \left(D_\infty \nabla_X c^p - \frac{M^p}{\rho^{pR}} \kappa \nabla_X p \right) \quad \text{where} \quad D_\infty = \frac{k_B T}{6\pi \bar{\mu}_f r_s} \tag{1.24}$$

Here, M^p is the average molar mass of ECM molecules and D_∞ is the free solution diffusivity defined by the Stokes-Einstein relation [129], r_s is the radius of gyration of small matrix molecules. The effect of the gel resistance on molecule transport can then be captured by realizing that when the ratio of radius of gyration rs of ECM molecules is significantly smaller than the polymer mesh size ($r_s/\xi \ll 1$), gel resistance is negligible and the ECM molecule flux $\mathbf{q}^p$ becomes $\mathbf{q}^p_\infty$. However, as r_s increases, we assume that gel resistance results in a decrease of $\mathbf{q}^p$ that is expressed in the form:

$$\mathbf{q}^p = \mathbf{q}^p_\infty g(\xi) \quad \text{where} \quad g(\xi) = \frac{1}{2}\left[1 + \text{erf}\left(\frac{2}{\Delta}(\xi - \Delta - r_s)\right)\right] \tag{1.25}$$

where Δ is a parameter of the Gauss error function erf.

The function g used in this study attempts to capture the nonlinear relationship between ECM transport processes and the relative sizes of ECM molecules and hydrogel mesh. As shown in Fig. 1.6, this function clearly implies that (i) as ECM molecules become larger than the hydrogel mesh size, ECM transport is fully hindered ($g \to 0$) and (2) as the hydrogel mesh size becomes significantly larger than ECM molecules size, gel resistance becomes negligible ($g \to 1$). This expression was originally motivated by the work of [89] in their method to describe the change in diffusivity with the ratio r/ξ.

1.4.2.3 Release of ECM molecules

As mentioned earlier (Table 1.1), chondrocytes produce different types of ECM molecules, which for our purposes may be distinguished by their size. Small molecules have a radius of gyration smaller than the initial hydrogel mesh size ξ and are therefore able to freely diffuse throughout the gel according to Eq. (25). Large molecules are distinguished by a radius that is larger than ξ and because they are unable to diffuse in the gel, they tend to accumulate between the cell and the scaffold, causing the gel to be pushed away from the cell. As depicted in Fig. 1.7, this behavior is modeled by prescribing appropriate flux boundary conditions at the cell membrane in the following fashion. We first introduce the normal ECM molecule flux release from the cell as $\mathbf{Q}^p_{cell}$ such that the release of large and small molecules can be split with the ratio f as:

$$\mathbf{Q}^p_{small} = f\mathbf{Q}^p \;\text{ and }\; \mathbf{Q}^p_{large} = (1-f)\mathbf{Q}^p \tag{1.26}$$

We note here that the value of f is entirely dependent on the cell metabolism and is not considered here as a tunable parameter. Considering the mass balance of the volume between the cell and the hydrogel, denoted by the pericellular matrix in Fig. 1.7, it can be shown that the above considerations translate into a two-fold boundary condition at the gel boundary $R = R_c$:

$$\begin{aligned} \dot{r}(R_c) &= (1-f)\mathbf{Q}^p_{cell} \\ c^p_{gel} &= f c^p_{cell} \end{aligned} \tag{1.27}$$

where a superimposed dot refers to a time derivative. Matrix molecule release is regulated by the cell itself, which is able to detect the surrounding ECM. Then, the small matrix molecule release is represented by a Dirichlet boundary condition. From these expressions, it is clear that if $f = 1$ all molecules released from chondrocytes get transported into the gel ($c^p(R_c) = c^p_{cell}$). If $f = 0$, however, ECM molecule release translates into a deformation of the gel at the cell/gel boundary ($\dot{r}(R_c)\mathbf{Q}^p_{cell}$) and no diffusion of unbound ECM molecules into the hydrogel is observed ($c^p(R_c) = 0$). A more realistic situation is actually in an intermediate range with $f \approx 0.8$, which is a reasonable estimate, such that both gel deformation and unbound ECM molecule diffusion occur simultaneously.

1.5 Results and discussion

This section presents a combined modeling and experimental approach to investigate the dynamics of tissue transport and deposition in various hydrogel environments. Briefly, the computational model consists of numerically solving the balance of mass and momentum equations presented in Eqs. (21) and (8), respectively, together with the constitutive equation describing the hydrogel. These nonlinear equations were discretized on a one-dimensional finite-element mesh using centro-symmetric assumptions and the resulting transient analysis was solved for three interacting fields (consisting of solid displacement $\mathbf{u}$, fluid pressure π and ECM molecule concentration c^p) with an implicit NewtonRaphson scheme as described in [45]. In the experimental component of our study, tissue production is measured by the deposition of chondroitin sulfate, an abundant linear glycosaminoglycan with an average molecular weight of 20 kDa [60] and is most closely associated with proteoglycans, specifically aggrecan. This molecule is advantageous from a modeling perspective because it can exist as part of a smaller proteoglycan (14 MDa, Table 1.1), or as a part of a larger aggrecan aggregate (100 MDa, Table 1.1), which will exhibit more restricted diffusion. Chondroitin sulfate thus provides a good model molecule to demonstrate the deposition of an extracellular matrix composed of molecules of different size scales.

Model parameters were chosen in agreement with experimental observation, i.e., the initial

volume fraction of cells was taken as $f_{cell} = 0.01$ and the cell radius was set to $R_c = 10\mu m$. The true density of the polymer was fixed at $\rho_{pegdm} = 1.07 g/cm^3$ and the true density of the matrix molecules was assumed to have the density of water i.e. $\rho^{pR} = 1 g/cm^3$. Other model inputs are described in Table 1.2.

1.5.1 Role of initial hydrogel mesh size on ECM distribution

We first aim to assess the effect of crosslink density on the diffusion of unbound ECM molecules throughout the gel in the absence of degradation. For this, gels were made with poly(ethylene glycol) dimethacrylate (PEGDM) with 10%, 15%, and 20% by weight compositions, yielding 0.11, 0.22, and 0.38 M crosslinking densities based on Eq. (18).

The concentration of chondroitin sulfate throughout the gel was evaluated by immunohistochemical staining 25 days after encapsulation. As shown in Fig. 1.8, results show that higher crosslink densities (i.e., 0.22 and 0.38 M) reduce unbound ECM molecule diffusion and consequently lead to localized elaboration of ECM surrounding the chondrocytes within the hydrogel. To better understand these processes, the presented mixture model was used to assess the variation of various quantities (hydrogel stress, strain, unbound ECM molecule concentration and hydrogel mesh size) for the three crosslink densities considered in experiments. Model results are generally in agreement with experimental observations with respect to the spatial deposition of chondroitin sulfate (Fig. 1.8). Most notably, the numerical results capture the presence of matrix molecules that have diffused far from the cell into the extracellular space of the hydrogel for the low crosslink gel (0.11 M), where there is a distinct lack of these matrix molecules in the extracellular space of the higher crosslink gels (0.22 and 0.38 M). They also illustrate a few important mechanisms of ECM deposition in hydrogels.

First, the change in chondroitin sulfate deposition for different crosslink densities can be explained by the fact that ECM diffusivity is an increasing function of hydrogel mesh size (Eq. (25)), which is dependent on crosslink density. Indeed, lower crosslink densities are associated with a higher swelling ratio (Fig. 1.4), a lower polymer volume fraction and thus, a larger mesh

size according to Eq. (23). This can be easily seen in the contour plots depicting mesh size distributions for the three considered crosslink densities in Fig. 1.8. This higher diffusivity enables ECM molecules to diffuse more homogeneously throughout the gel as seen in the concentration as a function of radial position plots in Fig. 1.8.

Second, the model clearly indicates the appearance of a pericellular matrix around the cell, consisting of large matrix molecules (MDa size scale, see Table 1.1) that accumulate between the chondrocyte and the surrounding gel due to their restricted diffusion. The growing pericellular matrix around the cell may result in compressive deformation of the gel near the cells, which is captured in the simulation results of Fig. 1.8. We note that this mechanism tends to decrease the mesh size immediately surrounding chondrocytes and may potentially hinder ECM diffusion in a local region around the cell.

1.5.2 Role of hydrolytic degradation on ECM transport

As observed in the previous section, homogeneous tissue deposition is difficult to achieve with non-degradable hydrogel systems. A solution to this problem therefore consists of introducing gels with crosslinks that can be cleaved over time and thus increase ECM molecule diffusivity over time. While this greatly improves ECM molecule transport, hydrogel degradation ultimately results in a weakening of the gel properties and if reverse gelation occurs before substantial tissue can be elaborated, complete loss of cells will occur. To investigate the effects of degradation, we compared the extent of ECM deposition after 28 days in (a) a non-degradable and (b) a degradable hydrogel, which both initially possess a crosslink density of 0.11 M (Fig. 1.9). The degradable gel was characterized by the degradation kinetics discussed in Section 1.3. Results presented in Fig. 1.9 show a dramatic increase of ECM molecule deposition and more homogeneous matrix deposition for the degradable system. Model predictions exhibit a similar trend and emphasize the underlying mechanisms of such behavior (Fig. 1.10a). As the hydrogel degrades, the radial stress decreases and swelling (or radial strain) increases under the effect of the osmotic pressure. These changes results in a significant increase in mesh size and, consequently, the enhancement

of the diffusivity of ECM molecules (Fig. 1.11). In comparison, non-degradable hydrogels do not see any changes in swelling and diffusivity of ECM molecules. ECM molecule deposition in this system is therefore highly restricted. As can be seen in Fig. 1.10b, the rate of degradation

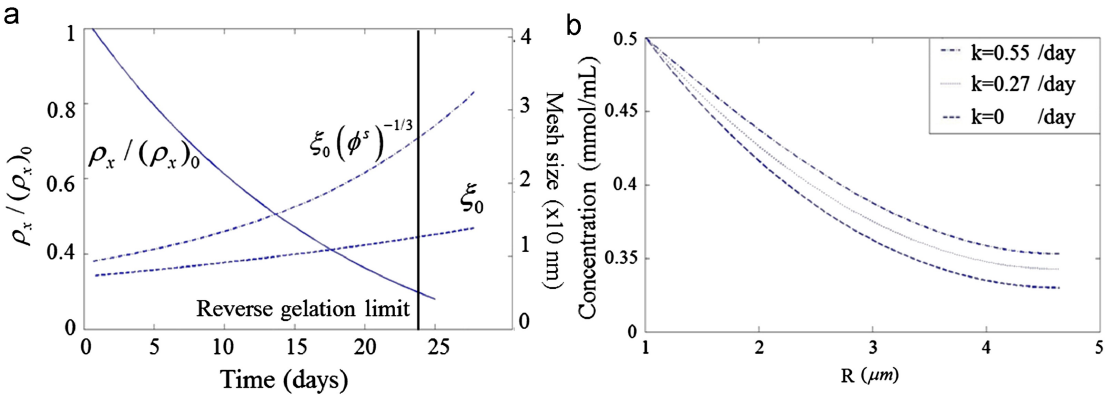

Figure 1.10: *(a) The effect of swelling on the mesh size, and (b) the effect of the degradation rate k on the distribution of matrix molecules in the scaffold at day 25.*

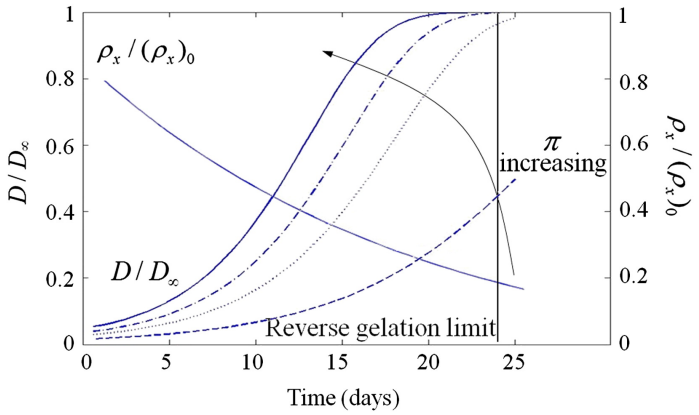

Figure 1.11: *The different osmotic pressures (20, 200, 300, and 400 kPa) applied on the model to see the evolution of the diffusivity.*

also has a large influence on the diffusion of matrix molecules within the hydrogel. In the process of designing a degradable hydrogel, the hydrolytic pseudo first order rate constant (Eqs. (15) and (16)) may be optimized to enable maximum ECM molecule deposition before the hydrogel scaffold reaches the reverse gelation point. From Eq. (18), it has been shown that for highly swollen gels ($Q > 10$) an estimate of the swelling can be found as $Q \simeq \rho_x^{-3/5}$ [100]. Then, we can estimate the reverse gelation point from swelling properties just before reverse gelation occurs by

$\rho_x/\rho_{x0} < (Q/Q_0)^{5/3}$. Using the values of Fig. 1.5 this happens when ρ_x/ρ_{x0} becomes smaller than 20% (Figs. 1.10a and 1.11). In Fig. 1.9, macroscopic tissue deposition was observed at day 28, indicating that the evolution of ECM was able to maintain some level of three dimensional integrity after the hydrogel scaffold was fully degraded. However, a previous assessment of the overall mechanics of similar cell-laden hydrogels showed a significant drop in compressive modulus from the initial cell-laden hydrogel to the engineered tissue as a result of hydrogel degradation [126]. These findings indicate that additional optimizations are needed to better match hydrogel degradation with tissue elaboration. With this mathematical model, we will now be able to better predict optimal degradation parameters that support macroscopic tissue evolution in degradable hydrogels without losing mechanical integrity.

1.5.3 Role of osmotic pressure in diffusion of molecules and creation of tissue

Osmotic pressure is an important player in tissue transport as it is responsible for gel swelling and consequently controls hydrogel mesh size (and thus ECM molecule diffusivity). To investigate this aspect, we used the theoretical model to predict the effect of changing osmotic pressure on the evolution of ECM diffusivity through a degradable gel. Fig. 1.11 shows the obtained trends for four different osmotic pressures (π =20, 200, 300 and 400 kPa). As expected, we observe that an increase in osmotic pressure precipitates a change in ECM molecule diffusivity through the gel. This observation is explained as follows: as a gel degrades, its bulk modulus decreases and its mechanical resistance to osmotic pressure becomes weaker; this results in significant gel swelling during degradation. Increasing the osmotic pressure tends to reinforce this swelling effect and thus enhance ECM molecule diffusivity due to the associated rise in mesh size. This mechanism is important as it could potentially enable a more homogeneous tissue distribution before a scaffold reaches the reverse gelation point.

1.5.4 Concluding remarks

The presented model provides a platform for better understanding the role of hydrogel scaffold structure on cartilage tissue engineering. It evaluates both degradable and non-degradable PEG-based hydrogels, which have shown promise in promoting neocartilage deposition. The developed model captures the limitations associated with tissue deposition in non-degradable PEGDM hydrogels and confirms the necessity of adding degradable units to hydrogels in order to enable the diffusion of ECM molecules throughout the scaffold. The model also demonstrates that very large ECM molecules will not diffuse throughout the hydrogel until after the reverse gelation point, a finding supported by experimental data. As an attempt to account for the existence of various ECM molecule sizes, the model splits these molecules in two categories, thus including the diffusion mechanism and the deposition of larger molecules forming the PCM. The model can accurately predict how crosslink density impacts ECM molecule diffusion. Moreover, the model is able to simulate the concentration distribution of molecules in the hydrogel, which is otherwise difficult to predict experimentally. The model also emphasizes that osmotic pressure is a key property for promoting diffusion through the gel.

However, there are several limitations to the current modeling approach and their acknowledgment is critical for improving mathematical models in the future. With regards to modeling the solvent, hydrogels are typically swollen in cell culture medium, consisting of proteins, growth factors, and salts. As opposed to water (as considered in our model), these components may interact with secreted ECM molecules, and can potentially affect both osmotic pressure and cell response. The model, while focusing on a single cell encapsulated in a spherical gel domain, accounts for the density of cells in the hydrogel through the cell volume fraction. The three-dimensional model presented in chapter 4, may show adhesion and inhomogeneous cell-cell interactions. Indeed, in order to create a macroscopic tissue, there must be overlap between the tissue being produced from different cells in order to create a homogeneous tissue structure. Finally, another component, which is ultimately difficult to model, is the dynamic nature of cells and the tissues they produce.

Once matrix is deposited, it is not permanent, but is subject to reorganization or degradation by secreted enzymes. This process is necessary in vivo to transport newly synthesized ECM molecules from the pericellular region to the extracellular space [104]. Similarly, modeling the secretion of matrix molecules from cells will be improved in chapter 4; cells can up- or down-regulate matrix synthesis in response to external cues, yet this process is not yet fully understood, meriting future investigation. Despite these limitations, this model captures the deposition of matrix molecules in non-degradable and degradable hydrogels, which is observed experimentally. Future directions of the model include considering mechano-transduction mechanisms to describe the regulation of ECM synthesis [50, 49]. In addition, accurate models of the membrane deformation and permeability [151, 152, 154, 148] will be critical in assessing the sensitivity of cells to mechanical loading and fluid flows, which are important in cartilage homeostasis and cartilage tissue engineering.

Overall, a computational triphasic model is demonstrated for tissue production by cells in hydrogels with varying structures and chemistries can generate simulations consistent with experimental observation. Despite the many assumptions and simplifications utilized, a powerful model has been developed that captures essential tissue dynamics in synthetic structures. The limitations serve to motivate future experimental work as well as eventually adding layers of complexity to the model. By validating the model in simple non-degradable and hydrolytically degradable systems, more complex chemistries and additives can feasibly be incorporated into the model in the future, such as incorporating physiological mechanical environments and some form of localized cell-mediated degradation [146]. This increasing level of sophistication could aid in the design and characterization of novel tissue engineering environments. These models can be employed to both predict and understand successful tissue engineering structures, which could lead to more rapid development of clinically applied therapies.

Chapter 2

Determination of the Polymer-Solvent Interaction Parameter for PEG Hydrogels in Water: Application of a Self Learning Algorithm

2.1 Introduction

PEG hydrogels are promising materials for numerous biomedical applications in drug delivery and tissue engineering [22, 108]. PEG hydrogels imbibe large amounts of water and mimic many aspects of the mechanics of biological tissues [4, 108]. By tuning the crosslink density, a wide range of hydrogel properties can be achieved. Furthermore, degradable linkages are readily incorporated into the crosslinks offering additional control and tunability of the hydrogel properties during degradation [22]. Controlling these properties, however, requires knowledge of the underlying physical and chemical mechanisms, together with an understanding of their connection to processing conditions.

The crosslink density of the polymer network controls two key properties which are important in biomedical applications: the degree to which the hydrogel swells and the resultant mechanical properties. The former depends on the polymer-solvent interaction parameter χ also known as the Flory-Huggins parameter. For a given chemistry and temperature, Flory-Huggins theory predicts a constant value for χ over the entire polymer volume fraction. For solutions of high molecular weight poly(ethylene oxide) hydrogels in water this relationship has been shown experimentally to be valid, resulting in a χ value of 0.426 [96]. However, a number of studies have reported that Flory-Huggins theory is an oversimplification and χ is in fact more complicated, depending on polymer volume fraction [77, 118, 116, 101, 95, 68] and on polymer molecular weight [117]. For

PEG in water, this dependence has been shown to be, in part, due to the nature of water association with PEG [55, 88, 56, 39]. Indeed a modified Flory-Huggins theory that included hydrogel bonding between water molecules and PEG has been shown to be able to capture the phase behavior of an experimental PEG-water system [14]. Furthermore, PEG hydrogels are often formed from PEG molecules that are functionalized with a polymerizable group, which alters the overall chemistry. Studies have shown that hydration of PEG molecules differ for methyl and hydroxyl terminated PEG [36]. Therefore, the interaction of PEG and water will depend on a number of factors, most notably, the nature of water association with PEG and the overall chemistry of the functionalized PEG, both of which will likely vary with polymer volume fraction in a crosslinked PEG hydrogel. As a result, it stands to reason that the polymer-solvent interaction parameter for PEG hydrogels in an aqueous solvent will vary with polymer processing conditions, polymer composition and degradation.

To determine the value of χ for different formulations of PEG hydrogels and as a function of degradation, we introduce a so-called *self-learning model*. This model can indirectly infer its own parameters (e.g., χ) by observing experimental data. By combining Flory's theory for swollen networks [47, 48] with theories of mixture and poroelasticity, this model can describe the transient gel response [62, 80, 65, 154] arising from the competition between polymer elasticity, that depends on cross-linking density [15, 42], and polymer-solvent interactions. The self-learning framework automatically learns from the experiments in an iterative loop. Each iteration results in an improvement or calibration/estimation of model parameters, in our case χ. The improvement is achieved by determining the relations between model and processing parameters so that material properties (e.g., swelling and modulus) are more accurately predicted over a range of parameters determined by the available experimental data. Once validated, the model may be employed to predict χ, along with a confidence level, and thus can be used to improve the hydrogel design process. Because the model continuously learns from the experimental data, the efficiency of the model calibration increases in terms of experimental efforts. As a result of the learning process, simple relations between design and model parameters are derived and the resulting model is validated with experimental data.

In this chapter, the PEG hydrogels formed from a step-growth mechanism between an eight-arm PEG functionalized with norbornene and the crosslinker PEG dithiol is investigated. The cross link density was varied by changing the processing conditions through the thiol to ene ratio and the polymer volume fraction in water prior to polymerization. The hydrogel properties, specifically equilibrium swelling ratio and compressive modulus, were measured experimentally. Hydrogels containing an ester linkage were subjected to accelerated hydrolysis in a basic solution and the hydrogel properties assessed. The self-learning model was employed to determine χ as a function of processing conditions and as a function of degradation. The predictive capability of the model was then demonstrated. First introducing the self-learning model coupled with a mechanistic model of hydrogels is introduced. Results of computer simulations follow, where we illustrate how the proposed algorithm learns from experimental data and refines the model accuracy to determine the value of χ for non-degrading and degrading PEG hydrogels under two scenarios: (a) assuming a constant value of χ and (b) allowing χ to vary.

2.2 Mapping PEG hydrogel processing to properties

PEG hydrogels are formed from a set of well-defined *control variables*, which include quantities such as percentage of each monomer in an aqueous solvent. Once polymerized, the behavior of the PEG hydrogel is assessed by several *properties of interest* such as swelling and stiffness. The design goal is to identify the range of control variables that yield the properties of interest for a desired application. In this context, the aim is to enable a statistical model that learns from experimental data and builds a predictive map between control variables and properties of interest. To accomplish this goal, identification of appropriate values of χ for each processing condition is necessary.

2.2.1 General approach

While we demonstrate the self learning approach to PEG hydrogels, this approach may be more broadly applied to other types of materials. Let us consider a material for which the n control variables are represented by the collection $\mathbf{C} = (C_1, C_2, \ldots, C_n)$ and the m properties of interest

are denoted by $\mathbf{G} = (G_1, G_2, \ldots, G_m)$. To map the vector $\mathbf{C}$ to $\mathbf{G}$, let us assume that one can introduce a model, that is *mechanistically* driven; that is, it is based on fundamental understanding of the physical mechanisms driving material behavior at the microscopic level. Due to its underlying physical basis, such a model can therefore be further utilized for design and predictions. Mechanistic models usually take the form of differential equations that do not always admit trivial solutions and exhibit a number of *material parameters*, which need to be calibrated. Furthermore, in order to provide the processing-properties relationship, two maps may be considered (Fig. 2.1): (a) a map from material's processing to microstructure and (b) a map between microstructure and properties [94]. From a mathematical standpoint, it is convenient to charaterize the microstructure by a set of quantities ξ_i, commonly denoted as *internal state variables (ISV)*. The change of a material's structure during its lifetime can then be cast in terms of evolution laws of the ISVs [128, 52, 93]. To characterize the relationship between processing and the material structure, we introduce a model of the type

$$\xi_i^0 = \xi_i^0 \left(\mathbf{C}, \bar{\mathbf{m}}\right), \tag{2.1}$$

where ξ_i^0 denotes the value of the i^{th} internal state variable where the superscript 0 denotes the initial swollen hydrogel (i.e., before degradation), and $\bar{\mathbf{m}} = (\bar{m}_1, \ldots, \bar{m}_{M_1})$ denotes the collection of the M_1 model parameters. The second component of the model maps the microstructure to the material's properties given by the model

$$G_i = G_i \left(\boldsymbol{\xi}^0, \bar{\bar{\mathbf{m}}}\right), \tag{2.2}$$

where $\bar{\bar{\mathbf{m}}} = (\bar{\bar{m}}_1, \ldots, \bar{\bar{m}}_{M_2})$ denotes the collection of M_2 model parameters associated with the structure-property map. Ultimately, the map between material processing and properties takes the form

$$G_i = G_i \left(\mathbf{C}, \mathbf{m}\right) = G_i \left(\boldsymbol{\xi}^0 \left(\mathbf{C}, \bar{\mathbf{m}}\right), \bar{\bar{\mathbf{m}}}\right), \tag{2.3}$$

in which the set of $M = M_1 + M_2$ material parameters is $\mathbf{m} = (\bar{\mathbf{m}}, \bar{\bar{\mathbf{m}}})$. For situations where the mapping $\xi_i^0 = \xi_i^0 \left(\mathbf{C}, \bar{\mathbf{m}}\right)$ is not explicitly available, the processing-microstructure parameters $\bar{\mathbf{m}}$ may not be inferred directly from the observations of G_i. In such cases, it is more appropriate to

include the (components of) vector $\boldsymbol{\xi}^0$ in $\bar{\mathbf{m}}$ for the inference. As we start to describe below, this applies to the application of interest in this study.

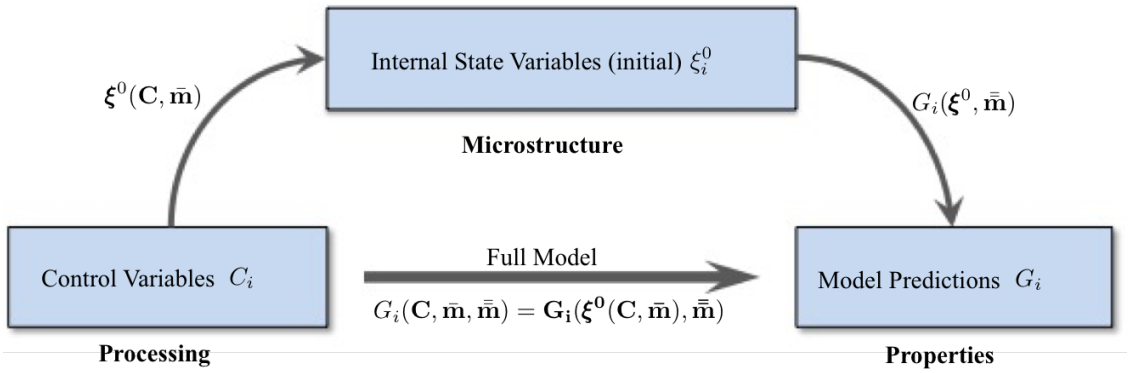

Figure 2.1: Processing-microstructure and microstructure-properties maps.

2.2.2 Application to PEG hydrogels

We apply the above framework to PEG hydrogels formed from thiol-ene monomers, which consists of two components: a polymer network (i.e., cross-linked polymer) and water. We examine two properties of interest: the swelling ratio $G_1 = Q(t)$ and the Young's modulus under compression $G_2 = E_c(t)$, which in the case of a degradable gel can be a function of time. In this work for a given 'ene' and thiol monomer, the initial degree of cross-linking is controlled by the thiol to 'ene' ratio $C_1 = r$ and the weight percentage of the polymer in solution prior to polymerization $C_2 = w$. For a degrading hydrogel, the degree of cross-linking of the hydrogel will change with time as cross-links are cleaved. One simple way to control degradation is to vary the ratio $C_3 = \eta$ of initial cross-links that are degradable. To simplify our analysis, we consider two extreme cases in which (a) none of the cross-links are degradable, i.e., $\eta = 0$ or (b) all of the cross-links are degradable, i.e., $\eta = 1$. After processing, the hydrogel microstructure can be described in terms of two internal state variables, namely, the initial cross-link density $\xi_1^0 = \rho_x^0$ and the polymer-solvent interaction parameter $\xi_2^0 = \chi^0$. For a given set of 'ene' and 'thiol' monomers, a summary of control variables, properties of interest and state variables is provided in Table 2.1.

Table 2.1: Control variables, internal state variables, and properties of interest in the hydrogel model.

Control variables ($\mathbf{C}$)	Thiol:ene ratio	r
	Weight percent	w
	Ratio of degradable cross-links	η
Internal state variables ($\boldsymbol{\xi}^0$)	Cross-link density	ρ_x^0
	Polymer-solvent interaction parameter	χ^0
Macroscopic properties ($\mathbf{G}$)	Compressive Young's modulus	$E_c(t)$
	Swelling ratio	$Q(t)$

2.2.2.1 Processing-microstructure mapping

In this work, we limit our investigation to one 'ene' monomer, an 8-arm PEG molecule functionalized with norbornene, and one thiol monomer. For a particular combination of a thiol and 'ene' monomer, we can directly relate the microstructure to the control parameters through relationships of the form

$$\rho_x^0 = \rho_x^0\left(w, r\right) \qquad \text{and} \qquad \chi^0 = \chi^0\left(w, r\right). \tag{2.4}$$

Note that these are a particular case of equation (2.1).

2.2.2.2 Mechanistic model: Microstructure-property mapping

The constitutive relation that describes the link between hydrogel structure and macroscopic properties is based on two competing internal forces governing hydrogel behavior: entropic elasticity and mixing forces.

Chemo-mechanical equilibrium. Following the theory by Flory [47], the free energy per unit volume of mixture is characterized by (a) a mechanical component that describes the increase of stored elastic energy in the polymer due to stretching and (b) a mixing component that characterizes the free energy of mixing of two phases (polymer and solvent)[34]. This yields the following free energy function

$$\Delta G_e = \underbrace{\frac{1}{2}\rho_x RT(\mathrm{tr}(\mathbf{F}^T\mathbf{F}) - 3 - \ln J)}_{\text{Elasticity}} + \underbrace{RTC_w(\chi\phi_p + \ln\phi_w)}_{\text{Mixing}}, \tag{2.5}$$

with R and T being the ideal gas constant and the absolute temperature, respectively. In expression (2.5), $\mathbf{F}$ is the deformation gradient, $J = \det(\mathbf{F})$ is the volumetric equilibrium swelling ratio of the hydrogel, ϕ_p and ϕ_w are the volume fractions of polymer and solvent, respectively, while C_w and ν_w are the nominal concentration and molar volume of solvent. Note that this free energy also involves the internal state variables ρ_x and χ, which are embedded in J. In addition to the free energy expression, one must also specify the mass conservation in the mixture. Assuming that the polymer and solvent are incompressible constituents (the latter having a specific volume ν_w), it has been shown that the constraint $J = 1 + \nu_w C_w$ must be considered [65]. In other words, the change of total hydrogel volume only occurs if solvent is added to the mixture. To account for this, one can modify the free energy function (2.5) as follows:

$$\Delta\hat{G}_e = \frac{1}{2}\rho_x RT(\mathrm{tr}(\mathbf{F}^T\mathbf{F}) - 3 - \ln J) + RTC_w(\chi\phi_p + \ln\phi_w) - \pi(J - 1 - \nu_w C_w), \tag{2.6}$$

where the Lagrange multiplier π is interpreted as the osmotic pressure in the solvent. Now considering a hydrogel specimen under a homogeneous state of (nominal) stress $\bar{\mathbf{P}}$ and in chemical equilibrium with its surrounding, the equilibrium conditions can be derived by minimizing the above energy functional [145, 151] as follows

$$\mathbf{P} = \frac{\partial\Delta\hat{G}_e}{\partial\mathbf{F}} = \frac{1}{2}\rho_x RT\left(2\mathbf{F} - \mathbf{F}^{-T}\right) - \pi J\mathbf{F}^{-T} = \bar{\mathbf{P}}; \tag{2.7}$$

$$\Delta\mu_w = \frac{\partial\Delta\hat{G}_e}{\partial C_w} = RT\left(\ln(\phi_w) + (1 - \phi_w) + \chi(1 - \phi_w)^2\right) + \nu_w\pi = 0. \tag{2.8}$$

Here, $\mathbf{P}$ and μ_w are, respectively, the nominal stress and solvent's chemical potential within the hydrogel. We used the fact that these quantities are energy conjugate of the deformation gradient and the solvent's nominal concentration, respectively.

Evolution of internal state variables. In this study, the evolution in gel structure over time is caused by hydrolytic degradation. Specifically, we consider a PEG hydrogel whereby an ester linkage is incorporated into the ends of each cross-link. With this functionality, hydrogels with the same initial cross-link density can display different degradation kinetics by varying the pH of the aqueous solution (i.e., via base-catalyzed hydrolysis of the ester) [12, 163]. From a modeling

perspective, degradation is thus written in terms of a first order differential equation [99] that depends on several factors, most notably the chemistry of the degradable linkage and the solvent. The evolution of cross-link density ρ_x is thus given by

$$\frac{d\rho_x}{dt} = -k'\eta\rho_x, \tag{2.9}$$

where k' is the pseudo first order rate constant for hydrolytic degradation. We note that k' is not the true kinetic constant of the ester bond, it rather encompasses water concentration and the hydroxyl ions (or hydronium depending on the solvent) that catalyze the reaction. When k' is constant, this equation admits a trivial solution of the form $\rho_x(t) = \rho_x^0 \exp(-k'\eta t)$. However, in this study, we will show that this coefficient in fact varies during the degradation process, such that $k' = k'(\rho_x)$ in the general case.

2.2.2.3 Summary and model parameters

As a summary, the full model that maps hydrogel processing to behavior is only partially known. As shown in Table 2.2, the *processing-microstructure* is mostly unknown as (a) it is difficult to measure the polymer-solvent interaction parameter experimentally and (b) it is not possible to directly measure cross-link density. The structure of the *microstructure-properties* model is well-posed through the free energy functional (2.6) and cross-link degradation kinetics (2.9). In this work, we therefore aim to build a methodology that allows us to (a) infer unknown model structure (i.e., crosslink density and χ) by analyzing experimental data and (b) determine unknown model parameters (i.e., degradation parameter $k'(\rho_x)$). This will be done by integrating experimental data with modeling, and by solving an inverse problem as described next.

Table 2.2: Summary of model structure and parameters for degradable PEG hydrogels

Model	**Structure**	**Parameters**	**Symbol**
Processing-microstructure	Unknown (Eq. (2.4))	n/a	n/a
Microstructure-properties	Eq. (2.6) and Eq. (2.9)	Degradation constant	$k(\rho_x)$

2.2.3 Integration of experimental data and modeling

In this study, we perform a set of macroscopic experimental measurements, denoted by the vector **g** and discuss how these can be compared with model predictions. For non-degradable gels, **g** may represent the swelling ratio ($g_1 = Q$) and elastic moduli ($g_2 = E_c$) measured for various processing conditions. Note that in the following, we use a lowercase symbol **g** for the measured properties of interest; this is in contrast with the uppercase symbol **G** used for model predictions.

2.2.3.1 Measurements and uncertainty

To simplify the approach, we assume that there is neither uncertainty nor noise in the measurements of the control parameters C_i, although there may be uncertainties in the measurement of the properties of interest g_i (Fig. 2.2). Quantification of this uncertainty is achieved as follows. For a fixed set of control parameters $C_i^{(k)}$ characterized by the superscript (k), $k = 1, \ldots, K$, we repeat the experiments (and thus the macroscopic measurements) R times. Measured quantities of interest are collected in a vector $(g_i^{(k_1)}, g_i^{(k_2)}, \ldots, g_i^{(k_R)})$, where k_r represents the measurement from the r^{th} repetition. This set of data may then be used to build a probability density function (PDF) for the property of interest $g_i^{(k)}$. We assume that each of the measured properties follows a Gaussian distribution whose mean and standard deviation can be estimated, respectively, from the mean $\bar{g}_i^{(k)}$ and standard deviation σ_i^k of data,

$$\bar{g}_i^{(k)} = \frac{1}{R}\sum_{r=1}^{R} g_i^{(k_r)} \qquad \text{and} \qquad \sigma_i^{(k)} = \sqrt{\frac{1}{R-1}\sum_{r=1}^{R}\left(g_i^{(k_r)} - \bar{g}_i^{(k)}\right)^2}. \tag{2.10}$$

Although model accuracy increases with the number of repetitions R, this number usually remains small because of the cost associated with each experiment. The common practice is then to factor in prior knowledge or expert opinion for an appropriate selection of $\bar{g}_i^{(k)}$ and $\sigma_i^{(k)}$. In the present study, we used $R = 3$ but verified that the resulting estimates are compatible with previous observations.

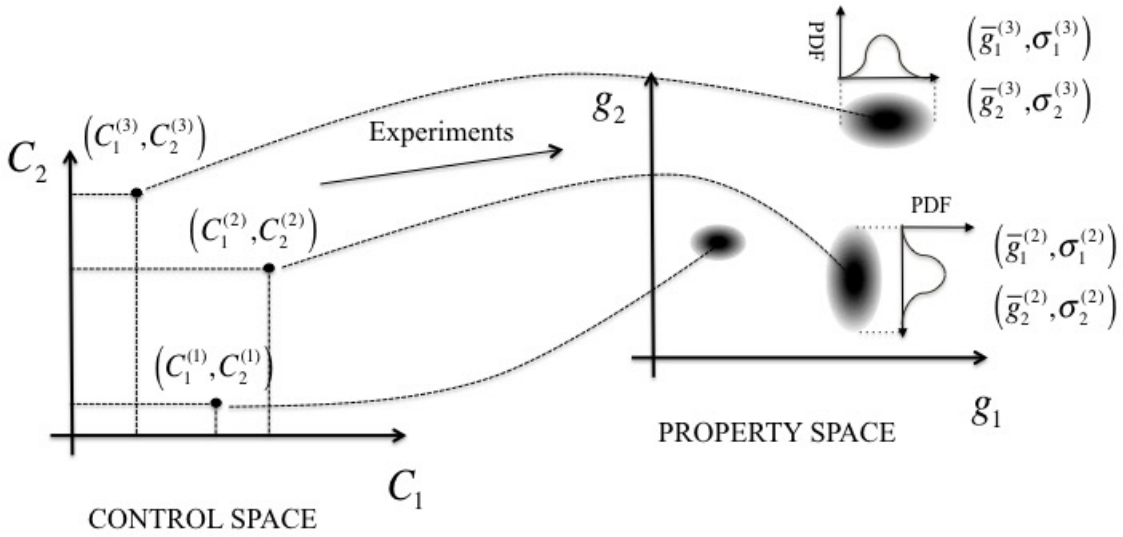

Figure 2.2: Experimental tests provide sample points of the map between the control space **C** and the property space **g**. Uncertainties in control variables propagate to the property space; this aspect can be quantified by measuring the probability density function (PDF) in both domains through the realization of several experiments under similar design conditions.

2.2.3.2 Measuring and predicting the properties of interest of a PEG hydrogel.

The mechanical response of PEG hydrogels was characterized experimentally by two macroscopic measurements: the equilibrium volumetric swelling ratio and the Young's modulus.

Equilibrium Swelling Ratio (Q): The experimentally determined mean values of Q along with the standard deviation for three different experiments are presented in Fig. 2.3. To simulate the above experimental procedure, we assume that swelling is isotropic, homogeneous and occurs in stress-free conditions, i.e., $\bar{\mathbf{P}} = \mathbf{0}$ in (2.7) [44]. In this case, the deformation gradient of the polymer network after swelling is $\mathbf{F} = \text{diag}(\lambda, \lambda, \lambda)$ (with λ the linear stretch ratio in each direction axis) and the equilibrium swelling ratio becomes $Q = \lambda^3$. This leads to the following simplified version of (2.7) and (2.8), respectively,

$$0 = \rho_x RT \left(\lambda - \frac{1}{2\lambda}\right) - \pi\lambda^2; \tag{2.11}$$

$$0 = RT \ln \frac{\lambda^3 - 1}{\lambda^3} + RT\chi \frac{1}{\lambda^6} + RT \frac{1}{\lambda^3} + \pi\nu_w, \tag{2.12}$$

where we used the relation $\phi_w = (J-1)/J$. This coupled system of nonlinear equations can be solved to determine gel swelling Q through the stretch ratio λ and the osmotic pressure π for any given value of the cross-link density and the polymer-solvent interaction parameter.

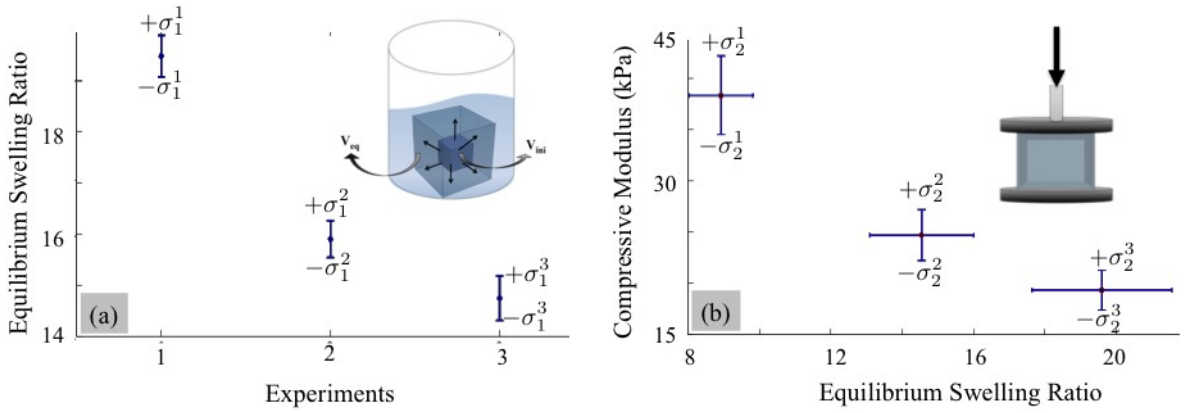

Figure 2.3: Confidence intervals for (a) the swelling ratio and (b) the compressive modulus of three hydrogel designs. For each design, the properties of interest were measured three times, independently. The data set for each independent experiment can be represented as an interval by using the mean and standard deviation values.

Young's modulus under compression: Hydrogels typically display a non-linear stress-strain relation when loaded in compression. However, to experimentally characterize their effective stiffness, we often measure a so-called secant modulus [26], which represents the average stiffness as the deformation reaches a given value chosen to be 15% in this study (see experimental section). The specimen usually remains cylindrical during the test so that one can assume a homogeneous deformation state measured from the gel's swollen state as $\mathbf{F} = \mathrm{diag}(\lambda_1, \lambda_2, \lambda_2)$. Here, λ_1 and λ_2 are the stretch ratios in the axis of the cylinder and in the lateral directions, respectively. Similarly, as the specimen is unconstrained on its side during compression, the nominal stress field is given by $\bar{\mathbf{P}} = \mathrm{diag}(f/A_0, 0, 0)$, where f is the compressive force and A_0 is the surface area of the specimen in its undeformed, swollen state.

Due to the relatively fast rate of loading, compared to the characteristic time to reach equilibrium swelling (few hours), it is acceptable to assume that the solvent/polymer mixture remains incompressible during the procedure. In other words, measured from the swollen state, the Jacobian

of the deformation J remains equal to 1. This means that no changes of osmotic pressure π occurs as the specimen is loaded. However, the relationship between nominal stress and deformation can be determined from (2.7) together with the above assumption on $\mathbf{F}$. This yields,

$$P_{11}(\lambda_1) \;=\; \frac{f}{A_0} \;=\; G_s\left(\lambda_1 - \frac{1}{2Q^{2/3}\lambda_1}\right) - \frac{\pi}{\lambda_1}, \tag{2.13}$$

in which we used the fact that $J = \lambda_1\lambda_2^2 = 1$. Note that the stretch ratios are written for a swollen polymer network and $G_s = \rho_x RTQ^{-1/3}$ is the shear modulus. The secant Young's modulus at a 15% compression strain can then be computed as

$$E_c = \frac{P_{11}\left(\lambda_1 = 1.15\right)}{0.15}. \tag{2.14}$$

Degradation kinetics. In this work, we monitor degradation by measuring the swelling ratio and the compressive modulus of a degradable ($\eta = 1$) hydrogel specimen in time. We assume that the degradation process is slow compared to the characteristic time of solvent diffusion in the gel, thus allowing us to use the equilibrium equations in the prediction step.

2.3 Mechanistic model calibration

The mechanistic model described above is critical to understand and eventually predict the behavior of hydrogels in many applications. Their reliability and accuracy however depend on parameters, such as ρ_x^0 and χ that are often not known *a priori* and evolve in time. To enhance the model's predictive accuracy, it is therefore essential to determine these parameters from, possibly sparse, measurements of the system responses (Fig. 2.4). Such a process, referred to as *model calibration*, may be naturally cast in the form of an inverse problem in which parameters of the mechanistic model are inferred, such that model predictions are as close as possible to the measurements. In doing so, however, several difficulties shall be accounted for. In particular, experimental measurements are often noisy as shown in measurements and uncertainty section, the mechanics model may be computationally expensive to simulate for a given realization of parameters, and the inversion process may be ill-posed in the sense that multiple values of model parameters may result

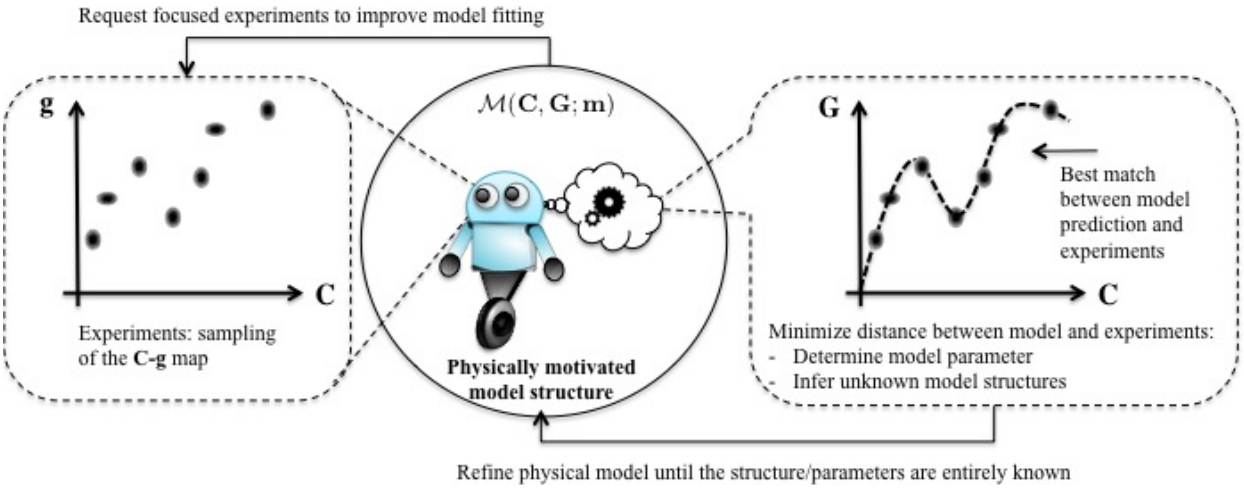

Figure 2.4: Framework for model calibration from experiments. We consider the model as an active entity, represented by a robot that can observe the relationship between input and output obtained from experiments and adjust its free parameters to best fit the data. If it fails at doing so, the model may request a modification of its own structure, represented by differential equations.

in (approximately) the same measurements. We propose here to estimate the unknown parameters by minimizing a cost function measuring the deviation of model predictions from experimental data. To accelerate this minimization, we construct a surrogate to the map between model parameters and predictions. This map is generated *a priori* by exploring discrete realizations in the parameter space and predicting, using the mechanistic model, their corresponding output (or properties of interest). We then use interpolation functions between these points to cheaply construct the full parameter-prediction map. Once the model parameters are estimated by learning from experiments, the model is then validated against independent experiments. If not invalidated, the calibrated mechanistic model may finally be utilized for purposes such as prediction of properties of interest, sensitivity analysis, and design of new experiments. This process is also summarized in Fig. 2.5.

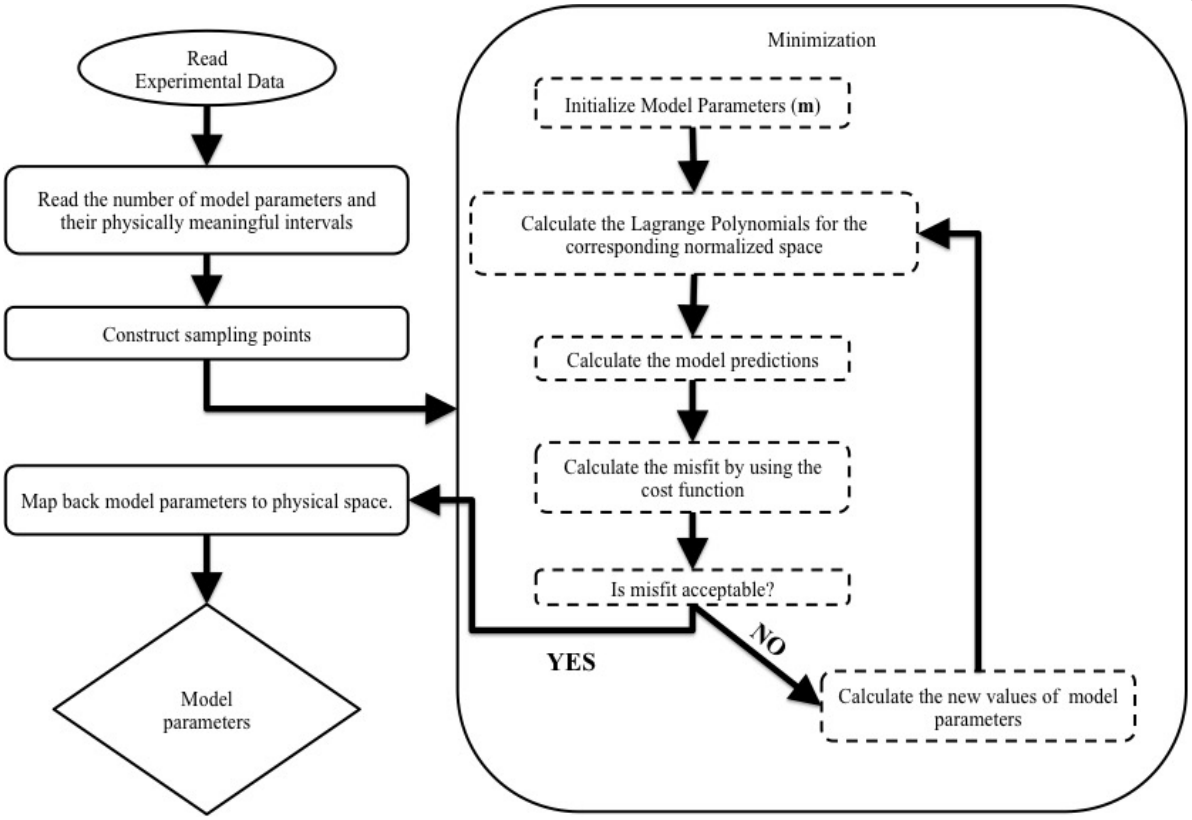

Figure 2.5: Flowchart of the utilized model calibration algorithm.

2.3.1 Inverse problem for mechanistic model calibration

In an inverse problem, model parameters $\mathbf{m} = (m_1, \ldots, m_M)$ are estimated by minimizing the misfit between model outputs $G_i^{(k)}(\mathbf{m})$ and experimental data $g_i^{(k)}$. Here, $i = 1, \ldots, I$ and $k = 1, \ldots, K$ are indices representing quantities of interest and replications of the experiments, respectively. This misfit is quantified by a cost function, here of a least-squares type assuming a normally distributed measurement error,

$$\mathcal{R}(\mathbf{m}) = \sum_{i=1,k=1}^{I,K} \left(\frac{G_i^{(k)}(\mathbf{m}) - g_i^{(k)}}{\sigma_i^{(k)}} \right)^2, \tag{2.15}$$

where $\sigma_i^{(k)}$ was defined in (2.10). Note that the summation in (2.15) is for all properties of interest and for every independent experiment. The only unknowns in the cost function are the model parameters $\mathbf{m}$. When $\mathbf{m}$ is sufficiently low-dimensional, the minimization may be performed using standard optimization techniques; here we resort to a Newton-Raphson implementation in MAT-

LAB. The result of this inversion are point estimates (i.e., deterministic values) of $\mathbf{m}$. To account for possible variability of parameter estimates, due to, for instance, uncertainty in the measured data, more advanced methods such as Bayesian inference [112] may be employed. After the estimation of model parameters, the experimental data and model outputs are compared in order to determine if there is a need for modification in the definition of the parameters or, possibly, the structure of the mechanistic model. In other words, we consider the model as an active entity, represented by the robot in Fig. 2.4, that can observe the relationship between input and output obtained from experiments and adjust its free parameters to best fit the data. If it fails to do so, the model may request a change in its own structure, represented by differential equations.

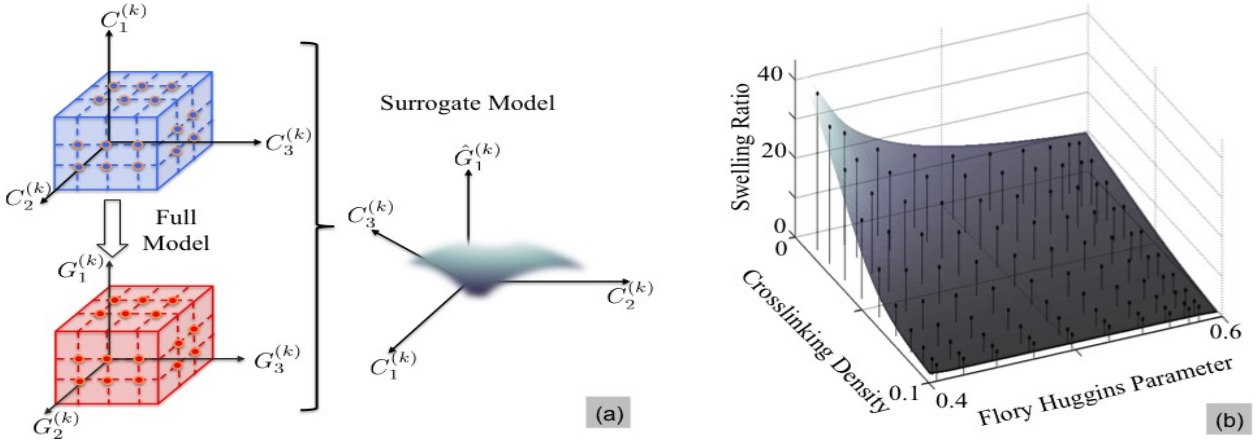

Figure 2.6: (a) A surrogate model is an approximation which is constructed by using a set of realizations of model parameters (defined over an appropriate range) and the corresponding solutions of interest. (b) Surrogate model for swelling ratio of the initial PEG hydrogel properties based on equation (2.6).

2.3.2 Acceleration via surrogate modeling

Finding a global minimum of (2.15) requires evaluation of $G_i^{(k)}(\mathbf{m})$, or equivalently solving the model problem of *microstructure-property mapping* for a potentially large number of $\mathbf{m}$. When the mapping between $\mathbf{m}$ and $G_i^{(k)}(\mathbf{m})$ is sufficiently smooth, as in the case of hydrogels considered here, a surrogate to $G_i^{(k)}(\mathbf{m})$ may be employed to reduce the optimization cost. Surrogate mod-

eling refers to the construction of an approximate (but cheap to evaluate) representation of the mapping between a model's input parameters and the response of interest [73, 120]. Such a model is constructed once based on full model simulations and is used to rapidly generate realizations of the solutions of interest. In particular, here we construct surrogates of Lagrange interpolation type for the mapping between $\mathbf{m}$ and $G_i^{(k)}(\mathbf{m})$, separately for each i. Specifically,

$$\widehat{G}_i^{(k)}(\mathbf{m}) \approx \sum_{j=1}^{J} G_i^{(k)}\left(\mathbf{m}^{(j)}\right) L_j(\mathbf{m}), \tag{2.16}$$

where the nodes $\mathbf{m}^{(j)} = (m_1^{(j_1)}, \ldots, m_M^{(j_M)})$, $j_k = 1, \ldots, J_k$ and $k = 1, \ldots, M$, are selected values of $\mathbf{m}$ as described below. Additionally,

$$L_j(\mathbf{m}) = \prod_{k=1}^{M} \ell_{j_k}(m_k) \quad \text{and} \qquad \ell_{j_k}(m_k) := \prod_{i=1, i\neq j_k}^{J_k} \frac{m_k - m_k^{(i)}}{m_k^{(j_k)} - m_k^{(i)}} \tag{2.17}$$

are the multi- and uni-variate Lagrange polynomials corresponding to nodes $\mathbf{m}^{(j)}$ and $m_k^{(j_k)}$, respectively. While several choices of nodes $m_k^{(j_k)}$ may be considered, here we choose them according to the Gauss-Legendre rule that is known to result in more stable interpolations [20]. The numbers J_k of nodes along parameters m_k control the accuracy of the surrogate $\widehat{G}_i^{(k)}(\mathbf{m})$. For smooth $G_i^{(k)}(\mathbf{m})$, increasing J_k results in more accurate surrogates. However, this will require a larger number $J = \prod_{k=1}^{M} J_k$ of parameter values $\mathbf{m}^{(j)}$ at which the model $G_i^{(k)}(\mathbf{m})$ has to be simulated. In the present study, we start with a regular subdivision of the parameter space (constant increments in J_k values), and refine these subdivisions gradually so that $\widehat{G}_i^{(k)}(\mathbf{m})$ is within some desirable distance of $G_i^{(k)}(\mathbf{m})$ at a small number of random realizations of $\mathbf{m}$.

2.4 Predictive modeling of PEG hydrogel to determine χ

In this section, we demonstrate how the presented model calibration approach can be used to determine χ for different PEG hydrogels and then used to predict χ for different processing conditions. The model can later be used to build a general model expressed in (2.1). To determine χ, we concentrate on the *microstructure-property* component of the model whose details are found in the mechanistic model. The unknown quantities are therefore (a) the model parameters $\bar{\bar{\mathbf{m}}} =$

($k'(\rho_x)$) and (b) the internal state variables $\boldsymbol{\xi}^0 = \left(\rho_x^0, \chi^0\right)$. In other words, the internal state variables are treated as model parameters and, referring to the previous section, the vector of model parameters, for a degradable PEG hydrogel becomes $\mathbf{m} = \left(\rho_x^0, \chi^0, k'(\rho_x)\right)$. The key objectives of this section are three-fold. First, we use the model calibration approach to predict the microstructure (or internal state variables) of PEG hydrogel fabricated under different conditions. We then relate processing conditions to microstructure to qualitatively understand the *processing-microstructure* relationship (Fig. 2.1). Second, we shift our focus to degradable hydrogels and use the model calibration approach to (a) quantify model parameters and (b) characterize the evolution of χ and crosslink density during degradation.

We note that for the following to remain within the physical range of parameter values, we restricted the optimization of $\mathcal{R}(\mathbf{m})$ in (2.15) to the values $\rho_x \in [0, 100]$ mM [54] , $\chi \in [0.4, 0.6]$ [96] and $k' \in [0, 0.3]$ (hr^{-1}) [97] based on literature values for PEG in water. The value for χ, however, is expected to be higher because star polymers have been shown to have a χ value higher than their corresponding linear polymer [161, 140]. In addition, the presence of hydrophobic norbornene moieties on the end of the PEG arms will reduce the overall hydrophilicity of the polymer. We note that for fixed choices of process variables $\mathbf{C}$, as described previously, the experimentally observed values $\mathbf{g}$ may be variable from one experiment to another. This variation can arise from slight variations in, for example, the monomer concentration in the final formulation. Such a variability here is accounted for by tuning the values of $\sigma_i^{(k)}$ in (2.15) directly from the experimental data associated with the same realizations of the process parameters $\mathbf{C}$.

2.4.1 Elucidating trends between control parameters and microstructure for PEG hydrogels

For a PEG hydrogel, the control variables consist of thiol to norbornene ratio r and weight percent of the 8-arm PEG norbornene (w), the properties of interest are the equilibrium swelling ratio and compressive modulus measurements and the model parameters reduce to $\mathbf{m} = (\rho_x^0, \chi^0)$.

In this section, we investigate PEG hydrogels in their initial equilibrium swollen state, but prior to degradation. Five independent experiments were performed to investigate the control parameter space, each of which was repeated three times to quantify the uncertainties in the measurement of properties of interest. The results are reported in Fig. 2.7. We explore two cases to determine the parameter $\mathbf{m}$. First under the assumption that the polymer-solvent interaction parameter is unknown but independent of processing conditions and second, under the assumption that this parameter varies with processing conditions.

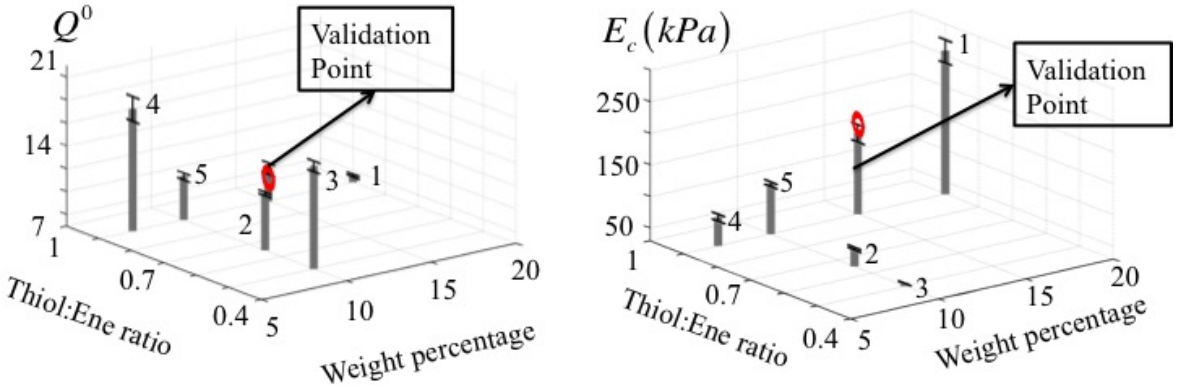

Figure 2.7: Graphical representation of experimental results. A total of five PEG hydrogel designs was processed, for which both the equilibrium swelling ratio and Young's modulus (compression) were determined. For each design, the tests were repeated three times in order to quantify uncertainties in measured quantities of interest (depicted by error bars). Apart from these another PEG hydrogel design is processed to validate the calibration.

Case of an independent polymer-solvent interaction parameter. While the control of cross-link density through processing conditions is, at least qualitatively understood, most studies [76, 96, 98, 164] assume that the polymer-solvent interaction parameter remains independent of formulation, for a PEG hydrogel. Using this assumption as our first hypothesis, for five experiments, we therefore look for six parameters, $\left(\rho_x^0\right)^{(k)}$, $k = 1, \ldots, 5$, and χ_0. In other words, the vector $\mathbf{m}$ becomes $\mathbf{m} = \left[\left(\rho_x^0\right)^{(1)}, \ldots, \left(\rho_x^0\right)^{(5)}, \chi^0\right]$. The cost function (2.15) therefore becomes

$$\mathcal{R}\left(\mathbf{m}\right) = \sum_{k=1}^{5} \left[\left(\frac{E_c^{(k)}\left(\mathbf{m}\right) - e_c^{(k)}}{\sigma_{E_c}^{(k)}} \right)^2 + \left(\frac{Q^{0(k)}\left(\mathbf{m}\right) - q^{0(k)}}{\sigma_{Q^0}^{(k)}} \right)^2 \right], \tag{2.18}$$

where $e_c^{(k)}$ and $q^{0(k)}$ denote the measured compressive modulus and equilibrium swelling ratio for

each experiment. The corresponding standard deviation $\sigma_{E_c}^{(k)}$ and $\sigma_Q^{(k)}$ are computed from the error bars shown in Fig. 2.7. Finally, the model values $E_c^{(k)}(\mathbf{m})$ and $Q^{0(k)}(\mathbf{m})$ are obtained from the surrogate model (See Fig. 2.6).

Upon minimization of $\mathcal{R}$, a map between processing conditions and microstructure could be established (Fig. 2.8), showing a monotonic increase of initial cross-link density with weight percentage and Thiol:ene ratio. However, it is clear that the assumption of an independent polymer solvent interaction parameter results in a poor match between experimental and modeling results (Fig. 2.8a), especially for extreme behaviors, i.e. either low cross-linked gels (large swelling ratio) or highly cross-linked gels (low swelling ratio). This observation implies that the polymer-solvent interaction parameter should in fact be dependent on the gel processing.

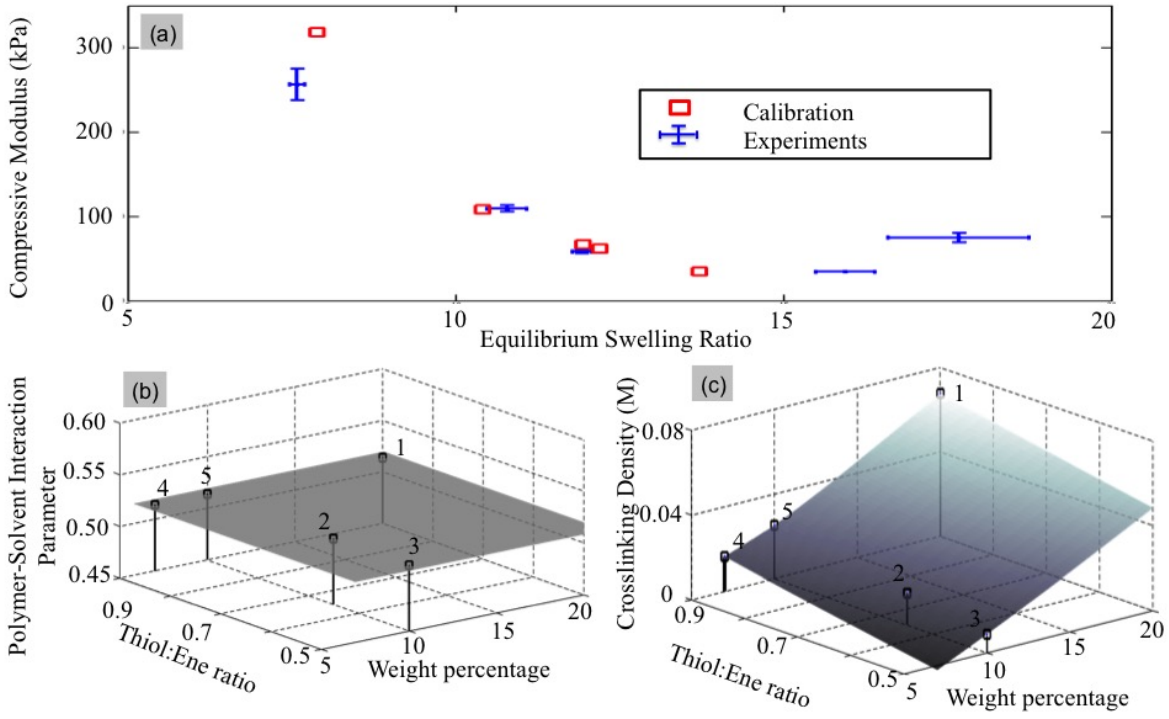

Figure 2.8: Minimization of the cost function (2.18) for an independent polymer-solvent interaction parameters: (a) Distance between experimental and model predictions in the $(Q^0 - E_c)$ space, (b) Value of the polymer-solvent interaction parameters as a function of control parameters, and (c) Initial cross-link density in terms of control parameters.

Case of a dependent polymer-solvent interaction parameter. Based on the above obser-

vations, we now let the parameter χ^0 vary in the physical range $[0.4, 0.6]$ for each independent experiment. The new cost function therefore takes the same form in (2.18), with the difference that χ^0 is now allowed to vary between independent experiments, that is, the parameter vector $\mathbf{m}$ takes the form $\mathbf{m} = \left[\left(\rho_x^0\right)^{(1)}, \ldots, \left(\rho_x^0\right)^{(5)}, \left(\chi^0\right)^{(1)}, \ldots, \left(\chi^0\right)^{(5)}\right]$. Fig. 2.9 shows an improved fit between experimental points and model findings. This result suggests that the polymer-solvent interaction parameter is dependent of the control parameters as depicted in Fig. 2.9(b). Interestingly, the model is highly sensitive to this parameter as slight variations in χ^0 lead to fairly large differences in swelling ratio and Young's modulus. Furthermore, the model can describe χ^0 for a given set of monomers, as a function of weight percentage of the 'ene' monomer and Tiol:Ene ratio. In particular, the model predicts that for a given Thiol:Ene ratio, an increase in weight percentage of the 'ene' monomer, and thus in polymer volume fraction, leads to higher χ^0 values.

The dependence of χ^0 on the polymer volume fraction is consistent with reports in the literature for other polymer and solvent combinations [77, 116, 119]. However, when the Thiol:Ene ratio is varied for a given wt% of 'ene' monomer, the effects of the processing parameters on χ^0 is more complicated. For example, point 2 (referring to the processing parameters of 10wt% of the 'ene' monomer and a Thiol:Ene ratio of 0.65) and point 5 (referring to the processing parameters of 10wt% of the 'ene' monomer and a Thiol:Ene ratio of 0.9), the χ^0 values are distinctly different at 0.516 and 0.510, respectively. This is counterintuitive as the latter has a higher polymer volume fraction, arising from the higher Thiol:Ene ratio, yet the value of χ^0 is lower. However, variations in the Thiol:Ene ratio for a given wt% of the 'ene' monomer will lead to changes in the chemistry of the polymer. For example the Thiol:Ene ratio will influence the number of unreacted arms endcapped with norbornene moieties and the number of reacted enes with norbornane flanked with PEG chains on both sides. In addition, the presence of dangling chain ends has been proposed to lead to higher χ^0 value owing to the fact that they effectively occupy additional space in the hydrogel [119]. While the exact relationship between the chemistry and molecular structure on χ^0 for these types of PEG hydrogels has not been studied in detail, it would not be surprising that

small changes to the chemistry and/or structure could have a significant influence on χ^0.

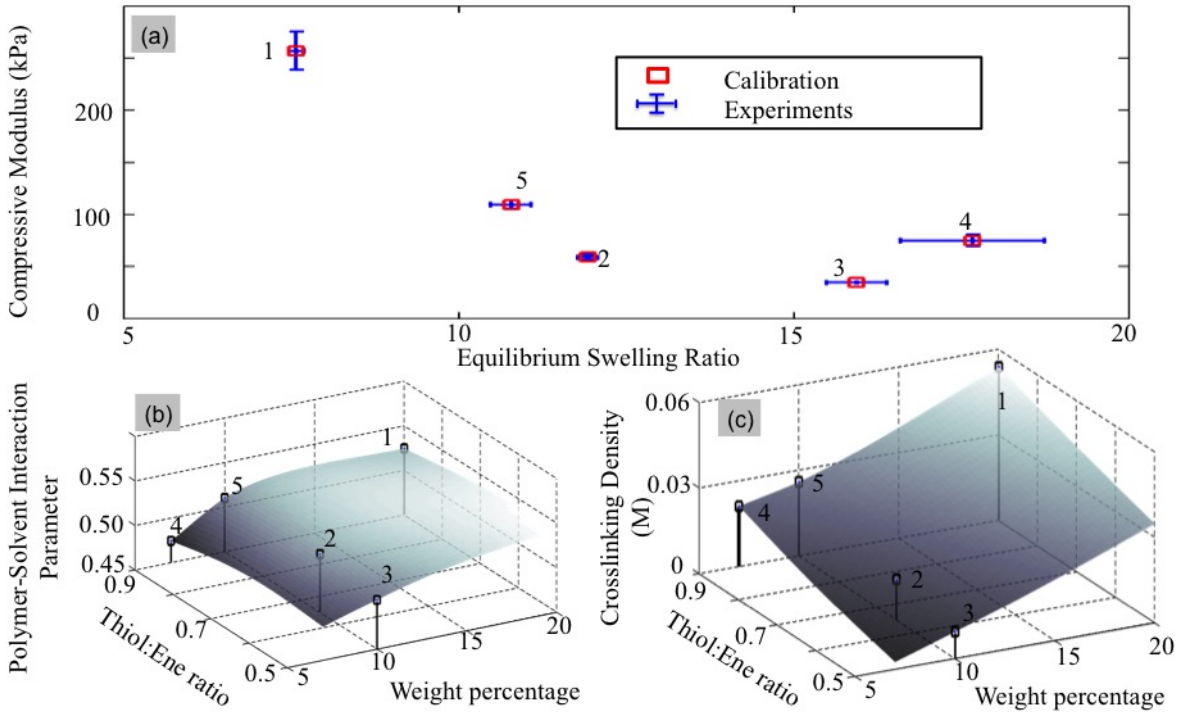

Figure 2.9: Minimization of the cost function (2.18) for a dependent polymer-solvent interaction parameter: (a) Distance between experimental and model predictions in the $(Q^0 - E_c)$ space, (b) Values of the polymer-solvent interaction parameter as a function of control parameters and (c) Initial cross-link density in terms of control parameters.

2.4.2 Model Validation

We now discuss the calibration results and the validity of the resulting model. For this, we chose a random point in the control space, corresponding to a Thiol:Ene ratio and Weight percentage of the ene monomer of 0.9 and 15, respectively (Fig. 2.7). These values were then located in the maps of Fig. 2.9(b) and 2.9(c) in order to determine a corresponding cross-link density of $\rho_x = 0.035\ M$ and polymer-solvent interaction parameter of $\chi = 0.516$. We then used these values in equations (2.11),(2.12) and (2.14) to determine the equilibrium swelling ratio and Young's modulus of the processed gel ($Q = 9.32$ and $E_c = 172.5\ kPa$). To verify whether

this predicted value was corroborated with experimental data, this gel was processed and tested experimentally. The comparison between prediction and experiment are depicted in Fig. 2.10. We find that, even with only five calibration points, the model prediction manages to be within ranges of the experimental measurements. We note, however, that the experimental data limits the development of a robust relationship for an extended parameter space.

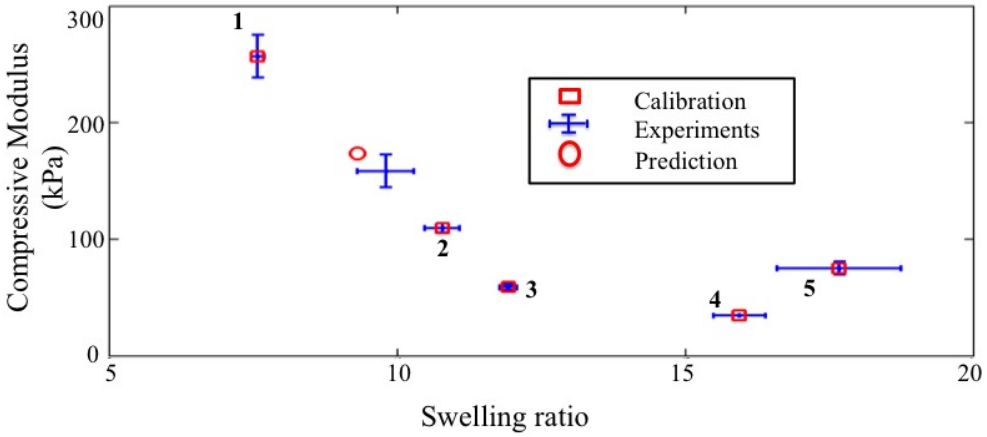

Figure 2.10: Model validation. For a given hydrogel formulation (validation point in Fig.2.7), the map shown in Fig 2.9 was used to determine the cross-link density and polymer-solvent interaction parameters that lead to the compressive modulus and swelling ratio shown here for the validation point. Experiments for this gel formulation were also performed and compared with the prediction. We show here both calibration and validation points in the E_c-Q^0 space.

2.4.3 Quantifying the polymer-solvent interaction parameter during hydrolytic degradation of PEG hydrogels

We extend our analysis to PEG hydrogels that are degrading ($\eta = 1$). We specifically seek to determine the relationship between the kinetic constant k' and the cross-link density (see Eq. (2.9)) and understand whether the polymer-solvent interaction parameter for a given set of processing conditions changes during degradation. For this, we experimentally investigated hydrogel degradation by measuring changes in swelling ratio and compressive modulus in time. The tests were performed at the initial time and repeated three times at intervals of one hour ($t = t_1, t_2, t_3$

and t_4 in our analysis). Two degradation kinetics were considered at a pH of 9 and 11. Data are shown in Fig. 2.11. Once again, our study is divided into two parts, each based on the assumption that the parameter χ is (a) constant and (b) changes with degradation.

Case of a non-evolving polymer-solvent interactions parameter. In this case, the parameter χ is unknown but assumed to be independent of cross-link density. The parameter vector is therefore $\mathbf{m} = \left[\rho_x^0, k'(t_k)^{(p)}, \chi^0\right]$ where the index $k = 1, \ldots, 4$ denotes the discrete measurement times and the index $p = 1, 2$ spans the two degradation kinetics. The cost function becomes

$$\mathcal{R}(\mathbf{m}) = \sum_{p=1,k=1}^{2,4} \left[\left(\frac{E_c^{(p)}\left(t_k, \mathbf{m}\right) - e_c^{(p)}(t_k)}{\sigma_E^{(p)}(t_k)} \right)^2 + \left(\frac{Q^{(p)}\left(t_k, \mathbf{m}\right) - q^{(p)}(t_k)}{\sigma_Q^{(p)}(t_k)} \right)^2 \right], \tag{2.19}$$

where $e_c^{(p)}(t_k)$ and $q^{(p)}(t_k)$, are respectively, experimental observations of $E_c^{(p)}(t_k)$ and $Q^{(p)}(t_k)$. Minimization of this function leads to the model prediction represented by circle and squares in Fig. 2.11(a) and (b). The best match between experiments and modeling was found for a polymer-solvent interaction parameter of 0.52 (Fig. 2.11(c)) and relation between k' and ρ_x shown in 2.11(d)). We observe that for the faster degradation rate ($pH = 11$), the kinetic constant decreases linearly with cross-link density while this is not the case when $pH = 9$. We also note that a poor match is observed for longer degradation times, either for compressive modulus or swelling ratio, depending on the experiment. This seems to imply that once again, our assumption of a non-evolving polymer-solvent interaction parameter does not capture the hydrogel physics.

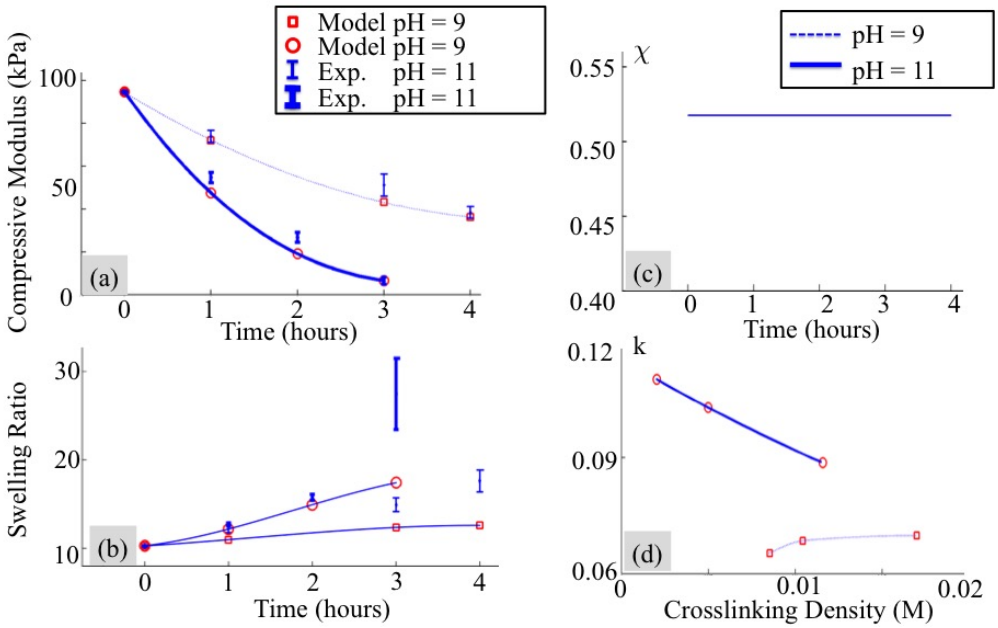

Figure 2.11: Experimental measurements and optimized model fitting assuming a constant value of the polymer-solvent interaction parameter during degradation. Evolution of (a) the compressive modulus and (b) the swelling ratio of a hydrogel immersed in aqueous solutions at pH of 9 and 11. (c) Predicted polymer-solvent interaction parameter and (d) change in kinetic coefficient with respect to the crosslinking density during degradation.

Case of an evolving polymer-solvent interaction parameter. To examine a changing χ during degradation, we let its magnitude vary in time between experiments in the physical range $[0.4, 0.6]$. The new cost function is now augmented by a different value of χ for all experiments and all testing times. This leads to $\mathbf{m} = \left[\rho_x^0, k'(t_k)^{(p)}, \chi^0(t_k)^{(p)}\right]$, the index being unchanged from the above analysis. Besides the change in the definition of $\mathbf{m}$, the cost function remains the same as given in (2.19). We see in Fig. 2.12(a),(b) that minimization of this function leads to a near perfect match between experimental results and predictions. It was found that the polymer-solvent interaction parameter and degradation kinetic constant both depend on the control parameters and the evolving hydrogel structure (crosslink depletion) during degradation in a nonlinear fashion (as shown in Figs. 2.12 (c) and (d)). We also show that the degradation constant is still a decreasing function of the cross-link density for $pH = 11$ and remains rather constant for $pH = 9$ (Fig.

2.12(d)).

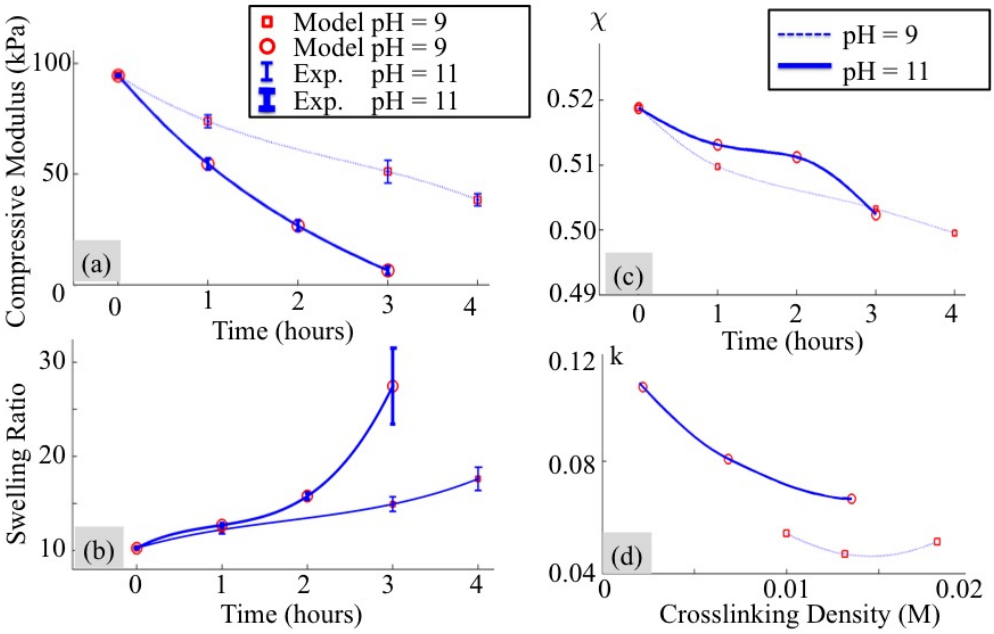

Figure 2.12: Experimental measurements and optimized model fitting for a variable Flory-Huggins parameter during degradation. Evolution of (a) the compressive modulus and (b) the swelling ratio of a hydrogel immersed in aqueous solutions at pH of 9 and 11. (c) predicted change in polymer-solvent interaction parameter and (d) kinetic constant with respect to the crosslinking density during degradation.

2.5 Summary and concluding remarks

To summarize, we have derived a self-learning simulation approach that integrates a mechanistic material's model to experimental data with the goal of fitting its unknown parameters and refine its structure. This approach provides a unique way to evaluate the value of material's parameters and internal state variables that are usually challenging to measure experimentally. We applied this methodology in order to better understand the complex behavior of PEG hydrogels and its relation to processing conditions. Based on the well-known Flory's theory [46], our objective was to shine a light on the relationship between cross-link density, polymer-solvent interaction parameter

and degradation with processing conditions and degradation. It was found that the polymer-solvent interaction parameter and degradation kinetic constant both depend on the control parameters and the evolving hydrogel structure during degradation in a nonlinear fashion. Our findings for PEG hydrogels support a growing body of literature describing that the polymer-solvent interaction parameter is indeed more complicated and varies with a number of polymer factors such as polymer volume fraction and subtle changes in the polymer chemistry. For instance, the polymer structure and even temperature [72] may affect the affinity of hydrogen bonds between water molecules and polymer chains [157]. Such effects have not been investigated in the present study due to the lack of available data. A better understanding of these is left for the future studies however, in which new experiments can be designed to investigate each factor explicitly.

The analysis is then extended to degrading PEG hydrogels and showed that χ also varies during degradation as the structure of the hydrogel evolves over time. While others have shown that the degradation kinetic constant for hydrolysis of PEG hydrogels varies with initial cross-link density[99, 111], we demonstrate that this kinetic constant dynamically changes during degradation as a result of the evolving hydrogel structure. The self-learning simulation approach offers a method to predict the values of χ and k' for a given set of monomers without requiring an in-depth knowledge of the relationship between these two parameters and the hydrogel, which would otherwise be difficult to achieve experimentally. For example variations in the polymer volume fraction encompass subtle changes in chemistry, making it difficult if not impossible to isolate. Overall, this self-learning simulation approach will improve our ability to design hydrogels by better predicting the processing conditions required to achieve a set of targeted material properties.

One final note, we acknowledge that our approach is based on a small amount of experimental data, but we have shown that even in this situation, the approach can do reasonably well at predicting the hydrogel behavior from its processing conditions. In the future, however, the self-learning methodology will allow the model to increase its accuracy and predicting power through a fast processing of a larger number of experimental data that can be added over time. More complex

materials (composites, tissue scaffolds) could also be investigated by combining this approach to full 3-dimensional finite element analysis. Efficiency will also be improved by integrating Bayesian methods [112] into the statistical description of the problem.

2.5.0.1 Experimental Section

Materials: The ene macromolecular monomer, 8-arm PEG norbornene was synthesizd from 8-arm PEG hexaglycerol (JenKem Technology) with a molecular weight of 10,000 g/mol following previously published protocols[43]. ^{1}H NMR was used to confirm that approximately 92% of the arms were functionalized with norbornene following previously published methods[54]. The thiol macromolecular monomer, PEG dithiol with a molecular weight of 1000 g/mol, was purchased (Sigma-Aldrich) and used as received. Hydrogels were formed by mixing the 'ene' and thiol monomers with 0.05% (g/g) photoinitiator (Irgacure 2959, BASF) in water and exposing to 365 nm light at 5 mW/cm^2 for 7 minutes. The Thiol:Ene ratio was varied from 0.5 to 0.9 and the weight percent of the 'ene' monomer was varied from $7 - 20\%$ (g/g). Cylindrical specimens (5mm height and 5mm radius) are prepared for testing.

Hydrogel Degradation: Hydrogels showed no signs of degradation in water (up to one week). Hydrogels that were pre-swollen in water were placed in a large bath of either 1 M or 2 M sodium hydroxide for up to four hours. The pH of each solution was determined to be 9 and 11 using an electronic pH meter. After each hour, hydrogels were removed from solution, rinsed multiple times in water for 15-30 minutes prior to measuring swollen mass, the dry polymer mass and the compressive modulus.

Methods of Measurements: Hydrogels were allowed to swell to equilibrium in water over night at room temperature to measure the initial hydrogel properties. For degrading hydrogels, the hydrogels at varying time points were placed in water prior to measuring the properties. For each hydrogel, the swollen hydrogel was weighed to determine the equilibrium swollen mass M_s. The hydrogel was lyophilized to remove the water and re-weighed to determine the dry polymer mass

M_d. The volumetric equilibrium swelling ratio Q was computed as[33]

$$Q = 1 + \frac{\rho_{peg}}{\rho_{sol}} \left(\frac{M_s}{M_d} - 1 \right). \tag{2.20}$$

where the densities were assumed to be 1.07 g/cm^3 and 1 g/cm^3 for the polymer (ρ_{peg}) and solvent (ρ_{sol}), respectively. A sample size of 3 was used. The data are reported as average with standard deviation as error bars.

The modulus was determined on swollen hydrogels by testing the cylindrical specimen under unconfined compression up to 15% strain at a rate of 0.5 mm/min (MTS Synergie 100, 10 N). A sample size of 3 was used. The data are reported as average with standard deviation as error bars.

Chapter 3

Tuning Reaction and Diffusion Mediated Degradation of Enzyme-Sensitive Hydrogels

3.1 Introduction

Synthetic-based hydrogels containing peptide crosslinks that degrade by cell-mediated mechanisms are promising platforms for cell encapsulation and tissue regeneration. To date, there has been significant progress toward demonstrating the feasibility of this type of hydrogel platform for a wide range of tissue engineering applications [90, 13, 123, 82, 136]. However, selecting a hydrogel design a priori to achieve desired hydrogel properties that evolve in space and time is challenging. Soft hydrogels (e.g., ≤ 1 kPa) are often employed such that a relatively low enzyme concentration is required to locally cleave the hydrogel crosslinks [90, 134]. However, in a low crosslinked hydrogel, enzymes can readily diffuse leading to a combination of local and bulk degradation of the hydrogel, resulting in unpredictable changes in the hydrogels macroscopic properties (e.g., transport and mechanics). Controlling the macroscopic properties of the hydrogel is particularly important given that cells sense and respond to their extracellular environment, which can influence their phenotype and function[74, 122]. In addition, successful translation of these materials in vivo will require control over the hydrogel properties to enable, for example, continuous mechanical integrity while simultaneously supporting tissue development. Given the promise of enzyme-sensitive hydrogels for cell encapsulation, a better understanding of their degradation behavior and the key parameters that control local and bulk degradation is needed.

Designing such a hydrogel whose crosslinks are sensitive to cell-secreted enzymes presents a

design challenge that is characteristic of classic reaction-diffusion systems. Enzymes are synthesized by embedded cells, released on their boundary and later transported into the extracellular space. On the one hand, enzyme diffusion through the hydrogel is dictated by the relative size of the enzyme compared to that of the polymer mesh. On the other hand, enzymes react with their substrate (i.e., the hydrogel) and as crosslinks are cleaved, hydrogel degradation proceeds. A competition therefore exists between the characteristic times of enzyme diffusion and enzyme reaction with its substrate. If the former dominates, enzymes will readily diffuse through the hydrogel and degradation will be characteristic of a bulk degrading hydrogel. If the latter dominates, enzymes react immediately with their substrate leading to a highly localized degradation in the immediate vicinity of the cell with minimal bulk degradation. Understanding how design parameters influence this competition will thus be critical to tuning and controlling the dynamics of hydrogel degradation.

Herein, we introduce a combined experimental and theoretical approach to identify key design parameters that control reaction-diffusion degradation mechanisms in an enzyme sensitive hydrogel that is being degraded by embedded cells (Figure 3.1 A). We employed a multiphasic mixture model that we have previously developed and applied to poly(ethylene glycol) (PEG) hydrogels [34, 154, 2]. We investigated a hydrogel platform based on a thiol-norbornene PEG hydrogel system with peptide crosslinks comprised of the collagenase-sensitive peptide VPLS-LYSG (Figure 3.1 B) [43, 3]. The enzyme used in this study was a commercially available collagenase blend. We first calibrated and validated our model with a simple 1D experimental system (Figure 3.1 C) and then applied it to a more complex 3D experimental hydrogel system mimicking enzyme-releasing cells (Figure 3.1 D). The governing equations in the mathematical model are given in the appendix. Once calibrated and validated, the model was nondimensionalized to identify key dimensionless quantities whose magnitude can describe the role of enzyme (e.g., size), hydrogel (e.g., initial crosslink density), and kinetics of the enzyme-substrate pair (i.e., MichaelisMenten) on the complex behavior of hydrogel degradation in time and space. The new dimensionless quantities can then serve as a guide for predicting and ultimately tuning the spatiotemporal hydrogel degradation behavior for a given application.

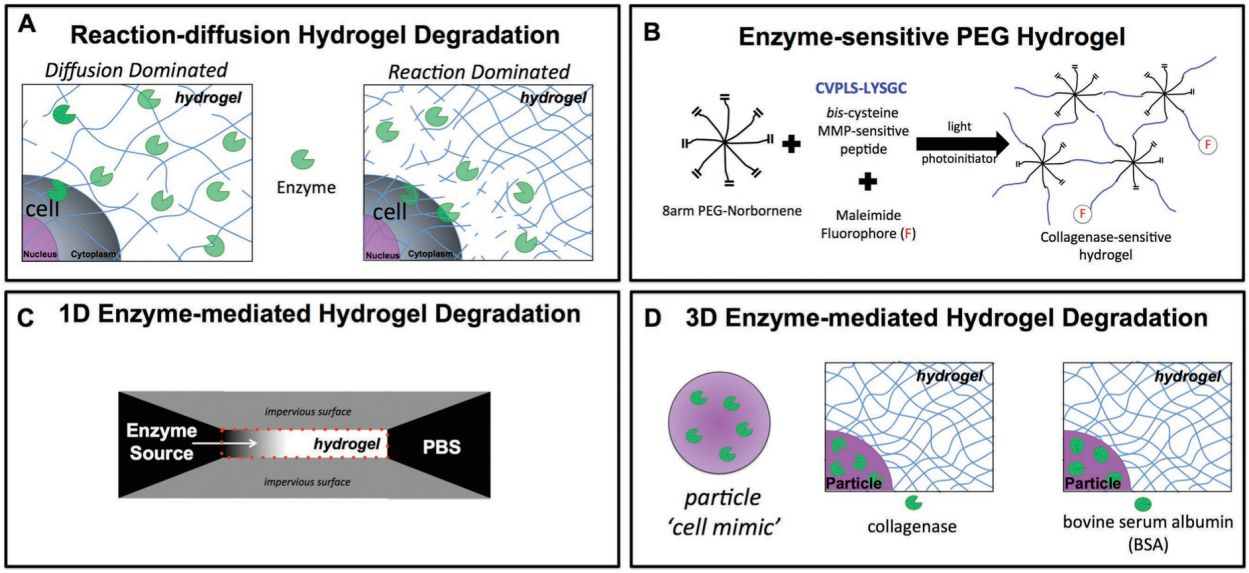

Figure 3.1: *(A) Schematic (left) represents diffusion-dominated hydrogel degradation where enzymes readily diffuse away from the encapsulated cell while simultaneously cleaving the crosslinks. Schematic (right) represents reaction-dominated hydrogel degradation where enzyme diffusion is restricted and/or enzymes are highly reactive to their substrate leading to hydrogel degradation immediately surrounding the encapsulated cell, leaving the bulk hydrogel in its original state. (B) Schematic of the enzyme-sensitive poly(ethylene glycol) (PEG) hydrogel used in the study, which is fabricated by photopolymerization of an 8 arm PEG functionalized with norbornene and a bis-cysteine peptide that is sensitive to collagenases. The hydrogel was fluorescently labeled by introducing a maleimide fluorophore, which reacts with pendant thiols. (C) Schematic of the 1D experimental system for studying enzyme-mediated hydrogel degradation. (D) Schematic of the 3D experimental system for studying enzyme-mediated hydrogel degradation whereby enzyme-loaded microparticles serve as cell-mimetics, which release enzymes with time but are not complicated by deposition of extracellular matrix.*

3.2 Assessment degradation-diffusion parameters in 1D experiments

We first applied the 1D experimental set-up (Figure 3.1 C) to study degradation of enzyme-sensitive PEG hydrogels where the initial hydrogel crosslink density and enzyme concentration were

Table 3.1: Three hydrogels with differing enzyme concentrations were investigated with their properties of: enzyme concentration (C_e^o), which was maintained throughout the experiment, network connectivity (β), initial volumetric swelling ratio (Q^0), initial compressive modulus (E^0), polymer-solvent interaction param- eter (χ), and initial crosslink density in the swelling solvent (i.e., phosphate buffered saline ($\rho_x^{s,0}$).

Low Crosslink Hydrogel			Indertmediate Crosslink Hydrogel			High Crosslink Hydrogel		
C_e^0	25	ng· ml^{-1}	C_e^0	200	ng· ml^{-1}	C_e^0	1000	ng· ml^{-1}
β_{ideal}	0.535	–	β_{ideal}	0.423	–	β_{ideal}	0.378	–
Q^0	34.5±3	–	Q^0	13.3±0.3	–	Q^0	6.9±0.1	–
E^0	1.4 ± 0.3	kPa	E^0	65 ± 5	kPa	E^0	191 ± 4	kPa
χ	0.509	–	χ	0.509	–	χ	0.509	–
$\rho_x^{s,0}$	13.7	μM	$\rho_x^{s,0}$	1300	μM	$\rho_x^{s,0}$	6500	μM

varied (Table 3.1). The PEG hydrogel was labeled with a fluorescent molecule (as shown in Figure 3.1 B) to monitor changes to the hydrogel over time and in particular to identify the point when the hydrogel reaches reverse gelation. Reverse gelation refers to the point when a critical number of crosslinks have been cleaved and the hydrogel transitions from a crosslinked solid polymer (i.e., fluorescent regions) to a soluble polymer where the polymer chains rapidly diffuse out into the bath (i.e., nonfluorescent regions). This critical point is correlated to the degree of network connectivity during hydrogel formation (i.e., the gel point), which has been described for an ideal network using a statistical network formation model (equation (B2), appendix)[103]. Experimentally, we observe a degradation front where the region of the hydrogel adjacent to the enzyme source is completely degraded, which advances along the length of the hydrogel, away from the enzyme source over time. By measuring the distance of the front as a function of time, front velocities were determined for each hydrogel system (Figure 3.2). The hydrogel with the fewest crosslinks that must be cleaved to reach reverse gelation (i.e., low crosslink hydrogel) exhibited the fastest front velocity (Figure 3.2 i,iv,v). On the other hand, the hydrogel with the most number of crosslinks that must be cleaved to reach reverse gelation exhibited the slowest front velocity (Figure 3.2 iiiv). Although the enzyme concentration was higher with increasing initial crosslinking, the enzyme concentration was not sufficient to overcome the higher number of crosslinks that had to be cleaved to reach velocities similar to the low crosslink hydrogel.

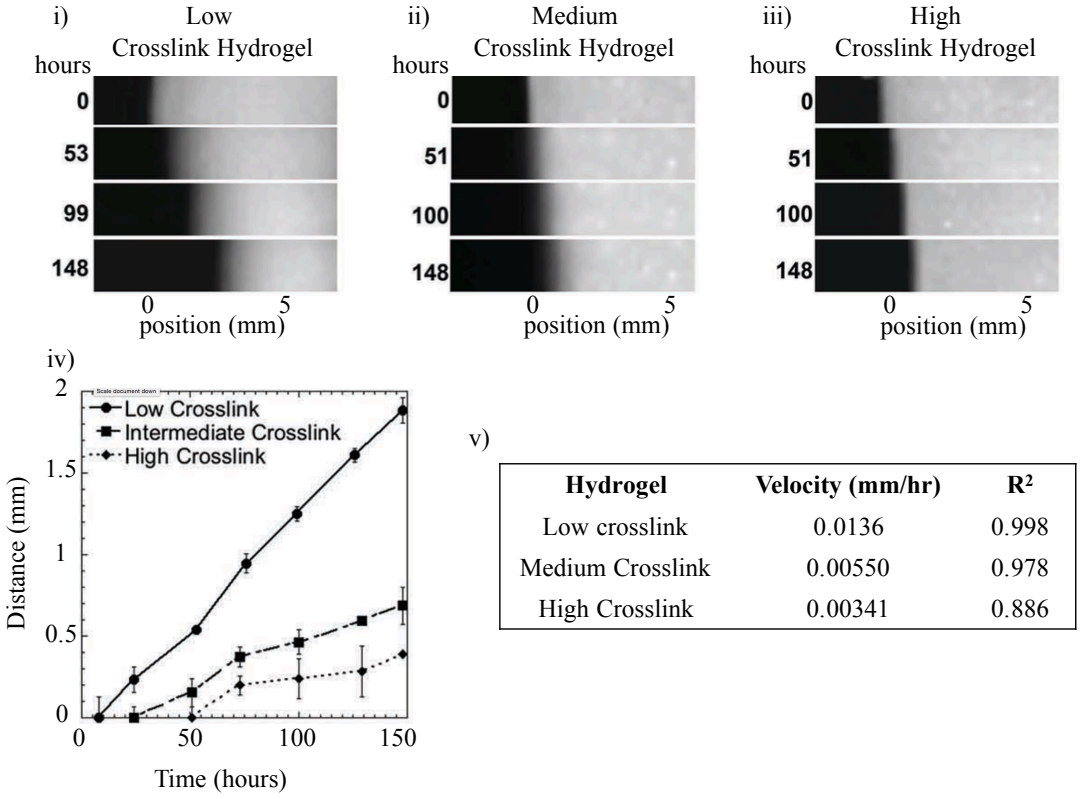

v)

Hydrogel	Velocity (mm/hr)	R^2
Low crosslink	0.0136	0.998
Medium Crosslink	0.00550	0.978
High Crosslink	0.00341	0.886

Figure 3.2: *Characterization of hydrogel degradation in 1D. Using the experimental set-up described in Figure 1C, fluorescent images are shown for each hydrogel case as a function of time whereby position 0 mm indicates the initial edge of the hydrogel prior to degradation (i, ii, iii). The enzyme source is located to the left of the hydrogel. The front, corresponding to reverse gelation, can be observed advancing away from the initial position (i.e., 0 mm) of the hydrogel over time. The velocity of the front was determined by plotting distance of the front as a function of time and using a linear fit (n = 3, data are mean with standard deviation as error bars) (iv, v).*

The computational model was fit to the experimental front velocity data (Figure 3.3 v,vi) by varying enzyme radius, hydrogel connectivity, and reaction kinetics with realistic constraints (see appendix). Initial values for hydrogel, based on experimentally determined equilibrium swelling ratio and compressive modulus, were used as inputs to the model to estimate the initial crosslink density in a nonsolvent using FloryRehner and Rubber elasticity theories [47] and the self learning algorithm (presented in the previous chapter) to estimate the polymer-solvent interaction parameter

[2]. The computational model was able to capture the experimental front velocity using an average enzyme radius of 8.5 nm and values for the MichaelisMenten kinetic constants, k_{cat} with a value of $2s^1$ and K_m with a value of 120×10^6 M, which were used for all hydrogel crosslink cases. The value for network connectivity (β) was varied independently for each hydrogel case (Figure 3.3 iiii) and assumed to be higher than the ideal value of β (Table 3.1) due to crosslinking imperfections (e.g., cyclization and dangling ends). Overall, we demonstrate that the computational model is able to capture the experimentally determined front velocities for each of the hydrogel cases.

In addition to front velocity, a second characteristic feature of the spatiotemporal degradation behavior of these hydrogels is the width of the front. The width of the front is defined as the distance from the point of reverse gelation (i.e., $\rho_x = 0$) near the enzyme source to the point where the gel is at its initial crosslink density (i.e., $\rho_x = 0.99\rho_x^0$). In the case where reaction dominates diffusion, the width of the front is narrow and the crosslink density of the bulk hydrogel is similar to the initial crosslink density prior to degradation. On the contrary, when diffusion dominates reaction, the width of the front becomes very large. For gels of finite thickness, this condition results in an overall decrease in crosslink density of the bulk hydrogel (i.e., bulk degradation). Using the same parameters identified for the simulations that match front velocity, the model was used to describe crosslink density as a function of distance away from the enzyme source over time (Figure 3.3 viviii). In the low crosslinked hydrogel case, a wide front that propagates quickly is observed resulting in an overall decrease in the crosslink density of the bulk hydrogel for finite distances (e.g., at 5 mm) (Figure 3.3 vi). In the intermediate and high crosslink hydrogel cases, a sharp front is observed and the initial bulk hydrogel properties are largely maintained (Figure 3.3 vii,viii). We demonstrate that the model is able to capture the propagating front and front width, especially for the intermediate and high crosslink hydrogel cases (**Figure B4, appendix**). However due to limitations in the experimental set-up, the fluorescence in the low crosslinked hydrogel does not directly correlate to crosslink density and therefore the front width could not be matched to the model (**see Figure B4, appendix**). Nonetheless, the model can be used to describe the spatiotemporal changes in crosslink density for each of the three hydrogel cases.

i) Low Crosslink Hydrogel

Parameter	Value	Unit
β	0.74	--
r_s	8.5	nm
k_{cat}	2	s^{-1}
K_m	120	μM

ii) Medium Crosslink Hydrogel

Parameter	Value	Unit
β	0.52	--
r_s	8.5	nm
k_{cat}	2	s^{-1}
K_m	120	μM

iii) High Crosslink Hydrogel

Parameter	Value	Unit
β	0.678	--
r_s	8.5	nm
k_{cat}	2	s^{-1}
K_m	120	μM

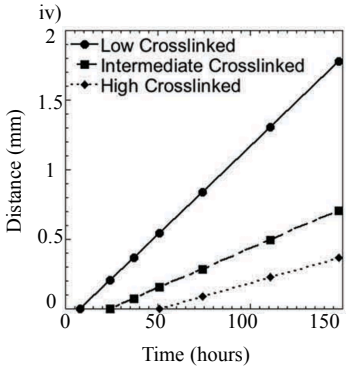

v)

Hydrogel	Velocity (mm/hr)
Low Crosslink	0.0127
Medium Crosslink	0.0057
High Crosslink	0.0038

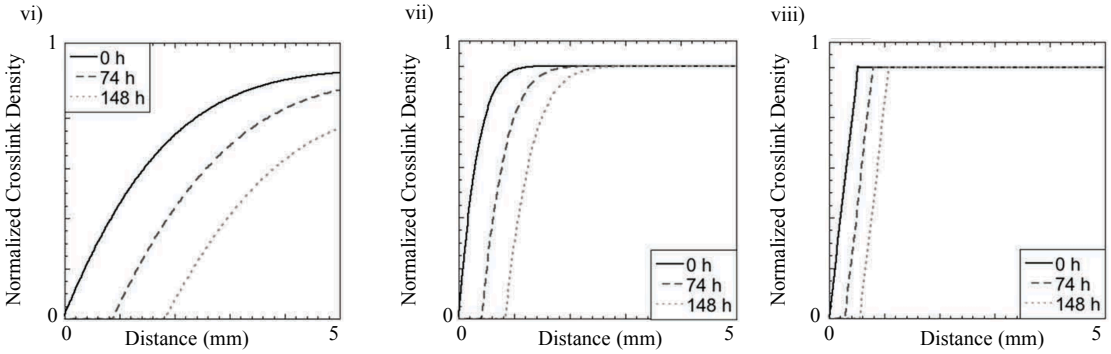

Figure 3.3: *Characterization of hydrogel degradation in 1D. The mathematical model was fit to the experimental data by varying network connectivity (β), radius of active enzyme (r_e), and the MichaelisMenten kinetic constants (k_{cat} and K_m), which are unknowns (i, ii, iii). The propagating front (distance versus time) and the corresponding velocity are shown for each hydrogel case (iv, v). In addition, spatiotemporal pattern of crosslink den- sity as a function of distance away from the enzyme source are shown for each crosslink hydrogel case for the initial time prior to degradation and after 74 and 148 h (vi, vii, viii). The initial variation in cross- link density was determined from the experimental system (at time 0), which arises from unconfined swelling at the edges of the hydrogel.)*

We next extended the experimental and computational analysis to 3D, using a low and high crosslinked hydrogel with formulations given in Table B1 and initial properties in Table 3.2. Experimentally, we developed a cell-mimetic platform (Figure 3.1 C) using collagenase-loaded PLGA microparticles encapsulated in the enzyme-sensitive PEG hydrogel. Prior to encapsulation, release

of collagenase from the microparticles was characterized by a rapid burst release followed by a slow yet sustained release of enzyme (Figure B5, appendix). This release profile, as a function of time, was input into the computational model to demonstrate the models capability of incorporating complex enzyme release profiles. Hydrogels were encapsulated with either collagenase-loaded microparticles or BSA-loaded microparticles and the spatiotemporal degradation behavior and macroscopic properties were evaluated over time. In the low crosslinked hydrogel, bulk degradation was evident by a rapid and overall decrease in hydrogel fluorescence (Figure 3.4 i,ii). Further, the compressive modulus (Figure 3.4 iii) decreased exponentially while the hydrogel wet weights (Figure B6, appendix) increased over time, consistent with the occurrence of bulk degradation. Simulations showed similar findings with respect to a diffuse boundary surrounding the cell-mimetic and a rapid loss in the compressive modulus of the bulk hydrogel (Figure 3.4 iv,v). On the contrary in the high crosslink hydrogel, degradation appeared to be restricted more locally in the region immediately surrounding the cell-mimetic. This observation is supported by the following results: (a) the hydrogel fluorescence was largely maintained over time, but the size of the nonfluorescent regions (originally correlating to the microspheres, which exhibited a distribution of sizes) increased statistically with time (Figure 3.5 iiii), (b) the compressive modulus decreased over time, but the change was gradual (Figure 3.4 iv), and (c) hydrogel wet weights were maintained over time (Figure B6, appendix). Simulations showed similar results with a relatively sharp boundary surrounding the cell-mimetic and a modulus that gradually decreased over time (Figure 3.4 v,vi). In addition, dual labeling of the hydrogel and enzyme qualitatively showed the spatiotemporal distribution of the hydrogel and enzyme over time, further supporting the above observations (Figure B7, appendix).

Table 3.2: Two hydrogels with the same microparticles were investigated with their properties of: initial volumetric swelling ratio (Q^0), initial compressive modulus (E^0), polymer-solvent interaction parameter (χ), network connectivity (β) as determined by the model, and initial crosslink density in the swelling solvent (i.e., phosphate buffered saline) ($\rho_x^{s,0}$).

Low Crosslink Hydrogel			High Crosslink Hydrogel		
Q^0	15.1±0.1	–	Q^0	7.4±0.3	–
E^0	38 ± 0.9	kPa	E^0	129 ± 17	kPa
β_{ideal}	0.7	–	β_{ideal}	0.7	–
χ	0.509	–	χ	0.509	–
$\rho_x^{s,0}$	700	μM	$\rho_x^{s,0}$	4300	μM

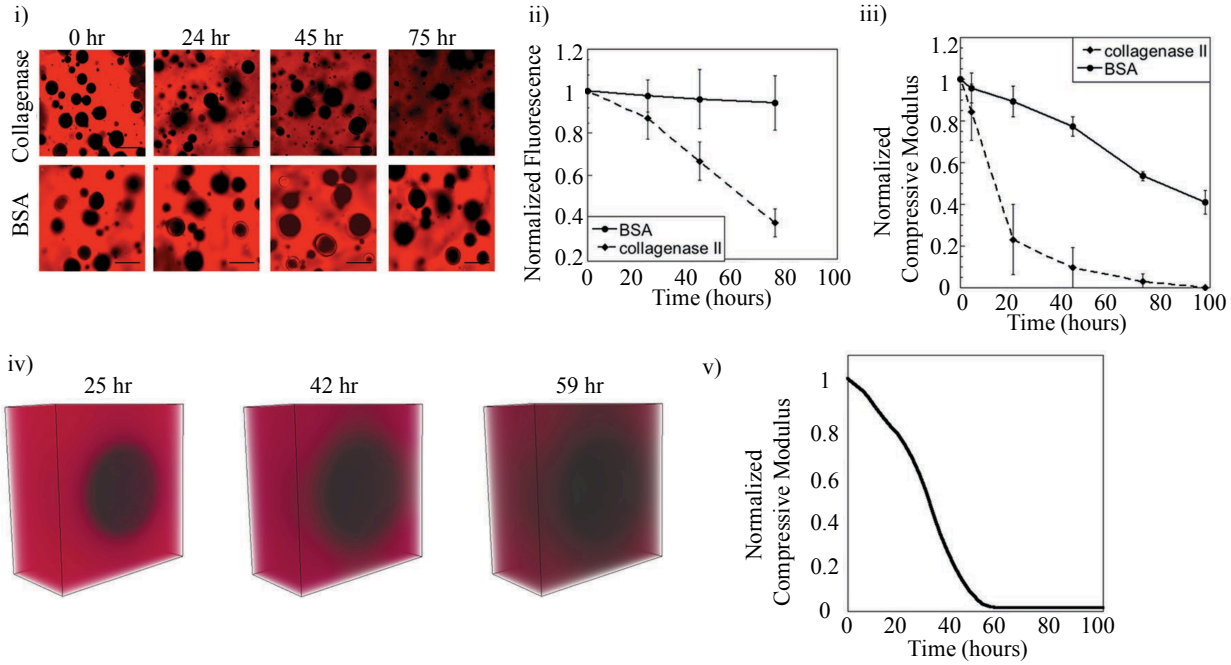

Figure 3.4: *Characterization of hydrogel degradation in 3D. In experiments, the set-up described in Figure 1D was used with a fluorescently labeled (red) hydrogel. In simulations, the enzyme radius and MichaelisMenten kinetic constants determined in the 1D experiments were used and the hydrogel was labeled red. Degradation of the low crosslink hydrogel is shown by representative confocal microscopy images of the hydrogel with void spaces (i), which at 0 h correspond to the microparticles. Over time, the overall fluorescence (ii) decreased as well as the compressive modulus (iii) for the hydrogel containing the collagenase-loaded microparticles. Hydrogels with BSA-loaded microparticles showed no change in overall fluorescence (ii) and a slow decrease in the compressive modulus (iii), corresponding to degradation of the microparticles. Simulation results matched experiments showing a diffuse front surrounding the microparticles (iv) and a rapid loss in the compressive modulus (v).*

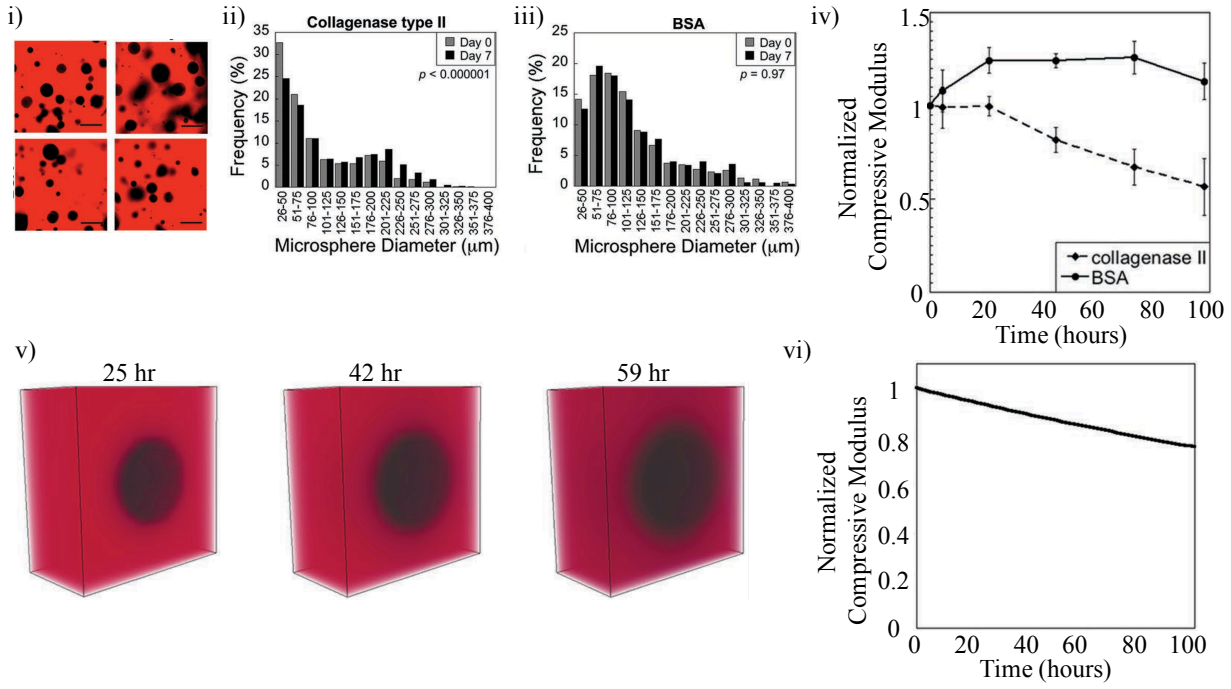

Figure 3.5: *Characterization of hydrogel degradation in 3D. In experiments, the set-up described in Figure 1D was used with a fluorescently labeled (red) hydrogel. In simulations, the enzyme radius and MichaelisMenten kinetic constants determined in the 1D experiments were used and the hydrogel was labeled red. Degradation of the high crosslink hydrogel is shown by representative confocal microscopy images of the hydrogel with void spaces (i), which at 0 h correspond to the microparticles. Over time, the overall fluorescence was maintained, but the void spaces became significantly larger in the hydrogel containing the collagenase-loaded microparticles, as shown in the histogram plot (ii). Hydrogels with BSA-loaded microparticles showed no change in the size of the voids, as shown in the histogram plot (iii). Statistical analysis was performed using a nonparametric KolmogorovSmirnov test* ($\alpha = 0.05$, $n = 8001300$)*. The compressive modulus (iv) decreased slowly over time in the hydrogels with the collagenase-loaded microparticles, but no change was observed in the BSA-loaded microparticles. Simulation results matched experiments showing a relatively sharp front surrounding the microparticles with a slight loss in hydrogel crosslinking (v) and correspondingly a slow loss in the compressive modulus (vi) over time.*

Overall, the 1D and 3D experimental and computational results point toward a degradation

profile that is more characteristic of diffusion-dominated degradation in the low crosslinked hydrogel and more characteristic of reaction-dominated degradation in the high crosslinked hydrogels. Having verified the multiphasic computational model with experimental results, we sought to identify dimensionless quantities that could be used to design hydrogels that are tuned to exhibit a desired reactiondiffusion degradation profile. To this end, we nondimensionalized the governing equations in the model to extract a set of dimensionless quantities that describe the spatiotemporal patterns in degradation, specifically the front velocity and the width of the front. The derivation can be found in (Equations (B9)(B15), appendix). We identified four dimensionless quantities (Figure 3.6 A) that are based on the properties of the polymer, initial hydrogel properties (e.g., equilibrium volumetric swelling ratio, Q^0), the degree of network connectivity, the radius of the enzyme, and the MichaelisMenten kinetics (i.e., k_{cat} and K_m).

The two dimensionless quantities that have the most significant effect on the spatiotemporal degradation pattern are α_e and κ. On the one hand, the quantity, α_e, is a measure of the relative enzyme radius to the mesh size of the hydrogel. Thus, the smaller the value of α_e the more easily the enzyme can diffuse through the hydrogel. On the other hand, the quantity, κ, describes the competition between reaction and diffusion, relating k_{cat}, enzyme concentration, diffusivity and crosslink density. Thus for high values of κ, reaction dominates diffusion and vice versa, for low values of κ, diffusion dominates reaction. We illustrate the effects of α_e and κ on front velocity and front width for a given value of ρ_x^{0*} and K_m^* (Figure 3.6 B). In brief, the nondimensionalized equations were solved for crosslink density as a function of time and distance (e.g., Figure 3.3) for a range of values for α_e (i.e., 0 to 0.8) and κ (i.e., 0 to 90). From these plots, a front velocity and front width were determined and the data combined to generate the contour plots shown in Figure 3.6 B. For very high values of κ, the front is sharp (i.e., narrow front width) and the front velocities are high regardless of the size of the enzyme. This is expected since the reactivity of the enzyme to its substrate is high. As the value of κ becomes smaller, the width and speed of the front depend largely on the relative size of the enzyme to the hydrogel mesh. When the enzyme is small compared to the mesh size, the front speed is fast, but the front width is large (characteristic

of the low crosslink density case in this study). On the contrary, when the enzyme is large and closer to the size of the hydrogel mesh, the front velocity slows, while the front becomes sharper (characteristic of the high crosslink density case). Increasing β, which indicates that fewer crosslinks must be cleaved to reach reverse gelation, leads to a shift to high magnitudes for front velocity and low magnitudes for front widths, but the overall shape of the contour plot remains. Finally, the quantity K_m^* is significant only for cases where the crosslink density in the swelling solvent is of similar magnitude (or lower) than K_m. This was true for the low crosslink density hydrogels used in the 1D experiment. Increasing K_m (and hence K_m^*) slows the front velocity and mm widens the front width. However, for more tightly crosslinked hydrogels, K_m^* has no effect on degradation.

A

$$\rho_x^{0*} = \frac{1}{\beta}$$

$$\alpha = \frac{r_e\sqrt{\rho_c}}{(Q^0)^{\frac{1}{3}}}\left(\frac{M_r}{3\ell^2 C_n \rho^P}\right)^{1/2}$$

$$\kappa = \frac{k_{cat} c_e^0 L^2}{D_\infty \rho_c}(Q^0 - 1)e^{1/(Q^0-1)}$$

$$K_m^* = \frac{K_m(Q^0 - 1)}{\rho_c}$$

Parameter	Description
β	Network connectivity
r_e	Enzyme radius
ρ_c	Critical crosslinking density
Q^0	Initial volumetric equilibrium swelling ratio
M_r	Molecular weight of repeat unit of polymer
ℓ	Average bond length
C_n	Characteristic ratio of polymer
ρ^P	Density of polymer
k_{cat}	Michaelis-Menten kinetics (substrate turn over)
K_m	Michaelis-Menten kinetics (equilibrium constant)
c_e^0	Initial enzyme concentration
D_∞	Diffusivity of enzyme in solvent

B

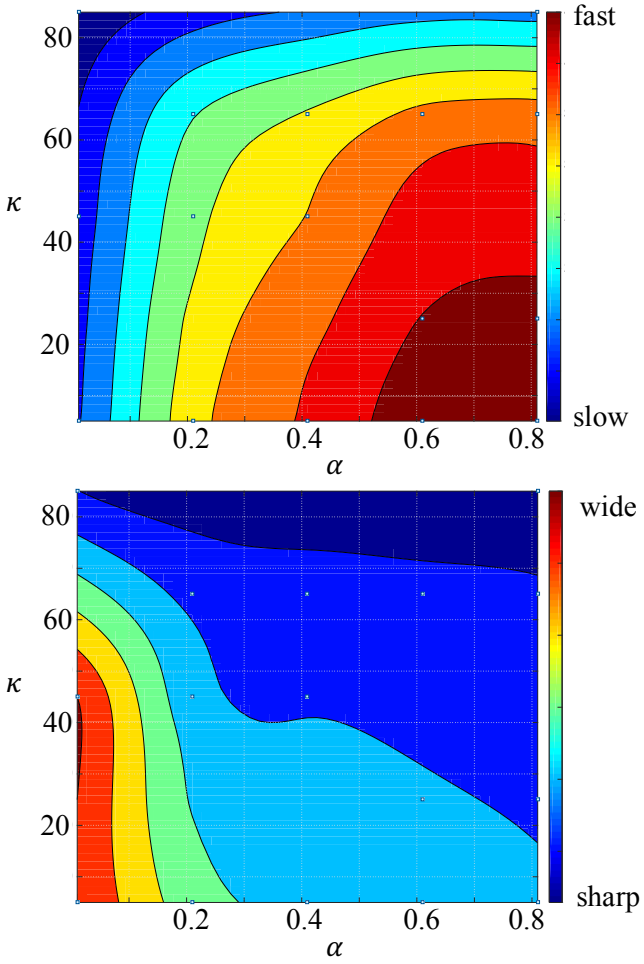

Figure 3.6: *(A) Dimensionless quantities identified by nondimensionalizing the governing equations for diffusion (Ficks second law) and reaction kinetics (MichaelisMenten kinetics) for enzyme-sensitive hydrogels. These four quantities are based on initial hydrogel properties, enzyme characteristics, and enzyme-substrate kinetics. The parameters and their description are listed in the table. (B) An example of contour plots for front velocity (in mm* h^1*) and front width (mm) as a function of* κ *and* α_e *for the case with a* $\beta = 0.6$*,* $K_m = 1010^6$ *M, and characteristic length of 2 mm.*

Overall by tuning the initial hydrogel properties and the enzymesubstrate pair, it is possible to achieve a wide range of spatiotemporal degradation patterns. The governing equations are appropriate for any neutral hydrogel [69, 114] and therefore the dimensionless quantities reported

in Figure 3 can be broadly applied to hydrogel chemistries beyond those explored in this work. Furthermore with information regarding the enzyme radius, the concentration of enzyme released by the cell, and the Michaelis-Menten kinetics for the enzyme-substrate (i.e., crosslink) pair, one can select an initial hydrogel crosslink density to achieve the desired degradation behavior. In summary, the above set of dimensionless quantities can be used as a design tool for engineering enzyme-sensitive hydrogels with controlled degradation patterns of reaction-dominated, diffusion-domi- nated, or a combination of reaction and diffusion behaviors.

3.3 Experimental section

Hydrogel Synthesis and Characterization: PEG hydrogels were formed by a photoclickable reaction between 8 arm PEG amine (M_w 10k and 20k) that was functionalized with norbornene [136] and CVPLS-LYSGC in the presence of a photoinitiator (0.05 wt% Irgacure 2959) and 352 nm light at 6 mW cm^2 for 8 min. Hydrogels were formed with varying monomer concentration, monomer molecular weights, and thiol:ene ratios (Table B1, appendix). Hydrogels were characterized by equilibrium volumetric swelling ratio, Q, which was estimated from mass swelling ratio and corresponding polymer and solvent densities. Compressive modulus was measured from the linear region of the stressstrain curve by compressing hydrogels at a rate of 10% per min to 15% strain (n = 34).

Cell-Mimetics: PLGA microspheres were synthesized via a double emulsion technique [7, 29] and loaded with protein encapsulants of BSA or collagenase type II. This process led to a distribution of particle sizes. Protein release in solution was quantified (NanoOrange protein quantification kit) over time in PBS at 37 ^{o}C in an infinite sink by continually replenishing with fresh PBS. Microparticles (50 mg mL^1) were encapsulated in PEG hydrogels (5 mm diameter, 1 mm height) and their wet weights and compressive modulus assessed (n = 34).

Degradation Experiments: The 1D and 3D experimental set-up is described in the appendix. Fluorescent hydrogels were prepared by introducing 0.01×10^3 M AlexaFluor-546 C5 maleimide in the precursor solution prior to polymerization. In the 1D experiments, the hydrogels

were allowed to equilibriate in PBS for 24 h prior to being exposed to enzyme and is referred to as the 0 h time point. At one side, the PBS bath was replaced with an enzyme bath, which was replaced daily to maintain a constant enzyme concentration. Fluorescence intensity of the degrading hydrogel was measured over time for each sample using an imaging system (BioRad VersaDoc 4000MP system). Fluorescence intensity at each time point was normalized to its maximum value for each condition and time point. In the 3D experiments for the low crosslink density hydrogels, total fluorescence was measured per image over time (n = 24 images per time point). For the high crosslink density hydrogels, void space diameters were measured (n = 8001300 measurements per time point), and the nonparametric Kolmogorov - Smirnov test was used to determine changes in the void size distributions changed after 7 d ($\alpha = 0.05$).

Simulations: The mathematical model of coupled enzyme diffusion and hydrogel degradation is described in the appendix. The dynamics of the hydrogel/enzyme system was investigated with a coupled system of partial differential equations consisting of a degenerate nonlinear diffusion equation for enzyme transport and a Michaelis-Menten degradation equation for the crosslink density. The model therefore captured the dependency of enzyme diffusion with hydrogel degradation and, conversely, the increase in hydrogel degradation with enzyme transport. Due to the strong nonlinearity of the system, we sought a numerical solution of these equations with a finite-element procedure relying on a Newton-Raphson approach and an implicit, backward-Euler algorithm for time integration. A convergence analysis of the method was performed for both the 1D and 3D analyses, which allowed us to select appropriate time step size and discretization that ensured maximum accuracy and low computational cost. Algorithms were written in Matlab.

Chapter 4

A computational model for hydrogels in tissue engineering part I: cell mediated degradation

4.1 Introduction

Tissue failure due to aging or diseases reduces the quality of life for individuals. In the case of cartilage tissue, for instance, the current solution is to use implants to fulfill the functional duties of native tissue. However, this approach has limitations, such as periodic replacement and number of the required operations [71, 121]. Tissue engineering provides an alternative approach in which the aim is to regenerate the native tissue by a population of cells encapsulated in a scaffold (i.e. hydrogels) [162, 71] (see Figure 4.1). Although this approach is promising, there are several limitations regarding the design of these scaffolds. First, the scaffolds should maintain the mechanical support until the neo-tissue is well developed. Second, the scaffolds have to enable the tissue growth by providing space for the new extra-cellular matrix (ECM) [71]. Experimental studies have shown that the cells can be promoted to regenerate tissue using different ways. For instance, Bryant et al. [111] showed that the cyclic loading of a construct (i.e., a population of cells encapsulated within a hydrogel) affects the rate of cell-mediated degradation which may be originated from enhanced degradation process or improved transport of building blocks of ECM. The experimental results show the connection between the mechanics and remodeling (or growth); however, the thorough understanding of this effect demands computational models due to the cost and time limitations of the experimental studies.

One advantage of computational models is the ability to capture the coupling between remodeling

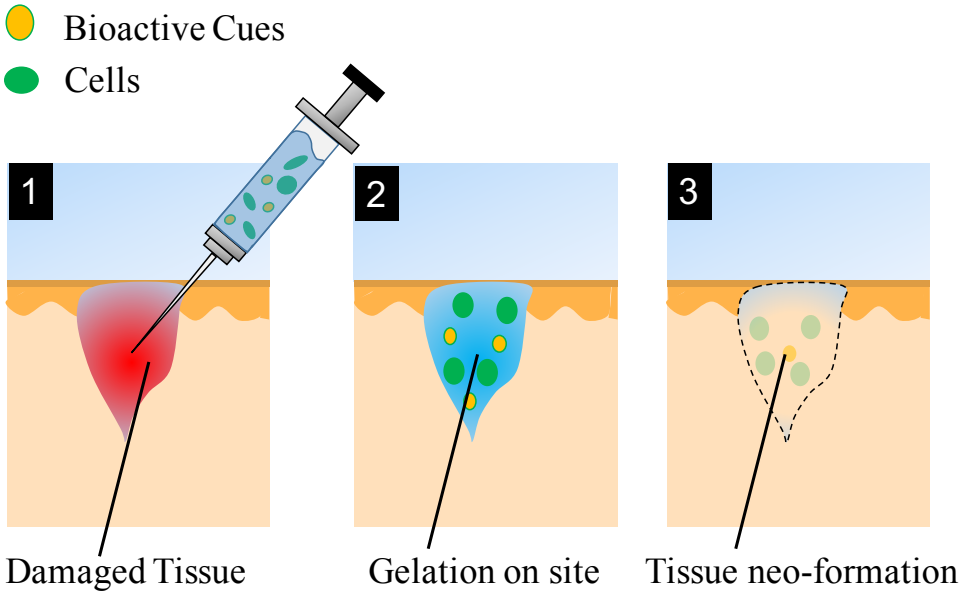

Figure 4.1: The objective of tissue engineering is to design scaffolds to encapsulate the cell, whose mission is to regenerate the damaged tissue in-vivo.

and mechanics [79, 87, 150]. In this context, consider the evolution in one of two ways: (a) removal of existing material (i.e. degradation), or (b) deposition of new material (i.e. tissue growth). Previous studies [70, 150, 53] shows that we can govern the material removal or deposition using the similar mathematical models that has opposite effect. In order to track the material deposition/removal, the transport and chemical reactions of the building/demolishing blocks should be captured [136, 1, 150], and both of these mechanisms are coupled with the mechanics of scaffold (or encapsulating medium). A number of frameworks based on continuum mechanics has been developed for finite growth [138, 127, 75, 38, 70, 10, 11, 53] to capture this coupling between remodeling and mechanics. These frameworks also enable us to quantify the evolution of the overall mechanical properties, and this has been shown in [34, 1]. Although the studies we have referred here have potential, the application of those models to tissue engineering is still in progress. For instance, Sengers et al. [132] investigated the competition among ECM degradation/deposition and transport using a 2D model and its effect on the overall construct stiffness. Trewenack et al. [142] proposed a multispecies formulation of cell-mediated growth in cartilage constructs, pointing out the

distinct roles of advection of diffusion fluxes at the microscopic level. Haider et al. [57] extended the phenomenological model of Wilson et al. [159] to incorporate experimentally measurable quantities, including the apparent densities of the scaffold, the deposited and the unlinked ECM. Recently Dhote et al. [34] have built a 1D model to capture the remodeling of hydrogel around a single cell, which showed that localized degradation followed by the neo-tissue formation can allow successful growth in terms of the mechanical integrity. Further, Vernerey presented a macroscopic growth model in [150] and incorporated the relations which enable us to track the coupling between growth and mechanics at finite strain. Finally, Akalp et. al. [1] presented a 3D growth model at small strain, and have shown that achieving the connectivity of tissue clusters before the complete degradation of the scaffold is important to maintain mechanical integrity. Although the computational tools mentioned above are helpful, in order to have a deep understanding of the evolution of hydrogel constructs, a 3D computational model at the cellular scale that captures the effects of finite strain is preferable.

The aim of this study is to present a 3D computational model based on the existing theories of remodeling in biological materials [87, 150, 70, 10, 53]. In this paper we will focus on remodeling by the removal of existing material, i.e. the cell-mediated degradation, and its dependence on the mechanics of the scaffold. For this purpose, we have developed our model based on mixture theory, and we have derived the equations governing the mechanics, transport, and degradation for a continuous medium, which represents the hydrogel scaffolds. The model captures the evolution of intercellular region at micro-scale, therefore, we carry our results to meso-scale using homogenization procedure. The next section will introduce the kinematics, governing equations. Section 3 will present the constitutive relations and the mathematical model while section 4 describes numerical application and homogenization procedure. Finally, in section 5 we will present our results.

4.2 Kinematics and Balance Laws for the scaffold

The scaffold of interest is composed of solid and fluid constituents which will be denoted by subscripts s and w in this paper. For instance, hydrogels are composed of a polymer network which is

built from the monomers and peptide cross-linkers, and a solvent which fills the pores of the network and cause its swelling. In this study, we assume that the pore size is small compared to the domain Ω of interest, therefore we consider the mixture of solid and fluid constituents at continuum level. Hence, every material point $\mathbf{X}$ at the reference configuration is composed of solid and fluid material and their volume fractions at $\mathbf{X}$ are $\phi_w(\mathbf{X}, t)$ and $\phi_s(\mathbf{X}, t)$. Note that the volume fractions are both functions of position and time t. We adopted mixture theory in this study because of its ability to describe the physics of scaffolds [34, 150, 1, 70, 53, 11]. We would like to make two assumptions before moving forward. First, it is assumed that the mass flux of the solid materials is always zero on the scaffold boundary $\partial\Omega$. Second, the mixture is always saturated, i.e. $\phi_w + \phi_s = 1$, which implies that there is no voids in Ω. Addition to the two constituents of scaffold, there can also be species that are released from the cells in fluid form. These species can have chemical interaction with each other or the scaffold, which triggers the material deposition or removal. In this study we will focus on the cell released enzyme which drives the degradation process of scaffold. Two assumptions regarding the cell released enzyme molecules are; (a) they are always in fluid form, (b) the volume fraction of enzyme ϕ_e in the system is low compared to the other constituents ($\phi_e \ll 1$ and hence $\phi_w + \phi_s \approx 1$). Although we will provide the general forms of the balance equations in the following subsections, we will be using these assumptions while building the final form of our model.

4.2.1 Kinematics

Based on the mixture theory, we track the displacement field $\mathbf{u}(\mathbf{X}, t) = \mathbf{x}(\mathbf{X}, t) - \mathbf{X}$ of the solid constituent where $\mathbf{x}(\mathbf{X}, t)$ is the position of material point $\mathbf{X}$ at time t. Then the deformation of the volume Ω can be described using the linear mapping function (i.e. deformation gradient) $\mathbf{F}(\mathbf{X}, t) = \partial\mathbf{x}(\mathbf{X}, t)/\partial\mathbf{X}$. The volumetric deformation is quantified by $J = det(\mathbf{F})$. Using the saturation condition and the fact that $J = 1$ in the absence of fluid material, we can define the volume fraction $\phi_w = (J - 1)/J$. Furthermore, in mixture theory, the kinematics of the fluid constituents are written with respect to the solid material. Let us first define the solid

velocity and the absolute velocity of fluid constituent α as $\mathbf{v}_s = \dot{\mathbf{x}}$ and $\mathbf{v}_\alpha$ respectively, where we dropped the terms $(\mathbf{X}, t)$ in the parenthesis for convenience. Then we can define the relative velocity of the fluid constituent α as $\tilde{\mathbf{v}}_\alpha = \mathbf{v}_\alpha - \mathbf{v}_s$. This velocities can be written with respect to the reference configuration (see Vernerey [150]) using the transformation $\mathbf{V}_s = \mathbf{F}^{-1}\mathbf{v}_s$ and $\tilde{\mathbf{V}}_\alpha = \mathbf{F}^{-1}\tilde{\mathbf{v}}_\alpha$. Further we can also transform the material flux on the boundary $\partial\Omega$ to the reference one on $\partial\Omega_0$ using the relation; $\mathbf{Q}_\alpha = J\mathbf{F}^{-1}\mathbf{q}_\alpha$ where $\alpha = w, e$. Since we build our approach on a Lagrangian definition of the motion, material derivative should be defined in the same reference frame for all constituent. That leads the transformation of the material derivative of constituent α, $d^\alpha(\cdot)/dt$ with respect to the solid material; $d^\alpha(\cdot)/dt = d(\cdot)/dt + \nabla(\cdot)\cdot\tilde{\mathbf{v}}_\alpha$ where $\nabla(\cdot) = \partial(\cdot)/\partial\mathbf{x}$ is the gradient operator. Note that this operator is defined in the current configuration Ω. The material derivative in reference configuration Ω_0 is obtained by following the classical continuum mechanics [64]; $D^\alpha(\cdot)/Dt = D(\cdot)/Dt + \nabla_{\mathbf{X}}(\cdot)\cdot\tilde{\mathbf{V}}_\alpha$ where $[D(\cdot)/Dt = \partial(\cdot)/\partial t + \nabla_{\mathbf{X}}(\cdot)\cdot\mathbf{V}_s]$ and $[\nabla_{\mathbf{X}}(\cdot) = \partial(\cdot)/\partial\mathbf{X}]$.

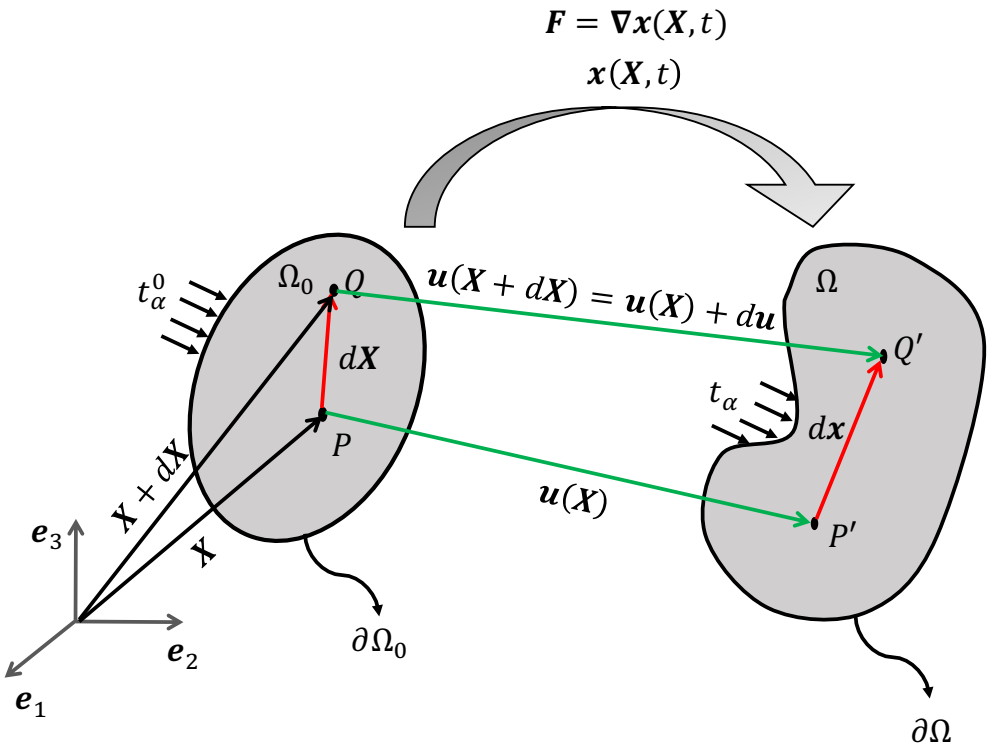

Figure 4.2: Configuration of the domain of interest at the initial and current frames

4.2.2 Mass Balance

In the literature, concentration [53, 150] or mass density [87, 75] is used to track the evolution of mass. In this study we choose the concentration (in units of mole per volume). We define the relation between volume fraction ϕ_α and true concentration c_α as $\phi_\alpha = c_\alpha \nu_\alpha$ where ν_α is the molar volume of the constituent $\alpha = s, w, e$. Further, the nominal concentration reads; $C_\alpha = J c_\alpha$. Based on the system described above, and following the work of [53, 41], the mass balance of solid material reads;

$$\frac{\partial C_s}{\partial t} = \Gamma_s \tag{4.1}$$

where Γ_s is the source for solid material in the reference configuration. Note that positive source represents deposition whereas the negative of the same represents the removal of existing material. Next let us derive the mass balance equation for the fluid constituents. We start with the localized mass balance in the current configuration Ω;

$$\frac{d^\alpha c_\alpha}{dt} + c_\alpha \nabla \cdot \mathbf{v}_\alpha = \gamma_\alpha \tag{4.2}$$

where γ_α is the source term in the current configuration. Now using the transformation for material derivative (which is given in the previous section), adding/subtracting the terms $\mathbf{v} \cdot \nabla c_\alpha$ and $c_\alpha \nabla \cdot \mathbf{v}$, and regrouping them gives the following form;

$$\frac{dc_\alpha}{dt} + c_\alpha \nabla \cdot \mathbf{v} + \nabla \cdot (c_\alpha(\mathbf{v}_\alpha - \mathbf{v}_w) + c_\alpha(\mathbf{v}_w - \mathbf{v})) = \gamma_\alpha \tag{4.3}$$

where $c_\alpha(\mathbf{v}_\alpha - \mathbf{v}_w)$ is the relative flux of constituent α with respect to the main fluid phase w and it vanishes for $\alpha = w$. The term $c_\alpha(\mathbf{v}_w - \mathbf{v})$ describes the flux of fluid constituent α with respect to the solid material. In the case of $\alpha = e$, it is the convective effect of the main fluid in the system ($\alpha = w$) while in the case of $\alpha = w$ it is the flux of main fluid with respect to the solid material. Now we carry this to the reference frame by performing the necessary algebra, which includes divergence theorem, Nanson's formula and regrouping the terms, and re-localizing it;

$$\begin{gathered} \frac{DC_\alpha}{Dt} + \nabla_{\mathbf{X}} \cdot (C_\alpha(\mathbf{V}_\alpha - \mathbf{V}_w) + C_\alpha(\mathbf{V}_w - \mathbf{V})) = \Gamma_\alpha \quad \text{or} \\ \frac{DC_\alpha}{Dt} + \nabla_{\mathbf{X}} \cdot (C_\alpha \tilde{\tilde{\mathbf{V}}}_\alpha + C_\alpha \tilde{\mathbf{V}}_w) = \Gamma_\alpha \end{gathered} \tag{4.4}$$

where $\tilde{\tilde{\mathbf{V}}}_\alpha = (\mathbf{V}_\alpha - \mathbf{V}_\mathbf{w})$.

4.2.3 Balance of momentum

Total mass of the material α in the system is $m_\alpha = \int_\Omega \varrho_\alpha c_\alpha dv$ where ϱ_α is the molar mass of α. Let us start by writing the balance of momentum in current configuration for a single specie α. The rate of change in momentum for constituent α emerges from the body forces on it, the interaction forces applied by other species, external loads applied on it in the form of surface traction, change in momentum due to conversion from/to other constituents, and finally, the mass flux incoming/outgoing with a velocity $\mathbf{v}_\alpha$.

$$\begin{aligned}\frac{d}{dt}\int_\Omega c_\alpha \varrho_\alpha \mathbf{v}_\alpha dv = \int_\Omega c_\alpha \mathbf{b}_\alpha dv + \int_\Omega c_\alpha \tilde{\mathbf{t}}_\alpha dv \\ + \int_\Omega \gamma_\alpha \varrho_\alpha \mathbf{v}_\alpha dv - \int_{\partial\Omega} (\mathbf{v}_\alpha \varrho_\alpha \mathbf{q}_\alpha)\cdot \mathbf{n} ds + \int_{\partial\Omega} \mathbf{t}_\alpha ds\end{aligned} \tag{4.5}$$

where $\mathbf{b}_\alpha$ is the body force, $\tilde{\mathbf{t}}_\alpha$ is the force applied to 'α' by other species, $\mathbf{t}_\alpha = \boldsymbol{\sigma}_\alpha \cdot \mathbf{n}$ is the traction on the boundary $\partial\Omega$. The normal of the boundary $\partial\Omega$ is $\mathbf{n}$ and the resulting Cauchy stress of the material point is $\boldsymbol{\sigma}_\alpha$ for α. We can write the linear momentum balance for a multi-constituent system as the summation over the species [53, 11];

$$\begin{aligned}\sum_\alpha \frac{d}{dt}\int_\Omega c_\alpha \varrho_\alpha \mathbf{v}_\alpha dv = \sum_\alpha \int_\Omega c_\alpha \mathbf{b}_\alpha dv + \sum_\alpha \int_\Omega c_\alpha \tilde{\mathbf{t}}_\alpha dv \\ + \sum_\alpha \int_\Omega \gamma_\alpha \varrho_\alpha \mathbf{v}_\alpha dv - \sum_\alpha \int_{\partial\Omega} (\mathbf{v}_\alpha \varrho_\alpha \mathbf{q}_\alpha)\cdot \mathbf{n} ds + \sum_\alpha \int_{\partial\Omega} \mathbf{t}_\alpha ds\end{aligned} \tag{4.6}$$

We would like to state that the change in momentum in the system is only due to the external effects; the interaction forces and the momentum due to mass conversion should be at equilibrium, i.e. $\sum_\alpha \int_\Omega c_\alpha \varrho_\alpha \tilde{\mathbf{t}}_\alpha dv + \sum_\alpha \int_\Omega \gamma_\alpha \varrho_\alpha \mathbf{v}_\alpha dv = 0$. This leads;

$$\begin{aligned}\sum_\alpha \frac{d}{dt}\int_\Omega c_\alpha \varrho_\alpha \mathbf{v}_\alpha dv = \sum_\alpha \int_\Omega c_\alpha \mathbf{b}_\alpha dv \\ - \sum_\alpha \int_{\partial\Omega} (\mathbf{v}_\alpha \varrho_\alpha \mathbf{q}_\alpha)\cdot \mathbf{n} ds + \sum_\alpha \int_{\partial\Omega} \mathbf{t}_\alpha ds\end{aligned} \tag{4.7}$$

Expanding the right-hand-side and using the mass balance and divergence theorem on the left-hand-side, the balance of momentum equation becomes;

$$\begin{aligned}\int_\Omega \sum_\alpha c_\alpha \varrho_\alpha \dot{\mathbf{v}}_\alpha dv = &- \int_\Omega \sum_\alpha (\nabla \cdot \mathbf{v}_\alpha)\varrho_\alpha \mathbf{q}_\alpha) dv \\ &+ \int_\Omega \sum_\alpha c_\alpha \mathbf{b}_\alpha dv - \int_\Omega \sum_\alpha \gamma_\alpha \varrho_\alpha \mathbf{v}_\alpha dv + \int_\Omega \sum_\alpha (\nabla \cdot \boldsymbol{\sigma}_\alpha) dv\end{aligned} \tag{4.8}$$

where $\dot{()}$ denotes the material time derivative. The linear momentum balance equation can be mapped to the reference configuration and its localized form is;

$$\sum_\alpha C_\alpha \varrho_\alpha \dot{\mathbf{V}}_\alpha = \sum_\alpha C_\alpha \mathbf{b}_\alpha - \sum_\alpha (\nabla_{\mathbf{X}} \cdot \mathbf{V}_\alpha)\varrho_\alpha \mathbf{Q}_\alpha - \sum_\alpha \Gamma_\alpha \varrho_\alpha \mathbf{V}_\alpha + \sum_\alpha \nabla_{\mathbf{X}} \cdot \mathbf{P}_\alpha \tag{4.9}$$

where $\mathbf{P}_\alpha = J\boldsymbol{\sigma}_\alpha \mathbf{F}^{-T}$ is first Piola-Kirchhoff stress tensor. Note that in this study there is only two constituents that contribute to the stress $\alpha = s, w$. Note that time derivative $\dot{\mathbf{V}}_\alpha = \partial \mathbf{V}_\alpha / \partial t$ since the balance equation is carried out in the reference configuration and the velocity field $\mathbf{V}_\alpha$ is a Lagrangian field variable. We also skip the balance of angular momentum due to the simplicity of our system, the detailed derivation of it can be found in [53, 70, 64]. Let us now state our assumptions to further simplify this form. First, we assume that the system is small enough to neglect the body forces ($\mathbf{b}_\alpha \approx 0$). Second, the evolution of the system due to mass flux and conversion is slow compared to the loading rates. Finally, the loading rates are slow enough that the system is assumed to reach mechanical equilibrium instantaneously. The latter two assumptions leads to: (i) $\dot{\mathbf{V}}_\alpha \approx 0$ (ii) $(\nabla_{\mathbf{X}} \cdot \mathbf{V}_\alpha)\varrho_\alpha \mathbf{Q}_\alpha \approx 0$ (iii) $\Gamma \varrho_\alpha \mathbf{V}_\alpha \approx 0$.Finally balance of momentum equation becomes;

$$\sum_\alpha \nabla_{\mathbf{X}} \cdot \mathbf{P}_\alpha = 0 \tag{4.10}$$

4.2.4 Balance of Energy and Entropy Inequality

In this study we follow the work of Garikipati et al. [53]. Before we derive the balance of energy let us state that the system we investigate here immersed in a relatively large fluid environment, therefore the system is considered as isothermal. The rate of change of energy (in the absence of body forces) of constituent α emerges from; (i) the kinetic energy transfer due to interaction

forces $\tilde{\mathbf{t}}_\alpha$, (ii) energy transfer $\tilde{e}_\alpha$ from other constituents, (iii) the energy of incoming/outgoing mass flux $\mathbf{q}_\alpha$, (iv) change in energy due to mass conversion γ_α and (v) work done on it by external loads $\mathbf{t}_\alpha = \boldsymbol{\sigma}_\alpha \cdot \mathbf{n}$. The energy balance equation reads;

$$\begin{aligned}\frac{d}{dt}\int_\Omega c_\alpha \left(e_\alpha + \frac{1}{2}\varrho_\alpha \|\mathbf{v}_\alpha\|^2\right) dv = \int_\Omega c_\alpha \tilde{\mathbf{t}}_\alpha \cdot \mathbf{v}_\alpha dv \\ + \int_\Omega c_\alpha \tilde{e}_\alpha dv + \int_\Omega \gamma_\alpha \left(e_\alpha + \frac{1}{2}\varrho_\alpha \|\mathbf{v}_\alpha\|^2\right) dv \\ + \int_{\partial\Omega} \mathbf{v}_\alpha \cdot \boldsymbol{\sigma}_\alpha \cdot \mathbf{n} ds - \int_{\partial\Omega} \mathbf{q}_\alpha \left(e_\alpha + \frac{1}{2}\varrho_\alpha \|\mathbf{v}_\alpha\|^2\right) \cdot \mathbf{n} ds\end{aligned} \tag{4.11}$$

where e_α is the energy per mole of material. Applying the divergence theorem to the flux and traction terms and mapping the equation back to reference configuration;

$$\begin{aligned}\frac{D}{Dt}\int_{\Omega_0} C_\alpha \left(e_\alpha + \frac{1}{2}\varrho_\alpha \|\mathbf{V}_\alpha\|^2\right) dV = \int_{\Omega_0} C_\alpha \tilde{\mathbf{t}}_\alpha \cdot \mathbf{V}_\alpha dV \\ + \int_{\Omega_0} C_\alpha \tilde{e}_\alpha dV + \int_{\Omega_0} \Gamma_\alpha \left(e_\alpha + \frac{1}{2}\varrho_\alpha \|\mathbf{V}_\alpha\|^2\right) dV \\ + \int_{\Omega_0} \nabla_{\mathbf{X}} \cdot (\mathbf{P}_\alpha \cdot \mathbf{V}_\alpha) dV - \int_{\Omega_0} \nabla_{\mathbf{X}} \cdot \left[\mathbf{Q}_\alpha \left(e_\alpha + \frac{1}{2}\varrho_\alpha \|\mathbf{V}_\alpha\|^2\right)\right] dV\end{aligned} \tag{4.12}$$

Using the mass balance on the left hand side;

$$\begin{aligned}\int_{\Omega_0} C_\alpha \frac{D}{Dt}\left(e_\alpha + \frac{1}{2}\varrho_\alpha \|\mathbf{V}_\alpha\|^2\right) dV = \int_{\Omega_0} C_\alpha \tilde{\mathbf{t}}_\alpha \cdot \mathbf{V}_\alpha dV \\ + \int_{\Omega_0} C_\alpha \tilde{e}_\alpha dV + \int_{\Omega_0} \nabla_{\mathbf{X}} \cdot (\mathbf{P}_\alpha \cdot \mathbf{V}_\alpha) dV \\ - \int_{\Omega_0} \nabla_{\mathbf{X}} \left[\left(e_\alpha + \frac{1}{2}\varrho_\alpha \|\mathbf{V}_\alpha\|^2\right)\right] \cdot \mathbf{Q}_\alpha dV\end{aligned} \tag{4.13}$$

Next we sum (4.13) over the species and then multiply the balance of momentum equation (4.9) with $\mathbf{V}_\alpha$ and substitute it in the balance of energy;

$$\begin{aligned}\int_{\Omega_0} \sum_\alpha C_\alpha \frac{\partial e_\alpha}{\partial t} dV = \int_{\Omega_0} \sum_\alpha C_\alpha \tilde{e}_\alpha dV \\ + \int_{\Omega_0} \sum_\alpha \mathbf{P}_\alpha : (\nabla_{\mathbf{X}} \mathbf{V}_\alpha) dV - \int_{\Omega_0} (\nabla_{\mathbf{X}} e_\alpha) \cdot \mathbf{Q}_\alpha dV\end{aligned} \tag{4.14}$$

Summing over the species, we know that the internal interactions should not change the overall energy of the system;

$$\begin{aligned}\int_{\Omega_0} \sum_\alpha \Gamma_\alpha \left(e_\alpha + \frac{1}{2}\varrho_\alpha \|\mathbf{V}_\alpha\|^2\right) dV + \int_{\Omega_0} \sum_\alpha C_\alpha \tilde{\mathbf{t}}_\alpha \cdot \mathbf{V}_\alpha dV \\ + \int_{\Omega_0} \sum_\alpha C_\alpha \tilde{e}_\alpha dV = 0\end{aligned} \tag{4.15}$$

Further we know from mass balance $\sum_\alpha \Gamma_\alpha = 0$ and $\sum_\alpha \Gamma_\alpha \mathbf{V} = 0$. Referring to the derivation of balance of momentum, we can state the relation

$$\sum_\alpha C_\alpha \tilde{\mathbf{t}}_\alpha \cdot \mathbf{V} = -\sum_\alpha \Gamma \varrho_\alpha (\mathbf{V}_\alpha - \mathbf{V}) \cdot \mathbf{V} \tag{4.16}$$

Therefore,

$$\int_{\Omega_0} \sum_\alpha \Gamma_\alpha \left(e_\alpha + \frac{1}{2} \varrho_\alpha \|\tilde{\mathbf{V}}_\alpha\|^2 \right) dV + \int_{\Omega_0} \sum_\alpha C_\alpha \tilde{\mathbf{t}}_\alpha \tilde{\mathbf{V}}_\alpha dV + \int_{\Omega_0} \sum_\alpha C_\alpha \tilde{e}_\alpha dV = 0 \tag{4.17}$$

Using this relation to substitute the $\tilde{e}_\alpha$ in energy balance equation and localizing it;

$$\begin{aligned} \sum_\alpha C_\alpha \frac{\partial e_\alpha}{\partial t} &= \sum_\alpha \mathbf{P}_\alpha : (\nabla_{\mathbf{X}} \tilde{\mathbf{V}}_\alpha) + \sum_\alpha \mathbf{P}_\alpha : (\nabla_{\mathbf{X}} \mathbf{V}) \\ &\quad - \sum_\alpha (\nabla_{\mathbf{X}} e_\alpha) \cdot \mathbf{Q}_\alpha - \sum_\alpha C_\alpha \tilde{\mathbf{t}}_\alpha \cdot \tilde{\mathbf{V}}_\alpha - \sum_\alpha \Gamma_\alpha \left(e_\alpha + \frac{1}{2} \varrho_\alpha \|\tilde{\mathbf{V}}_\alpha\|^2 \right) \end{aligned} \tag{4.18}$$

Once again we use the balance of momentum equation to substitute the $\tilde{\mathbf{t}}_\alpha$ term;

$$\begin{aligned} \sum_\alpha C_\alpha \frac{\partial e_\alpha}{\partial t} &= \sum_\alpha \mathbf{P}_\alpha : (\nabla_{\mathbf{X}} \tilde{\mathbf{V}}_\alpha) + \sum_\alpha \mathbf{P}_\alpha : (\nabla_{\mathbf{X}} \mathbf{V}) - \sum_\alpha (\nabla_{\mathbf{X}} e_\alpha) \cdot \mathbf{Q}_\alpha \\ &\quad + \sum_\alpha \left[-C_\alpha \varrho_\alpha \frac{\partial \mathbf{V}_\alpha}{\partial t} + \nabla_{\mathbf{X}} \cdot \mathbf{P}_\alpha - \varrho_\alpha \mathbf{Q}_\alpha (\nabla_{\mathbf{X}} \cdot \mathbf{V}_\alpha) \right] \cdot \tilde{\mathbf{V}}_\alpha \\ &\quad - \sum_\alpha \Gamma_\alpha \left(e_\alpha + \frac{1}{2} \varrho_\alpha \|\tilde{\mathbf{V}}_\alpha\|^2 \right) \end{aligned} \tag{4.19}$$

Since the inertial effects are negligible;

$$\begin{aligned} \sum_\alpha C_\alpha \frac{\partial e_\alpha}{\partial t} &= \sum_\alpha \mathbf{P}_\alpha : (\nabla_{\mathbf{X}} \tilde{\mathbf{V}}_\alpha) + \sum_\alpha \mathbf{P}_\alpha : (\nabla_{\mathbf{X}} \mathbf{V}) \\ &\quad - \sum_\alpha (\nabla_{\mathbf{X}} e_\alpha) \cdot \mathbf{Q}_\alpha + \sum_\alpha (\nabla_{\mathbf{X}} \cdot \mathbf{P}_\alpha) \cdot \tilde{\mathbf{V}}_\alpha - \sum_\alpha \Gamma_\alpha e_\alpha \end{aligned} \tag{4.20}$$

The equation (4.20) is the first law of thermodynamics for the mixture that we consider in this study. Second law of thermodynamics states;

$$\sum_\alpha \frac{d}{dt} \int_{\Omega_0} c_\alpha \eta_\alpha dv \geq \sum_\alpha \int_{\Omega_0} \gamma_\alpha \eta_\alpha - \sum_\alpha \int_{\Omega_0} \mathbf{q}_\alpha \cdot \mathbf{n} \eta_\alpha ds \tag{4.21}$$

where η_α is entropy per mole of constituent α; $\delta \Delta S = \eta_\alpha \delta N_\alpha$. Using mass balance equation, mapping back to reference configuration using divergence theorem and localizing the equation gives;

$$\sum_\alpha C_\alpha \frac{\partial \eta_\alpha}{\partial t} \geq -\mathbf{Q}_\alpha \cdot (\nabla_{\mathbf{X}} \eta_\alpha) \tag{4.22}$$

Multiplying this with absolute temperature and subtracting from the balance of energy we obtain the Clausius-Duhem inequality for the mixture;

$$\begin{aligned}\sum_{\alpha} C_{\alpha}\left(\frac{\partial e_{\alpha}}{\partial t}-T\frac{\partial \eta_{\alpha}}{\partial t}\right)-\sum_{\alpha}\mathbf{P}_{\alpha}:\dot{\mathbf{F}}+\sum_{\alpha}\mathbf{P}_{\alpha}:(\nabla_{\mathbf{X}}\tilde{\mathbf{V}}_{\alpha})\\ +\sum_{\alpha}\Gamma_{\alpha}\left(e_{\alpha}\right)+\left[\frac{1}{C_{\alpha}}\nabla_{\mathbf{X}}\cdot\mathbf{P}_{\alpha}-\nabla_{\mathbf{X}}(e_{\alpha}-T\eta_{\alpha})\right]C_{\alpha}\tilde{\mathbf{V}}_{\alpha}\leq 0\end{aligned} \tag{4.23}$$

where we used the flux relation $\mathbf{Q}_{\alpha}=C_{\alpha}\tilde{\mathbf{V}}_{\alpha}$. Assuming that internal energy is only function of deformation and entropy, we can write

$$\begin{aligned}\sum_{\alpha} C_{\alpha}\left(\frac{\partial e_{\alpha}}{\partial \eta_{\alpha}}-T\right)\frac{\partial \eta_{\alpha}}{\partial t}+\sum_{\alpha}\left(C_{\alpha}\frac{\partial e_{\alpha}}{\partial \mathbf{F}}-\mathbf{P}_{\alpha}\right):\dot{\mathbf{F}}+\sum_{\alpha}\Gamma_{\alpha}e_{\alpha}\\ +\sum_{\alpha}\mathbf{P}_{\alpha}:(\nabla_{\mathbf{X}}\tilde{\mathbf{V}}_{\alpha})-\left[-\frac{1}{C_{\alpha}}\nabla_{\mathbf{X}}\cdot\mathbf{P}_{\alpha}+\nabla_{\mathbf{X}}(e_{\alpha}-T\eta_{\alpha})\right]C_{\alpha}\tilde{\mathbf{V}}_{\alpha}\leq 0\end{aligned} \tag{4.24}$$

The process of remodeling has the physical restriction that is presented in inequality (4.24). The constitutive relations regarding the system must satisfy this restriction. With the aid of the works [53, 143], we can define the following constitutive relations;

$$\frac{\partial e_{\alpha}}{\partial \eta_{\alpha}}=T \tag{4.25}$$

$$C_{\alpha}\frac{\partial e_{\alpha}}{\partial \mathbf{F}}=\mathbf{P}_{\alpha} \tag{4.26}$$

$$\mathbf{Q}_{\alpha}=C_{\alpha}\tilde{\mathbf{V}}_{\alpha}=-\left(\bar{\boldsymbol{\kappa}}_{\alpha}\nabla_{\mathbf{X}}\cdot\mathbf{P}_{\alpha}+\mathbf{F}\mathbf{D}_{\alpha}\frac{C_{\alpha}}{RT}\nabla_{\mathbf{X}}(e_{\alpha}-T\eta_{\alpha})\right) \tag{4.27}$$

where the constitutive relation for mass flux is the generalized Darcy's law which suggests that for the dilute suspensions (i.e. enzyme) $\bar{\boldsymbol{\kappa}}_{\alpha}/\mathbf{D}_{\alpha}\approx 0$ and the transport is driven by Brownian motion, while for close-packed matrix of incompressible fluids $\mathbf{D}_{\alpha}/\bar{\boldsymbol{\kappa}}_{\alpha}\approx 0$ and relative motion is driven by the elastic stress [115]. Note that $\mathbf{D}_{\alpha}$ and $\bar{\boldsymbol{\kappa}}_{\alpha}$ are mobility tensors; diffusivity and permeability respectively, and both are positive definite in order to satisfy the inequality. $\mathbf{D}_{\alpha}$ is the mobility tensor in the reference configuration found by using the mapping relation; $\mathbf{D}_{\alpha}=\mathbf{F}^{-1}\bar{\mathbf{D}}_{\alpha}\mathbf{F}^{-T}$ where $\bar{\mathbf{D}}_{\alpha}$ is the apparent diffusivity respectively [51]. Permeability $\bar{\boldsymbol{\kappa}}_{\alpha}$, is the apparent and not mapped to the reference frame. This difference between $\mathbf{D}_{\alpha}$ and $\bar{\boldsymbol{\kappa}}_{\alpha}$ arises because the elastic stress $\mathbf{P}_{\alpha}$ is mapped to reference frame whereas the internal energy is not, since the energy considered here

is frame invariant. We assume that our system is isotropic (i.e. $\bar{\mathbf{D}}_\alpha = \bar{D}_\alpha \mathbf{I}$ and $\bar{\boldsymbol{\kappa}}_\alpha = \bar{\kappa}_\alpha \mathbf{I}$), therefore mobility tensor reduces to a scalar ($\bar{D}_\alpha$ or $\bar{\kappa}_\alpha$). The term $(e_\alpha - T\eta_\alpha) = \psi_\alpha = \partial\Psi_\alpha/\partial C_\alpha$ in (4.27) is the partial molar free energy (also known as chemical potential) where Ψ_α is the Helmholtz free energy. The partial molar free energy ψ_α is obtained by Legendre transformation $\psi_\alpha = e_\alpha - T\eta_\alpha$. Also note that we previously made the isothermal assumption, which leads to $\nabla_{\mathbf{X}}\psi_\alpha|_T = \nabla_{\mathbf{X}} e_\alpha - T\nabla_{\mathbf{X}}\eta_\alpha$. After introducing these constitutive relation, the Clausius-Duhem inequality reduces to the following thermodynamic constraint;

$$\sum_\alpha \mathbf{P}_\alpha : (\nabla_{\mathbf{X}} \tilde{\mathbf{V}}_\alpha) + \sum_\alpha \Gamma_\alpha e_\alpha \leq 0 \tag{4.28}$$

The inequality (4.28) is the final form of thermodynamic restriction, which should be satisfied in order to have a thermodynamically admissible system.

4.3 Constitutive relations and complete mathematical model

4.3.1 Constitutive Relations

In this study, we constitute the free energy of a bi-phasic material (which is composed of a solid network swollen by a fluid constituent) in two parts. First, the solid network has free energy Ψ_s as introduced in the previous section. Since the solid network can be considered as a single molecule, its entropic contribution η_s is negligible, and therefore $\partial\psi_s/\partial\mathbf{F} = \partial e_s/\partial\mathbf{F}$. Furthermore, we assume that the internal energy e_s to be independent of the mass i.e. $\partial e_s/\partial C_s = 0$ which allows us to write $\Psi_s = C_s\psi_s$. We adapted the elastic energy function developed by Arruda and Boyce [6] which is based on the well known theory of Flory for swollen networks [46]. The energy function of Boyce-Arruda differs from Flory's theory in that it captures the hardening effect in the network for high levels of swelling. Originated from the Flory's theory, Boyce-Arruda model assumes that the elasticity of the solid network is not scaled by the mass density but the crosslink density that connects the polymer chains. For this reason we define $C_s = \rho$ where ρ is the crosslink density in dry gel ($\phi_s = 1$). We would like to note that the elastic energy can also be written in terms of the

chain density (for instance in [18]) using the lattice models. The elastic energy is;

$$\begin{aligned} C_s e_s = \Psi_s(\rho, J_0, \mathbf{F}) = \rho RT \Bigg(& \frac{1}{2}(J_0^{2/3} I_1 - 3) + \frac{1}{20N}(J_0^{4/3} I_1^2 - 9) \\ & + \frac{11}{1050N^2}(J_0^{6/3} I_1^3 - 27) + \frac{19}{7000N^3}(J_0^{8/3} I_1^4 - 81) \\ & + \frac{519}{673750N^4}(J_0^{10/3} I_1^5 - 243) - \frac{1}{2}\ln(J_0 J) \Bigg) \end{aligned} \tag{4.29}$$

where R is the ideal gas constant and J_0 is the swelling ratio of the network prior to the remodeling process. Note that in order to describe the deformation during the remodeling process we apply the multiplicative decomposition $\tilde{\mathbf{F}} = \mathbf{F}\mathbf{F}_0$ and since the initial swelling of the network is isotropic $\mathbf{F}_0 = \lambda \mathbf{I}$. From this we conclude that $\lambda = J_0^{1/3}$ and $\tilde{\mathbf{F}} = J_0^{1/3}\mathbf{F}$. $I_1 = \mathrm{tr}(\mathbf{C})$ is the first invariant of the right Cauchy deformation tensor $\mathbf{C} = \mathbf{F}^T\mathbf{F}$. The elastic energy above captures the hardening of the network due to excessive deformation through the parameter N, which is the number of segments of a polymer chain between two crosslinks. As N increases, the end-to-end distance of a polymer chain can vary in a wide range, and therefore the hardening effect vanishes. In that case the model reduces to Flory's elastic energy (see Fig. 4.3). Also note that the shear modulus of this network is $G = \rho RT$. We also define a critical value ρ_c of crosslink density, at which the reverse gelation occurs and the elasticity of the polymer network vanishes:

$$\Psi_s = 0 \ \text{ if } \ \rho \leq \rho_c \tag{4.30}$$

Second part of the free energy arises from the mixing energy of the two phases and their interaction. Since we stated that the entropic contribution of solid phase is negligible, the mixing energy depends only on the fluid constituent $\alpha = w$. The mixing energy can be found from the Legendre transformation;

$$\Psi_w = C_w(e_w - T\eta_w) = RTC_w(\chi(1-\phi_w) + \ln(\phi_w)) \tag{4.31}$$

where the first term in the parenthesis is related solid-fluid interaction energy and the second term is the entropic contribution of the fluid constituent. The chemical potential ψ_w of the solvent is

interpreted as the osmotic pressure;

$$\begin{aligned} \pi &= -\frac{1}{\nu_w}\frac{\partial \Psi_w}{\partial C_w} \\ &= \frac{RT}{\nu_w}\left(\ln(\phi_w) + (1-\phi_w) + \chi(1-\phi_w)^2\right) \end{aligned} \tag{4.32}$$

The osmotic pressure π describes a chemical driving force for transport of fluid constituent w, and according to Flory's theory [46], it is equal to the elastic stress $\pi = p$ which is the mechanical pressure applied on the solid network. Note that Flory's theory considers the steady state, therefore we can use $\pi = p$ relation to find the initial swelling of the solid network. However, since the solvent molecules are considered to be close-packed hard spheres, the mass flux is driven by the elastic stress p. For this reason, we introduce the following elastic energy functional in order to define pressure p;

$$\mathcal{L} = C_w e_w = -p(J - 1 - \nu_w C_w) \tag{4.33}$$

where $\nu_w C_w = \Phi_w$ is the nominal volume fraction of the fluid. Note that p is a Lagrange multiplier, and the terms in parenthesis represent the saturation condition $(J - 1 - \nu_w C_w) = 0$. We can also interpret the saturation condition as the relation between solid deformation and the fluid volume fraction $\phi_w = (J-1)/J$ (remember $\phi_e \ll 1$). This allows us to calculate the volume fraction of the fluid constituent in the mixture directly from the solid deformation. Furthermore, using the relation (4.32) the chemical pressure applied can be calculated. We choose pressure "p" as the field variable for the solvent $\alpha = w$, which allows our formulation to be consistent with the classical poroelasticity [30].

We consider the total free energy of the mixture, i.e. the region where the remodeling occurs, as the summation of the free energies of the hydrogel and the cell released building/demolishing blocks (in our case only demolishing blocks, enzyme). The enzyme molecules are assumed to be neutral, in other words, there is no enthalpic interaction between them and the hydrogel. Since the enzyme molecules are always in fluid form and assumed to be small in volume fraction, their elastic energy is zero and their contribution to the fluid pressure is neglected. Using Legendre transformation,

the free energy of the enzyme reads;

$$\Psi_e = RTC_e \ln(\phi_e) \tag{4.34}$$

Note that $e_e = 0$ in the above equation because of zero elastic energy and no enthalpic interaction with other constituents. The enzyme molecules cleave the polymer chains by binding crosslinks to themselves and we call this process as degradation. We assume that the effect of free peptide crosslinkers on the energy state of total mixture is negligible. Furthermore, we assume that degradation process does not affect the energy state of the enzyme molecules, but it changes the crosslink density, following the Michaelis Menten kinetics equation [90];

$$\frac{D\rho}{Dt} = -\left(k' c_e \frac{\rho}{\rho + k''}\right) \tag{4.35}$$

where $k' = k_{cat}(J_0 - 1)$ and $k'' = K_M(J_0 - 1)$. k_{cat} is the maximum degradation rate, K_m is the crosslink density at which the degradation rate is halved, and, c_e is the enzyme concentration.
Finally, we will define the permeability for solvent constituent and diffusivity for enzyme. Following the work of Holmes and Mow [63], we define the apparent permeability;

$$\bar{\kappa} = \frac{a^2}{8\delta^2 \mu_w}\left(\frac{J_0 - 1}{J_0}\right) \tag{4.36}$$

where a is the effective radius of the pores, δ is the tortuosity factor, μ_w is the viscosity of the fluid (solvent), and the term in the parenthesis is the initial porosity of the structure. Furthermore, we adapted the scaling relation that is proposed by Lustig and Peppas [89];

$$\bar{D}_\alpha = \bar{D}_\alpha^\infty f(J, J_0)\left(1 - \frac{r_\alpha}{\xi(\rho, J)}\right) \tag{4.37}$$

where $\bar{D}_\alpha^\infty$ is the apparent diffusivity in pure solvent environment, $f(J, J_0) = \exp(-1/(JJ_0 - 1))$ is the probability function, r_α is the hydrodynamic radius of the diffusing particle, and, $\xi(J, \rho)$ is the mesh size of the polymer network. The detailed discussion of this scaling law can be found in [1]. The diffusivity of the macromolecules decreases with the mesh size, reaching to a zero value when the mesh size is equal to the hydrodynamic radius r_e. To increase diffusivity, crosslinking density should decrease, which can be achieved by degradation (Fig. 4.3).

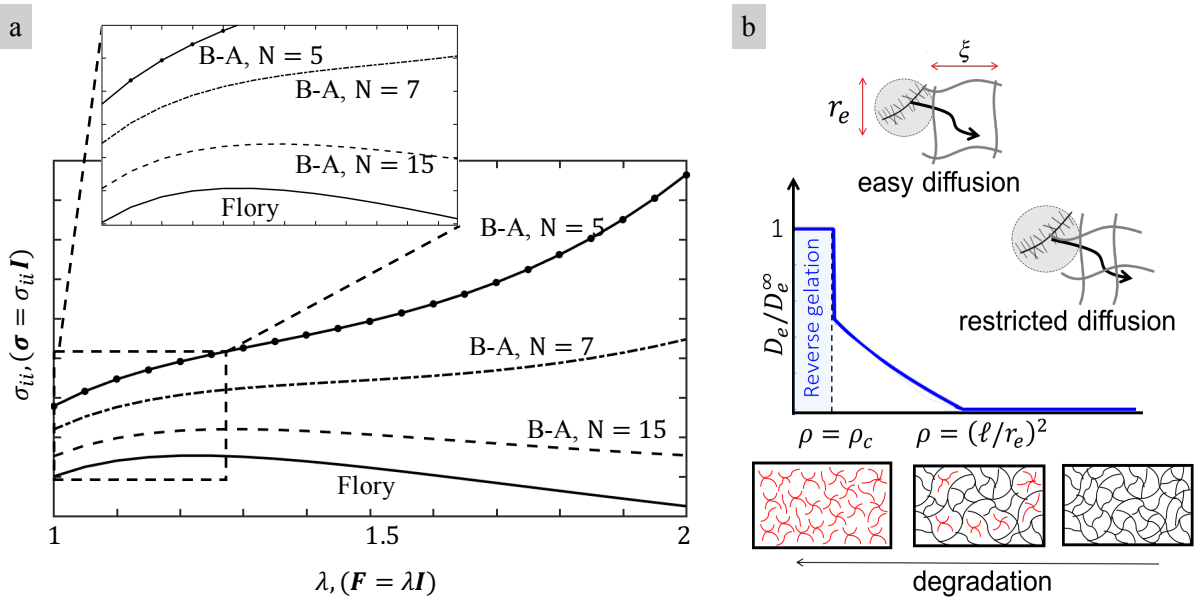

Figure 4.3: The constitutive relations of the model. (a) Boyce-Arruda (B-A) material model is a generalization of Flory's elastic potential for swollen networks. B-A captures the stiffening effect observed at high strain levels through the parameter N, which describes the level of flexibility of a polymer chain. (b) The diffusivity of cell-released particles follows the scaling law derived by Peppas et al. [89]. The diffusivity of the macromolecules decreases with the mesh size, reaching to a zero value when the mesh size is equal to the hydrodynamic radius r_e. To increase diffusivity, crosslinking density should decrease, which can be achieved by degradation.

4.3.2 Complete mathematical model and non-dimensional forms

The constitutive relations and the balance laws lead to final form of three coupled equations; (i) balance of momentum:

$$\sum_{\alpha} \nabla_{\mathbf{X}} \cdot (\mathbf{S}_{\alpha}\mathbf{F}) = 0 \tag{4.38}$$

where

$$\begin{aligned}\mathbf{S}_s = 2\frac{\partial \Psi_s}{\partial \mathbf{C}} = \rho RT \Bigg[\Bigg(1 + \frac{4}{20N} I_1 + \frac{66}{1050N^2} I_1^2 \\ + \frac{152}{7000N^3} I_1^3 + \frac{5190}{673750N^4} I_1^4\Bigg)\mathbf{I} - \frac{1}{2}\mathbf{C}^{-T}\Bigg]\end{aligned} \tag{4.39}$$

$$\mathbf{S}_w = pJC^{-1} \tag{4.40}$$

(ii) balance of mass for fluid w:

$$J(\nabla_{\mathbf{X}} \cdot \mathbf{V}) - \nabla_{\mathbf{X}} \cdot \left(\nu_w \bar{\kappa} \nabla_{\mathbf{X}} \cdot (\mathbf{C}^{-1} J p)\right) = 0 \tag{4.41}$$

and (iii) balance of mass for enzyme:

$$\frac{DC_e}{Dt} - \nabla_{\mathbf{X}} \cdot \left[\left(1 - \frac{r_e}{\xi(\rho, J)} \right) f(J, J_0) \left(C_e \frac{\bar{\kappa}\nu_w}{J-1} \nabla_{\mathbf{X}} \cdot (\mathbf{C}^{-1} J p) + \bar{D}_e^{\infty} \nabla_{\mathbf{X}} C_e \right) \right] = 0 \tag{4.42}$$

The mass balance equation (4.41) is based on poromechanics and written in terms of elastic pressure of hydrogel solvent p to govern the coupling between the solvent transport and the deformation of the solid material in the mixture. The mass balance of enzyme (4.42) governs the transport of cell-released enzyme molecules. The enzyme diffuses through the solvent, therefore its mass flux decomposed into two as explained before; (i) due to its transport by the solvent flow (first term in the parenthesis in (4.42)), and (ii) due to its concentration gradient in the solvent medium (second term in the parenthesis in (4.42)). Note that we applied the scaling factor from (4.37) to both flux terms because it applies to total flux of a macromolecule in a porous medium. In this study we decompose this motion to two parts; but overall, summation of these two is equal to the total mass flux for which the scaling law is derived in [89].

In addition to these equations, the balance of mass of polymer network (or the solid material of hydrogel) (4.1) and the degradation kinetics (4.35) leads to an evolution equation for crosslinking density ρ;

$$\Gamma_s = -\left(k' \frac{\rho(C_e/J)}{\rho + k''} \right) \tag{4.43}$$

where we interpret the degradation process as the conversion of solid material into fluid.

4.3.3 Non-dimensional form of the mathematical model

The governing equations given above applies at different scales, for instance length scale for the the transport of fluid constituents are different. The difference in the length scales can affect our solution approach and cause some numerical problems. To resolve this, we non-dimensionalize the governing equations using the following non-dimensional variables;

$$\mathbf{X}^{\star} = \frac{\mathbf{X}}{L}, \quad t^{\star} = \frac{tD_{\infty}^{e}}{L^2}, \quad p^{\star} = \frac{p}{RT}, \quad C_e^{\star} = \frac{C_e}{C_e^0}, \quad \rho^{\star} = \frac{\rho}{\rho_c} \tag{4.44}$$

where L is the characteristic length of the domain investigated, C_e^0 is the nominal concentration of enzyme in a native tissue [1]. We assume that the domain of interest is a cube with volume L^3 where $L = R_c\sqrt[3]{4\pi/3f}$, R_c is the cell radius and f is the cell density. The non-dimensional equations are;

$$\sum_{\alpha} \nabla_{\mathbf{X}}^{\star} \cdot (\mathbf{S}_{\alpha}^{\star}\mathbf{F}) = 0 \tag{4.45}$$

$$J(\nabla_{\mathbf{X}}^{\star} \cdot \mathbf{V}^{\star}) - \nabla_{\mathbf{X}}^{\star} \cdot \left((\Delta_{we})\nabla_{\mathbf{X}}^{\star} \cdot (\mathbf{C}^{-1}Jp^{\star})\right) = 0 \tag{4.46}$$

$$\begin{aligned}\frac{DC_e^{\star}}{Dt^{\star}} - \nabla_{\mathbf{X}}^{\star} \cdot \Big[& f(J, J_0)J^{-1/3}(J^{1/3} - r_e^{\star}\sqrt{\rho^{\star}}) \\ & \left(C_e^{\star}\frac{\Delta_{we}}{J-1}\nabla_{\mathbf{X}}^{\star} \cdot (\mathbf{C}^{-1}Jp^{\star}) + \nabla_{\mathbf{X}}^{\star}C_e^{\star}\right)\Big] = 0\end{aligned} \tag{4.47}$$

$$\Gamma_s = -\left(\kappa_e^I \frac{\rho^{\star}(C_e^{\star}/J)}{\rho^{\star} + \kappa_e^{II}}\right) \tag{4.48}$$

where the non-dimensional parameters are;

$$\Delta_{we} = \frac{\nu_w \bar{\kappa} RT}{D_e^{\infty}}, \quad r_e^{\star} = \frac{r_e}{\ell}, \quad \kappa_e^I = \frac{k' C_e^0 L^2}{D_e^{\infty}\rho_c}, \quad \kappa_e^{II} = \frac{k''}{\rho_c} \tag{4.49}$$

where $\ell = l\sqrt{3\rho^p C_n/(M_r\rho_c)}$ is the lumped length parameter and C_n is the characteristic ratio that defines the restricted rotation of a single polymer chain link, l is the average bond length in polymer, M_r is the molar weight of the polymer repeat unit and ρ^p is the density of polymer[1]. The non-dimensional stress tensors are $\mathbf{S}_{\alpha}^{\star} = \mathbf{S}_{\alpha}/RT$. Δ_{we} compares the transport speed of solvent molecules to the same of enzyme molecules. $r_e^{\star}$ is the ratio of the hydrodynamic radius of enzyme molecules to the mesh size of the polymer network right before reverse gelation ($\rho = \rho_c$). κ_e^I describes the competition between the degradation and enzyme transport, which, together with $r_e^{\star}$, affects the degradation characteristics of the gel as discussed in the results section. κ_e^{II} is the ratio of the gel's crosslinking density at half degradation rate and reverse gelation. Note that deformation metrics $\mathbf{C}$, $\mathbf{F}$ and J are non-dimensional by definition. In the further sections of this study we will use the non-dimensional forms and we will drop $\star$ for convenience. Note that non-dimensionalization using RT is valid only under the assumption of constant temperature.

4.4 Finite element formulation and numerical aspects

In order to solve the non-linear coupled governing equations, we follow the Newton-Raphson method. In this method, we linearize the system of equations with respect to the field variables that we solve for. For the system of equations introduced in the previous section, vector of field variables becomes:

$$\mathbf{d} = \begin{bmatrix} \mathbf{u} & p & C_e \end{bmatrix}^T . \tag{4.50}$$

Since the system we consider is transient, we define the time derivatives of this field variables as $\delta\mathbf{d} = \delta\dot{\mathbf{d}}\Delta t$. Now consider that $\mathbf{F}_{\text{ext}}$ is the vector of forces (or fluxes) applied on the boundary of the domain $\partial\Omega$, $\mathbf{F}_{\text{int}}$ is the system's response (force or flux). At the solution, these two forces should be at equilibrium. Using Newton-Raphson method, we can approximate the difference between these two forces as:

$$\mathbf{R}(\mathbf{d}, \dot{\mathbf{d}}) = \mathbf{F}_{\text{ext}} - \mathbf{F}_{\text{int}} \tag{4.51}$$

$$\mathbf{R}(\mathbf{d}, \dot{\mathbf{d}}) \approx \mathbf{R}(\mathbf{d}_0, \dot{\mathbf{d}}_0) + \left(\frac{\partial \mathbf{R}(\mathbf{d}, \dot{\mathbf{d}})}{\partial \mathbf{d}}\right) \delta\mathbf{d} + \left(\frac{\partial \mathbf{R}(\mathbf{d}, \dot{\mathbf{d}})}{\partial \dot{\mathbf{d}}}\right) \delta\dot{\mathbf{d}} \tag{4.52}$$

and since at solution $\mathbf{R}(\mathbf{d}, \dot{\mathbf{d}}) = 0$

$$\boldsymbol{C}\ \delta\dot{\mathbf{d}} + \mathbf{K}\ \delta\mathbf{d} = -(\mathbf{F}_{\text{ext}} - \mathbf{F}_{\text{int}}) \tag{4.53}$$

where $\boldsymbol{C}$ and $\mathbf{K}$ are the damping and stiffness matrices respectively. Those terms will be described in detail later. For now, let us assume that we know the force vectors and damping and stiffness matrices. The system is first solved for the $\dot{\mathbf{d}}$ iteratively;

$$\dot{\mathbf{d}}^i(t + \Delta t) = \dot{\mathbf{d}}^{i-1}(t + \Delta t) + \delta\dot{\mathbf{d}}^i \tag{4.54}$$

using the following linear system of equations:

$$\begin{aligned} \left(\boldsymbol{C}^{i-1}(t + \Delta t) + \mathbf{K}^{i-1}(t + \Delta t)\Delta t\right) \delta\dot{\mathbf{d}}^i(t + \Delta t) \\ = -\mathbf{F}_{\text{ext}}(t + \Delta t) + \mathbf{F}_{\text{int}}^{i-1}(t + \Delta t) \end{aligned} \tag{4.55}$$

then the solution $\mathbf{d}$ is found using backward Euler time integration;

$$\mathbf{d}^i(t + \Delta t) = \mathbf{d}^i(t) + \Delta t\dot{\mathbf{d}}^i(t + \Delta t) \tag{4.56}$$

Now let us explain the finite element implementation of the system of equations.

4.4.1 Weak form, linearization and discretization

Let us start by writing the weak form, using the test functions w^{α}:

$$\int_{\Omega_0} \sum_{\alpha} (\mathbf{w}^s) \cdot (\boldsymbol{\nabla}_{\mathbf{X}} \cdot \mathbf{S}_{\alpha}\mathbf{F}) dV = 0 \tag{4.57}$$

using divergence theorem;

$$\int_{\Omega_0} (\boldsymbol{\nabla}_{\mathbf{X}} \mathbf{w}^s) : \sum_{\alpha} (\mathbf{S}_{\alpha}\mathbf{F}) dV = \int_{\partial\Omega_0} \mathbf{w}^s \cdot \sum_{\alpha} \mathbf{t}_{\alpha} dS \tag{4.58}$$

where the left hand side corresponds to $\mathbf{F}_{\text{int}}$ while the right hand side is assembled to $\mathbf{F}_{\text{ext}}$. The weak form of mass balance of solvent is as follows;

$$\int_{\Omega_0} (\mathbf{w}^w) \left[J(\nabla_{\mathbf{X}} \cdot \mathbf{V}) - \nabla_{\mathbf{X}} \cdot \left((\Delta_{we}) \nabla_{\mathbf{X}} \cdot (\mathbf{C}^{-1} J p) \right) \right] dV = 0 \tag{4.59}$$

applying the divergence theorem;

$$\begin{aligned} \int_{\Omega_0} \left[(\mathbf{w}^w) J(\nabla_{\mathbf{X}} \cdot \mathbf{V}) + (\nabla_{\mathbf{X}} \mathbf{w}^w) \cdot \left((\Delta_{we}) \nabla_{\mathbf{X}} \cdot (\mathbf{C}^{-1} J p) \right) \right] dV \\ = \int_{\partial\Omega_0} \mathbf{w}^w \mathbf{Q}_w \cdot \mathbf{N} dS \end{aligned} \tag{4.60}$$

Similarly the weak form of the equation (4.47) is;

$$\begin{aligned} \int_{\Omega_0} (\mathbf{w}^e) \Bigg[\frac{DC_e}{Dt} - \nabla_{\mathbf{X}} \cdot \Big(f(J, J_0) J^{-1/3} (J^{1/3} - r_e \sqrt{\rho}) \\ \left(C_e \frac{\Delta_{we}}{J-1} \nabla_{\mathbf{X}} \cdot (\mathbf{C}^{-1} J p) + \nabla_{\mathbf{X}} C_e \right) \Big) \Bigg] dV = 0 \end{aligned} \tag{4.61}$$

$$\begin{aligned} \int_{\Omega_0} \Bigg[(\mathbf{w}^e) \frac{DC_e}{Dt} + (\nabla_{\mathbf{X}} \mathbf{w}^e) \cdot \Big(f(J, J_0) J^{-1/3} (J^{1/3} - r_e \sqrt{\rho}) \\ \left(C_e \frac{\Delta_{we}}{J-1} \nabla_{\mathbf{X}} \cdot (\mathbf{C}^{-1} J p) + \nabla_{\mathbf{X}} C_e \right) \Big) \Bigg] dV = \int_{\partial\Omega_0} \mathbf{w}^e \mathbf{Q}_e \cdot \mathbf{N} dS \end{aligned} \tag{4.62}$$

Note that in equations (4.60) and (4.62), the left hand side is assembled to $\mathbf{F}_{\text{int}}$ while the right hand side is assembled to $\mathbf{F}_{\text{ext}}$. We discretize these weak forms following finite element method. However, before applying finite element discretization, it is essential to define the two subsets of

our domain Ω region of cells and the construct (hydrogel + cell released blocks). We use level set function $\phi(\mathbf{X})$ to define the cell boundaries:

$$\begin{aligned} \mathbf{X} \in \Omega_c \ \text{ if } \ \phi(\mathbf{X}) < 0 \\ \mathbf{X} \in \Omega_g \ \text{ if } \ \phi(\mathbf{X}) > 0 \end{aligned} \tag{4.63}$$

where Ω_c and Ω_g are the domains of cells and construct respectively. A mesh refinement is performed on the surfaces $\phi(\mathbf{X}) = 0$, on which cell boundary condition is defined, therefore this surface is denoted as $\partial\Omega_c$. We use mixed $u - p$ formulation for the finite element discretization. We use quadratic shape functions for the displacement field and linear (first order) shape functions for pressure and concentration fields. We have two types of elements: hexahedral and tetrahedral. In the proximity of the cell boundary $\partial\Omega_c$, we use 10-node tetrahedral elements for displacement and 4-node of the same for pressure and enzyme concentration. The remaining regions are discretized with hexahedral elements; 27-node for displacement field and 8-node for pressure and concentration fields. The shape functions are derived using Lagrange polynomials [2]. Gauss quadrature rule for the quadratic polynomials is used for integration. We consider ρ as a state variable and store its value at the integration points during the analysis, while it is interpolated to the nodes for postprocessing purposes. The nodal discretization of the field variables in an element are; $\mathbf{u} = \mathbf{N}_I^{(2)}\widetilde{\mathbf{u}}_I^e$, $p = \mathbf{N}_I^{(1)}\widetilde{\mathbf{p}}_I^e$, $C_e = \mathbf{N}_I^{(1)}(\widetilde{\mathbf{C}}_e)_I^e$, where $\mathbf{N}_I^{(2)}$ and $\mathbf{N}_I^{(1)}$ are vectors of quadratic and linear shape functions respectively. Furthermore, as a part of Galerkin approximation, we choose the same shape functions for $\mathbf{w}$; $\mathbf{w}^s = \mathbf{N}_{IJ}\widetilde{\mathbf{w}}_{IJ}^s$ ($I = 1, 2, 3$ and $J = 1, ..., 10$ or 27) and $w^\alpha = \mathbf{N}_J\widetilde{\mathbf{w}}_J^\alpha$ ($J = 1, ..., 4$ or 8). Note that there are three test functions for the displacement field, one for each direction. The linearization with respect to the field variables are performed as follows [16]

$$\begin{aligned} \int_{\Omega_0} (\boldsymbol{\nabla}_{\mathbf{X}} \mathbf{w}^s) : \sum_\alpha \left(\frac{\partial \mathbf{S}_\alpha}{\partial \mathbf{u}} \mathbf{F}\delta\mathbf{u} + \frac{\partial \mathbf{S}_\alpha}{\partial p} \mathbf{F}\delta p + \mathbf{S}_\alpha \frac{\partial \mathbf{F}}{\partial \mathbf{u}} \delta\mathbf{u} \right) dV \\ = \int_{\partial\Omega_0} \mathbf{w}^s \cdot \sum_\alpha \mathbf{t}_\alpha dS \end{aligned} \tag{4.64}$$

$$\text{where} \quad \sum_\alpha \mathbf{S}_\alpha = \begin{cases} \mathbf{S}_s + \mathbf{S}_w & \text{if } \mathbf{X} \in \Omega_g \\ S_c = \lambda_c \text{tr}(\mathbf{E})\mathbf{I} + \mathbf{2}\mu_\mathbf{c}\mathbf{E} & \text{if } \mathbf{X} \in \Omega_c \end{cases}$$

$$\int_{\Omega_0}\Bigg[(\mathbf{w}^w)\left(\frac{\partial J}{\partial \mathbf{u}}\nabla_{\mathbf{X}}\cdot\mathbf{V}\delta\mathbf{u}+J\nabla_{\mathbf{X}}\cdot\delta\mathbf{V}\right)$$
$$+(\nabla_{\mathbf{X}}\mathbf{w}^w)\cdot\Delta_{we}\left((\nabla_{\mathbf{X}}p)^T\cdot\frac{\partial(\mathbf{C}^{-1}J)}{\partial\mathbf{u}}\delta u+\mathbf{C}^{-1}J\cdot\nabla_{\mathbf{X}}\delta p\right)\Bigg]dV \tag{4.65}$$
$$=\int_{\partial\Omega_0}\mathbf{w}^w\mathbf{Q}_w\cdot\mathbf{N}dS$$

$$\int_{\Omega_0}\Bigg[(\mathbf{w}^e)\delta\dot{C}_e+(\nabla_{\mathbf{X}}\mathbf{w}^e)\cdot\frac{\Delta_{we}}{J-1}\left(f(J,J_0)J^{-1/3}(J^{1/3}-r_e\sqrt{\rho})\right)$$
$$\left(\delta C_e(\mathbf{C}^{-1}J)(\nabla_{\mathbf{X}}\cdot p)+C_e(\nabla_{\mathbf{X}}p)^T\cdot\frac{\partial(\mathbf{C}^{-1}J)}{\partial\mathbf{u}}\delta u+\right. \tag{4.66}$$
$$\left.C_e(\mathbf{C}^{-1}J)\cdot\nabla_{\mathbf{X}}\delta p+\nabla_{\mathbf{X}}\delta C_e\right)\Bigg]dV=\int_{\partial\Omega_0}\mathbf{w}^e\mathbf{Q}_e\cdot\mathbf{N}dS$$

Note that λ_c and μ_c are Lame parameters for cell stiffness. In the above linearization procedure, we neglect the gradients of deformation metrics ($\mathbf{F}$ and J). The reason is that we use first order approximation for the mapping between current and the reference frame ($d\mathbf{x}=\mathbf{F}d\mathbf{X}$) while such gradients require a higher order approximation. Note that this is not related with the numerical implementation. Further discussion about the higher order approximation of deformation mapping can be found in [78]. We discretize the linearized forms to element volumes Ω_0^e, which, in order to find the final system of equations, are assembled after the calculation over the elements. Using the interpolation functions to the field variables and applying Galerkin's method, we find the following stiffness and damping matrices;

$$\mathbf{K}_{ss}^e=\int_{\Omega_0^e}\mathbf{B}_1^T\left(\sum_\alpha\frac{\partial\mathbf{S}_\alpha}{\partial\mathbf{C}}\right)\mathbf{B}_1dV+\int_{\Omega_0^e}\mathbf{B}_0^T\left(\sum_\alpha\mathbf{S}_\alpha\right)\mathbf{B}_0dV \tag{4.67}$$

$$\text{where}\quad\sum_\alpha(\partial\mathbf{S}_\alpha/\partial\mathbf{C})=\begin{cases}\mathbb{C}_s-p\mathbb{C}_w & \text{if } \mathbf{X}\in\Omega_g\\ \mathbb{C}_c & \text{if } \mathbf{X}\in\Omega_c\end{cases} \tag{4.68}$$

and

$$\mathbb{C}_s=\rho RT\left[\left(\frac{2}{5N}+\frac{44}{175N^2}I_1+\frac{114}{875N^3}I_1^2+\frac{4152}{67375N^4}I_1^3\right)\mathbf{I}\otimes\mathbf{I}-\boldsymbol{\mathcal{I}}\right] \tag{4.69}$$

$$\mathbb{C}_w=J\left(\frac{1}{2}\mathbf{C}^{-1}\otimes\mathbf{C}^{-1}+\boldsymbol{\mathcal{I}}\right) \tag{4.70}$$

where $\mathcal{I}_{IJKL}=-\frac{1}{2}\left[(C^{-1})_{IK}(C^{-1})_{JL}+(C^{-1})_{IL}(C^{-1})_{JK}\right]$ is a fourth order tensor and $\mathbb{C}_c$ is the cell stiffness matrix, which is based on linear elasticity.

$$\mathbf{K}_{sw}^e=\int_{\Omega_0^e}\mathbf{B}_1^T(J\mathbf{C}^{-1})N^{(1)}dV \tag{4.71}$$

$$\mathbf{K}^e_{sw} = \int_{\Omega^e_0} (\mathbf{N}^{(1)})^T J \mathbf{F}^{-T} (\nabla_{\mathbf{X}} \cdot \dot{\mathbf{u}}) \mathbf{B}_0 dV + \int_{\Omega^e_0} (\mathbf{B}_2)^T \Delta_{we} (\nabla_{\mathbf{X}} p) \mathbb{C}_w \mathbf{B}_1 dV \tag{4.72}$$

$$\mathbf{C}^e_{ws} = \int_{\Omega^e_0} (\mathbf{N}^{(1)})^T J \mathbf{B}_0 dV \tag{4.73}$$

$$\mathbf{K}^e_{ww} = \int_{\Omega^e_0} (\mathbf{B}_2)^T \Delta_{we} (J\mathbf{C}^{-1}) (\mathbf{B}_2) dV \tag{4.74}$$

$$\mathbf{K}^e_{es} = \int_{\Omega^e_0} \left(f(J, J_0) J^{-1/3} (J^{1/3} - r_e \sqrt{\rho}) \right) (\mathbf{B}_2)^T \frac{\Delta_{we}}{J-1} C_e (\nabla_{\mathbf{X}} p) \mathbb{C}_w (\mathbf{B}_1) dV \tag{4.75}$$

$$\mathbf{K}^e_{ew} = \int_{\Omega^e_0} (\mathbf{B}_2)^T \left(f(J, J_0) J^{-1/3} (J^{1/3} - r_e \sqrt{\rho}) \right) \left(\frac{\Delta_{we}}{J-1} C_e (J\mathbf{C}^{-1}) \right) (\mathbf{B}_2) dV \tag{4.76}$$

$$\begin{aligned} \mathbf{K}^e_{ee} = \int_{\Omega^e_0} (\mathbf{B}_2)^T \left(\left(f(J, J_0) J^{-1/3} (J^{1/3} - r_e \sqrt{\rho}) \right) \frac{\Delta_{we}}{J-1} C_e (J\mathbf{C}^{-1}) (\nabla_{\mathbf{X}} p) \right) (\mathbf{N}_{(1)}) dV \\ + \int_{\Omega^e_0} (\mathbf{B}_2)^T \left[\frac{\Delta_{we}}{J-1} f(J, J_0) J^{-1/3} \left(J^{1/3} - \frac{r_e}{\sqrt{\rho}} \right) \right] (\mathbf{B}_2) dV \end{aligned} \tag{4.77}$$

$$\mathbf{C}^e_{ee} = \int_{\Omega^e_0} (\mathbf{N}_{(1)})^T (\mathbf{N}_{(1)}) dV \tag{4.78}$$

These stiffness and damping matrices are can be assembled at the element level as follows;

$$\mathbf{K}^e = \begin{bmatrix} \mathbf{K}_{ss} & \mathbf{K}_{sw} & \mathbf{0} \\ \mathbf{K}_{ws} & \mathbf{K}_{ww} & \mathbf{0} \\ \mathbf{K}_{es} & \mathbf{K}_{ew} & \mathbf{K}_{ee} \end{bmatrix}, \boldsymbol{C}^e = \begin{bmatrix} \mathbf{0} & \mathbf{0} & \mathbf{0} \\ \mathbf{C}_{ws} & \mathbf{0} & \mathbf{0} \\ \mathbf{0} & \mathbf{0} & \mathbf{C}_{ee} \end{bmatrix}.$$

Then the element stiffness and damping matrices can be assembled to the global ones: $\mathbf{K} = \mathbb{A}^{nel}_{n=1} \mathbf{K}^e_n$ and $\boldsymbol{C} = \mathbb{A}^{nel}_{n=1} \boldsymbol{C}^e_n$. Finally, the non discretized terms in the above linearized weak form (for instance J, C_e or $\mathbb{C}_w$) are calculated using the values of variables calculated in previous Newton Raphson iteration; $d^{(}_I i) = N^{(a)}_J (\widetilde{d^{(}_I} i))_J$ where $a = 1, 2$ is the order of interpolation, i is the iteration index, $J = 1, 2, 3$ is the index for the field variables. Once again, note that ρ is calculated and stored at the integration points.

4.4.2 Concept of representative volume element and homogenization

The model presented above investigates the mechanics of biological remodeling at the cellular scale. The stress and strain states of the construct at the macro-scale are calculated by performing the classical homogenization numerically in the domain Ω_0;

$$\bar{\mathbf{u}}(\mathbf{X}, t) = \bar{\mathbf{F}} \cdot \mathbf{X} + \bar{\tilde{\mathbf{u}}}(\mathbf{X}, \mathbf{t}) \tag{4.79}$$

$$\bar{\mathbf{F}} = \frac{1}{V_0}\int_{\Omega_0} \mathbf{F} dV \tag{4.80}$$

$$\bar{\mathbf{P}} = \frac{1}{V_0}\int_{\partial\Omega_0} \mathbf{t} \otimes \mathbf{X} dS = \frac{1}{V_0}\int_{\Omega_0} \mathbf{P} dV \tag{4.81}$$

where $\bar{\mathbf{u}}(\mathbf{X}, t)$, $\bar{\mathbf{F}}$ and $\bar{\mathbf{P}}$ are macroscopic displacement field, deformation gradient and nominal stress (PK1) tensor respectively. $\bar{\tilde{\mathbf{u}}}$ is the displacement fluctuations. Then, the macroscopic secant modulus of the construct can be calculated as;

$$E_{ii} = \frac{\bar{P}_{ii}}{\bar{F}_{ii}} \tag{4.82}$$

where P_{ii} is the only non-zero component of the stress tensor, i.e. $i = 1$ or 2 or 3. without summation. The chosen domain for modeling purpose is a representative volume element (RVE) of the actual construct (see Figure 4.4). The homogenization procedure described above is applied to RVE which is a cube with an edge length L.

4.4.2.1 Initial and boundary conditions

The RVE is assumed to be a repeating unit in the construct, therefore periodicity of the fields should be satisfied. The periodic boundary conditions on the outer surface of RVE are;

$$\mathbf{g}|_{S_+} - \mathbf{g}|_{S_-} = L(\bar{\nabla}_{\mathbf{X}}\mathbf{g}) \tag{4.83}$$

where S_+ and S_- are the negative and positive surfaces of the RVE, assuming the origin is at the center of the RVE. Term $(\bar{\nabla}_{\mathbf{X}}\mathbf{g})$ is the macroscopic gradient of the field variables $\mathbf{g} = \{\mathbf{u}, p, C_e\}$. The cells are also periodic in the RVE, i.e. if there is a cell cut by S_+ then there should be another cell cut by S_-.

Due to the transient nature of the problem initial conditions of the field variables should be defined. Firstly, the enzyme concentration C_e in the RVE is initially zero; $C_e(\mathbf{X}, 0) = 0 \quad \forall \mathbf{X}$. Moreover initial displacement field at the beginning of the remodeling is zero; $\mathbf{u}(\mathbf{X}, 0) = 0 \quad \forall \mathbf{X}$. Note that $\mathbf{u}(\mathbf{X}, 0)$ is not the absolute displacement field; the decomposition rule of the deformation gradient described before gives the total deformation ($\tilde{\mathbf{F}} = J_0^{1/3}\mathbf{F}$). In order to calculate initial deformation

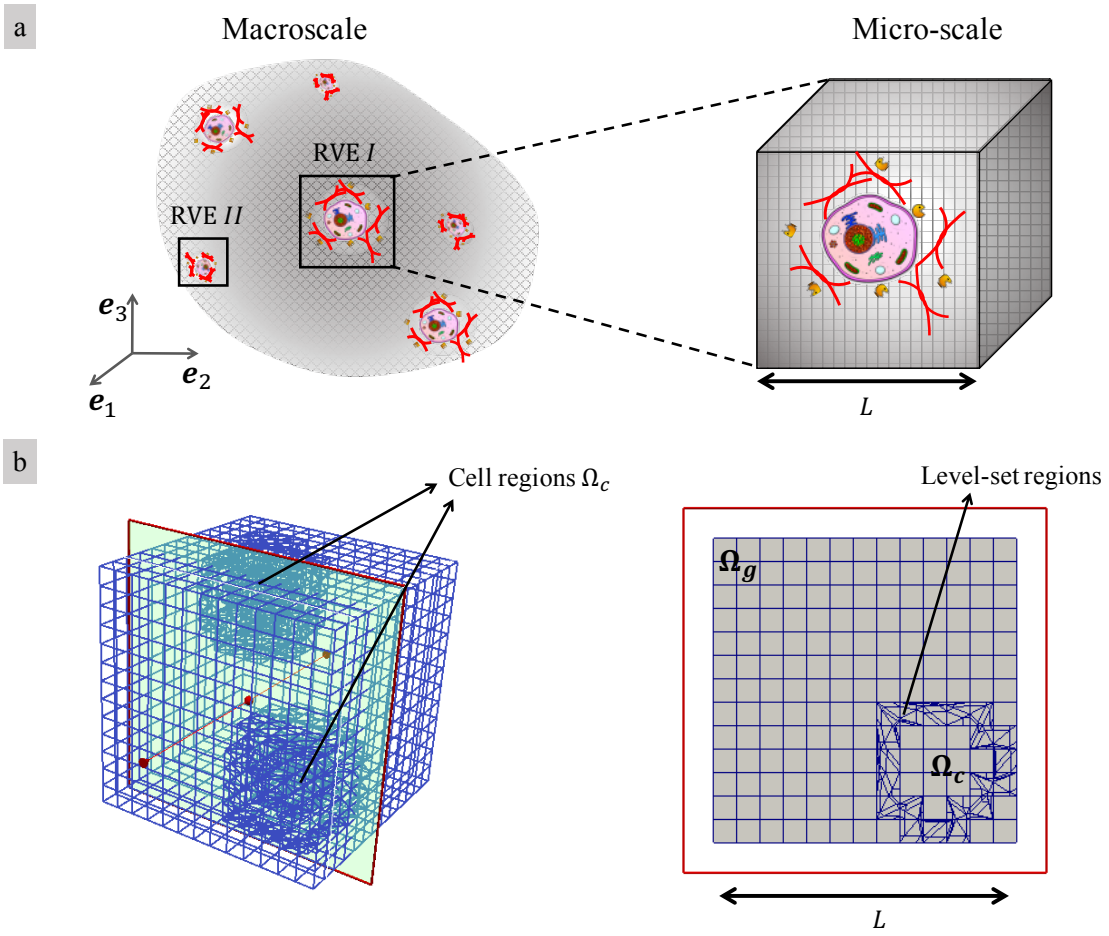

Figure 4.4: (a) For the scaffold remodeling simulations we use two RVE's; (I) far from the boundaries of macro-scale domain and (II) in the vicinity of the macro-scale boundaries. (b) RVEs contain two cells as shown in the figure. The mesh is built using level set method. Since the periodicity is assumed, the cell distribution in $RVE - I$ and $RVE - II$ are the same.

(swelling) of the hydrogel, we use the Flory's theory;

$$\begin{aligned} \sum_{\alpha} \mathbf{P}_{\alpha} &= 0 \\ \pi &= \frac{RT}{\nu_w}\left(\ln(\phi_w) + (1-\phi_w) + \chi(1-\phi_w)^2\right) \end{aligned} \tag{4.84}$$

A detailed discussion of this can be found in [2]. Solution of these two equations gives the initial condition for the pressure field ($p = \pi$) and J_0. Once again, we would like to note that the coupled system of equations above is based on Flory-Huggins theory and provides the steady state solution

for the swollen networks. We refer to the Hildebrand's theory [61] for the transient modeling of the swollen networks. That approach is not in the scope of this study. We also would like to note that the boundary conditions given in this section apply to all examples presented in the results section. The example-specific boundary conditions will be described for each case separately.

4.5 Results and Discussion

In this section, several examples are investigated to verify our modeling approach. First the Clausius-Duhem inequality is revisited, next the stress-strain relation of the construct is compared to the Mori-Tanaka solution for heterogeneous materials. Next we investigate the model's poroelasticity feature by comparing it to analytical solution of Mandel's problem, for which we also performed convergence study. Next we discuss the two extreme characteristics of degradation of scaffold, and afterwards we show the effect of fluid flow (convection) on degradation characteristics.

4.5.1 Revisiting the Clausius-Duhem Inequality

The final form of inequality represented in (4.28) leads to the following form after plugging the constitutive relations and using the balance of mass defined above;

$$\mathbf{P}_w : (\nabla_{\mathbf{X}} \tilde{\mathbf{V}}_w) + \Gamma_s (e_s - e_s^f) \leq 0 \tag{4.85}$$

which dictates two constraints on the system. Firstly the degradation should reduce the energy state of the polymer network; $e_s > e_s^f$. This is satisfied by the definition (4.30). Furthermore, the entropic contribution of the converted material $-RC_s^f \ln \phi_s^f > 0$ where ϕ_s^f is the volume fraction of the converted material. Bryant et al. [21] showed that the entropy can be used as a measure of degradation, therefore a direct constitutive relation can be built between the degradation kinetics and change in entropy. Derivation of such constitutive relation is beyond the scope of this study however we would like to note that the increase in entropy due to $-RC_s^f \ln \phi_s^f$ is consistent with the work of [21]. Second constraint is related fluid flow. Since the pressure in the fluid phase is in compression, and by definition $\mathbf{P}_w < 0$, which leads $(\nabla_{\mathbf{X}} \tilde{\mathbf{V}}_w) > 0$. The meaning of this inequality

is that during the remodeling the fluid flux incoming to the system is greater than the outgoing flux. This can also be interpreted as the increase of fluid mass, i.e. increase in the ϕ_w and therefore, increase in the volumetric deformation J. We actually observe this outcome when the Flory-Rehner theory is applied to find the steady state swelling ratio of the hydrogels with various crosslinking density (see Fig. 4.5).

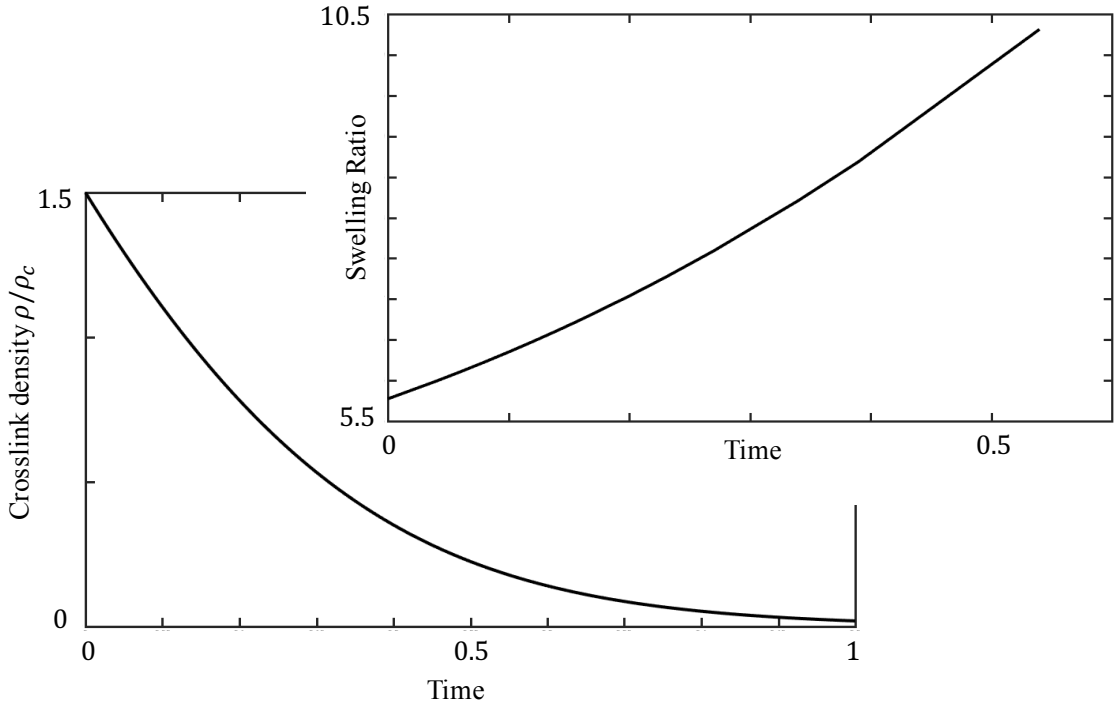

Figure 4.5: (a) The degradation of the hydrogel at constant enzyme concentration following the rule (4.48) where $\kappa_e^I = 20$, $\kappa_e^{II} = 2$, $\rho = 1.5$ and $C_e = 1$. The corresponding swelling ratios are calculated using the Flory's steady state solution, where $\rho_c = 0.08$ Mole/Liter. As the degradation progresses, the mass of fluid, and therefore the swelling ratio, increases. The swelling is due to the incoming fluid flux $\nabla_{\mathbf{X}}\tilde{\mathbf{V}}_w > 0$.

4.5.2 Model comparison with Mori-Tanaka analytic solution

We next investigate the capability of our model to capture the heterogeneity of materials. For that we consider the case of composite material in which soft spherical inclusions are added to a isotropic matrix. Based on the concept of averaged stress in the material, Mori-Tanaka solution

Table 4.1: Inputs used in the model.

Parameter	Definition	Value	Unit	Reference
k_e^0	Enzyme production rate	6×10^{-16}	$\frac{Mole}{cell \cdot week}$	[1]
C_e^0	Enzyme concentration at homeostasis	1.8×10^{-15}	$Mole$	[1]
r_{cell}	Cell radius	5	μm	[1]
$\beta = \rho_c/\rho$	Network connectivity	0.6		
D_∞^e	Diffusion of enzyme in pure solvent	6.6×10^{-7}	mm^2/s	[1]
T	Absolute temperature	310	K	
R	Gas constant	8.314	J/$(K \cdot Mole)$	
L	Length scale (cell spacing)	40	μm	
N	Number of rigid links between crosslinks	5	-	
χ	Polymer solvent interaction parameter	0.467	-	
κ	Permeability	5×10^{-6}	-	

for the bulk κ_M and shear moduli μ_M of the material are [86];

$$\kappa_M = \kappa_g + \frac{\phi_c}{\frac{1}{\kappa_c - \kappa_g} + \frac{3(1-\phi_c)}{3\kappa_g + 4\mu_g}} \tag{4.86}$$

$$\mu_M = \mu_g + \frac{\phi_c}{\frac{1}{\mu_c - \mu_g} + \frac{6(1-\phi_c)(\kappa_g + 2\mu_g)}{5\mu_g(3\kappa_g + 4\mu_g)}} \tag{4.87}$$

where κ_M and μ_M are the bulk and shear moduli of the composite, κ_g and μ_g are the moduli of the matrix (which is the domain Ω_g), κ_c and μ_c (which is the domain Ω_c) are the moduli, ϕ_c volume fraction of the inclusions. The elastic modulus can then be calculated as $E_M = (9\kappa_M\mu_M/(3\kappa + \mu_M))$. For our model we calculate the composite's elastic modulus $\bar{E}$ using the homogenization scheme described above. The bulk and shear moduli of the inclusions can be directly calculated form Lame parameters [16]. In particular, the matrix bulk modulus chosen to be high in order to define a nearly incompressible material for the calculations of (4.86) and (4.87). The material properties chosen for the elastic properties are presented in Table 4.1. Since the loading rates are relatively high compared to transport speed, we assumed a constant fluid pressure $p = \pi_0$ for $\mathbf{X} \in \Omega_g$, where π_0 is calculated from the initial conditions. Since we do not consider the evolution of the composite, we assume enzyme concentration is held zero; $C_e = 0$, $\forall \mathbf{X}$ and $\forall t$. The macroscopic nominal strain

applied is 20%;

$$\mathbf{u})|_{S_+} - \mathbf{u}|_{S_-} = \begin{cases} \frac{\partial u_x}{\partial X} = \sqrt{-\frac{\partial u_z}{\partial Z}} & \text{on } x_-,\ x_+ \\ \frac{\partial u_y}{\partial Y} = \sqrt{-\frac{\partial u_z}{\partial Z}} & \text{on } y_-,\ y_+ \\ L\frac{\partial u_z}{\partial Z} = -0.2 & \text{on } z_-,\ z_+ \\ 0 & \text{else} \end{cases} \tag{4.88}$$

where u_x, u_y, u_z are the displacement fields in x,y,z-directions respectively and they are normal on the corresponding surfaces. The non-zero transverse strain is due to the incompressibility. The comparison of model to the analytical solution is presented in Fig. 4.6,which shows a good match of both results.

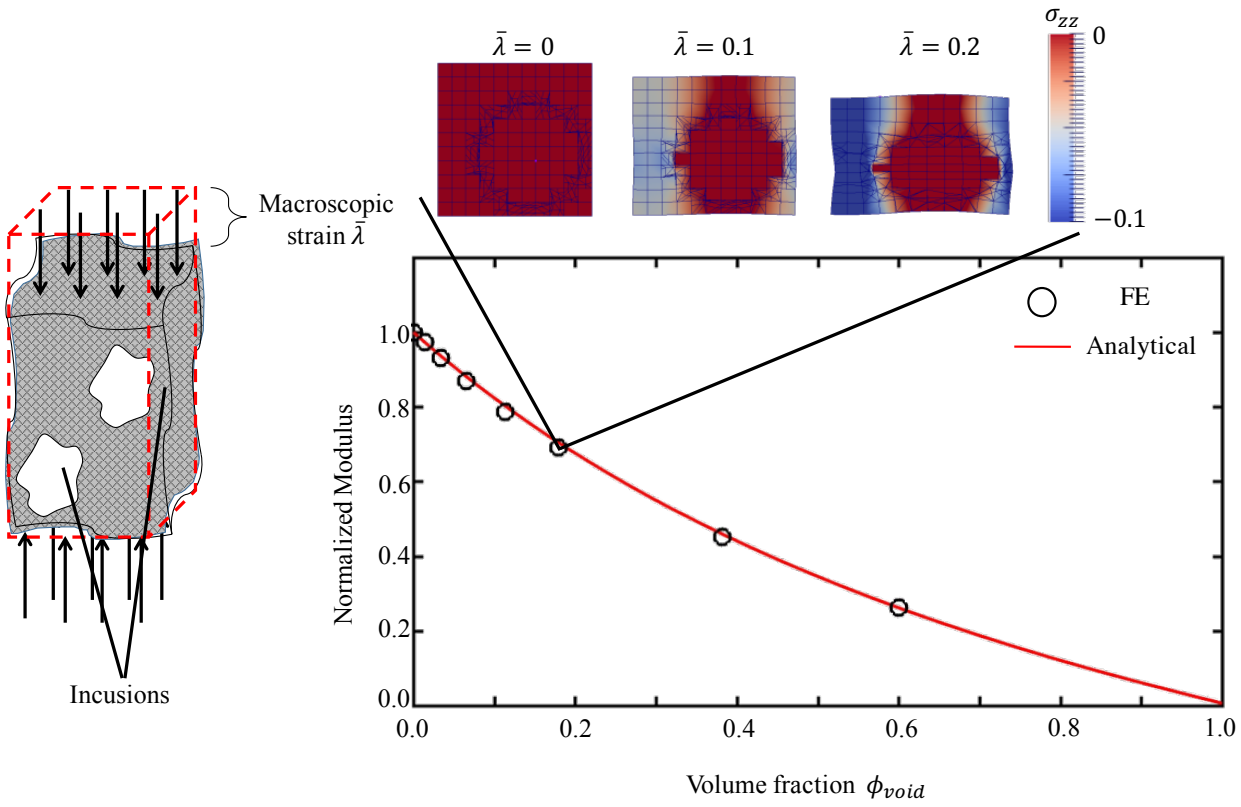

Figure 4.6: Comparison of the model results to the solution of Mori-Tanaka method. At the two extremes the elastic modulus of the composite converges to either the modulus of matrix or inclusions. Model also predicted the stress distribution around the soft inclusion is relatively low.

4.5.3 Mandel's Problem

Next example we investigated is the Mandels problem, in which a block of porous material, saturated with a fluid, is subjected to a compression in y-direction whereas in the other two directions it is unconfined (see Fig. 4.7). Only the surfaces with normal vectors in the x-direction are permeable ($\kappa_w = 0$ on y_+, y_-, z_+, z_-). Since the geometry is symmetric, the solution for the half domain can be derived, which is as follows [30];

$$\bar{p}(\bar{x}, \bar{t}) = 2 \sum_{n=1}^{n=\infty} \left(\frac{\cos(\alpha_n \bar{x}) - \cos \alpha_n}{\alpha_n - \sin \alpha_n \cos \alpha_n} \sin \alpha_n \right) \exp -\alpha_n^2 \bar{t} \tag{4.89}$$

where the variables are $\bar{p}$, $\bar{x}$, $\bar{t}$ are normalized such that they all lie between 0 and 1. The Fourier coefficients α_n can be calculated form the eigenvalue problem;

$$\frac{\tan \alpha_n}{\alpha_n} = \frac{1 - \nu_u}{1 - \nu} \tag{4.90}$$

where ν and ν_u are the Poisson's ratios. In the model, we prescribed zero fluid flux boundary conditions on the y and z surfaces. The load is applied in the y direction and again $C_e = 0$, $\forall \mathbf{X}$ and $\forall t$. Furthermore, periodicity of displacement field is removed, and zero traction conditions applied on the x and z surfaces while the model is constrained in y direction on y_- surface. The initial condition for p is calculated using the procedure above and the results are normalized using the initial values in order to compare to Mandel's solution. For the Mandel's solution, we used the first 50 terms in the series. The model results are in well agreement with the analytical solution (Fig. 4.7). Our model is able to capture the transient effect of loading; the pressure first increases due to the instantaneous loading and then decreases due to the increase in the outgoing fluid flux. This behavior is similar to relaxation of viscous materials [16, 30], which also shows the ability of poroelasticity in capturing the behavior of swollen polymer networks [11]. For this example, we performed convergence analysis and used the error norm;

$$e_2^p = \left[\int_{\Omega_0} (p^{k+1} - p^k)^2 dV \right]^{1/2} \tag{4.91}$$

where k is the index represents the change in mesh. We performed mesh convergence studies and showed that a second order mesh convergence is achieved. Further, we also investigated the

convergence of the Newton-Raphson solution and achieved quadratic convergence. This loading model will be the fundamental of our investigation regarding the effect of fluid flow on remodeling, since in the tissue engineering experiments the construct (cell and scaffold) is subjected to an external load.

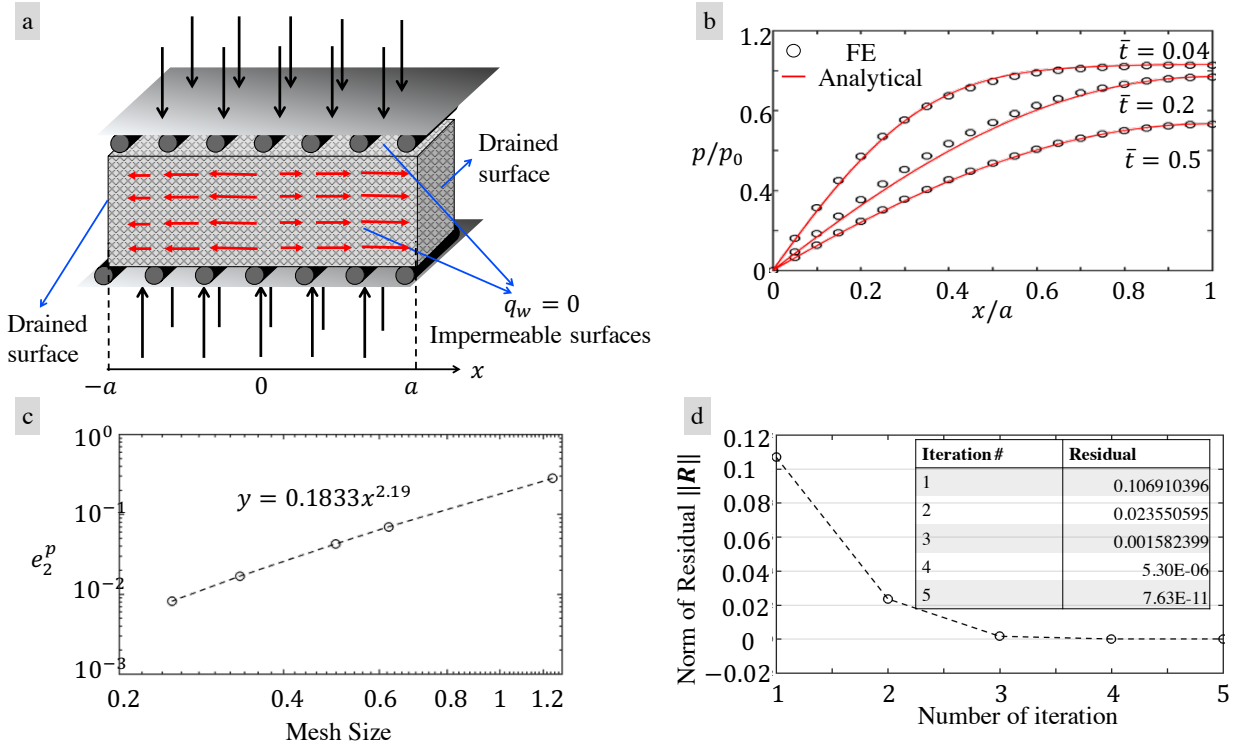

Figure 4.7: (a) Comparison of the model results to the analytical solution of Mandel's problem. (b) The model well captures the transient behavior described by the analytical solution. The pressure gradient generated a fluid flow through the end of the block. (c) Mesh convergence study show a second order convergence for the pressure field, which is in agreement with the theory. (d) Convergence of Newton-Raphson method is quadratic, as it is in the theory, which supports the accuracy of the linearization procedure.

4.5.4 Degradation-transport characteristics and its impact on the construct elasticity

We investigate the degradation characteristics through using two of the non-dimensional parameters; r_e and κ_e^I. We choose a RVE that consists two cells with the cell volume fraction 18%. Periodic boundary conditions are applied on the RVE as described in the previous section.

Furthermore, on the cell boundaries $\partial\Omega_c$, enzyme release is defined as:

$$\frac{DC_e}{Dt} = k_e^0 \left(1 - \frac{C_e}{C_e^0}\right) \tag{4.92}$$

where k_e^0 is the maximum production rate constant and C_e^0 is the target value. Figure 4.8 shows our findings for two extreme cases. In the first case we choose the $r_e = 0.6$ and $\kappa_e^I = 2$ for coupled degradation-diffusion system. The low κ values can be interpreted as diffusion dominates the coupled system. Indeed, the spatial distribution of the enzyme concentration (along the radial direction of the cell) reflects the characteristics of a simple diffusion profile. Moreover, since the degradation is a function of enzyme concentration, the crosslinking density profile has the similar trends in the opposite sense; it has a smooth variation spatially and it is a upside-down of the diffusion profile. In the other extreme case, our selection of $r_e = 2$ impedes the diffusion due to the mesh size - enzyme radius difference. Furthermore, we select $\kappa_e^I = 20$, therefore, degradation is a faster mechanism compared to the diffusion. These obstructions in the transport restricts the enzyme penetrate through the gel once they are released by the cells. The resulting degradation behavior is surface erosion, which quantitatively is observed as a wave front in the degradation (crosslink) profile. The speed of this profile can be controlled via two non-dimensional parameters/variables κ_e^I and ρ. As we mentioned degradation rate increases with κ_e^I, and likewise the speed of the traveling front. The effect of ρ is due to ρ_c which determines the amount of the critical crosslinks that has to be broken in order to reach reverse gelation, at which state the enzyme transport is maximized. The virtual mechanical tests are performed as described in inclusion example, and using the homogenization procedure we calculated the overall elastic modulus of the two extreme cases. We performed the mechanical tests at many time points of the remodeling process of the gel in order to capture the change in the elastic response over time. The loading rate is relatively high; the mass of the fluid does not change (zero flux on the boundary) therefore constant pressure $\dot{p} = 0$ is assumed during the compression test. The elastic stiffness of the gel depends on the level of degradation; load carrying capacity vanishes, if the gel is completely degraded. Furthermore, if the gel evolves into disconnected clusters due to degradation, the load carrying capacity is again lost. It is observed

that the rate of decrease in the gel stiffness is high for the diffusion dominated case since the gel almost experiences bulk degradation, while the reaction (or degradation) dominated case has a localized degradation. The advantage of the localized degradation is that the supporting structure remains for a longer time. These observations can obviously be reversed by changing the speed of the degradation front, however this is out of the scope of this study. In the next section, we will investigate the effect of fluid flow on these two extreme cases.

4.5.5 Impact of fluid flow on the gel degradation and its elasticity

Experimental studies [111] showed that the application of periodic loads on cell encapsulating scaffolds promotes the remodeling and tissue generation. In order to investigate this, we assume a half cycle of the loading from those experiments. The loading of the hydrogel is hypothetically analogous to the Mandel's problem; the fluid pressure should have a similar variation in the construct for the half cycle. This profile also states that the pressure gradient, therefore the fluid fluid varies in the construct; a faster fluid flow close to the specimen boundary. Based on these arguments we investigate the gel degradation for two different regions of the construct; (i) close to the center of specimen, where fluid flow is almost negligible and (ii) close to the boundary where the flow is significant. For the two cases we still assume that the RVE is confined, therefore the boundary conditions are;

$$\begin{aligned} \mathbf{u}|_{S_+} - \mathbf{u}|_{S_-} &= 0 \\ C_e|_{S_+} - C_e|_{S_-} &= 0 \end{aligned} \tag{4.93}$$

Due to the confinement, the pressure variation along the RVE is negligible while the fluid flow is stationary. Therefore, we apply the convective flux of enzyme due to fluid flow using the macroscopic pressure gradient;

$$\left| p|_{S_+} - p|_{S_-} \right|_{C_e} = \begin{cases} L\frac{\partial p}{\partial X} & \text{on } x_-,\ x_+ \\ 0 & \text{on } y_-,\ y_+,\ z_-,\ z_+ \end{cases} \tag{4.94}$$

whereas for the mechanics part of the problem $p|_{S_+} - p|_{S_-} = 0$ applies on all surfaces.

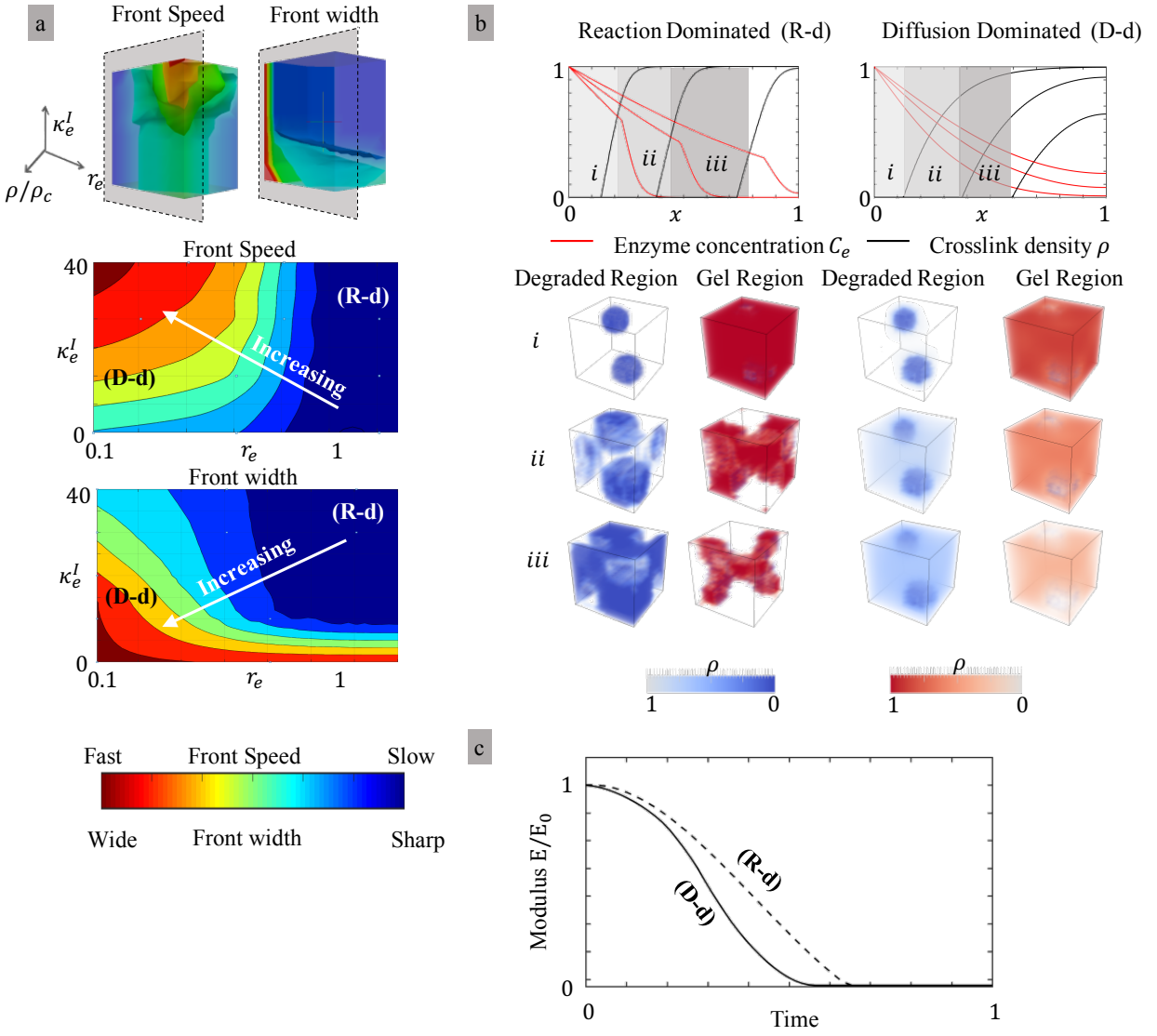

Figure 4.8: (a) Parametric study using $\kappa_e I$ and r_e shows that the degradation characteristics ranges from a wide diffusion-like profile to a sharp wave-like profile. Speed of the degradation is also directly affected by the same parameters, which is observed via front speed. (b) Model Prediction for two extreme cases of degradation-diffusion model; degradation dominated case shows a sharp variation in crosslinking density similar to a wave front, while in the diffusion dominated case variation is similar to a diffusion profile. (c) In the diffusion dominated load carrying capacity is lost faster than in the case of degradation dominated since degradation evolves faster. $E_0 = 0.74RT$ where R is gas constant and T is the absolute temperature. For simplicity of the plots, crosslink density normalized as ρ/ρ_0 where $\rho_0 = 0.038$ Mole/Liter.

The results of the simulations are shown in figure 4.9. As it can be seen, the fluid flow enhances the degradation speed. The effect of the fluid flow is evident in the degradation dominated case

($r_e = 2$, $\kappa_e^I = 20$) and this can be explained as follows. The enzyme molecules cannot diffuse through the gel unless it is completely degradaded. The diffusion of the enzyme in the degraded region is still slow and the enzyme concentration is low on the gel surface (see fig 4.8). The fluid flow helps the transport of the enzyme in the degraded region, and increases the concentration of enzyme on the gel surface, which enhances the degradation. In the diffusion dominated case, however, since the diffusion of the enzyme is fast (see figure 4.8), the effect of fluid flow is relatively small. In addition to that, the effect of the fluid flow can still be observed far from the cells, where the concentration levels are low.

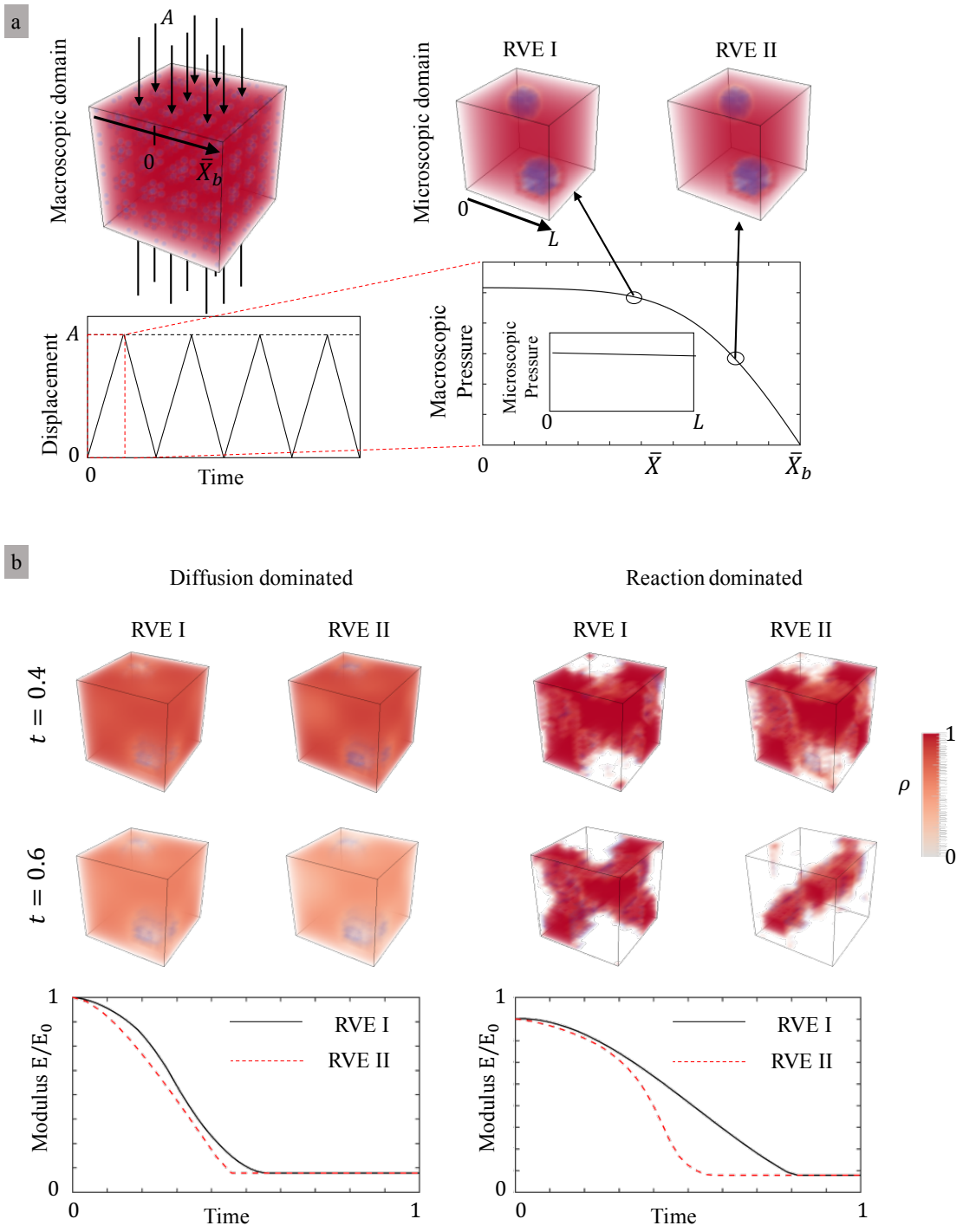

Figure 4.9: (a) Effect of cyclic loading can be simulated considering half cycle. The macroscopic pressure gradient causes a fluid flow while the pressure variation along a RVE is negligible. (b) Two RVE's selected from different macroscopic regions in order to model the effect of fluid flow on diffusion dominated and reaction dominated degradation. $E_0 = 0.74RT$ where R is gas constant and T is the absolute temperature. For simplicity of the plots, crosslink density normalized as ρ/ρ_0 where $\rho_0 = 0.038$ Mole/Liter.

In order to calculate the elastic response of the construct we perfomed the mechanical tests in the same way as explained in the previous section. We would like to note that for these tests we again considered the constant pressure $\dot{p} = 0$ since the loading rate of mechancial test is relatively high compared to the fluid flow. We observed that the enhanced transport shortens the time required to degrade the gel in both cases. The effect of the fluid flow is relatively higher in the case of sharp front; front speed increases with the speed of the pressure gradient. This leads to ta sharp decrease in the time required for complete degradation of the gel. In the diffusion dominated case, the change in the modulus vs. time curve is relatively small. From these results it can be said that the fluid flow has a significant effect on the gel degradation. Moreover we can deduce that the effect of loading on the degradation increases moving towards to the boundaries, where the flow rate increases due to pressure gradient.

4.6 Concluding remarks

In this study we derived a framework for cell-mediated remodeling of the scaffolds that are used in tissue engineering. The model follows the previous studies of mixture theory and based on the existing constitutive theories of swollen networks. We showed that the model is capable of capturing the elasticity of composite materials, and due to its multi-physics nature, it can be used to investigate the evolution in different processes (curing, heat treatment etc.). We also showed that the model is in well-agreement with the classical poroelasticity, for which we compared the model results to the analytical solution of Mandel's problem. Our findings regarding the scaffold remodeling is presented next, we showed the two extreme cases of coupled degradation-diffusion mechanism; diffusion dominated and degradation dominated. We showed that the gels designed to achieve degradation-dominated systems can prolong the gel elasticity, which can provide cells enough time for the neo-tissue generation [1]. We also showed that the fluid transport due to loading enhances the degradation significantly in the vicinity of the macroscopic boundary of the specimen. This mechanism can be a possible explanation of the enhanced remodeling via mechanical stimulus observed in the experiments [111].

Chapter 5

Tuning Tissue Growth with Scaffold Degradation in Enzyme-Sensitive Hydrogels: a Mathematical Model

5.1 Introduction

The degeneration of tissue such as cartilage and bone due to injury, aging or disease is a major source of disability, pain and economic burden in the U.S. and throughout the world. Current solutions range from prosthetic replacement to the autograft/allografts that replace the affected tissues, and thus alleviating the pain for a limited time. Tissue engineering presents a promising alternative whereby the damaged tissue is injected with a population of cells carried in a three-dimensional material that can stimulate repair mechanisms and restore normal function. Early successes have achieved skin regrowth [162], and recent progress in stem cell translation raises hope for the development of personalized strategies that uses the patients own stem cells without requiring a tissue biopsy to obtain tissue specific cells [67]. Despite these early successes, a number of obstacles still hinders applications to a broader population with consistent outcomes. A reason is that tissue growth requires multi-functional scaffolds that can simultaneously provide a mechanical support to the nascent tissue, convey adequate biological signals to implanted cells, enable mass transfer and degrade in time to provide sufficient space for tissue development [71].

Hydrogels have proven to be promising systems due to their controllable properties mimicking that of native tissues [37, 5], their ease of (non-invasive) implantation by injection, as well as their ability to support cell encapsulation and promote extracellular matrix (ECM) synthesis [156, 108]. They also have an enormous potential for functionalization in terms of adhesion, microarchitecture

and degradation to guide the behavior of encapsulated cells. Tuning the design of these complex hydrogels has been a significant challenge because of our limited understanding, and thus control, of how hydrogel structure and cell response evolve during growth. In particular, contrary to more classical tissue engineering in porous scaffolds [121], a challenging issue for injectable hydrogel-based techniques is to ensure sustained tissue growth while maintaining the scaffolds structural integrity during the development of engineered cartilage [71]. Indeed, on the one hand, nondegradable hydrogels possess a network of cross-links that inhibit the diffusion of most ECM molecules [109, 23] and restrict tissue development to the immediate region surrounding the cell [22, 28, 113]. One the other hand, degradable cross-links may solve the problem in the short-term, but ultimately leads to the loss of the hydrogels load carrying capacity (and thus construct failure) before the neotissue is formed. Solutions have been suggested to address this issue, such as introducing cell-mediated degradation [59, 83] but they often make the design more complex and harder to predict without theoretical guidance.

In contrast to most engineering materials, a major hindrance in hydrogel design has been the lack of theoretical and computational developments to assist and guide experimental efforts. One reason is that in tissue engineering, hydrogels are not designed for their instantaneous properties, but for the temporal evolution of their structure, which interact with a biologically active component (cells). A fundamental question can therefore be cast as follows: Is it possible to finely tune the structure and degradation properties of a cell-laden hydrogel in order to enable tissue growth and continuous mechanical integrity during its transition to native tissue? To explore this problem, an interdisciplinary approach was taken; first, theoretical models of tissue growth, accounting for mass transport and reaction kinetic, must be integrated with physical model of hydrogels and their degradations. Second, these models must be combined with micro-macro analysis (sometimes called multi-scale analysis), in order to identify how phenomena occurring at the scale of the cell and polymer structure yield an emerging behavior at the scale of the construct (scaffold + tissue). Third, these models must be validated and integrated with experiments in the field of tissue engineering. While the literature on growth models is rich [138, 127, 75, 38, 70, 10, 11, 53,

150], research on the interaction of growth mechanisms and the mechanics and degradation of a polymer scaffold has been more elusive. Generally, the scaffolds function is to provide a mechanical support for cells and a material onto which new material can be deposited. On the other hand, degradation not only is necessary to ensure the transition from construct to tissue but it can also be used to facilitate the transport and macromolecules that later becomes the new tissue. Hydrogel design can therefore direct the temporal and spatial evolution of swelling, degradation and therefore controls the way by which new tissue grows and acquires its mechanical properties [33, 34]. Few researchers have investigated these processes, through modeling [33, 142, 58, 133] at the cell-hydrogel level. In this context, Dhote et al. [34] built a single cell model under the centro-symmetry assumption and showed that localized degradation of the encapsulating scaffold helps maintain the mechanical integrity of the construct. Sengers et al. [133] investigated the competition among ECM degradation or deposition and transport using a 2D model and its effect on the overall construct stiffness. Trewenack et al. [142] proposed a multispecies formulation of cell-mediated growth in cartilage constructs, pointing out the distinct roles of advection of diffusion fluxes at the microscopic level. Finally, Haider et al. [58] extended the phenomenological model of Wilson et al. [159] to incorporate experimentally measurable quantities, including the apparent densities of the scaffold, the deposited and the unlinked ECM. Although these models provide a qualitative understanding hydrogel supported-growth, efforts are required to make simulation more realistic and closer to experimental systems so that they become predictive and guide the current efforts in designing appropriate scaffolds that can be translated to the clinical.

In this chapter, we investigated the possibility of growing a tissue in a cell-laden hydrogel through mathematical and numerical modeling. Without lack of generality, we focus our study on the case of cartilage cells (chondrocytes) embedded in a PEG-hydrogel. Due to their small mesh-size (few nanometers) compared to ECM molecules, growth in these systems has typically been hindered when degradation does not occur. The introduction of hydrolytic (or bulk) degradation has however not solved the problem since the scaffold loses its mechanical integrity before growth can occur. We investigate here how both issues can be resolved by using a scaffold that can be locally degraded

by enzymes produced by cells. For this, we build a multiphasic model of the growing construct that eventually materializes through a system of nonlinear reaction-diffusion equations whose key parameters can be tuned with hydrogel design. We show, through three-dimensional numerical simulation of tissue development and scaffold degradation around a cells that growth and sustained mechanical integrity can be achieved in a fairly narrow region of the gel design parameters. A discussion of these results, their impact on the field of tissue engineering and the motivation for new research direction are then provided.

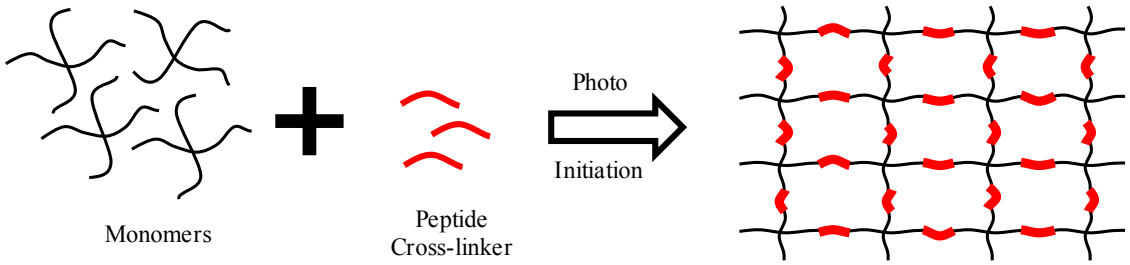

Figure 5.1: *Schematic of a enzymatically-degradable hydrogel made by photo-polymerization of monomers with enzyme sensitive peptide crosslinkers.*

5.2 Growth in enzyme degradable hydrogel scaffold

Tissue engineering starts with the encapsulation of chondrocytes (cartilage cells) in a hydrogel, followed by their local synthesis, diffusion and deposition of ECM molecules; in most cases, these processes occur under physiological loads so that their evolution into a fully functional tissue depends on the continued mechanical integrity of the scaffold. A better understanding of how scaffold design affects mechanics can be gained by investigating the evolution of the ECM/scaffold architecture at the cellular scale, and particularly the percolation of ECM into a viable neo-tissue. We concentrate here on a particular model of degradation, or enzymatic degradation, in which cell-mediated enzymes can diffuse and locally disrupt cross-links in the gel. More specifically, we concentrate on one example system, an enzyme-sensitive poly(ethylene glycol) hydrogel made by photo-polymerization of 8-arm PEG functionalized with norbornene and enzyme sensitive peptide crosslinks (Fig. 4.1). The hydrogels elastic modulus can be adjusted by changing the molecular

weight of the monomers or formulation [2], while its degradation kinetics can be controlled by changing the amino acids in the peptide [90]. As shown in Fig. 4.2, cell-mediated scaffold degradation and tissue growth can be summarized in a few steps. (a) The encapsulated cells release both enzyme and ECM molecules through their cell membrane. (b) Due to their small size, enzymes can diffuse through the polymer network and cleave existing cross-links following Michaelis-Menten kinetics [90]. The change of cross-link density ρ, defined as the number of cross-links per volume of hydrogel in the dry state (i.e. when no solvent is present) can therefore be written:

$$\frac{D\rho}{Dt} = -k' c_e \frac{\rho}{\rho + k''} \tag{5.1}$$

where D/Dt represents the material time derivative, c_e is the enzyme concentration while $k' = k_{cat}(J_0 - 1)$ is the degradation rate constant, $k'' = K_M(J_0 - 1)$ is the cross-link density at which the reaction rate is at half-maximum, while k_{cat} and K_M are Michaelis-Menten kinetic constants [90, 135], and J_0 is the initial swelling ratio after cell encapsulation, but before degradation occurs. Cross-link density will eventually reach the critical (or reverse-gelation) point ρ_c at which the polymer network loses its overall connectivity. In other words, the polymer locally loses its solid characteristics and its resistance to molecular diffusion. (c) The removal of cross-links enables the transport of large (unlinked) ECM molecules that can eventually link to form a new tissue. (d) A new tissue is formed when localized pockets of linked ECM percolate and are able to sustain mechanical loads without the support of the hydrogel. It is important to note that the above scenario is difficult to achieve experimentally since the point of reverse gelation must be closely matched to point when ECM percolation occurs. When reverse gelation occurs before ECM percolation, the result is a mechanical collapse (or dissolution) of the hydrogel and an overall loss in mechanical competence of the construct [126].

As stated above, one of the key mechanism underlying tissue growth in a hydrogel is molecular transport, and particularly the transport of enzyme and ECM molecules. The diffusivity of a molecule (denoted here by the index α) depends on the ratio, r_α/ξ, where its hydrodynamic radius r_α is compared to the hydrogel mesh size ξ. One well accepted model to describe this relationship

was derived by Lustig and Peppas [89] and displays a linear relationship between the diffusivity and the relative particle radius r_α/ξ of the form:

$$D_\alpha(r_\alpha, \rho, J) = D_\alpha^\infty f(J, J_0)\left(1 - \frac{r_\alpha}{\xi(\rho, J)}\right); \quad r_\alpha < \xi < \xi_c \tag{5.2}$$

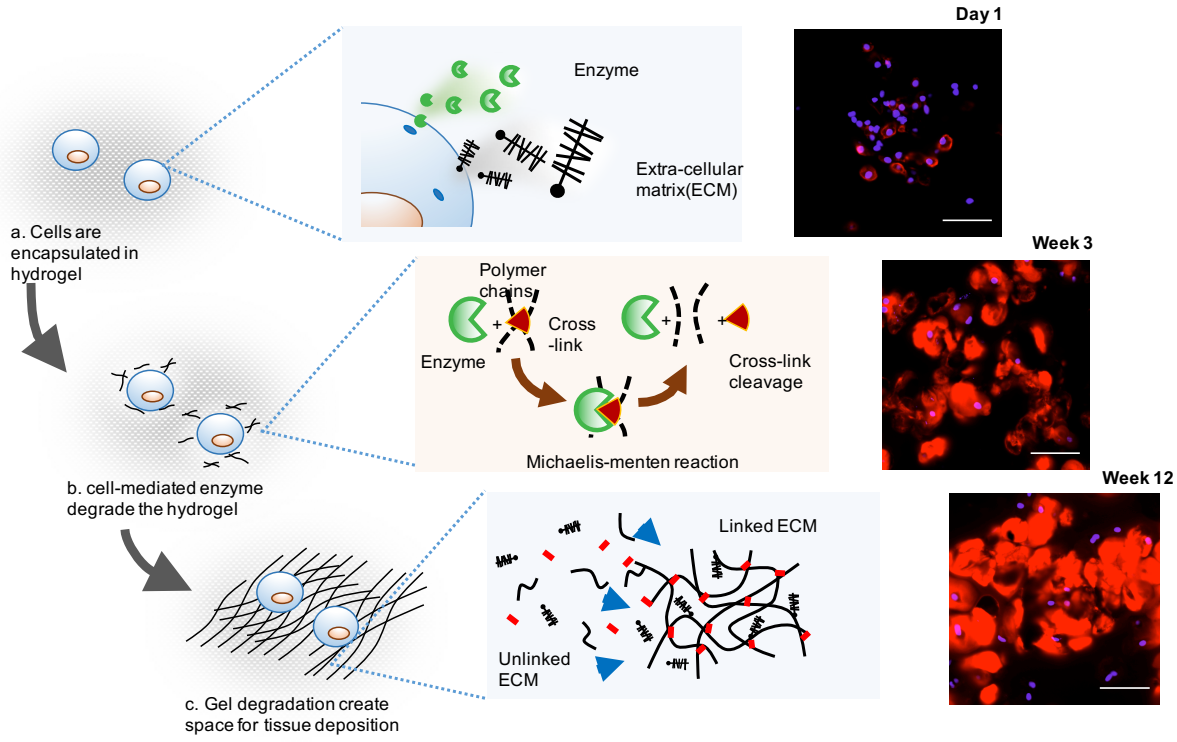

Figure 5.2: *Cell mediated tissue growth in a porous scaffold. (a) The construct is composed of cells and the mixture of solid and fluid phases which are either secreted by cell or key elements of a hydrogel. (b) Tissue growth in a hydrogel at the microscale is shown. For convenience we classify cell-secreted molecules under two groups: enzymes and ECM, which are essential to model tissue growth and hydrogel degradation. (c) Cartilage cells secreted extracellular matrix, shown by histological images stained for aggrecan (red), which increased as a function of time. By week 12, there was evidence of matrix connectivity in the hydrogel. The compressive modulus of the construct decreased with culture time indicating that the hydrogel was undergoing bulk degradation.*

where the mesh size ξ implicitly depends on cross-link density ρ and equilibrium volumetric

swelling ratio J and $\xi_c = \xi(\rho_c, J)$ is the mesh size when the gel reaches reverse gelation. Moreover, the function $f(J, J_0) = \exp(-1/(JJ_0 - 1))$ represents the probability of finding a space that is not obstructed by polymer network and large enough for a fluid particle to move. Note that once the hydrogel reaches reverse gelation, polymer chains are free to diffuse and assumed to quickly leave the construct. This means that as $\rho \to \rho_c$, chains eventually disappear, and since this process is relatively faster than the dynamics of growth, one assumes that the function $f(J, J_0)$ becomes unity as soon as $\rho = \rho_c$. We further note that relation (4.2) is only valid over the defined range $r_\alpha < \xi < \xi_c$; indeed, when $\xi < r_\alpha$, the small mesh size restrict diffusion and $D_\alpha \to 0$. When $\xi > \xi_c$, however, the mesh disappears ($\xi \to \infty$) and the diffusivity becomes that of a particle in a pure solvent, i.e. $D_\alpha = D_\alpha^\infty$ as given by the Stokes-Einstein relation [102]. While the radii of molecules cannot be changed, it is possible to tune the hydrogel mesh size via its cross-link density through the relation [89]:

$$\xi(\rho, J) = \frac{\ell J^{1/3}}{\sqrt{\rho}}; \quad \rho_c < \rho \tag{5.3}$$

where J is the swelling ratio of the gel from its dry state and the length ℓ is given by

$$\ell = C_n^{1/2} l \left(\frac{3\rho^P}{M_r} \right)^{1/2} \tag{5.4}$$

Here, C_n is the characteristic ratio that defines the restricted rotation of a single polymer chain, l is the average bond length in the polymer, M_r is the molar weight of the polymer repeat unit and ρ^P is the density of the polymer. We note that equation (4.3) is only valid before reverse gelation and diverges to infinity as $\rho \to \rho_c$. Two observations can be made based on equations (4.2) and (4.3). First, enzymes, due to their small hydrodynamic radius ($\sim$ 60-85 $\mathring{A}$ [135]) may enter the hydrogel space but their diffusion can be strongly hindered for tightly cross-linked gels. ECM molecules (in particular collagen and aggrecans) are however characterized by relatively large sizes, on the order of 200 $\mathring{A}$ and larger, and are therefore unable to be transported within the gel. Second, as the gel reaches reverse gelation, the diffusivity of ECM suddenly reaches a finite value, allowing for matrix transport. This means that diffusion of ECM molecules is only possible once the gel is fully degraded, a phenomenon that has been a major hindrance to successful tissue growth. Using

equations (4.2) and (4.3), Fig. 4.3a shows the dependency of the normalized diffusion constant D_α/D_α^∞ on cross-link density and its evolution during degradation for both enzyme and ECM. One can clearly see the sharp rise in diffusivity at normal gelation for large ECM particles in contrast to smaller enzymes. Fig. 4.3b confirms this trend by showing histological images of ECM (aggrecan and collagen) around the cartilage cells in two non-degradable gels characterized by their polymer fraction (10 and 20%, respectively) at the time of hydrogel formation. It is evident that due to their inability to diffuse, these molecules remain confined in the pericellular space. One notes that a stiffer gel (20% polymer fraction) provides a stronger confinement and thus a smaller pericellular matrix.

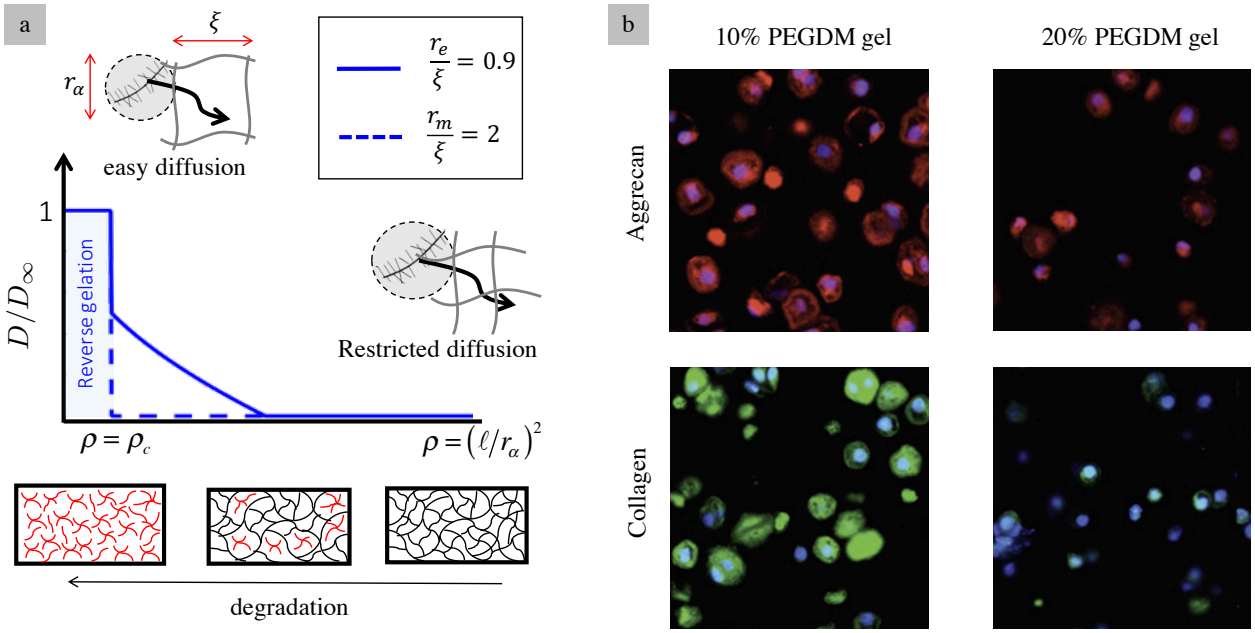

Figure 5.3: *(a) Relationship between particle diffusivity and cross-link density for two different particle sizes (enzyme and ECM molecules), characterized by the ratio r/ξ. (b) Restricted diffusion of two ECM building blocks (aggrecan and collagen) around chondrocytes encapsulated in 10% and 20% aggrecanase sensitive PEGDM hydrogels.*

5.3 Model formulation

To explore the interactions between molecular transport, polymer degradation and tissue growth, we propose here to develop a mathematical model based on (multiphasic) mixture theory [19, 17]. More precisely, the construct is described as a continuous mixture of fluid and solid constituents whose respective volume fraction are denoted, respectively by ϕ and $\tilde{\phi}$. Solid constituents including the polymer ($\tilde{\phi}_p$) and newly deposited matrix ($\tilde{\phi}_m$) primarily participate to the mechanical integrity of the construct. Fluid-like constituents, including water (ϕ_w), enzymes (ϕ_e) and freshly synthetized and unlinked matrix molecules (ϕ_w), play an important role in degradation and transport. We note here that the latter two constituents are typically found in very small proportions, such that $\phi_m \ll 1$ and $\phi_e \ll 1$. We further assume that the above constituents constitute the majority of the inter-cellular space, yielding the saturation condition:

$$\tilde{\phi}_m + \tilde{\phi}_p = \tilde{\phi}, \quad \phi_w \approx \phi, \quad \phi + \tilde{\phi} = 1 \tag{5.5}$$

where we omitted to specify the argument $(\mathbf{x}, t)$ for the sake of clarity. It is however clear that these quantities vary both in time and space during the growth process. We show next that the evolution of these quantities in time and space, together with the mechanical integrity of the mixture can be described in terms of a coupled system of reaction-diffusion equations and force balance over the physical domain of the construct.

5.3.1 Mass transfer

As the construct composition evolves, motion and mass transfer occurs in the inter-cellular space. In this dynamic process, all solid constituents typically follow the same displacement, denoted here as $\mathbf{u}(\mathbf{x}, t)$ from their reference location $\mathbf{x}$ during cell encapsulation. This concept allows us to consider a more amenable mathematical treatment known as the constrained mixture formulation [70]. Mass transfer within the construct may thus be described in terms of the velocities $v_\alpha \mathbf{u}(\mathbf{x}, t)$, $(\alpha = w,\ e,\ m)$ of each fluid-like constituent relative to the solid constituents. This description therefore attaches our point of observation to the solid phase, such that the total velocity

of a fluid phase in a fixed frame is $\mathbf{v} + \dot{\mathbf{u}}$, where $\dot{\mathbf{u}}$ denotes the solid velocity. Assuming that all constituents are incompressible, the continuity equation for the solvent takes the form [84]:

$$\nabla \cdot \dot{\mathbf{u}} - \nabla \cdot (\phi \mathbf{v}_w) = 0 \tag{5.6}$$

Where $\nabla \cdot \dot{\mathbf{u}}$ is to be interpreted as the rate of solid swelling and the fluid velocity is computed with Darcy's law as $\phi \mathbf{v}_w = -\kappa \nabla (p - \pi)$ in which p is the water pressure and π is the osmotic pressure. The continuity equation for cell secreted molecules then takes the form of a convection-diffusion-reaction system of the form:

$$\frac{Dc_\alpha}{Dt} = \nabla \cdot (D_\alpha \nabla c_\alpha) - \nabla \cdot (\mathbf{v}_w c_\alpha) - c_\alpha \nabla \cdot \dot{\mathbf{u}} - \Gamma_\alpha \quad \alpha = e, m \tag{5.7}$$

We recall here that the diffusivity D_α is a nonlinear function of cross-link density and swelling ratio as shown by equations (4.2) and (4.3). Furthermore, the molar concentrations are related to volume fractions by $c_\alpha = \phi_\alpha / \nu_\alpha$ with ν_α the molar volume of constituent α, all of which remain constant due to the incompressibility assumption. The first term is purely diffusive, the second is the convective term from the motion of the solvent, the third describes a change of concentration due to polymer swelling and the last is a reaction term that accounts for the rate of production or consumption of the constituent. We assume here that enzyme only affects gel degradation and does not transform during the process, i.e. $\Gamma_e = 0$. By contrast, unlinked ECM molecules do transform into linked ECM molecules and this process is described by the consumption rate Γ_m. Mass balance of solid constituents (polymer and linked matrix) may similarly be derived by cancelling the diffusion and convection terms in equation (4.7), which leads to:

$$\frac{D\tilde{c}_\alpha}{Dt} = -\tilde{c}_\alpha \nabla \cdot \dot{\mathbf{u}} + \Gamma_\alpha, \quad \alpha = p,\ m \tag{5.8}$$

where again, the only non-vanishing reaction term is the transformation rate Γ_m between unlinked and linked ECM. Motivated by the concept of homeostasis [27], the state that a biological system tends to evolve towards a specific target, we propose a model in which the rate of ECM linkage is regulated by the level of existing linked ECM as follows:

$$\Gamma_m = k_m \left(1 - \frac{\tilde{c}_m}{\tilde{c}_m^0}\right) c_m \tag{5.9}$$

where $\tilde{c}_m^0$ is the target ECM concentration and k_m is the intrinsic rate of linkage (i.e., the rate constant in the absence of deposited ECM ($\tilde{c}_m = 0$).)

5.3.2 Evolution of construct mechanics

As discussed above, an important aspect of hydrogel assisted growth is the evolution of mechanical properties, and especially the transition from a cell-laden hydrogel to a tissue. Since the construct possesses a heterogeneous structure during growth, this transition depends on both the spatial distribution and the load carrying capacity of each phase (hydrogel and linked ECM) in time. To characterize this evolution, let us consider that at a given time, the construct is subjected to a macroscopic deformation, which at the level of the intercellular space, yields a heterogeneous displacement field $\mathbf{u}(\mathbf{x}, t)$ around cells. Material deformation can therefore be characterized by the deformation gradient $\mathbf{F} = \mathbf{I} + \partial\mathbf{u}/\partial\mathbf{x}$, or alternatively the nonlinear strain $\epsilon = (\mathbf{F}^T\mathbf{F} - \mathbf{I})/2$, where $\mathbf{I}$ is the identity tensor. The change in material volume (or swelling ratio) from its initial equilibrium value prior to any degradation is then measured by $J = det(\mathbf{F})$. For an elastic material, strains give rise to the appearance of stresses, represented by the tensor $\boldsymbol{\sigma}$, that must verify the balance of linear momentum:

$$\nabla \cdot (\boldsymbol{\sigma} - p\mathbf{I}) = 0 \quad \text{and} \quad \boldsymbol{\sigma} = \frac{\partial \psi}{\partial \mathbf{F}} \frac{\mathbf{F}^T}{J} \tag{5.10}$$

More precisely, $\boldsymbol{\sigma}$ is the elastic stress supported by the hydrogel and the newly deposited ECM while p is the internal pressure in the solvent. When no external loads are applied to the construct, this pressure is equal to the osmotic pressure π in the hydrogel [150, 47]:

$$p = RT(\ln(\phi) + (1 - \phi) + \chi(1 - \phi)^2)/\nu_w \tag{5.11}$$

The elastic stress is further related to the deformation gradient through a strain energy function, which we assume to be additively decomposed [9] into polymer and ECM components as:

$$\psi(\rho, c_m, \epsilon) = \psi_p(\rho, \epsilon) + \psi_m(\tilde{C}_m, \epsilon) \tag{5.12}$$

The energy ψ_p stored in the polymer is expressed in terms of the classical Rubber elasticity theory as [47]:

$$\psi_p(\rho, \mathbf{F}) = \frac{\rho RT}{2}\left[J_0^{2/3} tr(\mathbf{F}^T\mathbf{F}) - 3 - \ln(J_0 J)\right], \quad \rho > \rho_c \tag{5.13}$$

where R and T are the gas constant and the absolute temperature, respectively, and J_0 is the initial equilibrium swelling ratio of the hydrogel prior to degradation. The latter term implies that the polymer is in a stressed state, balanced by the osmotic pressure of the solvent, equation (4.11), after cell encapsulation and equilibration with the solvent. The consequence of this phenomenon is that the stored elastic energy remains positive, even in the absence of deformation $\mathbf{F}$. One can note from equation (4.13) that a drop in cross-link density ρ tends to decrease the elastic energy stored in the gel and hence its load carrying capacity. Importantly, when the gel reaches reverse gelation ($\rho = \rho_c$), it loses all of its elasticity and:

$$\psi_p(\rho, \mathbf{F}) = 0 \quad \rho < \rho_c \tag{5.14}$$

This behavior creates a sharp discontinuity in the materials response as the hydrogel undergoes reverse gelation; this feature is most likely responsible for the sudden failure of the polymer network before a functional tissue can be obtained. Unlike the hydrogel, the elastic energy stored in the newly deposited matrix has not been well characterized [70, 53, 150]. However, for convenience and consistency with previous work [150], we choose here to express it in terms of a Saint-Venant strain energy function, that is a generalization of Hookes law in the context of finite deformation. The corresponding strain energy function reads:

$$\psi_m(\epsilon) = \tilde{C}_m\left[\frac{\lambda}{2}[tr(\epsilon)]^2 + \mu tr(\epsilon^2)\right] \tag{5.15}$$

where λ and μ are the Lame constants, expressed in units of energy per mole of linked ECM. This definition of material parameters implies that the stiffness of the material increases the apparent density of linked ECM [58]. In this study, we introduce the constraint $\lambda = 0.8\mu$ in order to satisfy the porous network behavior [105, 160] of linked ECM similar to the that of polymer. The total elastic stress at any point within the extra-cellular space is then $\boldsymbol{\sigma} = \boldsymbol{\sigma}_p + \boldsymbol{\sigma}_m$ where the stress in

the polymer and matrix are obtained from equation (4.10) as:

$$\boldsymbol{\sigma}_p = \rho H(\rho - \rho_c)\frac{RT}{J}\left(2J_0^{2/3}\mathbf{F}^T\mathbf{F} - \frac{1}{2}\mathbf{I}\right) \tag{5.16}$$

$$\boldsymbol{\sigma}_m = \tilde{C}_m(\lambda[tr(\epsilon)\mathbf{I}] + 2\mu\epsilon) \tag{5.17}$$

In which the Heaviside function $H(\rho - \rho_c)$ ensures that the polymer stress vanishes when $\rho = \rho_c$.

5.4 Model analysis and solution

In this study, we concentrate on the conditions by which the competition between hydrogel degradation and ECM deposition enables a smooth transition between scaffold and tissue properties. As shown in Fig. 4.4, for a homogeneous distribution of cells at small density, the analysis simplifies to the problem of a periodic representative volume of characteristic length L, centered on a single cell of radius R_c. The average spacing L between cells is further related to their volume fraction f in the construct as:

$$L = R_c\sqrt[3]{4\pi/3f} \tag{5.18}$$

To specify proper assumption and boundary conditions, one must first specify the external conditions surrounding the construct during the growth process. We first consider that the specimen is free of external loads (neither constant nor cyclic) at any time; consequence of this is that (a) external stresses on the external boundary of the represented domain vanish and (b) solvent permeation becomes negligible, i.e. $\mathbf{v}_w$. This means that the convective term in equation (4.7) is negligible and the transport of enzyme and ECM is described by a coupled system of diffusion-reaction equations. Further assuming that the hydrogel reaches its new equilibrium significantly faster than the dynamics of degradation and enzyme diffusion, the osmotic pressure can be shown to follow expression (4.11). Based on the periodicity assumption of the representative domain, boundary conditions (B.C.) for $\mathbf{g} = \{\mathbf{u}, p, C_e, C_m\}$ become [155]:

$$\mathbf{g}\mid_{S_+} - \mathbf{g}\mid_{S_-} = L\bar{\nabla}\mathbf{g} \tag{5.19}$$

where S_+ and S_- are two opposite boundaries of the representative domain while $\bar{\nabla}\mathbf{g}$ is macroscopic gradient of the field $\mathbf{g}$ over the domain. In particular, the absence of loading imposes that $\bar{\nabla}p = \bar{\nabla}C_\alpha = 0$, while $\bar{\nabla}\mathbf{u}$ is directly related to the overall strain experienced (such as swelling) by the domain during growth. This quantity is calculated by ensuring stress-free boundary conditions as described in [144]. Boundary conditions on the cell surface S_{cell} can further be specified in terms of enzyme and ECM productions as:

$$q_\alpha \mid_{S_{cell}} = q_\alpha^0 \left(1 - \frac{c_\alpha}{c_\alpha^0}\right) \tag{5.20}$$

where q_α^0 is the production rate of constituent $\alpha(= e, m)$. This simple relation indicates that cells produce enzyme and ECM molecule until they reach a homeostatic state, given by a target concentration c_α^0 [58].

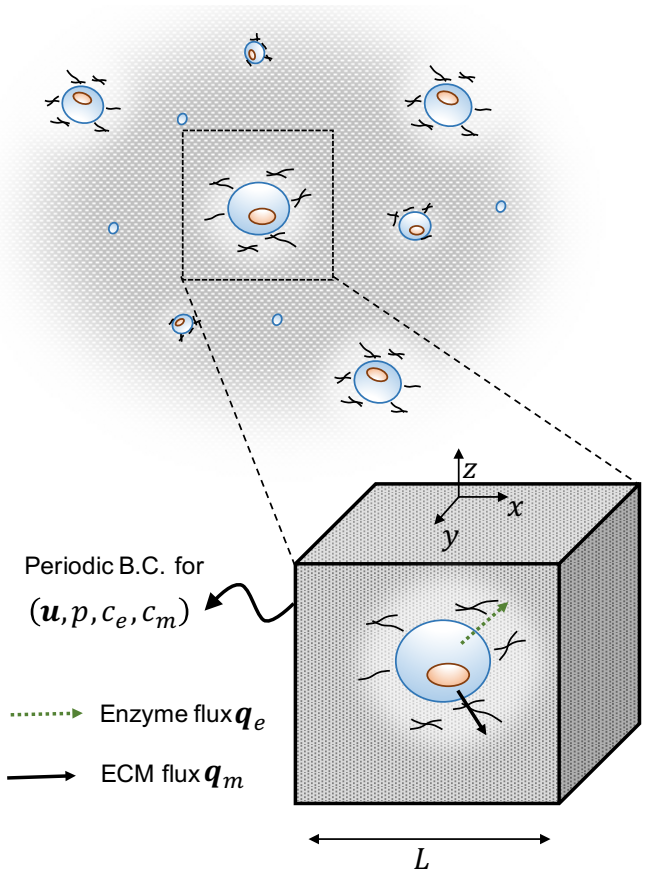

Figure 5.4: *Model domain and boundary conditions.*

To analyze the solution, we first apply the technique of non-dimensionalization that consists of rescaling all variables to reference dimensions and times as:

$$\mathbf{x}^* = \frac{\mathbf{x}}{L}, \quad t^* = \frac{tD_m^\infty}{L^2} \tag{5.21}$$

This operation aims to simplify the original equations and reduce the number of physically meaningful parameters for a better interpretation of the systems response. Using the above scaling relations, the new dimensionless variables become:

$$\mathbf{u}^* = \frac{\mathbf{u}}{L}, \quad c_\alpha^* = \frac{c_\alpha}{c_\alpha^0}, \quad p^* = \frac{p}{RT}, \quad \rho^* = \frac{\rho}{\rho_0} \tag{5.22}$$

Where the characteristic length scale L is determined by the average spacing between cells, energies are scaled with the thermal energy RT and all concentrations are defined in relation to their threshold value c_α^0 defined in equation (4.19). Substituting these variables in the original formulation, our final system preserves the structure of the original transport and mechanics equations (4.7) and (4.10), for which the critical parameters are expressed as follows. For the transport phenomena, normalized permeabilities are written as a fraction of the maximum value D_m^∞ for ECM molecules and are expressed in terms of swelling ratio, molecule radius and cross-link density as:

$$D_\alpha^*(J, r_\alpha^*, \rho) = \Delta_\alpha J^{-1/3} \exp\left(-\frac{1}{JJ\_1}\right)\left(J^{1/3} - r_\alpha^*\sqrt{\rho^*}\right) \tag{5.23}$$

with $\Delta_\alpha = D_\alpha^\infty / D_m^\infty$ and

$$r_\alpha^* = r_\alpha / \ell\sqrt{\rho_0} \tag{5.24}$$

It is clear here that r_α^* is interpreted as the relative size of an enzyme or ECM molecule compared to the hydrogel mesh size. Similarly, the normalized rate of degradation and rate of ECM deposition read:

$$\kappa_e^* = \frac{k' c_0^e}{D_m^\infty \rho_0} L^2, \quad \kappa_m^* = \frac{k_m}{D_m^\infty} L^2 \tag{5.25}$$

They characterize, respectively, the competition between enzyme degradation and diffusion and the competition between matrix deposition and diffusion. The flux boundary condition at the cell

boundary is similarly normalized as $(q_\alpha^0)^* = q_\alpha^0 L^2/(D_m^\infty c_m^0)$ and the properties of the ECM are written in relation to the polymer stiffness and RT as:

$$\mu^* = \frac{C_m^0 \mu}{RT}, \quad \lambda^* = \frac{\lambda}{\mu} \tag{5.26}$$

where Poissons ratio is $\nu = 0.5(1+(\lambda^*)^{-1})^{-1}$. Note here that the non-dimensional critical cross-link density is also known as the network connectivity parameter [135, 103]. This parameter is important to the degradation process as decrease in its value would imply an increase in the number of crosslink to be cleaved before reverse gelation. The parameters used in the non-dimensionalization, along with their value and corresponding references are listed in Table 4.1. These values are key as they enable the mapping of all non-dimensional results obtained in the next section into physical quantities.

Table 5.1: Inputs used in the model.

Parameter	Definition	Value	Unit	Reference
P_m^0	ECM production rate	2.3×10^{-15}	$\frac{Mole}{cell \cdot week}$	
P_e^0	Enzyme production rate	6×10^{-16}	$\frac{Mole}{cell \cdot week}$	
c_m^0	ECM concentration at homeostasis	6.9×10^{-15}	$Mole$	
c_e^0	Enzyme concentration at homeostasis	1.8×10^{-15}	$Mole$	
r_{cell}	Cell radius	10	μm	
β	Network connectivity	0.8		
D_∞^e	Diffusion of enzyme in pure solvent	6.6×10^{-7}	mm^2/s	
D_∞^m	Diffusion of ECM in pure solvent	1.3×10^{-7}	mm^2/s	
r_m	Hydrodynamic radius of ECM molecules	20	nm	
T	Absolute temperature	310	K	
R	Gas constant	8.314	$J/(K \cdot Mole)$	
L	Length scale (cell spacing)	400	μm	

5.5 Results

The above equations were solved numerically using a nonlinear finite element scheme, whose details are given in appendix. Our approach relies on investigating the spatial and temporal evolution of the hydrogel and ECM locally around cells and relating this to the temporal evolution in the overall construct mechanical properties. For clarity, we decompose our approach in three

steps; in the first example, we investigate the role of hydrogel design on the local hydrogel degradation dynamics, without transport of ECM molecules. The second example then investigates how hydrogel degradation and transport of ECM molecules interact to enable localized growth. We finally explore how various ECM growth/hydrogel degradation dynamics influence the mechanical integrity of the construct in time. This exercise allows us to identify a region in the hydrogel design that enables an optimized combination of ECM growth and mechanical integrity in time.

5.5.1 Degradation around a single cell

We first investigate the coupled mechanisms of enzyme transport-hydrogel degradation-enzyme diffusion without ECM production. For this problem, the relevant non-dimensional parameters can be reduced to the relative enzyme size , and the enzymatic relative degradation . The effect of polymer mesh size and cross-link density are implicitly contained in these quantities (equations (4.23) and (4.24)). For the sake of illustration, we consider a construct with low cell density ($L/r_c \approx 20$), $\beta = 0.8$ (see Table 4.1) and a constant enzyme production equal to $P_e^0 = 6 \times 10^{-16}$ $mole/(cell \cdot week)$ [158].

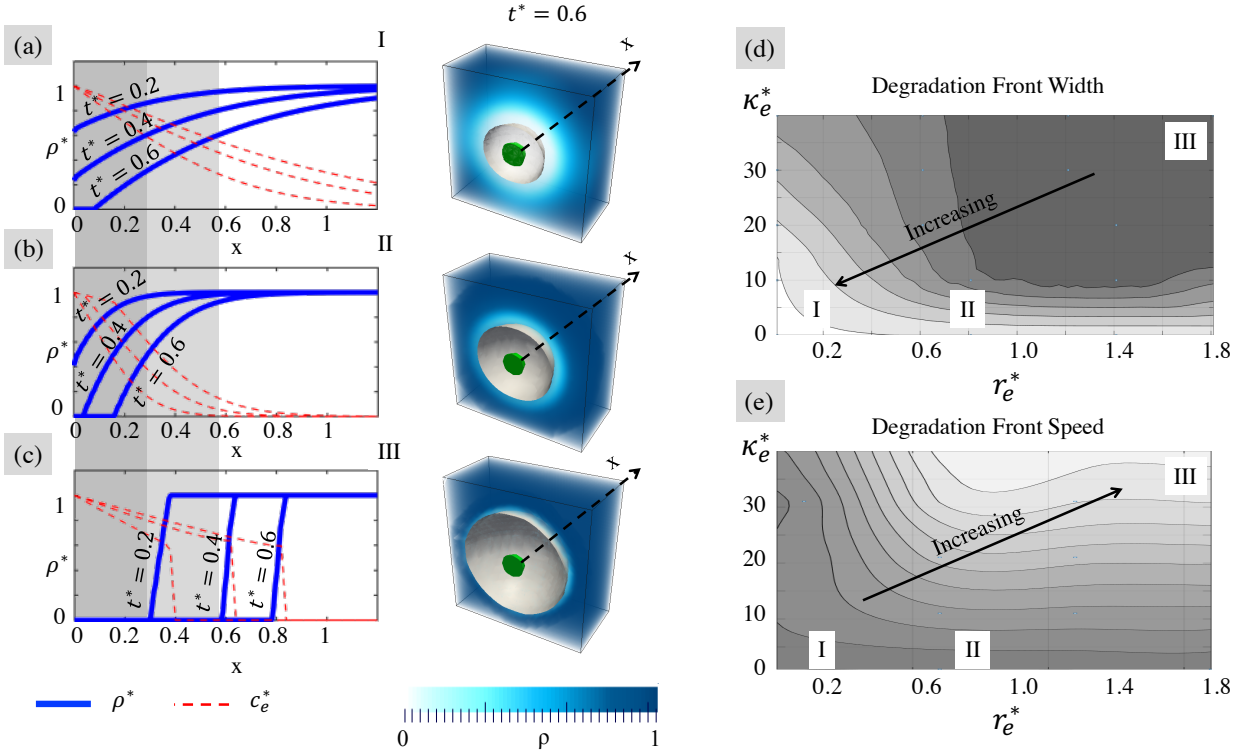

Figure 5.5: *Characteristics of degradation dynamics as a function of the normalized enzyme size* r_e^* *and degradation rate* κ_e^**. Plots (a,b,c) show the distribution of cross-link density in terms of the distance* x *from the cell surface for three specific times; one observes a transition from a diffusion-like profile to a narrow moving degradation front as* r_e^* *and* κ_e^* *increase. The relationship between the width and velocity of this traveling front and the parameters* (r_e^*, κ_e^*) *can be visualized on two-dimensional maps represented in (d) and (e), respectively.*

Degradation front: We show in Fig. 4.5 that, according to the value of parameters r_e^* and κ_e^*, the nonlinear diffusion-reaction equation yields an enzyme concentration profile that ranges from a diffusion-like appearance to a more narrow and propagating wave. The corresponding evolution in cross-link density exhibits similar features (Fig. 4.5 (a,b,c)) between the fully degraded region ($\rho^* = \beta$) and the intact region ($\rho^* = 1$). Importantly, we note that this transition region or degradation front travels away from the cell surface in time. In this study, this front is characterized in two ways: its speed is defined as that of the boundary ($\rho^* = \beta$) that separates the completely

degraded and non-degraded gel regions while its width is defined as the distance between the boundary ($\rho = \rho_c$) and the point at which $\rho^* = 0.99$.

Diffusion-dominated and diffusion-limited systems: Figs. 4.5 (a,b,c) clearly shows that the width and speed of the degradation front, can be controlled by varying κ_e^* and r_e^*. For large enzyme radius (or small hydrogel mesh size), the diffusivity becomes so small that it is the rate-limiting step. Such a diffusion-limited system typically exhibits a very sharp degradation front followed by a region of intact polymer (Fig. 4.5c). By contrast, when the enzyme size becomes small (or alternatively, when the hydrogel mesh size becomes large), the diffusivity is close to that experienced in a pure solvent and hydrogel degradation becomes the rate limiting step. In this case, the system is diffusion-dominated and the enzyme concentration and cross-link density both display a diffusion-like profile away from the cell surface (Fig. 4.5a).

Characterization of the degradation dynamics: At first sight, our results seem to imply that sharp fronts are faster than their wider counterpart. This can be seen in Fig. 4.5 a-c by comparing the evolution of the point $\rho^* = 0$ (shaded regions) for three gels exhibiting wide (I), intermediate (II) and sharp (III) fronts, respectively. To better understand this trend, we further investigated the role of the relative enzyme size and degradation on the width and speed of the degradation front. This was done by numerically scanning the space (r_e^*, κ_e^* and estimating the values of front width (w) and velocity (v) for each simulation. Results, recorded in the form of maps (Fig. 4.5 d,e) clearly show nonlinear relationships between the hydrogel design and the degradation behavior, but generally suggest that increasing r_e^* and κ_e^* results in a sharper and faster degradation front. We note here that these results cannot be generalized as different trends may be observed for different values of the network connectivity β [135]. A more general understanding of this system may be found by studying the role of β on the width and speed of the degradation front, yielding three-dimensional maps in the $(r_e^*, \kappa_e^*, \beta)$ space. This is however, beyond the scope of this study. Overall these results indicate that it is possible to tune the hydrogel design and specifically its mesh size, cross-link density as well as the sensitivity of degradable links to enzymes to yield a variety of localized degradation dynamics around cells. The way by which such dynamics

influence growth is discussed next.

5.5.2 The role of hydrogel degradation on the nature of ECM deposition

In this work, tissue growth is defined as cell-mediated (a) synthesis, (b) release, (c) transport and (d) deposition of ECM molecules within a hydrogel. Since the size of these macro-molecules (whether it is collagen, GAGs or other key constituents of native tissue) is usually a few times larger that of the hydrogel mesh size, their diffusion is strongly hindered in intact hydrogels as can be seen in Fig. 4.3. This means that growth is limited in non-degradable hydrogels. However, degradable hydrogels may enable transport via the depletion of their cross-links and the increase in mesh-size. This effect is especially important as the polymer crosses the reverse gelation point, due to the sudden disappearance of a mesh and the sudden increase in diffusivity.

Here, we study the interplay between hydrogel degradation and diffusion of ECM molecules and their deposition in an enzymatically degradable hydrogel through the solution of two coupled reaction-diffusion equations (4.1) and (4.7) of enzyme and ECM transport/deposition. We concentrate on the effect of three key parameters, r_e^*, κ_e^* and κ_m^*. Note that since the relative ECM size r_m^* is typically much larger than unity in applications (i.e., larger than the mesh size of the hydrogel at any point during degradation), we keep it fixed in all simulations. Furthermore, for the sake of clarity, we consider a pair of parameters r_e^* and κ_e^*, which display, respectively, a wide and sharp degradation and for each case, investigate the effect of small and large rates of ECM deposition. Results are shown in Fig. 4.6. subfigures (a) and (b) illustrate the case of a slow rate of ECM deposition coupled with a (a) wide and (b) sharp degradation front. In the first case, one can observe that the hydrogel undergoes significant degradation before ECM can be deposited. In the second case, free ECM can easily diffuse in the cavity left by the degradation front around a cell, but because of its slow conversion to solid ECM, growth remains concentrated in the peri-cellular region. By contrast, Fig. 4.6 (c) and (d) display the situation where the rate of ECM deposition is fast compared to the rate of degradation. When the degradation front is wide (Fig. 4.6 (c)), degradation is fairly uniform around cells, and the point of reverse gelation propagates slowly away

from the cell boundary. Because of its relatively slow speed, this degradation front is immediately followed by a reservoir of free ECM molecules that quickly convert into a solid phase. Eventually, the construct is made up of a composite of deposited ECM surrounded by a region of non-degraded gel. In the case of a sharp degradation front, however, the region between intact and fully degraded gel is extremely thin, and the degradation profile may be thought of as an expanding sphere centered around a cell. Within this sphere, ECM can freely diffuse and deposit at a high rate. This yields a situation where the degradation front is immediately followed by a deposition front and a construct that resembles a hydrogel matrix filled with expanding inclusions of ECM. Interestingly, this case maximizes the growth to degradation ratio, that is, we observe a significant amount of growth for a minimal level of gel degradation. Although all of the above situations allow for growth in time, one may ask whether they could maintain a continuous mechanical integrity in time.

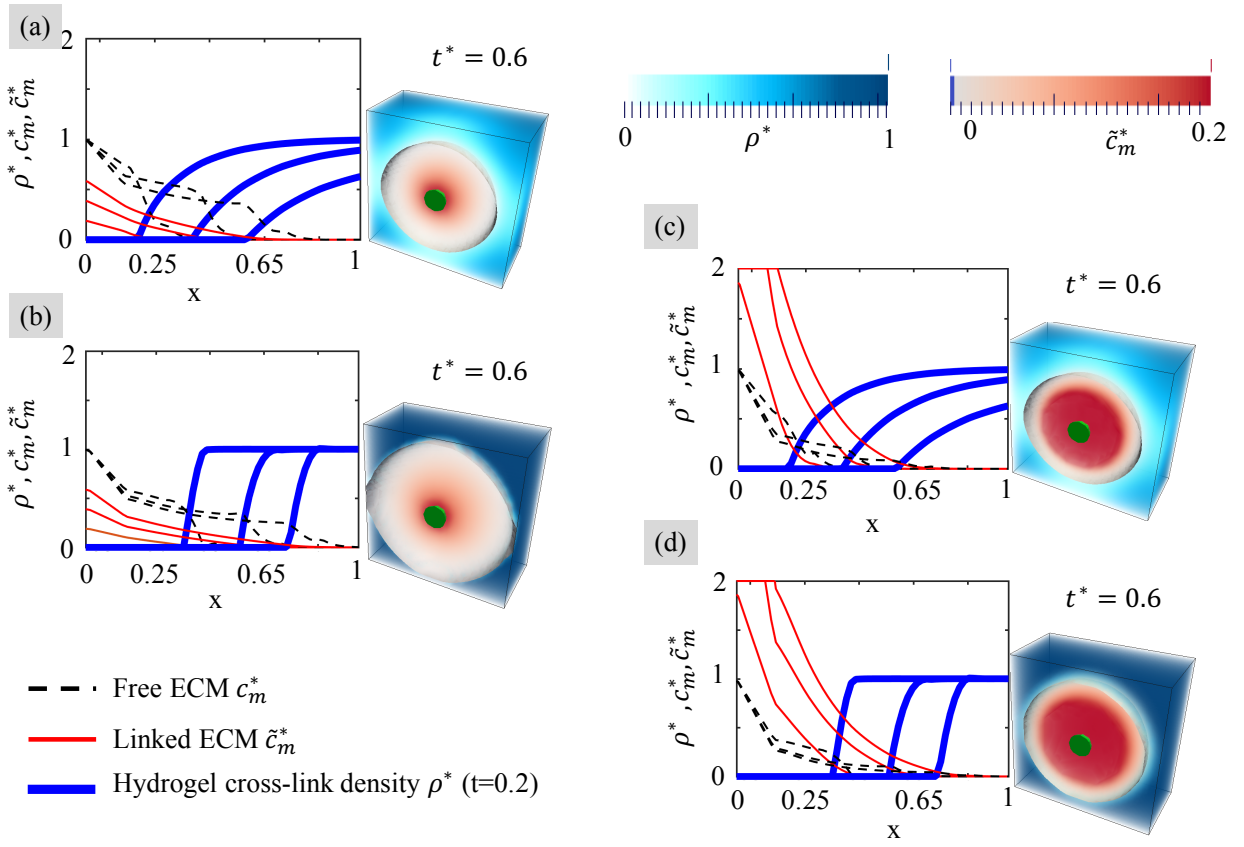

Figure 5.6: *Profile of polymer cross-link density, free ECM concentration and linked ECM concentration as a function of distance from the cell surface. Results are shown for three characteristic times during growth t=3.5, 7 and 10.5 day. (a) Slow ECM deposition in a hydrogel scaffold with a wide and slow degradation front; (b) Slow ECM deposition in a hydrogel scaffold with a sharp and and fast degradation front; (c) Fast ECM deposition in a hydrogel scaffold with a wide and slow degradation front and finally (d) Fast ECM deposition in a hydrogel scaffold with a sharp and and fast degradation front.*

5.5.3 Evolution of the construct's mechanical integrity during combined hydrogel degradation and ECM growth

The primary function of a tissue engineering scaffold is to provide a temporary mechanical support to cells as the new tissue grows. In vivo, this means that the construct must be able to resist physiological load at all time during its transition from scaffold to tissue. As discussed earlier,

current hydrogel-based strategies that are used for cell encapsulations often lead to dissolution and failure of the construct before the ECM can bear any load. Here, we propose to numerically investigate whether the concept of localized degradation has the potential to switch this paradigm and allow both tissue growth and continuity of the constructs mechanical integrity. For this, we use techniques of numerical homogenization that allows us to estimate the overall stress-strain response of the unit cell (Fig. 4.4) in time as the spatial composition of the construct evolves. More precisely, an overall state of deformation $\bar{\mathbf{F}}$ is applied to the domain Ω and the corresponding displacement field $\mathbf{u}(\mathbf{u})$ and stress $\bar{\boldsymbol{\sigma}}$ are calculated as [106]:

$$\mathbf{u}(\mathbf{x}) = \bar{\mathbf{F}} \cdot \mathbf{x} + \tilde{\mathbf{u}}(\mathbf{x}), \quad \bar{\boldsymbol{\sigma}} = \left(\frac{1}{V_0} \int_{\Gamma} \mathbf{t} \otimes \mathbf{X} d\Omega \right) \frac{\bar{\mathbf{F}}^T}{\bar{J}} \tag{5.27}$$

where $\tilde{\mathbf{u}}(\mathbf{x})$ are fluctuations in displacement that remain periodic on the domains boundary, $\mathbf{t}$ is the traction force vector on Γ and $\bar{J} = det(\bar{\mathbf{F}})$. The constructs Youngs modulus may then be estimated by the secant modulus at a 5% strain for a uniaxial deformation:

$$\bar{E}(t) = \frac{\bar{\sigma}_{xx}(t)}{\bar{\epsilon}_{xx}} = \frac{\bar{\sigma}_{yy}(t)}{\bar{\epsilon}_{yy}} = \frac{\bar{\sigma}_{zz}(t)}{\bar{\epsilon}_{zz}} \tag{5.28}$$

where $\bar{\epsilon}_{xx} = \bar{\epsilon}_{yy} = \bar{\epsilon}_{zz} = 5\%$ and the last two equalities stem from the symmetry of the unit cell. To understand how this modulus correlates with the evolution of the hydrogel and ECM composition around a cell, we further introduce a measure of connectivity as follows. A solid phase, polymer or ECM, is defined as connected if any two points within that space can be connected by a continuous path. We note here that polymer and ECM are considered mechanically non-existent if $\rho \leq \rho_c$ and $c_m^* = 0$, respectively. Furthermore, since the unit cell is periodic, a continuous path can cross an external boundary and reappear on its opposite side.

To compare the stiffness of the gel to that of the linked ECM, we define a new dimensionless parameter $E^* = E_{ECM}/E_{gel}$ where $E_{gel} = \rho RT(1.05J_0^{-1/3} - (2.1J_0)^{-1})$ is the secant modulus for 5% strain [2] and $E_{ECM} = \mu(3\lambda + 2\mu)/(\lambda + \mu)$. The evolution of the constructs properties is now affected by the three non-dimensional parameters r_e^*, κ_e^*, κ_m^* and the ECM properties μ^* and λ^*. However, to clarify the analysis, we show the four characteristic cases considered in Fig. 4.6 and

for each, explore the effect of different ECM participation to the overall stiffness; specifically, we consider $E^* = 0.5$ (the ECM is weaker than the gel), $E^* = 1$ (the ECM stiffness is comparable to the gel) and $E^* = 1.5$ (the ECM is stronger than the gel). Key results are presented in Fig. 4.7 for (a) a wide degradation front and slow deposition rate, (b) a sharp degradation front and slow deposition rate, (c) a wide degradation front and fast deposition rate and (d) a sharp degradation front and fast deposition rate. For each case, the figure shows the evolution of the Youngs modulus (curve) and the connectivity of each phase (shaded blue for hydrogel and shaded red for ECM). Three dimensional contours of polymer cross-link density (blue) and linked ECM concentration (red) are also depicted at three characteristic times during the constructs evolution.

When deposition is slow compared to degradation (Fig. 4.7 a and b), results show that the mechanical integrity of the construct monotonically drops with time until it completely dissolves ($\bar{E} = 0$). A closer look at the ultrastructure evolution clearly shows that regardless of the sharpness and speed of the degradation front, ECM deposition lags behind and is unable to produce a well-connected phase before the hydrogel fully degrades. Interestingly, we note that a sharper degradation front yields a faster loss in constructs stiffness; a phenomenon that can be attributed to the fact that sharper fronts move relatively faster than wide ones (Fig. 4.5 b and d). When ECM deposits fast (relative to degradation) one predicts that it can reach connectivity before the hydrogel is completely degraded. As a consequence, even in the case of a wide degradation front, the model suggests that the construct does not completely lose its mechanical integrity. Indeed, while there exists a time interval for which none of the phases are connected, their mechanical interactions allow for a load transfer between them and an overall non-zero (although small) elastic modulus. In the situation of a sharp degradation front however, ECM can effectively grow within the empty interstices left by the propagating front. This eventually leads to a situation in which both polymer and ECM are connected and an optimized continuity of the overall constructs modulus.

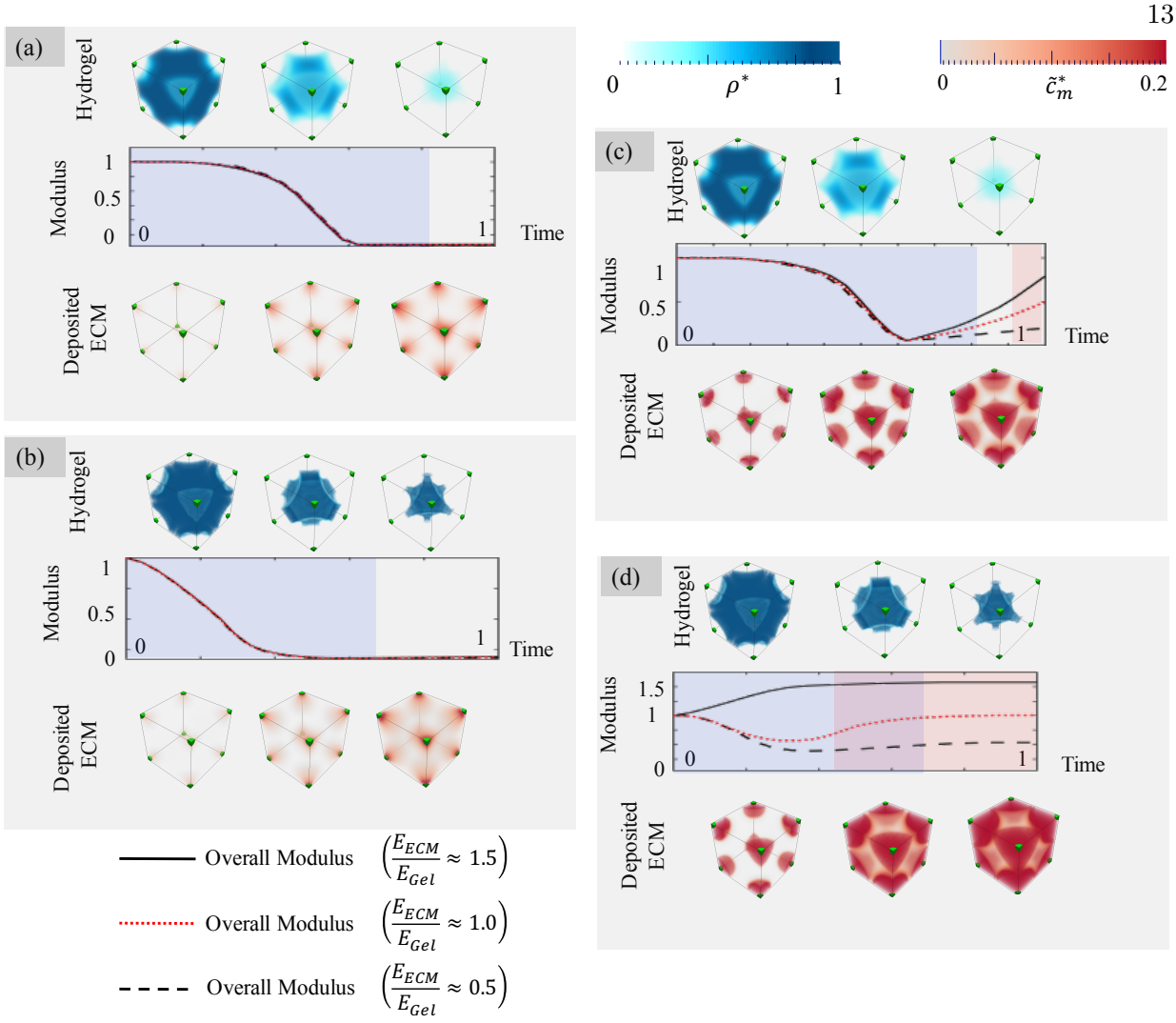

Figure 5.7: *Evolution of construct modulus over time. The mechanical integrity is preserved in the case of sharp degradation front and fast deposition relative to the front speed.*

5.6 Discussion and Concluding remarks

In summary, a multiphasic mixture model is constructed to represent the combined cell-mediated hydrogel degradation and tissue growth. The resulting model has the form of a coupled system of two reaction-diffusion equations corresponding to enzyme diffusion/hydrogel degradation and ECM diffusion/linkage. We have shown that according to the design of the hydrogel (in particular, its initial cross-link density and degradation kinetics), the systems behavior ranges from diffusion-dominated to diffusion-limited. The latter situation is associated with the appearance of

a localized, spherical degradation front propagating outwards from each cell. This space creates pockets of unhindered space enabling the diffusion of large ECM molecules. If the rate of ECM linkage is significantly faster than the rate of hydrogel degradation (and therefore the degradation front velocity), the model suggests that spherical bodies of solid ECM may grow within cavities left by degradation and eventually connect in time. In this case, the construct structure displays a double connected network of ECM and hydrogel, which eventually allows a smooth transition between hydrogel and tissue and continuous mechanical integrity. In a nutshell, the model therefore points out that continuous mechanical integrity of the construct can be achieved by tuning the hydrogel design to achieve both a sharp and slow moving degradation front.

Although it does not appear explicitly, the model also captures the role of cell density during growth. Indeed, due to the non-dimensionalization procedure, the typical width $\tilde{w} = w/L$ of the front is measured relative to the cell spacing L. Since L increases with decreasing cell density f as shown in equation (4.1), a degradation front appears sharper, and thus more favorable to the growth process for low cell densities. This also means that the predicted mechanism may be difficult to achieve for high cell density systems. Interestingly, experimental studies [124] have shown that strategies based on hydrolytic (bulk) degradation show a better potential when higher cell densities are employed. This suggests that optimized growth and degradation can be achieved with a controlled combination of bulk (hydrolytic) and localized (enzymatic) degradation kinetics. This dosage would move towards preferably hydrolytic in high cell density system to enzymatic in low cell-density systems. A quantitative analysis of these dynamics will be the object of future studies.

On a final note, it is important to mention that the scenario highlighted by our study may not be straightforward to reproduce experimentally due to the number of uncertainties and imperfections that characterizes both the polymer structure and the behavior of embedded cells. A number of effects may indeed affect the above model predictions. First of all, the homogeneous spatial distribution of cells is often not verified experimentally. Histology images (Fig. 4.3 b) indeed typically display a heterogeneous distribution containing local clusters of high cell density separated

by low density regions. This distribution can further evolve in time via cell division, migration and death [125]. This may affect the predicted mechanism by only allowing tissue growth in localized regions. To capture this mechanisms, the presented model would need to consider a large number of cells and their distribution, making the computational problem prohibitively costly. This issue can potentially be avoided by using multi-scale techniques based on homogenization as discussed in [78, 149]. Another uncertainty not captured by our model pertains to the behavior of cells, particularly in terms of enzyme and ECM production rate in time. Tissue-producing cells isolated from either tissue or derived from stem cells typically constitute a heterogeneous population that highly reactive to changes (chemical and mechanical) in their environment. The mechanisms discussed here could therefore display variations in space and time and be affected by the type of cell used. In addition to these, the enzymatic activity, i.e. degradation rate, can vary spatially due to the chemical and mechanical changes during the remodeling of the construct [90, 107]. Further experimental characterizations are needed to address these questions.

To summarize, promoting tissue growth in a hydrogel is a complex problem that relies on a deep understanding of the physical, chemical and biological interaction between cells and hydrogels. In this complexity, an integrated approach merging modeling and experimental research will be crucial to identify the dominating mechanisms that control growth, degradation and continuous mechanical integrity of the tissue construct. This study is a step towards identifying these mechanisms. As such, we point to a direction in which experimental efforts should be oriented.

Summary and Future Work

In this thesis a set of computational tools are presented to; (i) understand the coupling between the mechanics of hydrogels and the cell mediated tissue growth (ii) build a map between design parameters and the properties of hydrogels. We presented a self learning algorithm to build the design-structure-property relationship. In this thesis the algorithm is used to generate input data for the mechanistic model and simulate real cases, which will allow us to know where we are in our search for optimum scaffold properties. Second, a map between design parameters and physical properties has been built in order to direct our search in an efficient way. With sufficient experimental data, this tool can be powerful to predict the properties of a hydrogel for given design parameters. As the new experimental data is provided the algorithm keeps validating the assumptions made in the model. Next, a simple computational tool is built to investigate the enzymatic degradation in hydrogels. This tool provides a quantitative data on the characteristics of degradation i.e. how localized is the degradation and how fast degradation front travels through the gel. Furthermore, a 3D multi-scale FE model is built which is used to understand how growth and degradation mechanisms compete with each other and how this competition affects the overall mechanical properties. It is shown that successful tissue growth is feasible if a degradation front slow enough that the matrix deposition fills the space due to hydrogel degradation.

In future work these tools can be combined to obtain one predictive tool that can be used in experimental studies. Further a tissue-scale model can be combined with the current tool in order to reduce the computational cost and spatially track the tissue growth at the macro scale. Long term goal is to use this predictive tool and obtain the hydrogel design parameters based on the

patient's cellular activity data.

Bibliography

[1] Umut Akalp, Stephanie J. Bryant, and Franck J. Vernerey. Tuning tissue growth with scaffold degradation in enzyme sensitive hydrogels: a mathematical model. Soft Matter, 12(36):7505–7520, 2016.

[2] Umut Akalp, Stanley Chu, Stacey Skaalure, Stephanie J. Bryant, Alireza Doostan, and Franck J. Vernerey. Determination of the polymer-solvent interaction parameter for peg hydrogels in water: Application of a self learning algorithm. Polymer, 2015.

[3] Luke D. Amer, Audrey Holtzinger, Gordon Keller, Melissa J. Mahoney, and Stephanie J. Bryant. Enzymatically degradable poly(ethylene glycol) hydrogels for the 3d culture and release of human embryonic stem cell derived pancreatic precursor cell aggregates. Acta Biomaterialia, 22:103–110, August 2015.

[4] K. S. Anseth, N.C. Bowman, and L.B. Peppas. Mechanical properties of hydrogels and their experimental determination. Biomaterials, 17:1647–1657, 1996.

[5] C. G. Armstrong and V. C. Mow. Variations in the intrinsic mechanical properties of human articular cartilage with age, degeneration, and water content. The journal of Bone and Joint Surgery, 64(1):88–94, 1982.

[6] Ellen M. Arruda and Mary C. Boyce. A three dimensional constitutive model for the large stretch behavior of rubber elastic materials. Journal of the Mechancis and Physics of Solids, 41(2):389–412, 1993.

[7] Randolph S. Ashton, Akhilesh Banerjee, Supriya Punyani, David V. Schaffer, and Ravi S. Kane. Scaffolds based on degradable alginate hydrogels and poly(lactide-co-glycolide) microspheres for stem cell culture. Biomaterials, 28(36):5518–5525, December 2007.

[8] G. A. Ateshian, W. H. Warden, J. J. Kim, R. P. Grelsamer, and V. C. Mow. Finite deformation biphasic material properties of bovine articular cartilage from confined compression experiments. Journal of Biomechanics, 30(11-12):1157–1164, December 1997.

[9] Gerard A. Ateshian. On the theory of reactive mixtures for modeling biological growth. Biomechanics and Modeling in Mechanobiology, 6(6):423–445, 2007.

[10] Gerard A. Ateshian, Kevin D. Costa, Evren U. Azeloglu, Barclay Morrison, and Clark T. Hung. Continuum modeling of biological tissue growth by cell division and alteration of intracellular osmolytes and extracellular fixed charge density. Journal of Biomechanical Engineering, 131:101001, 2009.

[11] Gerard A. Ateshian and Tim Ricken. Multigenerational interstitial growth of biological tissues. Biomechanics and Modeling in Mechanobiology, 9(6):689–702, 2010.

[12] S. Atzet, S. Curtin, P. Trinh, S. Bryant, and B. Ratner. Degradable poly(2-hydroxyethyl methacrylate)-co-polycaprolactone hydrogels for tissue engineering scaffolds. Biomacromolecules, 9(12):3370–3377, 2008.

[13] Chelsea S. Bahney, Chih-Wei Hsu, Jung U. Yoo, Jennifer L. West, and Brian Johnstone. A bioresponsive hydrogel tuned to chondrogenesis of human mesenchymal stem cells. FASEB journal: official publication of the Federation of American Societies for Experimental Biology, 25(5):1486–1496, May 2011.

[14] Stefan Bekiranov, Robijn Bruinsma, and Philip Pincus. Solution behavior of polyethylene oxide in water as a function of temperature and pressure. Physical Review E, 55(1):577–585, January 1997.

[15] C. L. Bell and N. A. Peppas. Biomedical membranes from hydrogels and interpolymer complexes. In Prof Nicholas A. Peppas and Prof Robert S. Langer, editors, Biopolymers II, number 122 in Advances in Polymer Science, pages 125–175. Springer Berlin Heidelberg, 1995. DOI: 10.1007/3540587888_15.

[16] Ted Belytschko, Wing Kam Liu, and Brian Moran. Nonlinear Finite Elements for Continua and Structures. John Wiley and Sons Inc., 2000.

[17] Maurice A. Biot. Mechanics of Deformation and Acoustic Propagation in Porous Media. Journal of Applied Physics, 33(4):1482–1498, 1962.

[18] J.E. Bischoff, E.M. Arruda, and K. Grosh. A microstructurally based orthotropic hydperelastic constitutive law. Journal of Applied Mechanics, (570-579), 69.

[19] Ray M. Bowen. Incompressible porous media models by use of the theory of mixtures. International Journal of Engineering Science, 18(9):1129–1148, 1980.

[20] John P. Boyd. Chebysev and Fourier Spectral Methods. Courier Dover Publications, 2001.

[21] M.D Bryant, M.M Khonsari, and F.F Ling. On the thermodynamics of degradation. Proceedings of the Royal Society of London A: Mathematical, Physical and Engineering Sciences, 464(2096):2001–2014, 2008.

[22] Stephanie J. Bryant and Kristi S. Anseth. Hydrogel properties influence ECM production by chondrocytes photoencapsulated in poly(ethylene glycol) hydrogels. Journal of Biomedical Materials Research, 59(1):63–72, 2002.

[23] Stephanie J. Bryant and Kristi S. Anseth. Controlling the spatial distribution of ECM components in degradable PEG hydrogels for tissue engineering cartilage. Journal of Biomedical Materials Research Part A, 64A(1):70–79, January 2003.

[24] Stephanie J. Bryant, Ryan J. Bender, Kevin L. Durand, and Kristi S. Anseth. Encapsulating chondrocytes in degrading PEG hydrogels with high modulus: Engineering gel structural changes to facilitate cartilaginous tissue production. Biotechnology and Bioengineering, 86(7):747–755, June 2004.

[25] Stephanie J. Bryant, Tina T. Chowdhury, David A. Lee, Dan L. Bader, and Kristi S. Anseth. Crosslinking density influences chondrocyte metabolism in dynamically loaded photocrosslinked poly(ethylene glycol) hydrogels. Annals of Biomedical Engineering, 32(3):407–417, March 2004.

[26] William D. Callister. Materials Science and Engineering: An Introduction. John Wiley and Sons Inc., 7 edition, 2007.

[27] Walter B. Cannon. ORGANIZATION FOR PHYSIOLOGICAL HOMEOSTASIS. Physiological reviews, 9(3):399–431, 1929.

[28] Cindy Chung, John Mesa, Mark A. Randolph, Michael Yaremchuk, and Jason A. Burdick. Influence of Gel Properties on Neocartilage Formation by Auricular Chondrocytes Photoencapsulated in Hyaluronic Acid Networks. Journal of Biomedical Materials Research Part A, 77(3):518–525, 2006.

[29] Smadar Cohen, Toshio Yoshioka, Melissa Lucarelli, Lena H. Hwang, and Robert Langer. Controlled Delivery Systems for Proteins Based on Poly(Lactic/Glycolic Acid) Microspheres. Pharmaceutical Research, 8(6):713–720, June 1991.

[30] Olivier Coussy. Poromechanics. John Wiley and Sons Inc., 2004.

[31] J.M.G. Cowie and V. Arrighi. Polymers: Chemistry and Physics of Modern Materials, Third Edition, July 2007.

[32] Rene de Borst, Mike A. Crisfield, Joris J.C. Remmers, and Clemens V. Verhoosel. Non-linear Finite Element Analysis of Solid and Structures. Computational Mechanics. Wiley, United Kingdom, 2 edition, 2012.

[33] Valentin Dhote, Stacey Skaalure, Umut Akalp, Justine Roberts, Stephanie J. Bryant, and Franck J. Vernerey. On the role of hydrogel structure and degradation in controlling the transport of cell-secreted matrix molecules for engineered cartilage. Journal of the Mechanical Behavior of Biomedical Materials, 19:61–74, March 2013.

[34] Valentin Dhote and Franck J. Vernerey. Mathematical model of the role of degradation on matrix development in hydrogel scaffold. Biomechanics and modeling in mechanobiology, 13:167–183, 2014.

[35] Michael A. DiMicco and Robert L. Sah. Dependence of Cartilage Matrix Composition on Biosynthesis, Diffusion, and Reaction. Transport in Porous Media, 50(1-2):57–73, January 2003.

[36] Elena E. Dormidontova. Influence of End Groups on Phase Behavior and Properties of PEO in Aqueous Solutions. Macromolecules, 37(20):7747–7761, October 2004.

[37] Jeanie L. Drury and David J. Mooney. Hydrogels for tissue engineering: scaffold design variables and applications. Biomaterials, 24(24):4337–4351, 2003.

[38] S. M. Klisch ad T. J. Van Dyke and A. Hoger. A theory of Volumetric Growth for Compressible Elastic Biological Materials. Mathematics and Mechanics of Solids, 6(6):551–575, 2001.

[39] Ali Eliassi, Hamid Modarress, and G. Ali Mansoori. Measurement of Activity of Water in Aqueous Poly(ethylene glycol) Solutions (Effect of Excess Volume on the FloryHuggins -Parameter). Journal of Chemical & Engineering Data, 44(1):52–55, January 1999.

[40] J. Elisseeff, K. Anseth, D. Sims, W. McIntosh, M. Randolph, and R. Langer. Transdermal photopolymerization for minimally invasive implantation. Proceedings of the National Academy of Sciences of the United States of America, 96(6):3104–3107, March 1999.

[41] M. Epstein and G.A. Maugin. Thermomechanics of volumetric growth in uniform bodies. International Journal of Plasticity, 16:951–978, 2000.

[42] B. Erman and P.J. Flory. Experimental Results Relating Stress and Birefringe to Strain in Poly(dimethylsiloxane) Networks. Comparison with Theory. Macromolecules, 16(10):1607–1613, 1983.

[43] B. D. Fairbanks, M. P. Schwartz, A. E. Halevi, C. R. Nuttelman, C. N. Bowman, and K. S. Anseth. A versatile synthetic extracellular matrix mimic via thiol-norbornene photopolymerization. Advanced Materials, 21(48):5005–5010, 2009.

[44] M. Farsad and F.J. Vernerey. An xfem-based numerical strategy to model mechanical interactions between biological cells and a deformable substrate. International Journal of Numerical Methods in Engineering, 92(3):238–267, 2012.

[45] Mehdi Farsad and Franck J. Vernerey. An XFEM-based numerical strategy to model mechanical interactions between biological cells and a deformable substrate. International Journal for Numerical Methods in Engineering, 92(3):238–267, October 2012.

[46] P. J. Flory. Principles of Polymer Chemistry. Cornell University Press, 1953.

[47] Paul J. Flory. Principles of Polymer Chemistry. The George Fisher Baker Non-Resident Lectureship in Chemistry at Cornell University. Cornell University Press, Ithaca, NY, December 1953.

[48] P.J. Flory and B. Erman. Theory of Elasticity of Polymer Networks. 3. Macromolecules, 15:800–806, 1982.

[49] Louis Foucard and Franck J. Vernerey. Dynamics of Stress Fibers Turnover in Contractile Cells. Journal of Engineering Mechanics, 138(10):1282–1287, 2012.

[50] Louis Foucard and Franck J. Vernerey. A thermodynamical model for stress-fiber organization in contractile cells. Applied physics letters, 100(1):013702, 2012.

[51] Marios M. Fyrillas and Keiko K. Nomura. Diffusion and brownian motion in lagrangian coordinates. Journal of Chemical Physics, 126(164510), 2007.

[52] Luigi Gambarotta and Sergio Lagomarsino. A microcack damage model for brittle materials. International Journal of Solids and Structures, 30(2):177–198, 1993.

[53] K. Garikipati, E. M. Arruda, K. Grosh, H. Narayanan, and S. Calve. A continuum treatment of the growth in biological tissue: the coupling of mass transport and mechanics. Journal of the Mechanics and Physics of Solids, 52:1595–1625, 2004.

[54] S.T. Gould, N.J. Darling, and K.S. Anseth. Small peptide functionalized thiol-ene hydrogels as culture substrates for understanding valvular interstitial cell activation and de novo tissue deposition. Acta Biomaterialia, 8:3201–3209, 2012.

[55] N. B Graham, M Zulfiqar, N. E Nwachuku, and A Rashid. Interaction of poly(ethylene oxide) with solvents: 2. Water-poly(ethylene glycol). Polymer, 30(3):528–533, March 1989.

[56] N. B. Graham, M. Zulfiqar, N. E. Nwachuku, and A. Rashid. Interaction of poly(ethylene oxide) with solvents: 4. Interaction of water with poly(ethylene oxide) crosslinked hydrogels. Polymer, 31(5):909–916, May 1990.

[57] M. A. Haider, J.E. Olander, R.F. Arnold, D.R. Marous, A.J. McLamb, K.C. Thompson, W.R. Woodruff, and J.M. Haugh. A phenomenological mixture model for biosynthesis and linking of cartilage extracellular matrix in scaffolds seeded with chondrocytes. Biomech Model Mechanobiol, 10(6):915–24, Dec 2011.

[58] Mansoor A. Haider, Jeffrey E. Olander, Rachel F. Arnold, Daniel R. Marous, April J. McLamb, Karmethia C. Thompson, William R. Woodruff, and Janine M. Haugh. A phenomenological mixture model for biosynthesis and linking of cartilage extracellular matrix in scaffolds seeded with chondrocytes. Biomechanics and Modeling in Mechanobiology, 10(6):915–924, January 2011.

[59] Donny Hanjaya-Putra, Kyle T. Wong, Kelsey Hirotsu, Sudhir Khetan, Jason A. Burdick, and Sharon Gerecht. Spatial control of cell-mediated degradation to regulate vasculogenesis and angiogenesis in hyaluronan hydrogels. Biomaterials, 33(26):6123–6131, 2012.

[60] Tim Hardingham. Proteoglycans and glycosaminoglycans. In Dynamics of Bone and Cartilage Metabolism., pages 85–98. Academic Press, 2006.

[61] J. H. Hildebrand. Solubility of non-electrolytes. New York: Reinhold Publishing Corp., 1936.

[62] M. H. Holmes and V. C. Mow. The nonlinear characteristics of soft gels and hydrated connective tissues in ultrafiltration. Journal of Biomechanics, 23(11):1145–1156, January 1990.

[63] M.H. Holmes and V.C. Mow. The nonlinear characteristics of soft gels and hydrated connective tissues in ultrafiltration. Journal of Biomechanics, 23(11):1145–1156, 1990.

[64] Gerard A. Holzapfel. Nonlinear Solid Mechanics: A Continuum Approach for Engineering. John Wiley and Sons Inc., 2000.

[65] W. Hong, X. Zhao, and Z. Suo. Large defromation and electrochemistry of polyelectrolyte gels. Journal of the Mechanics and Physics of Solids, 58:558–577, 2010.

[66] Jennifer M. Hootman and Charles G. Helmick. Projections of US prevalence of arthritis and associated activity limitations. Arthritis & Rheumatism, 54(1):226–229, January 2006.

[67] Daniel Howard, Lee D. Buttery, Kevin M. Shakesheff, and Scott J. Roberts. Tissue engineering: strategies, stem cells and scaffolds. Journal of Anatomy, 213(1):66–72, 2008.

[68] Long Huang and Katsuyoshi Nishinari. Interaction between poly(ethylene glycol) and water as studied by differential scanning calorimetry. Journal of Polymer Science Part B: Polymer Physics, 39(5):496–506, March 2001.

[69] M. R. Huglin. Hydrogels in medicine and pharmacy Edited by N. A. Peppas, CRC Press Inc., Boca Raton, Florida, 1986 (Vol. l), 1987 (Vols 2 and 3). Vol. 1 Fundamentals, pp. vii + 180, 72.00, ISBN 0-8493-5546-X; Vol. 2 Polymers, pp. vii + 171, 72.00, ISBN 0-8493-5547-8; Vol. 3 Properties and Applications, pp. vii + 195, 8000, ISBN 0-8493-5548-6. British Polymer Journal, 21(2):184–184, January 1989.

[70] J. D. Humphrey and K. R. Rajagopal. A Constrained Mixture Model for Growth and Remodeling of Soft Tissues. Mathematical Models and Methods in Apllied Sciences, 12(3):407–430, 2002.

[71] Yoshito Ikada. Challenges in tissue engineering. Journal of Royal Society of Interface, 3:589–601, 2006.

[72] Jacob Israelachvili. The different faces of poly(ethylene glycol). Proceedings of the National Academy of Sciences, 94(16):8378–8379, August 1997.

[73] Chen R. Jin and W. T. Simpson. Comparatice studies of metamodelling techniques under multiple modelling criteria. Structural and Multidisciplinary Optimization, 23:1–13, 2001.

[74] Albert J. Keung, Sanjay Kumar, and David V. Schaffer. Presentation Counts: Microenvironmental Regulation of Stem Cells by Biophysical and Material Cues. Annual Review of Cell and Developmental Biology, 26(1):533–556, 2010.

[75] Stephen M. Klisch, Silvia S. Chen, Robert L. Sah, and Anne Hoger. A growth mixture theory for cartilage with application to growth-related experiments on cartilage explants. Journal of Biomechanical Engineering, 125(2):169–179, 2003.

[76] Peter Kofinas, Vassiliki Athanassiou, and Edward W. Merrill. Hydrogels prepared by electron irradiation of poly(ethylene oxide) in water solution: unexpected dependence of crosslink density and protein diffusion coefficients on initial peo molecular weight. Biomaterials, 17:1547–1550, 1996.

[77] R. Koningsveld and L. A. Kleintjens. Liquid-liquid phase separation in multicomponent polymer systems. x. concentration dependence of the pair-interaction parameter in the system cyclohexane-polystyrene. Macromolecules, 4(5):637–641, 1971.

[78] V. G. Kouznetsova, M. G. D. Geers, and W. A. M. Brekelmans. Multiscale second-order computational homogenization of multi-phase materials: a nested finite element strategy. Computer methods in applied mechanics and engineering, 193:5525–5550, 2004.

[79] Manuel K.Rausch and Ellen Kuhl. On the mechanics of growing thin biological membranes. Journal of the Mechanics and Physics of Solids, 63:128–140, 2014.

[80] Michael K. Kwan, W. Michael Lai, and Van C. Mow. A finite deformation theory for cartilage and other soft hydrated connective tissues—I. Equilibrium results. Journal of Biomechanics, 23(2):145–155, 1990.

[81] Soo-Hong Lee, Jordan S. Miller, James J. Moon, and Jennifer L. West. Proteolytically Degradable Hydrogels with a Fluorogenic Substrate for Studies of Cellular Proteolytic Activity and Migration. Biotechnology Progress, 21(6):1736–1741, January 2005.

[82] Jennifer L. Leight, Emi Y. Tokuda, Caitlin E. Jones, Austin J. Lin, and Kristi S. Anseth. Multifunctional bioscaffolds for 3d culture of melanoma cells reveal increased MMP activity and migration with BRAF kinase inhibition. Proceedings of the National Academy of Sciences, 112(17):5366–5371, April 2015.

[83] Stephane G. Levesque and Molly S. Shoichet. Synthesis of Enzyme-Degradable, Peptide-Cross-Linked Dextran Hydrogels. Bioconjugate chemistry, 18(3):874–885, 2007.

[84] Chao Li, Ronaldo I. Borja, and Richard A. Regueiro. Dynamics of porous media at finite strain. Computer Methods in Applied Mechanics and Engineering, 193(36–38):3837–3870, September 2004.

[85] Sheng Lin-Gibson, Sidi Bencherif, James A. Cooper, Stephanie J. Wetzel, Joseph M. Antonucci, Brandon M. Vogel, Ferenc Horkay, and Newell R. Washburn. Synthesis and Characterization of PEG Dimethacrylates and Their Hydrogels. Biomacromolecules, 5(4):1280–1287, July 2004.

[86] Nick Lombardo. Properties of Composite Containing Spherical Inclusions Surronded by an Inhomogeneous Interphase Region. PhD thesis, RMIT University, June 2007.

[87] Vlado A. Lubarda and Anne Hoger. On the mechanics of solids with a growing mass. International Journal of Solids and Structures, 39:4627–4664, 2002.

[88] S. Lüsse and K. Arnold. The Interaction of Poly(ethylene glycol) with Water Studied by 1h and 2h NMR Relaxation Time Measurements. Macromolecules, 29(12):4251–4257, January 1996.

[89] Steven R. Lustig and Nikolaos A. Peppas. Solute diffusion in swollen membranes. IX. Scaling laws for solute diffusion in gels. Journal of Applied Polymer Science, 36(4):735–747, August 1988.

[90] M. P. Lutolf, J. L. Lauer-Fields, H. G. Schmoekel, A. T. Metters, F. E. Weber, G. B. Fields, and J. A. Hubbell. Synthetic matrix metalloproteinase-sensitive hydrogels for the conduction of tissue regeneration: Engineering cell-invasion characteristics. Proceedings of the National Academy of Sciences, 100(9):5413–5418, 2003.

[91] Klaus von der Mark. Chapter 1 - Structure, Biosynthesis and Gene Regulation of Collagens in Cartilage and Bone A2 - Bilezikian, Markus J. SeibelSimon P. RobinsJohn P. In Dynamics of Bone and Cartilage Metabolism (Second Edition), pages 3–40. Academic Press, Burlington, 2006.

[92] Mariah N. Mason, Andrew T. Metters, Christopher N. Bowman, and Kristi S. Anseth. Predicting Controlled-Release Behavior of Degradable PLA-b-PEG-b-PLA Hydrogels. Macromolecules, 34(13):4630–4635, June 2001.

[93] Patrick T. Mather, Xiaofan Luo, and Ingrid A. Rousseau. Shape memory polymer research. Annual Review of Materials Research, 39:445–471, 2009.

[94] D. L. McDowell and G.B. Olson. Concurrent design of hierarchical materials and structures. Journal of Scientific Modeling and Simulation, 15(1-3):207–240, 2008.

[95] Gregory B. McKenna, Kathleen M. Flynn, and Yihong Chen. Swelling in crosslinked natural rubber: experimental evidence of the crosslink density dependence of χ. Polymer, 31:1937–1945, 1990.

[96] Edward W. Merrill, Kathleen A. Dennison, and Cynthia Sung. Partitioning and diffusion of solutes in hydrogels of poly(ethylene oxide). Biomaterials, 14(15):1117–1126, January 1993.

[97] A. T. Metters, K. S. Anseth, and C. N. Bowman. Fundamental studies of a novel, biodegradable PEG-b-PLA hydrogel. Polymer, 41(11):3993–4004, May 2000.

[98] Andrew Metters and Jeffrey Hubbell. Network formation and degradation behavior of hydrogels formed by michael-type addition reactions. Biomacromolecules, 6:290–301, 2005.

[99] Andrew T. Metters, Christopher N. Bowman, and Kristi S. Anseth. A Statistical Kinetic Model for the Bulk Degradation of PLA-b-PEG-b-PLA Hydrogel Networks. The Journal of Physical Chemistry B, 104(30):7043–7049, August 2000.

[100] Andrew T. Metters, Christopher N. Bowman, and Kristi S. Anseth. Verification of scaling laws for degrading PLA-b-PEG-b-PLA hydrogels. AIChE Journal, 47(6):1432–1437, June 2001.

[101] Antonios G. Mikos and Nikolaos A. Peppas. Flory interaction parameter χ for hydrophilic copolymers with water. Biomaterials, 9:419–423, 1988.

[102] Christina Cruickshank Miller. The Stokes-Einstein Law for Diffusion in Solution. Proceedings of the Royal Society of London A: Mathematical, Physical and Engineering Sciences, 106(740):724–749, December 1924.

[103] Douglas R. Miller and Christopher W. Macosko. A New Derivation of Post Gel Properties of Network Polymers. Macromolecules, 9(2):206–211, March 1976.

[104] S. S. Mok, K. Masuda, H. J. Häuselmann, M. B. Aydelotte, and E. J. Thonar. Aggrecan synthesized by mature bovine chondrocytes suspended in alginate. Identification of two distinct metabolic matrix pools. The Journal of Biological Chemistry, 269(52):33021–33027, December 1994.

[105] V. C. Mow, M. C. Gibbs, W. M. Lai, W. B. Zhu, and Kyriacos A. Athanasiou. Biphasic Indentation of Articular Cartilage - II A Numerical Algorithm and An Experimental Study. Journal of Biomechanics, 22(8/9):853–861, 1989.

[106] Sia Nemat-Nasser and Muneo Hori. Micromechanics: Overall Properties of Heterogeneous Materials, volume 37 of Applied Mathematics and Mechanics. Elsevier Science Publishers, North-Holland, 1993.

[107] G. D. Nicodemus and S. J. Bryant. Mechanical loading regimes affect the anabolic and catabolic activities by chondrocytes encapsulated in PEG hydrogels. Osteoarthritis and Cartilage, 18(1):126–137, January 2010.

[108] G. D. Nicodemus and Stephanie J. Bryant. Cell encapsulation in biodegradable hydrogels for tissue engineering applications. Tissue Engineering Part B, Reviews, 14(2):149–165, 2008.

[109] G. D. Nicodemus and Stephanie J. Bryant. The role of hydrogel structure and dynamic loading on chondrocyte gene expression and matrix formation. Journal of Biomechanics, 41(7):1528–1536, 2008.

[110] G. D. Nicodemus, S. C. Skaalure, and S. J. Bryant. Gel structure has an impact on pericellular and extracellular matrix deposition, which subsequently alters metabolic activities in chondrocyte-laden PEG hydrogels. Acta Biomaterialia, 7(2):492–504, February 2011.

[111] G.D. Nicodemus, K.A. Shiplet, S.R. Kaltz, and S.J. Bryant. Dynamic compressive loading influences degradation behavior of peg-pla hydrogels. Biotechnology Bioengineering, 102(3):948–959, 2009.

[112] William L. Oberkampf and Christopher J. Roy. Verification and Validation in Scientific Computing. Cambridge University Press, 2010.

[113] Hansoo Park, Xuan Guo, Johnna S. Temenoff, Yasuhiko Tabata, Arnold I. Caplan, F. Kurtis Kasper, and Antonios G. Mikos. Effect of swelling ratio of injectable hydrogel composites on chondrogenic differentiation of encapsulated rabbit marrow mesenchymal stem cells in vitro. Biomacromolecules, 10(3):541–546, 2009.

[114] N. A. Peppas, J. Z. Hilt, A. Khademhosseini, and R. Langer. Hydrogels in Biology and Medicine: From Molecular Principles to Bionanotechnology. Advanced Materials, 18(11):1345–1360, June 2006.

[115] S.S.L. Peppin, J.A.W. Elliott, and M.G. Worster. Pressure and relative motion in colloidal suspensions. Physics of Fluids, 17(053301), 2005.

[116] H. M. Petri and B. A. Wolf. Concentration-dependent thermodynamic interaction parameters for polymer-solutions - quick and reliable determination via normal gas-chromatography. Macromolecules, 27(10):2714–2718, 1994.

[117] H.M. Petri and B. A. Wolf. Composition-dependent flory-huggins parameters: molecular weight influences at high concentrations. Macromolecular Chemistry and Physics, 196(7):2321–2333, 1995.

[118] Caibo Qian, Stephen J. Mumby, and B. E. Eichinger. Phase diagrams of binary polymer solutions and blends. Macromolecules, 24:1655–1661, 1991.

[119] B. F. Qiao and D. L. Zhao. A theory of polymer solutions without the mean-field approximation in flory-huggins theory. Journal of Chemical Physics, 121(10):4968–4973, 2004.

[120] Nestor V. Queipo, Raphael T. Haftka, Wei Shyy, Tushar Goel, Rajkumar Vaidyanathan, and P. Kevin Tucker. Surrogate-based analysis and optimization. Progress in Aerospace Sciences, 41(1):1–28, 2005.

[121] Buddy D. Ratner and Stephanie J. Bryant. BIOMATERIALS: Where We Have Been and Where We are Going. Annual Review of Biomedical Engineering, 6:41–75, 2004.

[122] Florian Rehfeldt, Adam J. Engler, Adam Eckhardt, Fariyal Ahmed, and Dennis E. Discher. Cell responses to the mechanochemical microenvironment—Implications for regenerative medicine and drug delivery. Advanced drug delivery reviews, 59(13):1329–1339, November 2007.

[123] Jeffrey J. Rice, Mikaël M. Martino, Laura De Laporte, Federico Tortelli, Priscilla S. Briquez, and Jeffrey A. Hubbell. Engineering the Regenerative Microenvironment with Biomaterials. Advanced Healthcare Materials, 2(1):57–71, January 2013.

[124] Mark A. Rice and Kristi S. Anseth. Controlling Cartilaginous Matrix Evolution in Hydrogels with Degradation Triggered by Exogenous Addition of an Enzyme. Tissue Engineering, 13(4):683–691, 2007.

[125] Justine J. Roberts and Stephanie J. Bryant. Comparison of photopolymerizable thiol-ene PEG and acrylate-based PEG hydrogels for cartilage development. Biomaterials, 34(38):9969–9979, 2013.

[126] Justine J. Roberts, Garret D. Nicodemus, Eric C. Greenwald, and Stephanie J. Bryant. Degradation Improves Tissue Formation in (Un)Loaded Chondrocyte-laden Hydrogels. Clinical Orthopaedics and Related Research®, 469(10):2725–2734, February 2011.

[127] E. K. Rodriguez, Anne Hoger, and Andrew D. Mcculloch. Stress-dependent finite growth in soft elastic tissues. Journal of Biomechanics, 27(4):455–467, 1994.

[128] F. Roters, D. Raabe, and G. Gottstein. Work hardening in heterogeneous alloys- a microstructural approach based on three internal state variables. Acta Materialia, 48:4181–4189, 2000.

[129] Michael Rubinstein and R. Colby. Polymers physics, volume 767. Oxford Oxford, UK, 2003.

[130] Amarpreet S. Sawhney, Chandrashekhar P. Pathak, and Jeffrey A. Hubbell. Bioerodible hydrogels based on photopolymerized poly(ethylene glycol)-co-poly(.alpha.-hydroxy acid) diacrylate macromers. Macromolecules, 26(4):581–587, February 1993.

[131] B. G. Sengers, C. C. van Donkelaar, C. W. J. Oomens, and F. P. T. Baaijens. The Local Matrix Distribution and the Functional Development of Tissue Engineered Cartilage, a Finite Element Study. Annals of Biomedical Engineering, 32(12):1718–1727, December 2004.

[132] B.G. Sengers, M. Taylor, C.P. Please, and Oreffo R.O.C. Computational modelling of cell spreading and tissue regeneration in porous scaffolds. Biomaterials, 28:1926–1940, 2007.

[133] BramG Sengers, Mark Taylor, Colin P. Please, and Richard O. C. Oreffo. Computational modelling of cell spreading and tissue regeneration in porous scaffolds. Biomaterials, 28:1926–1940, 2007.

[134] Samir P. Singh, Michael P. Schwartz, Justin Y. Lee, Benjamin D. Fairbanks, and Kristi S. Anseth. A peptide functionalized poly(ethylene glycol) (PEG) hydrogel for investigating the influence of biochemical and biophysical matrix properties on tumor cell migration. Biomaterials Science, 2(7):1024–1034, June 2014.

[135] Stacey C. Skaalure, Umut Akalp, Franck J. Vernerey, and Stephanie J. Bryant. Tuning Reaction and Diffusion Mediated Degradation of Enzyme-Sensitive Hydrogels. Advanced Healthcare Materials, 2016.

[136] Stacey C. Skaalure, Stanley Chu, and Stephanie J. Bryant. An Enzyme-sensitive PEG Hydrogel Based on Aggrecan Catabolism for Cartilage Tissue Engineering. Advanced healthcare materials, 4(3):420–431, February 2015.

[137] Stacey C. Skaalure, Ian L. Milligan, and Stephanie J. Bryant. Age impacts extracellular matrix metabolism in chondrocytes encapsulated in degradable hydrogels. Biomedical Materials, 7(2):024111, 2012.

[138] R. Skalak, G. Dasgupta, and M. Moss. Analytical Description of Growth. Journal of Theoretical Biology, 94(555-577), 1982.

[139] Brandon V. Slaughter, Shahana S. Khurshid, Omar Z. Fisher, Ali Khademhosseini, and Nicholas A. Peppas. Hydrogels in Regenerative Medicine. Advanced Materials, 21(32-33):3307–3329, September 2009.

[140] A. Striolo and J. M. Prausnitz. Osmotic second virial coefficient for linear and star poly(ethylene oxide). Polymer, 42(10):4773–4775, 2001.

[141] L. R. G. Treloar. The Physics of Rubber Elasticity. Oxford University Press, USA, December 1975.

[142] Abbey J. Trewenack, Colin P. Please, and Kerry A. Landman. A continuum model for the development of tissue-engineered cartilage around a chondrocyte. Mathematical Medicine and Biology, 26(3):241–262, September 2009.

[143] C. Truesdell and W. Noll. The Non-linear Field Theories. Springer Berlin Heidelberg, 1965.

[144] J. M. Tyrus, M. Gosz, and E. DeSantiago. A local finite element implementation for imposing periodic boundary conditions on composite micromechanical models. International Journal of Solids and Structures, 44:2972–2989, 2007.

[145] F.J. Vernerey and M. Farsad. A mathematical model of the coupled mechanisms of cell adhesion, contraction and spreading. Journal of mathematical biology, 68(4):989–1022, 2013.

[146] Franck J. Vernerey. On the Application of Multiphasic Theories to the Problem of Cellsubstrate Mechanical Interactions. In Prof Shaofan Li and Prof Bohua Sun, editors, Advances in Cell Mechanics, pages 189–224. Springer Berlin Heidelberg, 2011. DOI: 10.1007/978-3-642-17590-9_6.

[147] Franck J. Vernerey. A theoretical treatment on the mechanics of interfaces in deformable porous media. International Journal of Solids and Structures, 48(22–23):3129–3141, November 2011.

[148] Franck J. Vernerey. The Effective Permeability of Cracks and Interfaces in Porous Media. Transport in Porous Media, 93(3):815–829, March 2012.

[149] Franck J. Vernerey. A Microstructure-Based Continuum Model for Multiphase Solids. Mechanics of Advanced Materials and Structures, 21(6):441–456, 2014.

[150] Franck J. Vernerey. A mixture approach to investigate interstitial growth in engineering scaffolds. Biomechanics and Modeling in Mechanobiology, pages 1–20, 2015.

[151] Franck J. Vernerey and Mehdi Farsad. A constrained mixture approach to mechano-sensing and force generation in contractile cells. Journal of the Mechanical Behavior of Biomedical Materials, 4(8):1683–1699, November 2011.

[152] Franck J. Vernerey and Mehdi Farsad. An Eulerian/XFEM formulation for the large deformation of cortical cell membrane. Computer Methods in Biomechanics and Biomedical Engineering, 14(5):433–445, May 2011.

[153] Franck J. Vernerey, Louis Foucard, and Mehdi Farsad. Bridging the Scales to Explore Cellular Adaptation and Remodeling. BioNanoScience, 1(3):110–115, July 2011.

[154] Franck J. Vernerey, Eric C. Greenwald, and Stephanie J. Bryant. Triphasic mixture model of cell-mediated enzymatic degradation of hydrogels. Computer Methods in Biomechanics and Biomedical Engineering, 15(11):1197–1210, 2012.

[155] Franck J. Vernerey, Wing K. Liu, Brian Moran, and Gregory B. Olson. A Micromorphic Model for the Multiple Scale Failure of Heterogeneous Materials. Journal of the Mechancis and Physics of Solids, 56(4):1320–1347, 2008.

[156] I. Villanueva, D. S. Hauschulz, D. Mejic, and S. J. Bryant. Static and dynamic compressive strains influence nitric oxide production and chondrocyte bioactivity when encapsulated in PEG hydrogels of different crosslinking densities. Osteoarthritis and Cartilage, 16(8):909–918, August 2008.

[157] H. B. Wang, M. Dembo, and Y.L. Wang. Substrate flexibility regulates growth and apoptosis of normal but not transformed cells. Americal Journal of Physiology Cell Physiology, 279(5):C1345–1350, 2000.

[158] Scott M Wilhelm, Arthur Z. Eisen, Mari Teter, Sheryl D. Clark, Annemarie Kronberger, and Gregory Goldberg. Human fibroblast collagenase: Glycosylation and tissue-specific levels of enzyme synthesis. Proceedings of the National Academy of Science, 83:3756–3760, 1986.

[159] Christopher G. Wilson, Lawrence J. Bonassar, and Sean S. Kohles. Modeling the dynamic composition of engineered cartilage. Archives of Biochemistry and Biophysics, 408(2):246–254, 2002.

[160] M. Wong, M. Ponticiello, V. Kovanen, and J. S. Jurvelin. Volumetric changes of articular cartilage during stress relaxation in unconfined compression. Journal of Biomechanics, 33:1049–1054, 2000.

[161] X. P. Xiong, J. Eckelt, and B. A. Wolf. Linear versus three-arm star polybutadiene: Effects of polymer architecture on the thermodynamic solution behavior. Macromolecules, 45(23):9539–9546, 2012.

[162] I. Yannas, E. Lee, D. P. Orgil, E. M. Skrabut, and G. F. Murphy. Synthesis and characterization of a model extracellular matrix that induces partial regeneration of adult mammalian skin. Proceedings of the National Academy of Science, 86(3):933–937, 1989.

[163] H. Zhang, A. Patel, A. K. Gaharwar, S. M. Mihaila, G. Iviglia, S. Mukundan, H. Bae, H. Yang, and A. Khademhosseini. Hyperbranched polyester hydrogels with controlled drug release and cell adhesion properties. Biomacromolecules, 14(5):1299–310, 2013.

[164] Jiaping Zhang, Xuanhe Zhao, Zhigang Suo, and Hanqing Jiang. A finite element method for transient analysis of concurrent large deformation and mass transport in gel. Journal of Applied Physics, 105, 2009.

Appendix A

Derivation of Diffusion-Reaction Models

Mathematical Model of Enzymatic Degradation in Hydrogels: In localized degradation, the degrading region is largely confined by the bulk hydrogel. As a result, changes in swelling can be assumed to be negligible and therefore the volumetric equilibrium swelling ratio, Q, is taken as its initial value and is assumed constant throughout degradation, referred to as Q^0. As degradation proceeds a point is reached where the gel undergoes reverse gelation, i.e. the point when a critical number of crosslinks has been broken resulting in highly branched, soluble polymers chains. This point is referred to as the critical crosslink density, ρ_c. This parameter can be directly related to network connectivity, β, which represents the ratio of the minimum number of connections needed to form a solid, crosslinked hydrogel to the total number of crosslinks We thus define ρ_c by

$$\rho_c = \beta \rho_x^0 \tag{A.1}$$

where ρ_X^0 is the initial crosslink density prior to degradation. Network connectivity can be described by a statistical network formation model of an ideal network where every macromer is assumed to form an effective crosslink as follows[2,3]:

$$\beta_{ideal} = \frac{1}{\sqrt{r(f_{ene}-1)(f_{thiol}-1)}} \tag{A.2}$$

where r is the [thiol]/[norbornene] ratio, f_{ene} is the number of PEG arms functionalized with norbornene, and f_{thiol} is the number of PEG arms functionalized with thiols. For a real network, the value of β will be higher due to imperfections in the network (e.g., cyclization, dangling ends).

Localized hydrogel degradation can be described with the following system of equations. We assume Fickian diffusion for the enzyme through the hydrogel, and describe enzyme concentration (c_e) as a function of location and time by:

$$\frac{Dc_e}{Dt} = \nabla \cdot [D_e(\rho_x)\nabla c_e] \tag{A.3}$$

where diffusivity of the enzyme, D_e, through the hydrogel is dependent on hydrogel crosslink density, which also changes in space and time. Diffusivity is estimated using a free-volume approach described by Lustig and Peppas[4] and which has been applied to PEG hydrogels[5]. Diffusivity is, thus, determined by:

$$D_e(\rho_x) = D_\infty e^{-Y/(Q_0-1)}\left(1 - \frac{r_e}{\xi}\right) \quad \text{for} \quad r_e < \xi \tag{A.4}$$

and $D_e = 0$, otherwise. Here, D_∞ is the enzyme diffusivity in water estimated by the Stokes-Einstein relationship, Y is the critical volume required for a successful translational movement of the enzyme molecule relative to the average free volume of a water molecule and is assumed to be equal to one, r_e is the radius of the enzyme and ξ is the mesh size. The mesh size, which describes the distance between two adjacent crosslinks, is estimated by [6]:

$$\xi = Q_0^{1/3}\ell\left(\frac{3C_n\rho^P}{M_r}\right)\frac{1}{\sqrt{\rho_x}} \tag{A.5}$$

where ℓ is the average length in the polymer chain, C_n is the characteristic ratio, ρ^P is the density of the polymer, M_r is the molecular weight of the repeat unit. For PEG hydrogels, the values of these parameters are given in Table S2. We introduce a Heaviside step function to describe the sudden increase of mesh size as the crosslink density reaches its critical value by:

$$\xi = Q_0^{1/3}\ell\left(\frac{3C_n\rho^P}{M_r}\right)\frac{1}{H(\rho_x - \rho_x)}\frac{1}{\sqrt{\rho_x}} \tag{A.6}$$

In other words, when ρ_x is greater than ρ_c and the hydrogel is intact and the Heaviside step function equals one. However, when ρ_x is equal to or is less than ρ_c , the hydrogel has reached reverse gelation and the Heaviside step function equals zero. In this case, mesh size goes to infinity. Equation (S6) may then be substituted into (S4) to obtain a relationship between enzyme diffusivity and crosslink density.

Hydrogel degradation is assumed to follow Michaelis-Menten kinetics, which has been described previously for enzyme-sensitive PEG hydrogels [3]. Because the peptide is the crosslink, we can directly relate substrate concentration to crosslink density in the swelling solvent (ρ_x^s) and describe degradation by:

$$\frac{D\rho_x^s}{Dt} = -k_{cat}c_e\left(\frac{\rho_x^s}{K_M + \rho_x^s}\right) \tag{A.7}$$

We can relate ρ_x^s to ρ_x, which describes crosslink density for the non-solvent case, by

$$\rho_x^s = \rho_x/(Q_0 - 1) \tag{A.8}$$

Table A.1: Hydrogel formulations

Experiment	Nomenclature	8arm PEG-NB MW (g/mol)	8arm PEG-NB wt% (g/g)	Thiol:ene Ratio
1D Diffusion	High crosslinking	10000	15	1:1
1D Degradation	Low crosslinking	20000	5	0.5:1
1D Degradation	Intermediate crosslinking	20000	10	0.8:1
1D Degradation	High crosslinking	10000	15	1:1
3D Degradation	Low crosslinking	20000	5	0.9:1
3D Degradation	High crosslinking	10000	15	1:1

Table A.2: Hydrogel formulations

Parameter	Symbol	Value	Unit
Characteristic Ratio	C_n	4	–
Average bond length	l	1.47	$\mathring{A}$
Molecular weight (MW) Repeat unit	M_r	44	g/mol
Polymer density	ρ^P	1.07	g/ml

A.1 1D diffusion of enzyme in non-degrading hydrogel and estimation of enzyme characteristics

We characterized 1D diffusion of the enzyme through a non-degradable hydrogel, where the peptide crosslinks were exchanged for stable PEG dithiol crosslinks of similar molecular weight, in

order to estimate a minimum average enzyme size for the collagenase blend. Our 1D experimental set-up (Figure S1A) consisted of a rectangular hydrogel with diffusion restricted to one dimension, where one reservoir contained phosphate buffered saline (PBS) bath with a constant concentration of fluorescently labeled collagenase and the other reservoir contained PBS. Enzyme diffusion into the hydrogel was monitored by fluorescence over time and distance (Figure S1B). The multi-phase mixture model [7] was used assuming Fickian diffusion and scaling laws for solute diffusion in swollen hydrogels based on free volume theory [4] to fit the experimental data (Figure S1B and S1C). Based on this fit, we estimated a minimum average enzyme radius of ≈6.5 nm for the collagenase blend. Independently, we estimated the molecular weights of the different species in the blend (Figure S2A) and their activities (Figure S2B) using gel electrophoresis stained with Coomassie Blue staining and a gelatin zymogram, respectively. Based on the zymography results, the higher molecular weight species ≈65 to 130 kDa showed the highest activity, which is attributed to either a higher reactivity or a greater abundance. We, therefore, estimated an average molecular weight for the active enzyme blend to be ≈100 kDa, which is consistent with the manufacturer for active collagenase. These data suggest that 6.5 nm is the minimum enzyme radius and the true radius of the active enzyme will be larger.

We next estimated Michaelis-Menten kinetics using a commercially available kit for a generic MMP substrate. The characterizations are shown in Figure S3. From these plots, we estimated kcat and Km for collagenase in solution. While these values provide a starting point, the peptide used in this study likely has different kinetic constants than the peptide provided by the commercial kit. Furthermore, a different study confirmed that when the peptide is attached to PEG, the kinetic constants differ from those in solution and have been reported to be higher [3].

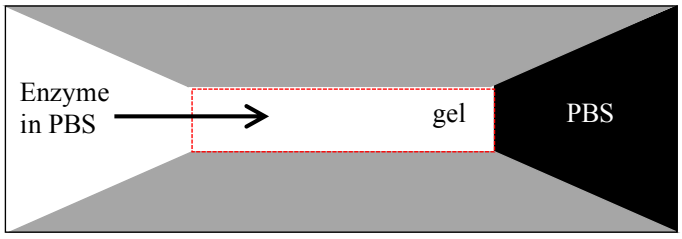

Parameter	Value	Unit
Q^0	7.9 ± 0.8	--
G^0	66 ± 7	kPa
E^0	252 ± 14	kPa
ξ^0	17.6 ± 1.6	nm
c_e^0	0.25	mg/ml

Figure A.1: *The experimental set-up, the initial hydrogel properties for the non- degradable hydrogel, and enzyme concentration used in this study.*

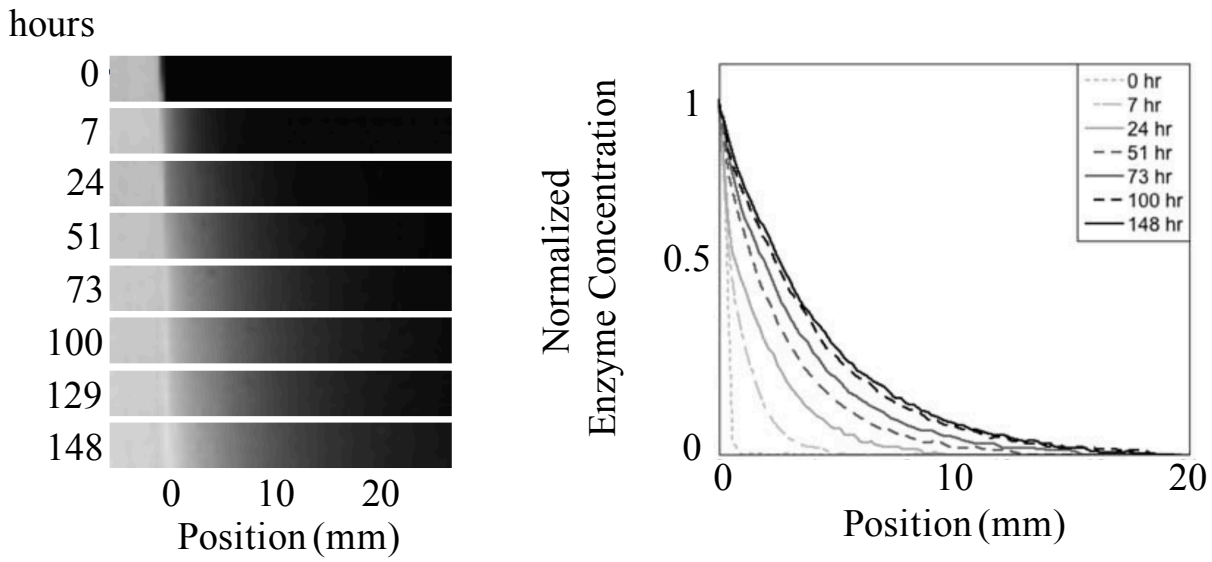

Figure A.2: *Images were acquired of the fluorescently labeled collagenase as it diffused into the hydrogel over time. Fluorescence intensity, correlating to enzyme concentration, was determined as a function of position and time and normalized to the intensity in the reservoir. The reservoir was replenished daily to maintain a constant enzyme concentration.*

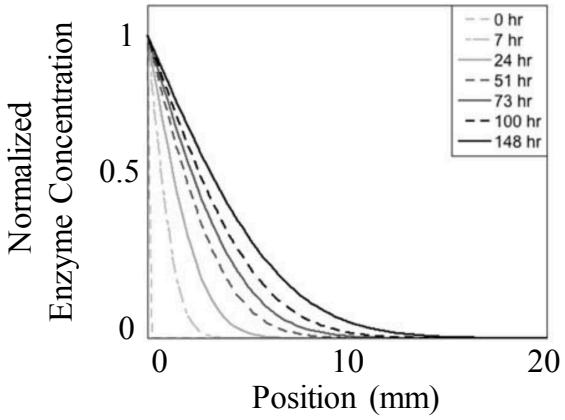

Parameter	Value	Unit
r_e	6.5	nm

Figure A.3: *The mathematical model was fit to experimental data and the average radius of the enzyme was estimated to be 6.5 nm.*

A.2 Calibration and validation of the mathematical model with experimental data

Results from the mathematical model were also compared to the experimental data with respect to normalized fluorescence in the hydrogel as a function of distance from the enzyme source for the experiments and to normalized hydrogel crosslink density as a function of distance from the enzyme source for the simulations. Select time points for the experimental and simulation results for each crosslinked hydrogel case are shown in Figure S4. Overall, the simulation results matched well with the experimental data with respect to front velocity and front width for all three hydrogel cases. However for the low crosslink density case, the model predicted an overall decrease in the bulk hydrogel crosslink density, which was not captured in the experiments. This discrepancy can be explained by the nature in which the experiments were performed. The hydrogels were maintained in an incubator at 37 ^{o}C and therefore it was not possible to continuously image the same sample throughout the course of the experiment. As a result, the fluorescence intensity varied every time the sample was imaged, due to limitations inherent to the camera. To account for sample-to-sample variations, the fluorescence was normalized to the maximum fluorescence within each sample and at each time point. For the intermediate and high crosslink hydrogel cases,

which did not experience any significant bulk degradation, the maximum fluorescence correlates to the initial crosslink hydrogel. The normalized fluorescence values matched well with normalized crosslink density values from the model. On the contrary, for the low crosslink density case where bulk degradation occurred, crosslink density in the bulk hydrogel should decrease over time, as predicted by the model. However, it was not possible to capture the changes in fluorescence intensity that occurred over time in our experimental set-up. For this reason, the normalized fluorescence intensity values over-predicted the crosslink density and did not match the simulations. However having verified the front velocities and confirmed the model matches the intermediate and high crosslink hydrogel cases, we can use the model for the low crosslink density case to provide insight into the actual changes in crosslink density as a function of space and time.

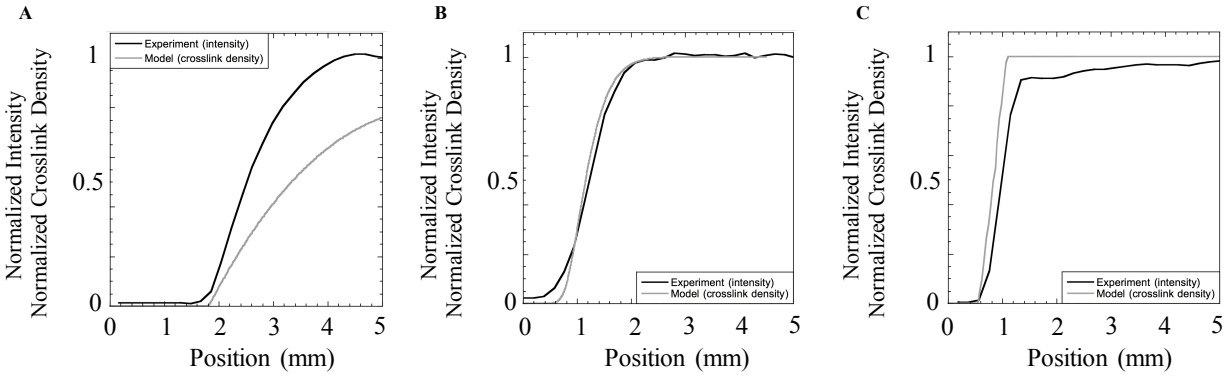

Figure A.4: *Comparisons between experimental and model results for the 1D experiments for the 148 hour time point. The fluorescence intensity at each location in a given hydrogel and time point was normalized to the maximum fluorescence intensity. In the simulations, crosslink density is calculated as a function of time and distance away from the enzyme source. The model matches well to the experiments with respect to the propagating front and front width for all hydrogel cases. However due to the inherent experimental system limitations, the fluorescence intensity for the low crosslink density case did not match the predicted normalized crosslink density.*

A.3 Non-dimensionalizing the governing equations

The degradation behavior of enzyme-sensitive hydrogels can be described by two governing and coupled equations, Equation S3 and Equation S7. However to simplify the equations and identify parameters that can be used as a design tool, we non-dimensionalized the governing equations. For this, we describe diffusion and degradation for the 1D case with the cartesian coordinate system and introduce the following non-dimensional variables:

$$x^* = \frac{x}{L}, \quad t^* = \frac{tD_\infty e^{1/(Q_0-1)}}{L^2}, \quad c_e^* = \frac{c_e}{c_e^0}, \rho_x^* = \frac{\rho_x}{\rho_c}, \quad K_M^* = \frac{K_M(Q_0-1)}{\rho_c} \tag{A.9}$$

where L is a typical length scale of the problem under investigation. In this study, we chose 2 mm as the characteristic length. Here, c_e^0 is the enzyme concentration in the reservoir. Substituting the above variables in S3 and S7 the governing equations become:

$$\frac{Dc_e^*}{Dt^*} = \frac{\partial}{\partial x^*}\left[\left(1 - H(\rho_x^* - 1)\alpha\sqrt{\rho_x^*}\right)\frac{\partial c_e^*}{\partial x^*}\right] \tag{A.10}$$

and

$$\frac{D\rho_x^*}{Dt} = -\kappa c_e^*\left(\frac{\rho_x^*}{K_M^* + \rho_x^*}\right) \tag{A.11}$$

where the following dimensionless parameters were identified:

$$\alpha_e = \frac{r_e\sqrt{\rho_c}}{Q_0^{1/3}}\left(\frac{M_r}{3\ell^2 C_n \rho^P}\right)^{1/2}, \tag{A.12}$$

$$\kappa = \frac{k_{cat}c_e^0 L^2}{D_\infty \rho_c}(Q_0 - 1)e^{1/(Q_0-1)} \tag{A.13}$$

$$\rho_x^{0*} = \frac{\rho_x^0}{\rho_c}, \text{ and} \tag{A.14}$$

$$K_M^* = \frac{K_M(Q_0-1)}{\rho_c} \tag{A.15}$$

We can see here that α_e is a relative measure of the enzyme size (compared to the hydrogel mesh size),κ represents the competition between enzyme degradation and enzyme diffusion, while ρ_x^{0*} and K_M^* were normalized with the critical crosslink density.

Appendix B

Finite Element Formulation for 3D Growth Model at Finite Strain

In this chapter, we will summarize the transport and mechanics equations for cell-mediated tissue growth. The transport of the ECM building blocks (molecules) follows the same governing equations as the enzyme molecules:

$$\frac{DC_m}{Dt} - \nabla_{\mathbf{X}} \cdot \left[\left(1 - \frac{r_m}{\xi(\rho, J)} \right) f(J, J_0) \left(C_m \frac{\bar{\kappa}\nu_w}{J-1} \nabla_{\mathbf{X}} \cdot (\mathbf{C}^{-1} J p) + \bar{D}_m^{\infty} \nabla_{\mathbf{X}} C_m \right) \right] = \Gamma_m \tag{B.1}$$

where the diffusivity scaling law is:

$$\bar{D}_m = \bar{D}_m^{\infty} f(J, J_0) \left(1 - \frac{r_m}{\xi(\rho, J)} \right) \tag{B.2}$$

In other words, for the transport, we distinguish the ECM molecules only by their hydrodynamic radius and deposition/degradation kinetics lumped to Γ_m. The mass balance of the deposited ECM follows the same form of the mass balance law as the scaffold, that is;

$$\frac{\partial C_m^{\star}}{\partial t} = \Gamma_m \tag{B.3}$$

The deposition of the ECM results in a new material with elasticity. Before going into the mechanics of deposited material let us first discuss its kinematics. Consider that the fluid specie Φ_α is active and deposited between time 0 and t at a material point $\mathbf{X}$ with a rate Γ_α. Then the nominal volume fraction of bounded counterpart $\Phi_\alpha^{\star}$ at time t becomes;

$$\Phi_\alpha^{\star}(t) = \Phi_\alpha^{\star}(0) + \int_0^t \Gamma_\alpha \nu_\alpha dt \tag{B.4}$$

In order to determine the state of the mixture at time t, the current position $\mathbf{x}$ of a material point $\mathbf{X}$ should be determined. Here we define the current position $\mathbf{x} = \boldsymbol{\chi}(\mathbf{X}, t)$ as a differentiable function of initial position and time. Now consider that an infinitesimal material $\delta\Phi_\alpha^\star$ is bounded to its solid phase at time $\bar{t}$ at a material point $\mathbf{X}$. The deformation of this material at time t depends on; (a) the its state of deformation at $\bar{t}$, (b) the deformation experienced from $\bar{t}$ to t. Deformation gradient at time $\bar{t}$ can be decomposed to its pure rotation and stretch components as $\mathbf{F}(\mathbf{X}, \bar{t}) = \mathbf{R}(\mathbf{X}, \bar{t})\mathbf{U}(\mathbf{X}, \bar{t})$. Here we assume that the fluid material experiences the same rotation with the solid material, which allows us to define the deformation using symmteric stretch tensor. For convinience, we will continue to call residual deformation tensor as $\bar{\mathbf{F}}$. We know that the total deformation of the material $\delta\Phi_\alpha^\star$ at time t is the multiplicative addition of its initial deformation and the deformation it has experienced in its solid state, which can be written as;

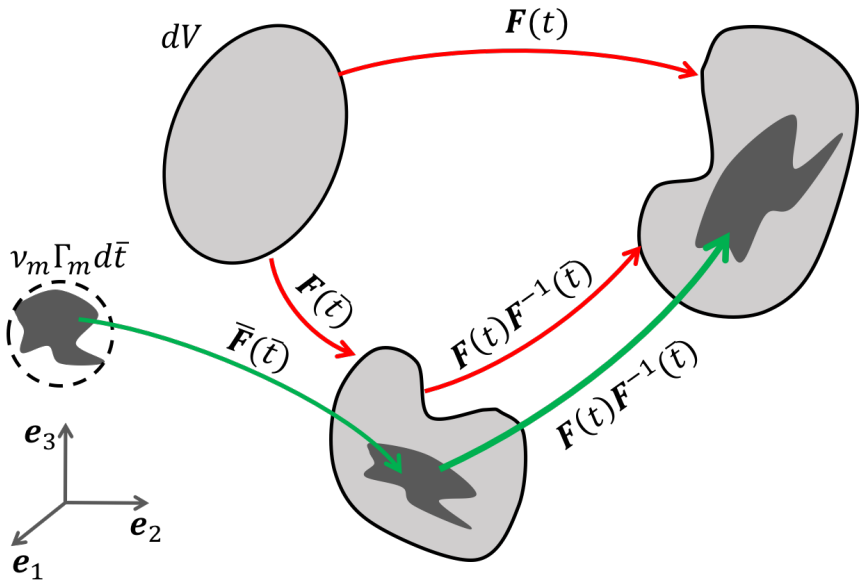

Figure B.1: Configuration of the domain of interest at the initial and current frames

$$\mathbf{F}_\alpha(t; \bar{t}) = \mathbf{F}(t)\mathbf{H}_\alpha(\bar{t}) \tag{B.5}$$

where $\mathbf{H}_\alpha(\bar{t}) = [\mathbf{F}(\bar{t})]^{-1}\,\bar{\mathbf{F}}_\alpha(\bar{t})$ is called growth history tensor of solid specie α. Recall that both the deformation gradient and growth history tensor are function of initial position and the term $\mathbf{X}$ is

dropped for only for clarity. In solid mechanics, it is convenient to use symmetrical tensors as right Cauchy deformation $\mathbf{C}_\alpha(t,\bar{t})$ and Green-Lagrange strain $\mathbf{E}_\alpha(t,\bar{t})$ tensors, which take the form;

$$\mathbf{C}_\alpha(t,\bar{t}) = \mathbf{H}_\alpha^T(\bar{t})(\mathbf{F}^T\mathbf{F})\mathbf{H}_\alpha(\bar{t}) \tag{B.6}$$

$$\mathbf{E}_\alpha(t,\bar{t}) = \frac{1}{2}\left[\mathbf{C}_\alpha(t,\bar{t}) - \mathbf{I}\right] \tag{B.7}$$

Note that we omitted the term t in the deformation gradient if it is the mapping between time 0 and t. Once again, consider the infinitesimal material $\delta\Phi_\alpha^\star(\bar{t})$ deposited at time $\bar{t}$ while its fluid counter part would be $\delta\Phi_\alpha(\bar{t})$. Its elastic energy per unit reference volume at time t is $\psi_\alpha(\mathbf{E}(t;\bar{t}))$ which depends on the history of deformation starting from the deposition time. An infinitesimal material volume can be defined as $\delta(\Phi_\alpha^\star(\bar{t})) = \nu_\alpha\Gamma_\alpha d\bar{t}$. Since the deposition is a continuous process, elastic energy of the constituent α at time t is expressed as;

$$\Delta G_\alpha^{el} = (\Phi_\alpha^\star(0))\psi_\alpha(\mathbf{E}(t;0)) + \int_0^t \nu_\alpha\Gamma_\alpha(\bar{t})\psi_\alpha(\mathbf{E}_\alpha(t;\bar{t}))d\bar{t} \tag{B.8}$$

The first term in the right hand side is the elastic energy of the material that exists at the beginning, and it is function of the total deformation. The second term is the energy of the deposited material is a function of its deformation at free configuration and the deformation subjected after deposition. This is a generalized definition of elastic energy for evolving material, which can also be applied to the polymer network of the scaffold. In our case, the energy of the polymer network is the first term on the right hand side of equation B.8 and its mass decreases over time ue to degradation. We capture this by removal of material, i.e. decrease in the mass $\Phi_\alpha^\star$.

The extracellular matrix (ECM) has an elasticity based on the properties of its building blocks (such as collagen and proteoglycan) and their assembly mechanics. Because it is extremely challenging to measure such properties, we assume that the elasticity of ECM can be represented by Saint Venant-Kirchhoff material model;

$$\psi_m(\mathbf{E}_m) = \frac{\lambda}{2}[\mathrm{tr}(\mathbf{E}_m)]^2 + G\mathrm{tr}(\mathbf{E}_m^2) \tag{B.9}$$

where λ and G are Lame parameters. Here we would like to recall that there is no ECM in the construct initially, therefore $\Phi_m^\star(0) = 0$. After introducing the relations above, the balance of

momentum changes to

$$\nabla^{\star}_{\mathbf{X}} \cdot (\mathbf{S}_s + \mathbf{S}_w + \mathbf{S}_m\mathbf{F}) = 0 \tag{B.10}$$

where

$$\mathbf{S}_m(t) = \int_0^t \nu_m \Gamma_m \mathbf{H}_m(\bar{t}) \left(\lambda \mathrm{tr}(\mathbf{E}_m)\mathbf{I} + 2G\mathbf{E}_m\right) \mathbf{H}_m^T(\bar{t}) d\bar{t} \tag{B.11}$$

for the deposition we use the follwing firs order kinetics relation:

$$\Gamma_m = k_m^f c_m - k_m^{\star} c_m^{\star} \tag{B.12}$$

where k_m^f and $k_m^{\star}$ are deposition and disassociation rates respectively.

The numerical procedure for linearization is similar to that given in the chapter 4. Furthermore, a numerical strategy is necessary for calculating the linearized form of the stress state of the bounded matrix because of the history dependence. For this reason we introduce a discretized form of the equation B.11 assuming that time increment Δt is small enough;

$$\mathbf{S_m} = \sum_r \nu_m \Gamma_m(t_r) \mathbf{H}_m(t_r) \left(\lambda tr(\mathbf{E}_m(t_r))\mathbf{I} + 2G\mathbf{E}_m(t_r)\right) \mathbf{H}_m^T(t_r) \Delta t \tag{B.13}$$

where $t_r = r \times \Delta t$ and $r = 0, 1, 2, 3, 4...s$. Note that this equation can be rewritten in terms of its only unknown $\mathbf{u}$ using the kinematic relation B.6. We define the elasticity tensor $(\mathbb{C}_m)_{IJKL}$ as the response of the deposited material to the variation in the deformation tensor $\mathbf{C}(t)$, in other words it is mapped to the reference configuration. To find such definition, we use the chain rule;

$$(\mathbb{C}_m)_{IJKL} = \frac{\partial (S_m)_{IJ}}{\partial E_{KL}} = \frac{\partial (S_m)_{IJ}}{\partial (E_m)_{PQ}} \frac{\partial (E_m)_{PQ}}{\partial E_{KL}} \tag{B.14}$$

when the equations B.7 and B.13 are plugged in, the elasticity tensor of bounded ECM becomes;

$$(\mathbb{C}_m)_{IJKL} = \sum_r^s \left[\nu_m \Gamma_m \left(\lambda (H_m)_{IR}(H_m)_{JR}\delta_{ST} + 2G(H_m)_{IS}(H_m)_{JT}\right)(H_m)_{KS}(H_m)_{LT}\right] \Delta t \tag{B.15}$$

where δ_{ST} is kronecker delta. For simplicity we assume that initial deformation of bounded material $\bar{\mathbf{F}}(\bar{t})$ does not depend on time of deposition, which allows us to calculate history tensor $\mathbf{H}_m$ using the deformation history of the construct. Therefore storing the displacement field history is sufficient

to calculate the stress of the bounded ECM. We introduce a new term into the linearization of momentum balance:

$$\int_{\Omega_0} (\boldsymbol{\nabla}_{\mathbf{X}} \mathbf{w}^s) : \sum_{\alpha} \left(\frac{\partial \mathbf{S}_\alpha}{\partial \mathbf{u}} \mathbf{F} \delta \mathbf{u} + \frac{\partial \mathbf{S}_\alpha}{\partial p} \mathbf{F} \delta p + \mathbf{S}_\alpha \frac{\partial \mathbf{F}}{\partial \mathbf{u}} \delta \mathbf{u} + \frac{\partial \mathbf{S}_m}{\partial C_m} \mathbf{F} \delta C_m \right) dV = \int_{\partial \Omega_0} \mathbf{w}^s \cdot \sum_{\alpha} \mathbf{t}_\alpha dS \tag{B.16}$$

The rest of the numerical implementation of balances of mass and momentum for the ECM can be done following the chapter 4. The final form of the stiffness and damping matrices become:

$$\mathbf{F} = \begin{bmatrix} \mathbf{F}^s \\ \mathbf{F}^w \\ \mathbf{F}^e \\ \mathbf{F}^m \end{bmatrix} \; ; \; \mathbf{K} = \begin{bmatrix} \mathbf{K}_{ss} & \mathbf{K}_{sw} & \mathbf{0} & \mathbf{K}_{sm} \\ \mathbf{K}_{ws} & \mathbf{K}_{ww} & \mathbf{0} & \mathbf{0} \\ \mathbf{K}_{es} & \mathbf{K}_{ew} & \mathbf{K}_{ee} & \mathbf{0} \\ \mathbf{K}_{ms} & \mathbf{K}_{mw} & \mathbf{0} & \mathbf{K}_{mm} \end{bmatrix} \; ; \; \boldsymbol{C} = \begin{bmatrix} \mathbf{0} & \mathbf{0} & \mathbf{0} & \mathbf{0} \\ \mathbf{C}_{ws} & \mathbf{0} & \mathbf{0} & \mathbf{0} \\ \mathbf{0} & \mathbf{0} & \mathbf{C}_{ee} & \mathbf{0} \\ \mathbf{0} & \mathbf{0} & \mathbf{0} & \mathbf{C}_{mm} \end{bmatrix} \tag{B.17}$$

Appendix C

Finite Element Formulation for 3D Growth Model at Small Strain

In order to describe the tissue growth in porous scaffolds we use three balance law; balance of linear momentum (equation (3.6)), balance of mass (equation (3.3)) and the equation of osmotic pressure (equation (3.6)):

$$\nabla \cdot (\boldsymbol{\sigma}_p + \boldsymbol{\sigma}_m - p\mathbf{I}) = \mathbf{0} \tag{C.1}$$

$$\frac{Dc_m^*}{Dt^*} = \nabla \cdot (D_m^* \nabla c_m^*) - c_m^* \nabla \cdot \dot{\mathbf{u}}^* - \kappa_m^* \left(1 - \frac{\tilde{c}_m^*}{\tilde{c}_m^0}\right) c_m^* \tag{C.2}$$

$$\frac{Dc_e^*}{Dt^*} = \nabla \cdot (D_e^* \nabla c_e^*) - c_m^* \nabla \cdot \dot{\mathbf{u}}^* \tag{C.3}$$

$$\ln \phi_w + (1 - \phi_w) + \chi(1 - \phi_w)^2 + p^* \nu_w = 0 \tag{C.4}$$

These governing equations are solved in three-dimension for the displacement field $\mathbf{u}$, the pore pressure p, the concentration of enzyme c_e and ECM c_m. Moreover we treat the crosslinking density ρ and concentration of deposited ECM $\tilde{c}_m$ as internal state variables for which we use degradation/deposition kinetics law (equations (4.1) and (3.5)). We use finite element method to solve the system of equations for which the weak form is written as follows:

$$\int_V \nabla \mathbf{w}_1^T \cdot (\boldsymbol{\sigma}_p + \boldsymbol{\sigma}_m - p^* \mathbf{I}) dV = \int_{S_0} \mathbf{w}_1^T \mathbf{t}_0 dS \tag{C.5}$$

$$\int_V \mathbf{w}_2^T \frac{\partial c_m^*}{\partial t^*} + \nabla \mathbf{w}_2^T \cdot (\dot{\mathbf{u}}^* c_m^*) dV + \int_V \nabla \mathbf{w}_2^T (D_m^*) \nabla c_m^* dV + \int_V \mathbf{w}_2^T \kappa_m^* \left(1 - \frac{\tilde{c}_m^*}{\tilde{c}_m^0}\right) c_m^* dV = \int_{S_0} \mathbf{w}_2^T \mathbf{Q}_m dS \tag{C.6}$$

$$\int_V \mathbf{w}_2^T \frac{\partial c_e^*}{\partial t^*} + \nabla \mathbf{w}_2^T \cdot (\dot{\mathbf{u}}^* c_e^*) dV + \int_V \nabla \mathbf{w}_2^T (D_e^*) \nabla c_e^* dV = \int_{S_0} \mathbf{w}_2^T \mathbf{Q}_e dS \tag{C.7}$$

$$\int_V \mathbf{w}_2^T (\ln \phi_w + (1 - \phi_w) + \chi (1 - \phi_w)^2 + p^* \nu_w) dV = 0 \tag{C.8}$$

Note that these equations are coupled and nonlinear in terms of the field variables. Also note that if the deformation field is small (5-10% strain) then the nonlinearities due to deformation and material behavior vanishes which leads the linear the balance of of linear momentum equation. The linearized forms are as follows:

$$\int_V \nabla \mathbf{w}_1^T \cdot \left[\left(\frac{\partial \boldsymbol{\sigma}_p}{\partial \boldsymbol{\epsilon}} + \frac{\partial \boldsymbol{\sigma}_m}{\partial \boldsymbol{\epsilon}} \right) \frac{\partial \boldsymbol{\epsilon}}{\partial \mathbf{u}^*} \delta \mathbf{u}^* + \mathbf{I} \delta p^* \right] dV = \int_{S_0} \mathbf{w}_1^T \mathbf{t}_0 dS \tag{C.9}$$

$$\int_V \mathbf{w}_2^T \frac{\partial \delta c_m^*}{\partial t^*} + \nabla \mathbf{w}_2^T \cdot (\delta \dot{\mathbf{u}}^* c_m^* + \dot{\mathbf{u}}^* \delta c_m^*) dV + \int_V \nabla \mathbf{w}_2^T (D_m^*) \nabla \delta c_m^* dV + \int_V \mathbf{w}_2^T \kappa_m^* \left(1 - \frac{\tilde{c}_m^*}{\tilde{c}_m^0}\right) \delta c_m^* dV = \int_{S_0} \mathbf{w}_2^T \mathbf{Q}_m dS \tag{C.10}$$

$$\int_V \mathbf{w}_2^T \frac{\partial \delta c_e^*}{\partial t^*} + \nabla \mathbf{w}_2^T \cdot (\delta \dot{\mathbf{u}}^* c_e^* + \dot{\mathbf{u}}^* \delta c_e^*) dV + \int_V \nabla \mathbf{w}_2^T (D_e^*) \nabla \delta c_e^* dV = \int_{S_0} \mathbf{w}_2^T \mathbf{Q}_e dS \tag{C.11}$$

$$\int_V \mathbf{w}_2^T \left[\left(\frac{1 - \phi_w}{\phi_w} - 2\chi (1 - \phi_w) \right) J^{-2} \frac{\partial J}{\partial \mathbf{u}^*} \delta \mathbf{u}^* + \nu_w \delta p^* \right] dV = 0 \tag{C.12}$$

where the left and right hand sides are called internal $\mathbf{F}_{int}$ and external $\mathbf{F}_{ext}$ force vectors respectively. After linearization our solution scheme becomes iterative in which we are solving for $\delta \mathbf{d} = [\delta \mathbf{u}^* \delta p^* \delta c_e^* \delta c_m^*]$ with the stopping criterion $|\mathbf{R}|_\infty \approx 0$ where $\mathbf{R} = \mathbf{F}_{ext} - \mathbf{F}_{int}$. As the iterative method we chose Newton-Raphson, and in order to capture the transient behavior we implemented this method in backward Euler time integration scheme:

$$\delta\dot{\mathbf{d}}^i(t^*+\Delta t^*) = [\mathbf{C}^{i-1}(t^*+\Delta^*) + \mathbf{K}^{i-1}(t^*+\Delta t^*)\Delta t^*]^{-1}\mathbf{R}^{i-1}(t^*+\Delta t^*) \tag{C.13}$$

$$\dot{\mathbf{d}}^i(t^*+\Delta t^*) = \dot{\mathbf{d}}^{i-1}(t^*+\Delta t^*) + \delta\dot{\mathbf{d}}^i(t^*+\Delta t^*) \tag{C.14}$$

$$\mathbf{d}(t^*+\Delta t^*) = \dot{\mathbf{d}}(t^*+\Delta t^*)\Delta t^* + \mathbf{d}(t^*) \tag{C.15}$$

where $\mathbf{C}$, $\mathbf{K}$, $\mathbf{R}$ are the damping matrix stiffness matrix and residual vector respectively. In order to calculate these matrices and vector we use the FE discretization as follows. We used a mixed $\mathbf{u}-p$ formulation, that is 27-node element for and 8-node element for p^*. Moreover for the concentration fields c_m^* and c_e^* 8-node element formulation is used. The test functions $\mathbf{w}_1$ and $\mathbf{w}_2$ and the interpolation of the fields then becomes:

$$\begin{gathered}\mathbf{w}_1 = \mathbf{N}_{27}\bar{\mathbf{w}}_1 \quad \text{and} \quad \mathbf{w}_2 = \mathbf{N}_8\bar{\mathbf{w}}_2 \\ \mathbf{u}_1^* = \mathbf{N}_{27}\bar{\mathbf{u}}^* \quad p^* = \mathbf{N}_8\bar{\mathbf{p}}^* \quad c_m^* = \mathbf{N}_8\bar{\mathbf{c}}_m^* \quad \text{and} \quad c_e^* = \mathbf{N}_8\bar{\mathbf{c}}_e^*\end{gathered} \tag{C.16}$$

Note that same interpolation rules are used for the rates of these fields. The stiffness and damping matrices become:

$$\mathbf{K} = \begin{bmatrix} \mathbf{K}_{uu} & \mathbf{K}_{up} & \mathbf{0} & \mathbf{0} \\ \mathbf{K}_{pu} & \mathbf{K}_{pp} & \mathbf{0} & \mathbf{0} \\ \mathbf{0} & \mathbf{0} & \mathbf{K}_{mm} & \mathbf{0} \\ \mathbf{0} & \mathbf{0} & \mathbf{0} & \mathbf{K}_{ee} \end{bmatrix}.$$

$$\mathbf{C} = \begin{bmatrix} \mathbf{0} & \mathbf{0} & \mathbf{0} & \mathbf{0} \\ \mathbf{0} & \mathbf{0} & \mathbf{0} & \mathbf{0} \\ \mathbf{C}_{mu} & \mathbf{0} & \mathbf{C}_{mm} & \mathbf{0} \\ \mathbf{C}_{eu} & \mathbf{0} & \mathbf{0} & \mathbf{C}_{ee} \end{bmatrix}.$$

where

$$\mathbf{K}_{uu} = \sum_1^{el} \int_{V_0} \mathbf{B}_1^T(\mathbf{C}_p + \mathbf{C}_m)\mathbf{B}_1 dV \tag{C.17}$$

$$\mathbf{K}_{up} = \sum_{1}^{el} \int_{V_0} \mathbf{B}_1^T(\mathbf{I}) \mathbf{N}_8 dV \tag{C.18}$$

$$\mathbf{K}_{pu} = \sum_{1}^{el} \int_{V_0} \mathbf{N}_8^T \left(\frac{1-\phi_w}{\phi_w} - 2\chi(1-\phi_w) \right) J^{-2} \mathrm{adj}(\mathbf{F}) \mathbf{B}_1 dV \tag{C.19}$$

$$\mathbf{K}_{pp} = \sum_{1}^{el} \int_{V_0} \mathbf{N}_8^T(\nu_w) \mathbf{N}_8 dV \tag{C.20}$$

$$\mathbf{K}_{mm} = \sum_{1}^{el} \int_{V_0} \left[\mathbf{N}_8^T(\dot{\mathbf{u}} + \kappa_m \left(1 - \frac{\tilde{c}_m^*}{\tilde{c}_m^0} \right) + \mathbf{B}_2^T(D_m^*) \mathbf{B}_2 \right] dV \tag{C.21}$$

$$\mathbf{K}_{ee} = \sum_{1}^{el} \int_{V_0} \left[\mathbf{N}_8^T(\dot{\mathbf{u}}) + \mathbf{B}_2^T(D_e^*) \mathbf{B}_2 \right] dV \tag{C.22}$$

$$\mathbf{C}_{mu} = \sum_{1}^{el} \int_{V_0} \mathbf{N}_8^T(c_m^*) \mathbf{N}_{27} dV \tag{C.23}$$

$$\mathbf{C}_{mm} = \sum_{1}^{el} \int_{V_0} \mathbf{N}_8^T \mathbf{N}_8 dV \tag{C.24}$$

$$\mathbf{C}_{eu} = \sum_{1}^{el} \int_{V_0} \mathbf{N}_8^T(c_e^*) \mathbf{N}_{27} dV \tag{C.25}$$

$$\mathbf{C}_{ee} = \sum_{1}^{el} \int_{V_0} \mathbf{N}_8^T \mathbf{N}_8 dV \tag{C.26}$$

where

$$\mathbf{C}_p = 2\rho H(\rho - \rho_c) RT \frac{J_0^{2/3}}{J} \mathbf{C} \tag{C.27}$$

$$\mathbf{C}_m = \tilde{C}_m^* (\lambda^* (\mathbf{I} \otimes \mathbf{I}) + \mu^*(\mathbf{C})) \tag{C.28}$$

$$\boldsymbol{\mathcal{B}}_1 = \begin{bmatrix} \frac{\partial \mathbf{N}_{27}}{\partial \mathbf{x}^*} & \mathbf{0} & \mathbf{0} \\ \mathbf{0} & \frac{\partial \mathbf{N}_{27}}{\partial \mathbf{x}^*} & \mathbf{0} \\ \mathbf{0} & \mathbf{0} & \frac{\partial \mathbf{N}_{27}}{\partial \mathbf{x}^*} \end{bmatrix} \tag{C.29}$$

$$\mathbf{B}_2 = [\partial \mathbf{N}_8 / \partial \mathbf{x}^*] \tag{C.30}$$

Verification of the model is performed by comparing the solution with that of 1D degradation-diffusion model presented in [135] (Figure C.1 c). In order to check the consistency of the model, we investigated the spatial and temporal change of crosslinking density ρ along the diffusion direction. Note from equation (4.1) that any numerical error in the enzyme transport affects the calculated

crosslinking density. The error in crosslinking density depending on the mesh size (Figure C.1 a) and time step (Figure C.1 b) is calculated using UN norm:

$$e_2^\rho = \left[\int_V (\rho^{k+1} - \rho^k)^2 dV \right]^{1/2} \tag{C.31}$$

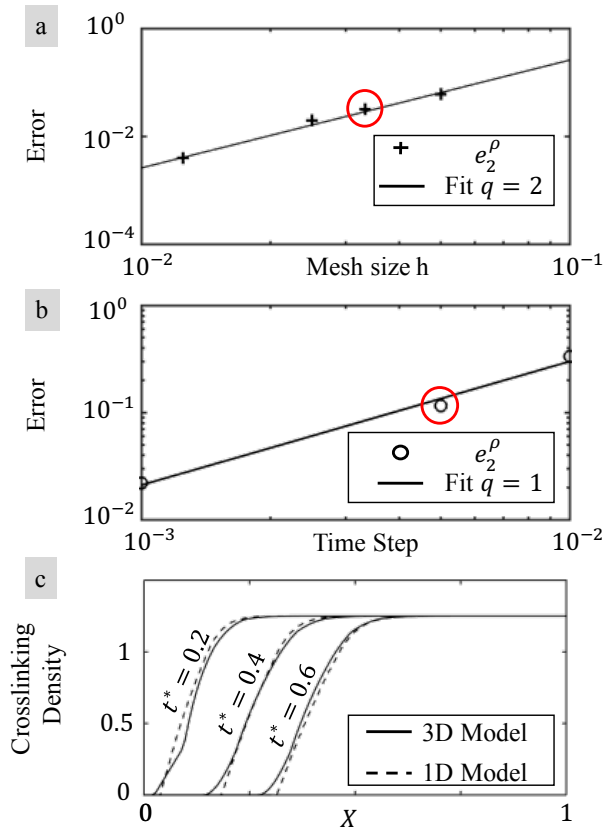

Figure C.1: *Convergence study. (a) Convergence of the error measure (C.31) in as a function of mesh size h. (b) Convergence of the error measure (C.31) in as a function of time step. (c) Comparison of the model prediction with the one presented in [135] for the evolution of crosslinking density using the mesh size and time step that are marked with red circles in (a) and (b).*

The convergence rate of the error is determined by fitting a least square curve to the calculated errors. The convergence rate with respect to the mesh size is quadratic, in agreement with theoretical predictions [32]. Moreover the convergence of the Euler time integration scheme is linear as expected [32]. For the analysis in this paper we chose a mesh size and time step given by $h^* = 0.08$ (shown in red circle in Figure 8 a) and $\Delta t^* = 0.006$ (shown in red circle in Figure C.1 b), which provides reasonable accuracy (Figure C.1 c).